



Engineering cardiac microenvironments for functional drug safety screening

Christensen, Rie Kjær

Publication date:
2020

Document Version
Publisher's PDF, also known as Version of record

[Link back to DTU Orbit](#)

Citation (APA):
Christensen, R. K. (2020). *Engineering cardiac microenvironments for functional drug safety screening*. DTU Health Technology.

General rights

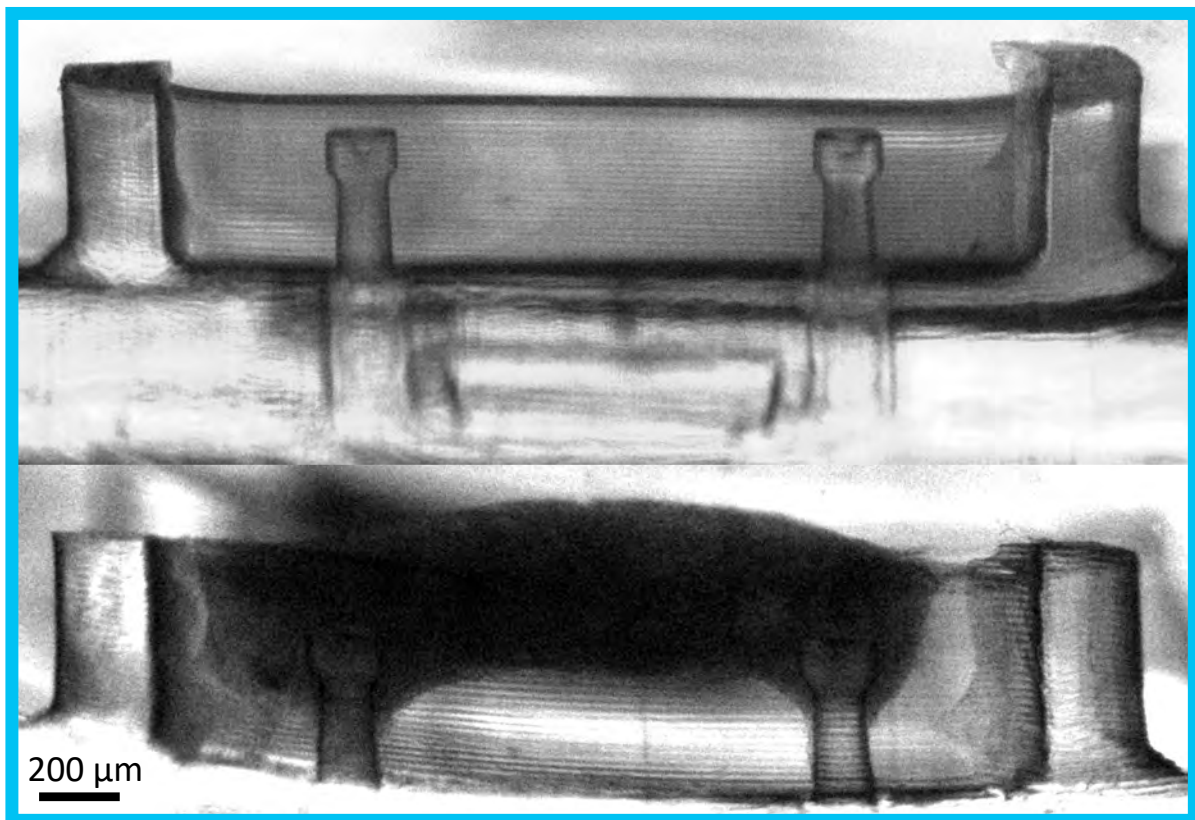
Copyright and moral rights for the publications made accessible in the public portal are retained by the authors and/or other copyright owners and it is a condition of accessing publications that users recognise and abide by the legal requirements associated with these rights.

- Users may download and print one copy of any publication from the public portal for the purpose of private study or research.
- You may not further distribute the material or use it for any profit-making activity or commercial gain
- You may freely distribute the URL identifying the publication in the public portal

If you believe that this document breaches copyright please contact us providing details, and we will remove access to the work immediately and investigate your claim.

Engineering cardiac microenvironments for functional drug safety screening

Ph.D. Thesis by Rie Kjær Christensen



An industrial Ph.D. project with:
Sophion Bioscience A/S
Technical University of Denmark
Department of Health Technology

Supervisors:
Professor Niels Bent Larsen
Ph.D. Sandra Wilson
Ph.D. Peder Skaft-Pedersen

Preface

This thesis is submitted as partial fulfillment of the formal requirements to acquire the Ph.D. degree at the Technical University of Denmark (DTU). I have been enrolled as an industrial PhD student at DTU and employed with Sophion Bioscience A/S. The work has taken place from February 2017 to March 2020. The work has been carried out at DTU Lyngby, in the Department of Health Technology (former Department of Micro- and Nanotechnology), at Sophion Bioscience A/S in Denmark, and at Instituto de Biologia Experimental e Tecnológica (iBET) in Portugal. The industrial Ph.D. studies have been funded by Innovation Fund Denmark (Grant 5189-00149B) and part of the project has been funded through EUREKA Eurostars grant Cardiocontract (Grant 01032018).

The project has been supervised by Professor Niels Bent Larsen from the Immunology and Biomimetics section, Polymer Cell group, at DTU, Ph.D. Sandra Wilson and Ph.D. Peder Skafte-Pedersen at Sophion Bioscience A/S. During my external stay from May 2019 to July 2019 I was working in the Animal Cell Technology Unit led by Ph.D. Maria Margarida Serra.

Acknowledgments

I want to thank everyone at Sophion Bioscience A/S for making my Ph.D. a pleasant experience. Thanks for all of the help, moral support, and cheering that I have experienced during my Ph.D., especially during the last months. Without the encouraging attitude that I have experienced the last few months it would have been a very different experience. A special thanks to Peder and Louise for always being ready to help on the spot with whatever problem I might have, and for tireless proofreading of my thesis during the past month. Torben and Jens for always having solutions to software and hardware issues. Mette, Kadla, and Anders for helping out in the laboratory and helping me understand electrophysiology. And a special thanks to Sandra for always supporting my decisions with a helping critical eye, and giving me room to try all of my ideas.

I also want to thank all of my colleagues in the PolyCell group and fellow Ph.D. students at DTU for good talks, help, and for being great friends. I have enjoyed the environment at the University for being a place to share experiences and concerns about the Ph.D. journey. I have experienced a group of people from whom you can always ask for help and where a favor can always be asked. Particularly Christoffer who have been an invaluable help during tough times and a good partner for discussion during the last year of my Ph.D. Aysel for always being a great friend and for the help to characterize my samples with immunohistochemistry. A special thanks also to my supervisor Niels, who always managed to find time to help and answer questions, both in the lab and for professional back-and-forth about various topics.

During my external stay at iBET I encountered several people; Ph.D.'s, Post. Doc's, and PI's who all were great at teaching me the Portuguese life-style including coffee drinking habits and introducing me to Portuguese cuisine (eating snails!) as well as being good colleagues in the lab. A special thanks to Margarida for hosting me and making me a part of your group and to Marta for endless hours in the lab together and for many good talks. I also want to thank the rest of the friends I got at iBET for many interesting conversations over lunch and fun nights out. I look forward to seeing you in the future and wish you all the best.

Thanks to all of my family and friends who have been extremely supportive, patient and understanding over the last 3 years, especially during those very busy periods where it was difficult for me to commit to plans with you. I am happy that you were compassionate and generous enough to reschedule to fit my experimental timeline numerous times and also that you kept in contact when I was in my Ph.D. bubble. I'm really looking forward to making up for all the lost time and seeing you loads in the future. Of course, very special thanks to Mikkel, your endless support has meant everything to me.

"If you want to be great at something, there's a choice you have to make. What I mean by that is, there are inherent sacrifices that come along with that. Family time, hanging out with friends, being a great friend, being a great son, nephew, whatever the case may be." – Kobe Bryant

My Ph.D. journey would not have been the same without all the great people around me. Thank you all for supporting me in this process and giving me the space to be successful in its demands, even though it meant spending less time with you for a period of time.

Abstract

Cardiotoxic side effects of non-cardiovascular pharmaceutical agents reported in the late 1980's resulted in the safety and efficacy testing guidelines that is used today to evaluate the risk of adverse cardiac effects. However, the current testing method relies on single ion channel testing which has low specificity and results in unnecessary dismissal of potential new drug candidates. Attrition of drug candidates in the late development phases is associated with high costs in addition to the inconvenience to patients missing out on potential useful pharmaceuticals. The use of human induced pluripotent stem cells (hiPSCs) is heavily explored to reach a more human relevant testing model. Both single cell testing with a multiple ion channel approach and the development of engineered cardiac tissues *in vitro* are explored. Engineered cardiac tissues benefits from increased physiological relevance compared to single cell testing as the development potential of stem cell derived cardiomyocytes increases in a 3D environment. Further, engineered cardiac tissues rely on the response from a syncytium of cells with an increased physiological response resembling that of the adult myocardium.

This work focuses on the formation of engineered cardiac tissues by developing a cell seeding multiassay platform (MAP) with room for multiple *in vitro* tissues cultured in parallel. The manufacturing approach uses a novel stereolithographic 3D printing approach to produce MAPs in a compliant non-toxic material. MAPs contain mechanical microenvironments to promote tissue formation including vertical flexible posts with tunable stiffness. Characterization of mechanical properties gives the opportunity to support easy read-out of tissue contraction force using optical tracking. When a cell-loaded scaffold material with muscle mimicking stiffness is seeded into the designed MAPs, engineered tissues self-assemble around the flexible posts to form a defined *in vitro* tissue. Mouse myoblast cells form a confined tissue strip within 3 days of culture with uniaxially aligned cells. The tissue formation can be tracked by following the deflection of the flexible posts during tissue compaction. Upon culturing cardiac progenitor cells inside MAPs the resulting engineered cardiac tissues are synchronously beating suggesting that cellular connections are formed between cells. The contraction force of the cardiac tissues causes the posts to deflect and offer optical read-out of tissue contraction force. Engineered cardiac tissues response to electrical stimulation and allows continuous pacing at 1 Hz for up to 2 weeks. Extended culture time of engineered cardiac tissues under these conditions reveal an increased contraction force with time in culture.

MAPs show promising results for formation of engineered cardiac tissues using a manufacturing method with upscaling potential for industrial use. Engineered cardiac tissues develops inside MAPs to form cellular connection and shows possibility for functional read-out. Further work is needed to show functionality of cardiotoxicity testing using pharmaceutical drugs known to have a high sensitivity with current testing methods.

Resumé

I slutningen af 1980'erne blev der indrapporteret en række utilsigtede kardiotoxiske komplikationer af lægemidler uden tiltænkt virkning på hjerte-kredsløbet. Dette førte til indførelse af de farmakologiske test, der i dag benyttes til at evaluere alvorlige og utilsigtede effekter af lægemidler på hjerte-kredsløbet. De anvendte test beror på påvirkningen af en enkelt ionkanal, hvilket resulterer i en lav specificitet og dermed mulig forkastelse af potentielt virksomme lægemidler. Når nye lægemiddel kandidater kasseres sent i udviklingsfasen er det dyrt for virksomhederne som har lagt et stort udviklingsarbejde bag, samtidig med at potentielle virksomme og nyttige lægemidler ikke finder vej til markedet og de patienter, der har behov for dem. Inducerede pluripotente stamceller afledt fra menneskeceller (hiPSCs) har vundet stort indpas på grund af deres evne til at udvikle sig til hjerteceller og deres brug i udviklingen af kunstige hjertevæv udviklet *in vitro*. Ved at udvikle kunstige væv i et 3D miljø kan man opnå en større fysiologisk lighed til vævet *in vivo* og dermed en effekt som minder om den virkelige respons af hjertemuskulaturen.

Dette studie fokuserer på at udvikle kunstige hjertevæv ved at designe platforme med plads til flere væv i parallel. Fabrikation af platformene er foretaget med en ny stereolitografisk metode til 3D print i et eftergivende materiale som er cellekompatibelt. Platformene indeholder mikromekaniske strukturer til at fremme vævsformation af kunstige væv inklusiv fleksible søjler med en stivhed som kan justeres efter behov. Karakterisering af de mekaniske egenskaber skaber mulighed for at omsætte udlæsningen af vævsrespons til kraft ved hjælp af optisk udlæsning. Celler indlemmet i et blødt hydrogel-materiale, der imiterer *in vivo* muskelhårdhed, omdannes spontant til en vævs-lignende struktur omkring de fleksible søjler. Vævsdannelse med myoblaster fra mus viser at cellerne differentiere og får en aflang ensrettet struktur når de dyrkes i platformene. Vævsdannelsen kan monitoreres over tid ved at følge bøjningen af de fleksible søjler når cellerne trækker hydrogel materialet sammen. Når hjertemuskel væv dannet af stamceller dyrkes i disse platforme begynder hjertecellerne at slå synkront hvilket, indikerer at der er dannet forbindelse imellem cellerne. Kontraktionskraften af det kunstige hjertevæv får de fleksible søjler til at bøje og gør det muligt optisk at aflæse kontraktionskraften ud fra viden om søjlernes mekaniske egenskab. Ved hjælp af en elektrisk stimulering kan de kunstige hjertevæv slå med en frekvens på 1 Hz i op til 2 uger, hvorefter der ses en forbedret kontraktionskraft over tid.

De stereolitografisk fremstillede platforme demonstrerer lovende resultater for brug til formering af kunstige hjertemuskelvæv og metoden kan opskaleres til brug i industrien. De fremstillede hjertemuskelvæv viser tegn på, at der er dannet inter-cellulære forbindelser, der medvirker til dannelsen af et egentligt muskelvæv og vævene kan benyttes til funktionel udlæsning. Fremtidige studier bør fokusere på at teste funktionel respons af lægemidler som er kendt for at teste positivt med de nuværende testmetoder.

Nomenclature

List of abbreviations

AP	Action potential
CAD	Computer aided design
CiPA	Comprehensive In vitro Proarrhythmia Assay
Cx43	Connexin-43
DI	Deionized water
DLP	Digital light processing
DMD	Digital mirror device
DMEM	Dulbecco's modified Eagle's medium
DPBS (PBS)	Dulbecco's phosphate buffered saline
DTU	Technical University of Denmark
ECG	Electrocardiogram
ECM	Extracellular matrix
EMA	European Medicines Agency
FBS	Fetal bovine serum
FDA	Food and Drug Administration
GelMA	Gelatin methacrylate
hERG	Human-ether-à-go-go-related gene
hiPSC	Human induced pluripotent stem cell
hiPSC-CM	Human induced pluripotent stem cell derived cardiomyocyte
iBET	Instituto de Biologia Experimental e Tecnológica
ICH	International conference on harmonization
ICWG	Ion Channel Working Group
LAP	Lithium phenyl-2,4,6-trimethylbenzoylphosphinate
LED	Light emitting diode
MAP	Multiassay platform
MMP	Matrix metalloproteinase
MW	Molecular weight
O/N	Over night
PDMS	Poly (dimethyl siloxane)
PEG	Poly(ethylene glycol)
PEGDA	Poly(ethylene glycol) diacrylate
PEGDMA	Poly(ethylene glycol) dimethacrylate
PI	Propidium iodide
PLA	Poly(lactic acid)

PVA	Poly(vinyl alcohol)
P/S	Penicillin/Streptomycin
PS	Polystyrene
RGD	Peptide sequence (Arg-Gly-Asp)
RT	Room temperature
qRT-PCR	Quantitative real-time polymerase chain reaction
SLA	Stereolithographic apparatus
TCPS	Tissue culture grade polystyrene
TCR	Tissue compaction ratio
TnC	Troponin C
TnI	Troponin I
TnT	Troponin T
UV	Ultraviolet
QY	Quinoline yellow

List of symbols

d	Distance OR diameter (use is specified)
δ	Deflection
E	Young's modulus
ε	Engineering strain
F	Force
G	Shear modulus
I	Intensity OR Moment of inertia (use is specified)
I_x	Ionic currents
$I_{Ca,L}$	Ca^{2+} long, (Cav1.2)
I_{K1}	Inward rectifier, (Kir2.1)
I_{Kr}	Rapid, (hERG)
I_{Ks}	Slow delayed rectifier, (KvLQT1, Kv7.1)
I_{Na}	Rapid, (Nav1.5)
I_{to}	Transient outward, (Kv4.3)
k	Stiffness
l	Initial length
L	Length OR Final Length (use is specified)
λ	Extension ratio
m	Mass
M_n	Molecular weight
ρ	Density
σ	Engineering stress
Q	Volumetric swelling degree
q	Mass swelling ratio
V	Volume
ν	Poisson's ratio
x	The point of application

Definition of terms

Term (synonyms)	Explanation
Engineered tissue (Tissue, engineered cardiac tissue, engineered muscle tissue, engineered contractile tissue)	The term engineered tissue is used throughout this thesis to explain the formation of an in vitro tissue formed by a suspension of cells and scaffold material. The short name of this will be termed “tissue”. The derivative “engineered cardiac tissue” is used when the referred tissue is composed of cardiomyocytes or cardiac progenitor cells. “Engineered muscle tissue” refers to tissue composed of muscle cells or muscle precursor cells. “Engineered contractile tissue” refers to a tissue composed of contractile cells.
The 3D printer	Short description for the home-built stereolithographic 3D printer with projection of one XY image per print layer.
Multiassay Platform (MAP)	This term is used throughout the thesis to describe the cell seeding platform developed in this project. “Multi” describes the ability to have up to 20 replicates on one platform. “Assay” is used to describe that this is a testing device for cardiac drug safety screening. “Platform” describes the single-use entity as a whole.
Cell seeding mold (well)	The shaped element used to seed cell-loaded scaffold into. The molds contain microfeatures for shaping of the cell-loaded scaffold. Molds can also be termed “wells”. To avoid confusion between standard cell culture well-plates and the hydrogel molds used in this work the word “mold” is preferred.
Scaffold (matrix material)	The soft hydrogels material for cell embedding are termed scaffolds. They are not pre-shaped or modified to contain any structural cues as this will be achieved by the cell seeding molds. The scaffold material can also be identified as a matrix material, however the word scaffold is preferred in this work to avoid any confusion associated with the word “matrix”.
Post(s)	The term “post” is used to describe the vertically extruded cylindrical or rectangular feature that is incorporated in mold designs to give a functional read-out of tissue contraction. Beside “posts” these are also termed “vertical cantilevers”, “rods”, or “pillars” in the literature.

List of publications

Peer reviewed journal paper (Appendix 2):

1. **Christensen, R. K.**; Von Halling Laier, C.; Kiziltay, A.; Wilson, S.; Larsen, N. B. 3D Printed Hydrogel Multiassay Platforms for Robust Generation of Engineered Contractile Tissues. *Biomacromolecules* **2019**, acs.biomac.9b01274. <https://doi.org/10.1021/acs.biomac.9b01274>

Conference contributions:

1. Workshop: Italian-Nordic Polymer Future, September 2017 Pisa:
 - i. Poster presentation: 3D Engineering PEG-Diacrylate hydrogels for mimicking human mechanical microenvironments., **Christensen, R. K.**, Wilson, S., Skaft-Pedersen, P., & Larsen, N. B. (2017), Italian-Nordic Polymer Future Workshop, Pisa, Italy.
 - ii. Abstract: 3D Engineering PEG-Diacrylate hydrogels for mimicking human mechanical microenvironments, **Christensen, R. K.**, Larsen, N. B., Wilson, S., & Skaft-Pedersen, P. (2017), Italian-Nordic Polymer Future Workshop, Pisa, Italy.
2. Select Bio Organ-on-a-Chip, June 2018 Rotterdam:
 - i. Poster: Developing an automated functional cardiotoxicity drug screening platform, **Christensen, R. K.**, Skaft-Pedersen, P., Wilson, S., & Larsen, N. B. (2018), Organ-on-a-Chip & Tissue-on-a-Chip Europe 2018, Rotterdam, Netherlands.

Patent application:

1. Patent covers core technology for the development of a contractility measurement device based on the work carried out during this project.
 - i. Submitted December 23rd 2019, listed as inventor.

List of collaborations

Section	Collaborators contribution	My contribution
Section 4.2	<u>Maria Ludvigsen</u> : Obtained 3T3 tissues in culture.	Design idea, optimizing cell and scaffold concentration studies, PEGDA surface treatment for termination of free acrylates.
Section 4.4	<u>Christoffer Laier</u> : Optimizing fibrin and collagen protocols (pre-cell experiments).	Optimizing GelMA protocol to allow cell mixing. Seeding cells and maintaining experiment for 30 days as well as collection of data.
Section 4.5.1	<u>Christian Pless</u> : Developing and testing of the mechanical microactuator. <u>Christoffer von Halling Laier</u> : Developing of a mechanical actuation system to function on multiple tissues in parallel.	Feedback on design ideas. Background knowledge of mechanical actuation and tissue engineering. Assisted in obtaining tissue formations. Performed characterization of platform.
Section 4.5.2	<u>Peder Skafte-Pedersen</u> and <u>Jens Henneke</u> : Building and test-validation of the electrical pacing unit.	Determining settings used to pace engineered cardiac tissues in PEGDA MAPs.
Section 4.6	<u>Marta Paiva</u> : Cell differentiation and handling. Cell characterization protocols for differentiation yields. <u>Christoffer von Halling Laier</u> : Producing MAPs to send to Portugal. <u>Torben Nielsen</u> : Developing software for automatic tracking of post movement in obtained videos. <u>Aysel Kiziltay</u> : Cryosectioning and. Immunostaining.	The idea for experiments, planning of studies, experimental planning, performing some experiments together with Marta Paiva, designing the used MAPs, obtaining videos and images, processing of samples, data handling, and analysis of obtained results.
Appendix 2 – Peer reviewed journal paper	<u>Aysel Kiziltay</u> : Cryosectioning and Immunostaining. <u>Christoffer von Halling Laier</u> : Live/dead fluorescence imaging.	Framing the scope of the paper and writing manuscript. Revising based on comments from supervisor and other co-authors. Performing experiments, analyzing data and comprising figures.

Table Of Contents

Preface	i
Acknowledgments	iii
Abstract	v
Resumé	vii
Nomenclature	ix
Definition of terms	xiii
List of publications	xv
List of collaborations	xvii
Chapter 1 Introduction	1
1.1. Project aim and objectives	2
1.2. Business case – brief overview	2
1.3. Cardiotoxicity induced by pharmaceutical drugs	4
1.4. Advancing strategies for cardiac safety testing	6
1.5. Thesis outline from Chapter 1 to Chapter 6	8
Chapter 2 <i>In vitro</i> formation of engineered muscle tissues: Theory and background	11
2.1. Physiological background	11
2.1.1. Cell to muscle development and function <i>in vivo</i>	11
2.1.2. <i>In vitro</i> muscle development	14
2.2. Materials and fabrication methods to develop engineered muscle tissues	16
2.2.1. Cell environment influences cell binding and shape	17
2.2.2. Scaffold materials of choice	18
2.2.3. Common materials and fabrication techniques for tissue engineering platforms	21
2.3. Cells and tissue shaping: Methods to obtain functional muscle tissues	24
2.3.1. Planar cell shaping	24
2.3.2. Advanced geometric and assembly based designs	26
2.4. Maturation methods for engineered muscle tissues	28
2.4.1. Mechanical stimulation	29
2.4.2. Electrical stimulation	31
2.5. Choosing the right strategy: Design, production methods, materials, and culture conditions used to produce cardiac tissues for drug safety screening	32

2.5.1. Platform design criteria	32
2.5.2. Tissue formation and culture conditions.....	34
2.5.3. Implementation strategy	35

Chapter 3 Design and manufacture of a multiassay cell seeding platform for tissue formation **37**

3.1. Introduction to the home-built stereolithographic 3D printer	37
3.1.1. Print resin.....	38
3.2. Print resolution and the influence of swelling on design limitations	40
3.2.1. Design resolution is dependent on light exposure pattern.....	40
3.2.2. Effect of swelling.....	42
3.3. Mechanical stability of 3D printed PEGDA structures	44
3.3.1. Shear modulus	44
3.3.2. Printability of microscale beams for fatigue testing	45
3.3.3. Production of an unsupported test beam	48
3.3.4. Fatigue test	49
3.4. Designing a multiassay platform	50
3.4.1. Engineered tissue formation based on a vertical post design	50
3.4.2. Design of mechanical cues for vertical positioning of tissues.....	52
3.4.3. Elevated floor reduces seeding volume and assists tissue positioning.....	53
3.4.4. Optical markers for detection and calibration in a multiassay platform	54
3.4.5. Characterization of flexible posts for functional read-out	56
3.5. Summary of the multiassay platform design	58
3.5.1. Design variability between PEGDA MAPs.....	59
3.6. Cell loading into PEGDA based multiassay platforms	60
3.6.1. Manual cell seeding	60
3.6.2. Automatic cell seeding based on a modified dispensing system	62
3.7. Conclusions.....	64
3.8. Experimental details.....	64
3.8.1. 3D printing using a home-built stereolithographic printer	64
3.8.2. Coverglass treatment	66
3.8.3. Constructing small features – Spatial resolution.....	66
3.8.4. Fatigue test	66
3.8.5. Determining the swelling of printed PEGDA hydrogels	67
3.8.6. Compression modulus analysis of printed PEGDA hydrogels	67
3.8.7. Automatic dispensing	67
3.8.8. Characterization of bendable posts.....	67

3.8.9. Optimization of gelation time	68
Chapter 4 Formation and characterization of engineered contractile tissues	71
4.1. Defining and quantifying engineered tissues in PEGDA MAPs.....	71
4.2. Tissue formation using 3T3 Swiss Albino fibroblasts.....	73
4.2.1. Optimizing cell- and scaffold concentrations.....	74
4.2.2. Forming a fibroblast tissue strip	74
4.3. Tissue formation using C2C12 mouse myoblasts	77
4.3.1. C2C12 tissue formation and differentiation in GelMA scaffolds	78
4.3.2. Design dependent tissue formation	80
4.4. Cardiac tissue formation in three types of cell-loaded scaffolds	82
4.4.1. Cardiac tissue formation and culturing using a 30 days differentiation protocol	83
4.4.2. Effect of scaffold stiffness and cell seeding density on cardiac tissue formation	83
4.5. Maturation methods for Cardiac tissues	87
4.5.1. Cyclic mechanical stimulation of PEGDA MAPs	88
4.5.2. Parameter optimization of the custom-built electrical stimulation system.....	89
4.5.3. Investigation of cell toxicity induced by continuous electrical pacing	93
4.6. Characterization of engineered cardiac tissues in PEGDA MAPs	94
4.6.1. Shape and viability of electrically paced cardiac tissues of different sizes	95
4.6.2. Assessment of engineered cardiac tissue maturation using gene expression	98
4.6.3. Characterization of tissue contraction force in electrically paced cardiac tissues.	100
4.6.4. Functional tissue development depends on the environment	104
4.7. Conclusions	105
4.8. Experimental details	105
4.8.1. Print settings used for producing PEGDA MAPs	105
4.8.2. Surface treatment of PEGDA MAPs	106
4.8.3. Preparation of 3D printed PEGDA molds for cell seeding	107
4.8.4. Preparation and gelation of cell seeding scaffolds	107
4.8.5. Cell culture of 3T3 cells	108
4.8.6. Cell culture of C2C12 cells.....	108
4.8.7. Determining cell concentration of 3T3 fibroblasts encapsulated in GelMA	108
4.8.8. Seeding of 3T3 fibroblasts and C2C12 mouse myoblasts	108
4.8.9. 2D culture and harvesting of cardiomyocyte progenitor cells	108
4.8.10. Seeding of cardiomyocyte progenitors into PEGDA MAPs.....	109
4.8.11. 3D culture of cardiomyocytes inside PEGDA MAPs	109
4.8.12. Electrical stimulation of engineered cardiac tissues.....	109
4.8.13. Tests of electrical pacing unit	110

4.8.14. Contraction analysis	111
4.8.15. Quantitative real-time polymerase chain reaction (qRT-PCR)	111
4.8.16. Live/dead staining.....	113
4.8.17. Immunohistochemistry	113
Chapter 5 Discussion	115
5.1. Development of a microenvironment to promote tissue formation.....	115
5.2. Characterization of device functionality	116
5.3. Development of engineered cardiac tissues.....	117
5.4. Improving robustness of engineered tissues	118
5.5. Readiness level and competitor evaluation	119
Chapter 6 Conclusions and outlook	121
6.1. Conclusions.....	121
6.2. Outlook.....	122
6.2.1. Validation of cardiac tissues by functional and biological characterization	123
6.2.2. Engineered cardiac tissue formation.....	123
6.2.3. Maturation of engineered cardiac tissues.....	123
6.2.4. Potential applications	124
References	125
Appendix 1 Design features to promote scaffold entrapment and tissue robustness	139
Appendix 2 Peer reviewed journal paper	141

Chapter 1

Introduction

In our everyday life, we all need to take medication once in a while for different reasons. This may be due to allergies, infections or more serious illnesses. Taking medication should be a safe experience associated with the fewest possible risks and worries about adverse side effects. Regulatory authorities, such as the American Food and Drug Administration (FDA) and European Medicines Agency (EMA) help us get the most risk-free medicines by making sure all pharmaceutical drugs (“drugs”) are validated using proper guidelines and test procedures before becoming available on the market. When new knowledge about adverse side effects appears or more precise and safe testing procedures are developed, these will be incorporated as new guidelines for testing to ensure up-to-date and safe testing and validation of all pharmaceutical agents that enter the markets. Adverse side effects from non-cardiovascular drugs were discovered in the late 1980’s and revealed a risk of heart failure in individuals that appeared to have no congenital heart defects^{1,2}. As a result, some drugs were taken off the market and new procedures to assess cardiac safety in all new drug approvals were initiated. These procedures have been formulated in the pharmaceutical guidelines from the International Conference on Harmonization (ICH), an organization that collects safety and efficacy test guidelines, to achieve a better and more uniform baseline of tests worldwide and they act as a bridge between the pharmaceutical industry and regulatory authorities.

The release of a new drug happens through multiple test and validation gates to ensure drug efficiency and safety but also to assist the development process of pharmaceutical companies. If a drug candidate fails in an early phase it is likely discontinued and never reaches the market³. Only slightly above 60 % of all drugs pass preclinical trials⁴ and only around 10 % of all drugs are approved after clinical trials⁵. When a drug candidate fails in the preclinical or clinical trials it is associated with a substantial economic impact on the company. Up to 17 % of drugs fail in the preclinical trial and 25 % of drugs in clinical trials are failing due to cardiovascular related events⁴.

Preclinical drug safety testing aims to assess any risks and capture any adverse effects of pharmaceutical agents before the clinical trial phase. Preclinical and clinical trial evaluations of new drug candidates follow an extensive period of development and research of specific drug candidates. Preclinical tests is performed according to the ICH S7B (preclinical ion channel testing)⁶ and the E14 (clinical testing on healthy volunteers)⁷ which is used in early phase clinical trials. These protocols have been implemented specifically to accommodate the need for a cardiac safety screening to prevent adverse effects emerged by the ability of some non-

antiarrhythmic drugs to cause cardiovascular side effects and, in worst case, induce cardiac arrest.

The current testing paradigm suffers from low specificity in preclinical testing as it relies on testing of a single ion channel⁸. A shift in the testing paradigm aims to increase specificity and sensitivity by relying on responses from organisms instead of single ion channel or single cell testing. This work focuses on the development of engineered cardiac tissues to use as an early detection tool in preclinical testing of drug induced cardiotoxicity.

1.1. Project aim and objectives

The work presented as a part of this Ph.D. thesis focuses on developing a cell seeding multiassay platform for functional drug-safety screening with mechanical microenvironments that enhance tissue formation. The fabrication is based on a novel method to produce the platform in a compliant material in order to form and analyze engineered cardiac tissues. The platform can be used to mature engineered tissues and is designed to provide easy read-out options for functional parameters such as force and rhythm.

In this project, mouse cell lines of fibroblasts and skeletal precursor cells as well as hiPSC derived cardiomyocyte progenitor cells are used to form engineered tissues using the designed cell seeding platform. Cells are acquired from commercial vendors or external collaborators and are not produced as a part of this project.

The specific goals of the work are to:

- Design a microenvironment that promotes cell-to-tissue development of specific organ cells using synthetic soft polymer materials relevant for industrial upscaling using novel precision 3D fabrication processes.
- Characterize the mechanical properties of design features to promote a functional device suitable for response analysis.
- Using the designed device to show tissue formation properties over extended culture time and evaluate the biological advantage of tissue culture in a physiologically relevant environment.
- Demonstrate optical read-out of contractile behavior.

1.2. Business case – brief overview

The tissue-on-a-chip market for drug safety screening and other applications such as studying individualized medicine and disease models is rapidly developing. It is estimated that the market value for tissue-on-chip technologies will be around \$170 million by 2023⁹. Sophion Bioscience A/S has a strong background in development of automated systems for single cell analysis and has great potential to develop a system for testing and analysis of engineered

cardiac tissues that is reliable and easy to use. One of the key challenges for developing an automated test system is to develop a single-use bio-chip platform containing engineered cardiac tissues. Developing of the platform will be the main goal of this work, Figure 1.1.

Focusing on using cheap, scalable materials and novel fabrication methods that can meet the current needs will help develop the field toward a more advanced testing regime, thus creating better and safer drugs faster. Aiming for the single-use chip platform as a separate project includes development of the platform and development of a robust biological model.

Risks surrounding the field especially involves the current technological readiness level⁹ of hiPSC derived cardiomyocytes that are still immature compared to adult cardiomyocytes, and difficulties in implementing new technologies into the regulatory field. However, overcoming the challenges reveals the potential of a market share in an increasingly growing field in the future of drug safety screening as well as other potential applications related to tissue on a chip development. The system is being developed to be cost effective, time and resource saving, and in a format that offers a turnkey system for customer use worldwide.

In the following chapters, the physiological background and material considerations are explained and different methods to achieve the presented objectives are presented and discussed.

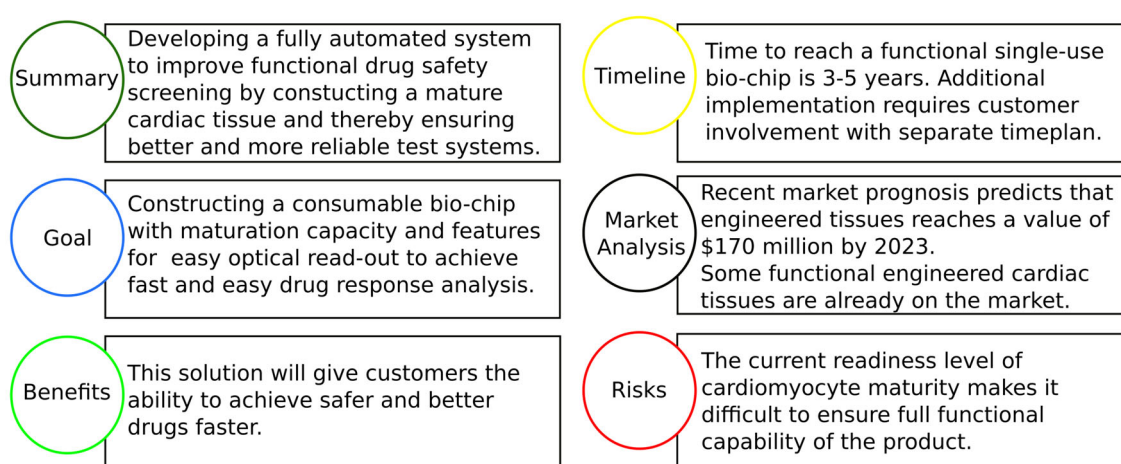


Figure 1.1 | Developing a fully automated system to improve functional drug safety screening by making a platform for mature engineered cardiac tissues will benefit the market of drug safety testing. The market is currently estimated to be \$170 million in 2023 with a growing rate. Most existing systems offer contract research services where customers can send their compounds for testing. By delivering a ready-to-use product, customers will be able to develop safer and better drugs faster using the technology at their own facility. The resulting product will have a worldwide sales potential offering both the single use bio-chip as well as cell handling, read-out, and analysis features.

1.3. Cardiotoxicity induced by pharmaceutical drugs

To better understand the ability of certain non-antiarrhythmic drugs and their metabolites to affect cardiac function, one must first understand the cellular processes behind normal cardiac function.

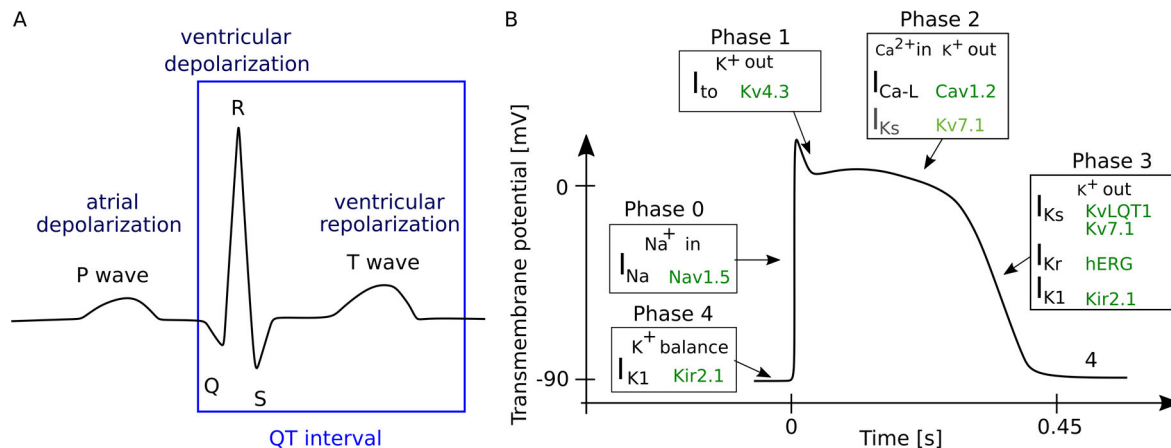


Figure 1.2 | A) Electrocardiogram (ECG). Each phase represents a part of the cardiac contraction as indicated on the figure. The QT interval can be prolonged if the ventricular repolarization is delayed and hence cause cardiac arrhythmia. (B) The ventricular cardiac action potential (AP) for the left ventricular cardiomyocytes. Activation and inactivation of ion channels are divided into five phases that indicate the currents (I_x) which can be measured by the influx and efflux of ions¹⁰.

Every heartbeat happens as a response to an action potential (AP), an electric signal propagating through the heart that makes the heart muscle cells contract. Electrical recordings of the heartbeat are acquired in an electrocardiogram (ECG), Figure 1.2A, with information about the heart's beat rate, rhythm and electrical propagation. Each section of the electrocardiogram explains different phases of the cardiac contraction. The P wave shows atrial depolarization, the QRS complex shows the ventricular depolarization and the T wave the ventricular repolarization. The QT interval is mainly contributed from depolarization and repolarization of the ventricle. Abnormalities detected in the ECG, allow for the detection of specific medical issues. This section focuses explicitly on the risk of prolonging the QT interval.

The hearts' main function is to pump blood through the body. Blood reaches the lungs through contraction of the right ventricle whilst blood pumped from the left ventricle reaches the rest of the body. If the left ventricular ejection fraction is impaired, blood is not sufficiently emptied from the heart and the muscular tissue in the left ventricle might become overstretched which further reduces the function and hence the cardiac output. An impaired function of the left ventricle might lead to subsequent heart failure and death. Some antiarrhythmic drugs prolong

the QT interval by delaying cardiac repolarization and thereby show a proarrhythmic potential with risk of impaired cardiac function or cardiac arrest as an adverse effect.

The cardiac ventricular action potential (AP) is divided into 5 phases (0-4) as seen in Figure 1.2B. The phases of the cardiac ventricular AP are determined based on the activation and inactivation of ion channels that leads to a flow of ions through the ion-channels which changes the transmembrane potential. The ion flow are noted as the currents (I_x) measured by patch clamp¹¹. Initiation of the AP happens as the transmembrane potential reaches its threshold and is hence electrically stimulated. The first phase (0) starts with a rapid depolarization caused by influx of Na^+ ions through voltage gated Na^+ channels. The depolarization is terminated by inactivation of the Na^+ channels and the depolarization phase is followed by an early repolarization phase (1). In the early repolarization there is an efflux of K^+ ions through K^+ channels. Thereafter follows a plateau phase (2) where a balance between influx of Ca^{2+} and efflux of K^+ currents stabilizes the potential. The downstroke and the late repolarization phase of the AP is a result of the delayed rectifier K^+ channels through which there is an efflux of K^+ ions (3). The I_{K1} current maintains the resting potential during the last phase (4) until a new AP is triggered.

Some antiarrhythmic drugs have shown to have proarrhythmic potential by inhibiting the potassium ion channel regulated by the human-ether-à-go-go-related gene (hERG) responsible for the I_{Kr} current in the ventricular AP. Inhibiting this channel will decrease the outward potassium current, I_{Kr} , and cause a delayed repolarization of the ventricular cardiomyocytes⁸. This will be seen in the ECG as a prolonged QT interval. Prolonging the QT interval can lead to Torsades de Pointes (TdP), a specific type of cardiac arrhythmia. The arrhythmia might stop spontaneously and can be hard to diagnose afterwards, however it can also lead to ventricular fibrillation¹² with a high mortality rate¹³. Adverse events leading to QT elongation were the leading cause of withdrawal of certain drugs in the 1980's and the reason that a new drug-safety testing approach was introduced. Since then, several initiatives to identify drugs with QT elongation potential have been developed including the ICH S7B and E14 guidelines².

During preclinical evaluation, tests are performed to assess the predisposition of a drug to induce delayed ventricular repolarization in non-inherited TdP by evaluating the I_{Kr} current. However, focusing on the I_{Kr} current inhibition alone has been proven to be a poor indicator of TdP as I_{Kr} alone cannot predict delayed repolarization². Many drugs failing in preclinical trial are potentially false positives^{14,15}; thus drugs that are potential marketable are discontinued as a result of inhibition of the I_{Kr} although cardiotoxicity is not observed *in vivo*. Studies show that up to 60 % of tested drugs tests positive for I_{Kr} current inhibition and are discontinued or down-prioritized¹⁶. It is therefore important to ensure that the positive response is due to an actual risk of inducing clinical proarrhythmia. It might be possible to design an extra test that can identify false positives but it will come at high cost and involve a large number of animal

studies⁸. It would therefore be beneficial to have a testing method that does not lead to false positives in the first place.

While false positives mainly have an economic impact the safety issue of false negatives is highly concerning. Drug candidates failing in the clinical trials due to cardiac safety that have not been caught in the preclinical trials pose a danger to the test subjects and should be identified during the preclinical phase. False negatives might be due to the effect of torsadogenic compounds that are not specifically related to the hERG-channel tested but can induce a long QT syndrome. Moreover, species-related differences from testing on non-human cells can also contribute to the high rate of false negatives⁸. Kramer et. al¹⁴ have shown that 6 out of 26 drugs with a torsadogenic risk actually tests negative when relying solely on the effect on the I_{Kr} by testing only hERG channels.

Since the introduction of tests based on S7B and E14 in 2005, no drugs have been released to the market with later proof of torsadogenic potential. However, the drawbacks of economic impact of false positives, and risk potential in clinical trials of the false negatives, have driven forward the investigation of new approaches to overcome these issues¹⁷. Testing the effect on a single ion channel, is not sufficient to give an overall picture of compound activity on the heart. One of the major initiatives to overcome the issues in the field is the Comprehensive In vitro Proarrhythmia Assay (CiPA) initiative. CiPA was started as a result of a think tank meeting in 2013 to solve the issues presented and was sponsored by the Cardiac Safety Research Consortium, Health and Environmental Sciences Institute together with the US Food and Drug Administration (FDA).

1.4. Advancing strategies for cardiac safety testing

The CiPA initiative with the ion channel working group (ICWG) directs the research towards single cell testing using human induced pluripotent cardiomyocytes (hiPSC-CMs). The approach is to develop a test matrix that measures multiple ion channels instead of relying only on the I_{Kr} inhibition. This approach is expected to solve the species differences and single ion channel type responses that account for some of the false negatives and false positives described above.

While the CiPA initiative solves the previous challenges in cardiotoxicity screening, it relies on the differentiation of hiPSC-CMs as a preclinical human-based cardiotoxicity testing strategy using ventricular cardiomyocytes to mimic the simplest functional unit of the heart. Despite many advances to terminally differentiate stem cell derived cardiomyocytes, there is still a gap between hiPSC-CMs and adult cardiomyocytes with regards to both structure and function^{18,19,20}. Protocols to differentiate hiPSC-CMs are constantly improving and though some studies have shown appropriate responses to known pro-arrhythmogenic and non-arrhythmogenic drugs²¹ the question still remains whether the cells obtained in vitro through these protocols are adequate surrogates for the human adult myocardium²².

“Maturation” is the term most often used to describe how developed the stem cell derived cardiomyocytes are compared to adult cardiomyocytes. There is no defined measure for maturity and therefore the term “more mature” is often used when comparing between morphological factors such as sarcomere length and functional measure such as conduction velocity, beat rate, and contractile force. The more mature cells become, the more they will resemble human adult cardiomyocytes with similar structural characteristics. As they mature, the spontaneous beating seen in immature cardiomyocytes slows down in beat rate and the conduction velocity and contractile force increases as a result of increased cellular connections and intracellular organization. Discoveries in stem cell differentiation show that obtaining terminally differentiated mature hiPSC-CMs requires physiologically relevant environmental factors that cannot be obtained using 2D cultures²³. Differentiating and maturing cells in 3D to use in 2D single cell analysis shows ineffective results as cells tend to de-differentiate when removed from their 3D environment²⁴. An inherent drawback of single cell analysis therefore remains unsolved.

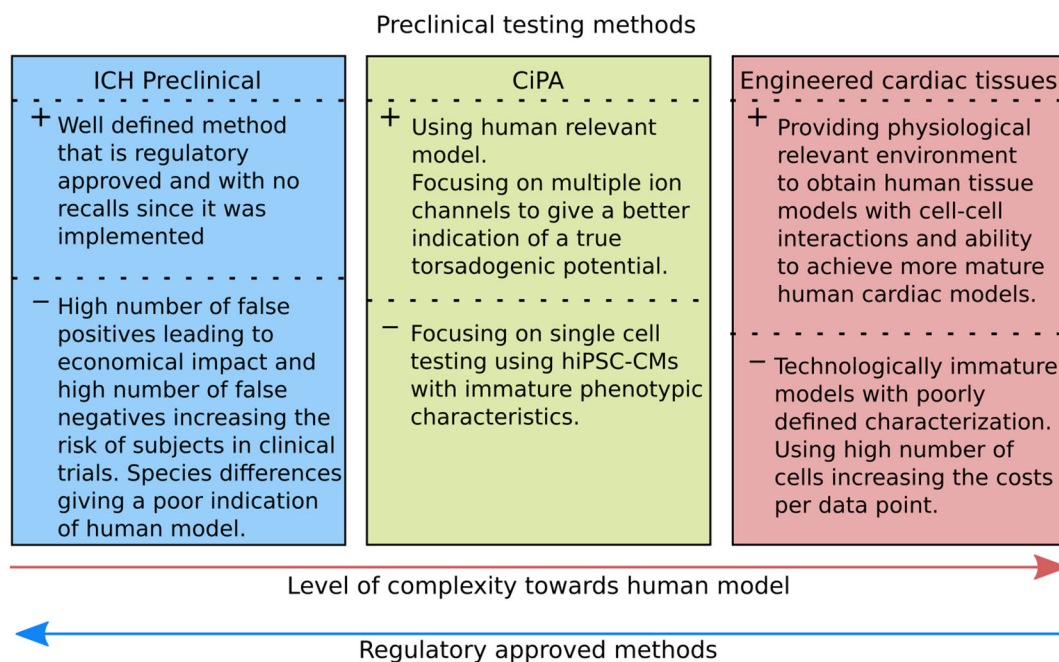


Figure 1.3| Preclinical drug safety testing methods used today and recognized by regulatory bodies are not optimal due to a high number of false positives and false negatives. Therefore, new initiatives are being made to accommodate a change in the drug safety paradigm to make safer tests based on more physiologically relevant methods. Both single cell testing on multiple ion channels based on hiPSCs and engineered cardiac tissue models are explored. The CiPA initiative is based on single cell testing which is challenged by the end differentiation potential of cells cultured in 2D. Development of engineered cardiac tissues overcomes this by having the potential to further develop cardiomyocytes to better mimic human adult cardiac tissue and relies on multiple cell response for a more physiological relevant model.

Moving forward from the limitations of single cell analysis to obtain more physiologically relevant test specimens can be done by using tissue engineering approaches including formation of engineered cardiac tissues using hiPSC-CM, such as muscle tissue strips^{25–27}. Engineered cardiac tissues consist of hiPSC-CMs that mimic an *in vivo* environment through the cell-cell interactions and signaling processes and a more physiologically relevant morphology. By testing cardiotoxicity on engineered cardiac tissues, the effect on the tissue is mimicked and the drawbacks of using single cells eliminated. Although there has been an intense development of engineered tissues for cardiotoxicity studies, none of the currently available models have yet been translated into assays or methods used as standard in drug discovery. In summary, the necessity of better preclinical testing is evolving to demand more physiologically relevant models. While single cell analysis and the CiPA initiative is a prosperity to single ion channel testing, a more efficient drug discovery process will require the use of a more complex system. The establishment of tissue engineered approaches have the potential to play a vital role, also shown in Figure 1.3. The motivation behind developing engineered cardiac tissues is to create the most physiologically relevant models that will be able to accommodate the challenges with single ion channel testing and single cell testing and give a more reliable drug safety testing method.

1.5. Thesis outline from Chapter 1 to Chapter 6

Chapter 1 Introduction

Description of the motivation and background for the project including specific aims and objectives for the project and a business case overview.

Chapter 2 *In vitro* formation of engineered muscle tissues: Theory and background

Description of relevant background theory on muscle cell development, cell encapsulation, materials, and fabrication methods and as short review of current tissue engineering approaches presented in literature. This chapter also includes a summary of relevant strategic considerations made for the work in this thesis. A discussion of compromises and benefits of the different choices for materials and design constraints when designing the platform for tissue engineering and subsequent culture conditions are included.

Chapter 3 Design and manufacture of a multiassay cell seeding platform for tissue formation

This chapter focuses on the development of multiassay cell seeding platforms and explain the basic of principles applied, details on manufacturing, and design constraints. Mechanical characterization and physical properties of the used materials are performed and explained using relevant theory to present and discuss obtained results. Usability of the platforms are evaluated using existing tissue engineering platforms from literature, reproduced using the chosen material and production method presented. An industrial applicable cell loading

method is also briefly explored. Experimental details and supplementary results are described at the end of the chapter and can be omitted.

Chapter 4 Formation and characterization of engineered contractile tissues

Investigation of tissue forming properties using the platforms presented in Chapter 3 are performed using three contractile cell lines; mouse fibroblasts, mouse myoblasts and hiPSC derived cardiac progenitors. An engineered tissue is specified in terms of compaction capabilities from initial seeded volume to end-compacted state. The ability of the designed platforms to facilitate engineered tissues are evaluated using mouse fibroblasts and myoblasts. Different scaffold materials are investigated for the formation of engineered cardiac tissues and the read-out of contractile behavior is demonstrated together with biological characterization of the cardiac tissues. Experimental details are described in the end of the chapter.

Chapter 5 Discussion

This chapter presents a summary of discussions on results from Chapter 3 and Chapter 4 and a comparison to other work in the field of tissue engineering for use in drug safety testing.

Chapter 6 Conclusions and outlook

Conclusions are summarized and followed by a description of the future work that are recommended to elaborate on the findings in this work. Potential use of the work in other contexts are also presented here.

Chapter 2

In vitro formation of engineered muscle tissues: Theory and background

In order to form an engineered muscle tissue, the background behind muscle tissue physiology and cell differentiation must first be understood. This chapter describes both the physiological structure and function of striated muscle cells and the *in vitro* cell differentiation to form striated muscle cells *in vitro*. The process of forming engineered tissues does not rely solely on the understanding of muscle tissues but equally on the environment surrounding it. This environment is constructed of different materials that both functions as extracellular environment and as a shaping element. By controlling the environment, the shape and function of the engineered muscle tissues are impacted. Materials used to shape the engineered tissues are therefore also reviewed in this chapter along with applied fabrication methods to obtain desired culture molds to shape the tissues. Prior work in this field is covered to describe the functionality and prospects of the different methods described.

The end of the chapter summarizes the design criteria based on the covered materials, methods, and prior work described. An in depth evaluation is given of the strategy chosen for the work carried out in this thesis.

2.1. Physiological background

This section describes the development of striated muscle cells. Both skeletal and cardiac striated muscle cells, will be described to understand the basis of *in vitro* tissue engineering of muscle tissues from muscle progenitor cells. A common feature of striated muscle cells is the regular microscopic organization of the contractile proteins actin and myosin that create a striation pattern, due to the difference in optical reflection of the proteins, giving the name of this type of muscle tissues. Muscle contraction happens as the functional unit, the sarcomere, shortens. A functional engineered tissue requires a fully working contractile system.

2.1.1. Cell to muscle development and function *in vivo*

Skeletal muscle is built from muscle cells (muscle fibers) which are divided into myofibrils as seen in Figure 2.1A. Fibers in the human body have a length between 1 mm and 30 cm and are enclosed by the sarcolemma. The muscle fibers are individual, parallel entities that do not connect with neighboring fibers²⁸. Skeletal muscle fibers have multiple nuclei located near the sarcolemma and contain all the regular cellular components in their sarcoplasm together with

the myofibrils. The multinucleated structure arises from the differentiation of muscle fibers from the muscle precursor cells, myoblasts, that fuse together and form myotubes which grow and develop into skeletal muscle fibers²⁸.

In both skeletal and cardiac muscle cells, one sarcomere unit is defined between two Z lines, Figure 2.1B. I bands appear adjacent to the Z discs. I bands are composed of thin filaments (e.g. actin, troponin) and appears light. The A bands contain thick filaments (mostly composed of myosin) and appear dark. Inside the center of the A band is the M line which appears as a dark line inside a lighter region called the H zone. The light and dark appearances of the sarcomeres result from the isotropic (light) and anisotropic (dark) regions and are visible due to difference in refractive indexes. Each thick filament is surrounded by thin filaments in a hexagonal pattern, seen in a transversal cut through the A band, where the thick and thin filaments overlap. Muscle cell contraction occurs from the motion between thick and thin filaments. When the muscle is relaxed there will only be little overlap between the thick and thin filaments. As the muscle contracts, the I band and the H zone become narrower whereas the width of the A band is unchanged as the filaments overlap. Myosin moves along the actin filament in a repetitive action by converting the chemical energy stored in the phosphate bond of adenosine triphosphate into kinetic energy by ATPase activity. This repetitive action, called the cross-bridge cycle, makes the continuous movement of myosin down the actin filament and creates the muscle contraction.

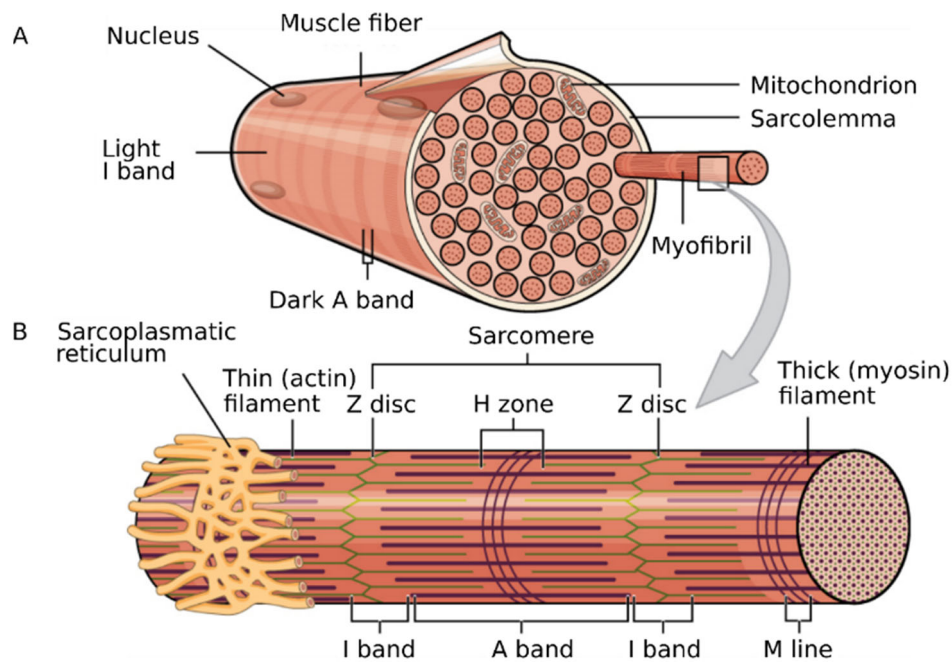


Figure 2.1| A) Skeletal muscle fibers are built up of myofibrils. Each muscle fiber is a multinucleated individual entity that is not connected to neighboring muscle fibers. B) A sarcomere unit consisting of thick (myosin) and thin (actin) filaments. In striated muscle cells, both cardiac and skeletal, the sarcomere unit is responsible for contraction and force development. The head on the thick filament alternates between two conformations controlled by Ca^{2+} binding that makes the thick filament slide over the thin filament in a repetitive motion called the crossbridge cycle. This causes the sarcomere, and hence the muscle cell, to shorten during a contraction. Reprinted with permission from Creative Commons Attribution License²⁹. (<https://creativecommons.org/licenses/by/4.0/legalcode>).

In the evaluation of muscle tissue development, sarcomere appearance is an important indicator of muscle cell development. There is a clear difference in appearance of the sarcomere units between highly developed muscle cells and immature muscle cells. The sarcomere unit is visible at high magnifications after staining of the tissues. When evaluating muscle health, sarcomere units can reveal muscle tissue damage or hypertrophy and may be used as an indicator for cell development.

A schematic overview of the heart muscle tissue, Figure 2.2, shows a branching of the muscle tissue that is different from the shape of the skeletal muscle fibers, which are parallel and not connected to neighboring muscle fibers. Cardiac muscle fibers branch and connect with muscle fibers that are both parallel and adjacent to form a network-like structure. Cardiac muscle fibers are shorter than their skeletal equivalents (up to 100 μm in length) and typically only contain one nucleus. Cardiac muscle tissue are composed of cardiomyocytes that have connected end to end via intercalated discs. The end to end connection is important for the function of the cardiac syncytium as the intercalated discs contain gap junctions that enable fast conduction

of the action potential between connected cells. In this way the heart muscle cells have a rapid intercellular communication that makes it possible to beat synchronized. The branched network structure of the functional cardiac syncytium allows a synchronous twitching contraction that works as a pump to effectively empty the heart.

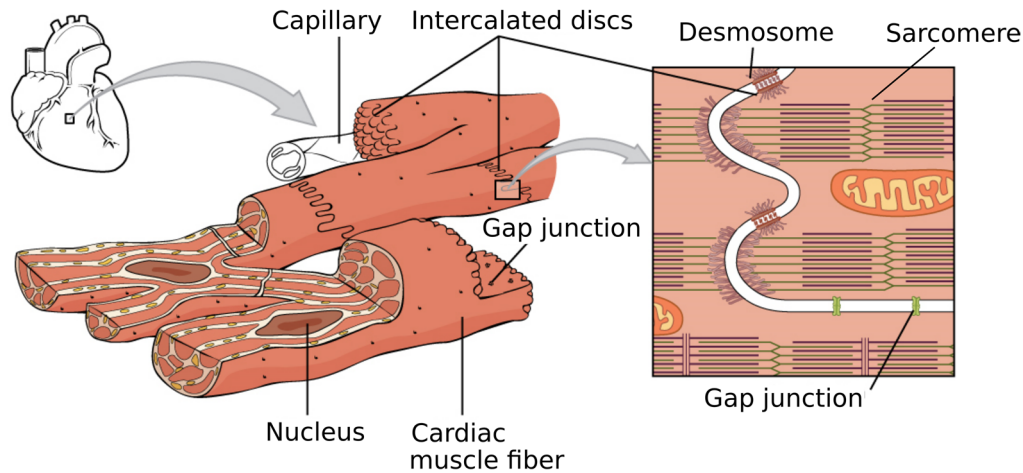


Figure 2.2| The functional cardiac syncytium reveals a branched structure allowing the heart to perform a twitching contraction and efficiently empty the heart within each heartbeat. Individual cardiomyocytes are connected via intercalated discs containing gap junctions which allow for fast conduction of the action potential from cell to cell. Reprinted with permission from, Creative Commons Attribution License³⁰ (<https://creativecommons.org/licenses/by/4.0/legalcode>).

2.1.2. *In vitro* muscle development

Developing skeletal precursor cells, myoblasts, into skeletal muscle cells *in vitro* happens by activation of specific genes that mediate differentiation. Specific growth factors ensure that myoblasts are maintained in an undifferentiated proliferative state. Therefore, growth medium contains high amounts of fibroblast- and hepatocyte growth factors, known to inhibit differentiation³¹. At the onset of differentiation, the growth medium is replaced by a differentiation medium containing a low serum concentration and therefore a lower amount of growth factors. Differentiation using a low serum concentration will make the myoblasts fuse and form myotubes that will develop an extensive cytoskeleton as seen in Figure 2.3 and will generate a striated appearance over time. However, differentiation requires more cues in order to proceed into a terminal state including scaffold interactions and alignment^{32,33}.

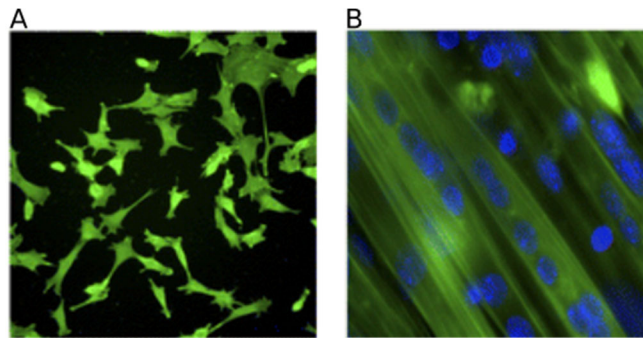


Figure 2.3| Micrographs showing: (A) Unfused single myoblasts in an undifferentiated state. (B) Myotubes have fused together to form a myotube network with multinucleated fibers. Figure modified with permission from Yamamoto et al.³⁴.

In vitro cardiac tissue development is initiated from cardiac precursors often derived from stem cells. In this work, hiPSC derived cardiac progenitor cells are used. Developing hiPSC derived cardiomyocytes happens through various steps via directed differentiation through cardiac progenitor cells³⁵, Figure 2.4. All stages of differentiation are dependent on biochemical factors to direct the development from pluripotent stem cells to the primitive mesoderm and further to cardiac mesoderm making the cells committed to the cardiac lineage. Through an appropriate combination of biochemical factors, the cells are directed to become cardiac progenitor cells and early, immature, cardiomyocytes with spontaneous beating. Further maturation into more mature cardiomyocytes is achieved through the use of different chemical factors that can change the cell metabolism³⁶, but also via physical characteristics which is described in sections 2.2.1 and 2.4.

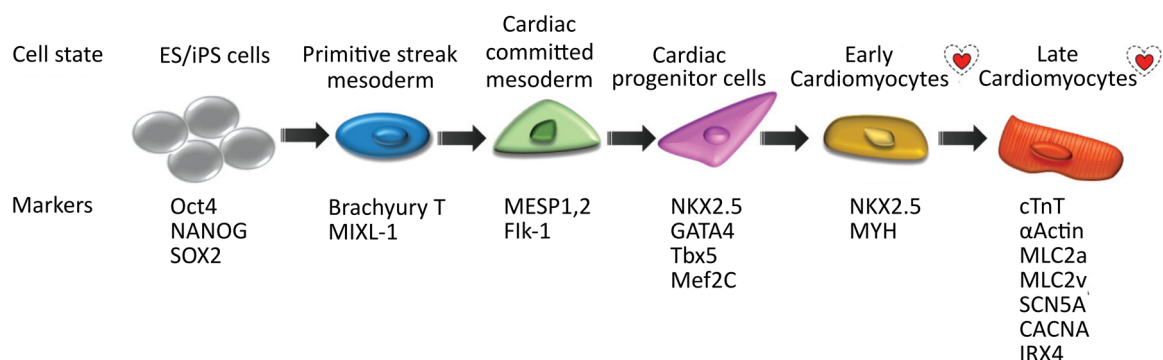


Figure 2.4| Development from stem cell to cardiomyocyte development. Biochemical factors are used to drive the differentiation of pluripotent stem cells through to the desired lineage of differentiation. Cardiomyocytes are differentiated through the mesoderm to become cardiac mesoderm and cardiac progenitor cells. Further differentiation drives them towards early cardiomyocytes that are developed to more mature cardiomyocytes by both biochemical and physical stimuli. Early and late cardiomyocytes are beating cells. Adapted with permission from Jeziorowska et al³⁷.

When forming a tissue, the aim is to create an adherent 3D structure of cells with both anchoring junctions and channel-forming junctions in order for the cells to both transfer force and signal to each other. This relies on an effective development of the seeded cells into a more mature form by chemical differentiation as well as the physical conditions surrounding the cells. Material stiffness and composition of the material in which the cells are embedded both effect the ability of the cells to mature^{38–40} and are therefore of utmost importance in the formation of a 3D tissue.

A tissue composed of cells with limited intercellular connections will have a lower contraction force than a tissue developed via highly developed intercellular connections through intercalated discs. Structural development is assessed via immunostaining and electron microscopy to visualize the development of the cytoskeleton structural alignment. In the evaluation of muscle tissue, sarcomere appearance is an important indicator of muscle cell development. There is a clear difference in appearance of the sarcomere units between highly developed muscle cells and immature muscle cells with adult myocytes having a sarcomere length of 2.2 μm and most reported engineered cardiac tissues having shorter sarcomere lengths (1.6 μm)³⁵.

Development of cardiomyocytes into the branched structure of the functional cardiac syncytium has been reported by using co-culture⁴¹, embedding in a scaffold material with a stiffness matching the myocardium⁴², introducing an “afterload”⁴³, by directing the cell alignment via mechanical cues⁴⁴, and by using electrical stimulation⁴⁵. Cell development into a tissue-like network is important for force generation and a more natural behavior of the engineered muscle tissues. In section 2.3, different methods to achieve more mature cardiomyocytes from stem cells using both 2D and 3D configurations are reviewed.

2.2. Materials and fabrication methods to develop engineered muscle tissues

To mimic the physical properties of the natural environment, cells are often incorporated into scaffold materials composed of a naturally occurring polymer hydrogel solution such as collagen (or its hydrolysis product gelatin), fibrin, alginate, and hyaluronic acid (HA).⁴⁶ These can all be adapted to be low-stiffness polymers (kPa) that mimic the stiffness of various natural tissues. Cell-binding peptide motifs, can be incorporated into the polymers to enhance or specialize cell binding^{47–49}. The cell-loaded scaffold can be shaped to ensure that tissue formation is obtained by loading it into a “mold” of a harder polymer material as seen in Figure 2.5. To obtain the desired shape and size of cell-loaded scaffolds, both molding techniques as well as bioprinting fabrication techniques have been used^{50–54}.

The following section describes relevant scaffold materials for embedding muscle cells and suitable methods to create the mold for geometrically well-defined tissue constructs.

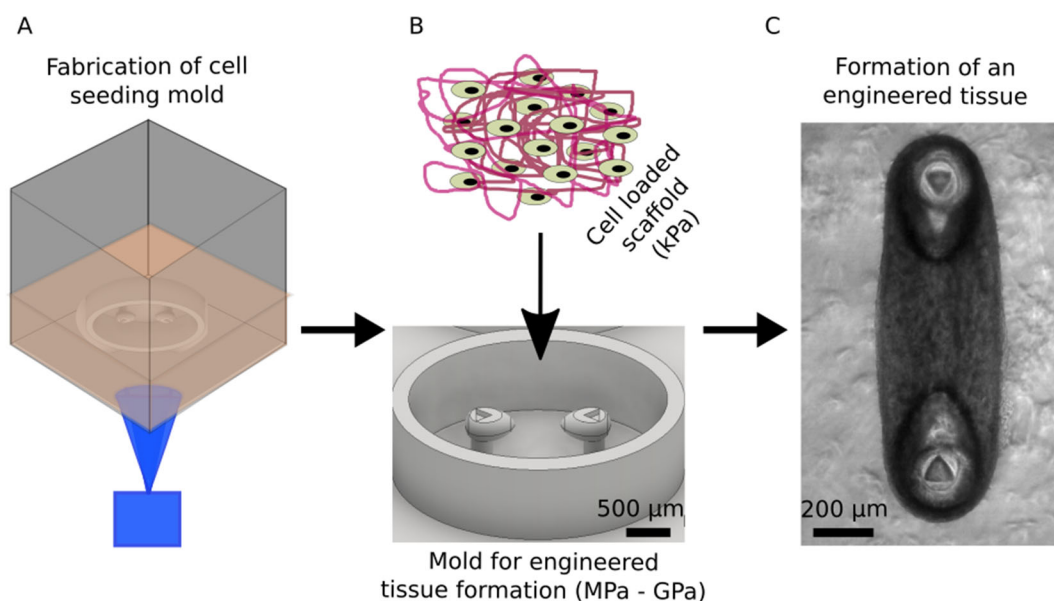


Figure 2.5| A) Mold production can be achieved by various fabrication methods and often consists of polymer materials with a modulus in the MPa to GPa range. The shape and features of the mold aid the shape of the final engineered tissue. B) Cell-loaded scaffold materials are loaded into the seeding mold. Upon gelation, the scaffolds will have a tissue mimicking stiffness. C) The mold features confine the engineered tissue which is shaped as a tissue strip in between the two post-structures. Figure “C” is adapted with permission from (Christensen et al., 2019, DOI: 10.1021/acs.biomac.9b01274) American Chemical Society.

2.2.1. Cell environment influences cell binding and shape

Culturing of cardiomyocyte progenitor cells in different scaffold materials requires the cells to be able to remodel the scaffold and form engineered tissues. The cell-material interaction takes place via cell binding motifs (ligands) in the material. Integrins are cell adhesion receptors composed of two subunits (α and β) present on the cell surface that can bind to specific ligands. Ligands are often composed of short peptide sequences such as the well-known Arg-Gly-Asp (RGD).

During differentiation, cardiomyocytes express different integrins depending on the state of development⁵⁵. In early development, integrins $\alpha1\beta1$, $\alpha3\beta1$, and $\alpha5\beta1$ are dominant⁵⁶ while the $\alpha7$ subunit is only present in the adult heart. Different integrins show high affinity for different materials depending not only on the ligand but also on the configuration of scaffold. In some molecules, the cell binding domains are not available due to its structural configuration and hence cell binding cannot take place.

In collagen, the ligand called GFOGER is present for cell binding and is compatible with cells containing the $\alpha1\beta1$ integrin⁵⁷ whereas the RGD binding integrins $\alpha3\beta1$ and $\alpha5\beta1$ ⁵⁸ cannot access the RGD domain. In denatured collagen, the RGD sequence is available and in fibronectin

and fibrinogen, the RGD binding domains are structurally presented for cell binding making them suitable for seeding of cardiac progenitor cells expressing RGD binding integrins.

Some integrins are also known to be mechanosensing, meaning that the cell can sense the rigidity of the material to which it is attached. When cells sense the material stiffness they can convert the mechanical sensing into biochemical signaling⁵⁶ through mechanotransduction and thereby alter phenotype and shape⁵⁹. Choosing a substrate or scaffold material in the physiological range of the natural tissue therefore helps guiding the cells in the direction of a mature phenotype.

2.2.2. Scaffold materials of choice

Hydrogels are water-insoluble, hydrophilic polymer networks that can have a water content of more than 90 %⁶⁰. Hydrogels can be modified to better resemble the native extracellular matrix (ECM) of muscle tissues in mechanical stiffness by controlling the polymer content. Hydrogels permit diffusion of oxygen, nutrients, and cellular signals making them an ideal material choice for encapsulation of cells in tissue engineering. However, certain properties are essential for it to be a suitable scaffold material including a stiffness similar to the native tissue, cell binding motifs, gelling time, and gelling conditions. Muscle tissues have a stiffness in the range of 10 kPa to 15 kPa⁵⁹ why scaffold materials should be around the same stiffness. Gelling of the scaffold happens with cells encapsulated and therefore needs to be a non-toxic process and occur with a controlled temperature (around 4 °C – 37 °C), neutral pH, and a reasonable gelling time that prevents the cells and scaffold from drying out during gelation. These requirements limit the choice of materials suitable for the purpose of this thesis.

In tissue engineering, whether the tissue consists of fibroblasts, skeletal muscle cells, or heart muscle cells, the scaffold material needs to contain cell binding motifs for the cells to attach. Hydrogels can be divided into synthetic and natural hydrogels and both classes are used for cell encapsulation. Synthetic polymers such as poly(ethylene glycol) PEG, poly(lactic acid) (PLA), and poly(vinyl alcohol) (PVA) needs chemical modification in order to contain cell binding motifs⁴⁸. Synthetic hydrogels are often used for drug delivery or in tissue engineering for their degradable nature⁶¹. However, in tissue engineering where cell binding is important synthetic hydrogels are used less frequently. Some natural hydrogels such as the polysaccharides HA and alginate also contains no cell binding motifs for fibroblasts and muscle cells so it is necessary to add them into the network for cell binding to occur. Hydrogels that do not contain motifs are not an obvious choice of scaffold for tissue formation in this work due to simplicity, and availability of hydrogels with natural occurrence of cell binding motifs. The three scaffolds used are gelatin methacrylate (GelMA), fibrin, and collagen. All are naturally occurring hydrogels that are widely used for cell culturing allowing both cell encapsulation and binding. They mimic the natural environment⁴⁶ with mechanical properties in the range of natural muscle tissues^{62–64} and contain cell binding motifs needed for cell binding.

Degradation of the scaffold by the embedded cells is a well-known process that happens for most natural hydrogels used as tissue scaffolds. Degradation of collagen^{46,65}, GelMA⁶⁶, and fibrin⁴⁶ can take place via the enzyme-family matrix metalloproteinases (MMPs) which is secreted by both fibroblasts and some muscle cells. MMPs can play an important role in the ability to remodel the scaffold in which the cells are embedded⁶⁷. However, if the cells degrade the scaffold before proper cell-cell connections are formed, the tissue will be in risk of disintegrating why it is important to consider the impact of scaffold degradation. The degradation can be counteracted by introducing a protease inhibitor to the culture medium or by increasing hydrogel concentration. However, the latter may change the overall stiffness or the scaffold and lead to remodeling complications.

2.2.2.1. Collagen and collagen derived GelMA

In vivo tissues contain various types of collagen with varying stiffness. *In vitro* collagen and collagen derived products can be altered to have a muscle mimicking stiffness. In skeletal muscle tissue, collagen type I and collagen type III are the most common⁶⁸. In cardiac muscle tissue, collagen type I, -III, and -IV are present with only type IV being produced by the cardiomyocytes themselves and the majority of the collagen being produced by the cardiac fibroblasts as type I and III⁶⁹. Collagen assembles in a triple helix structure composed by three collagen fibrils⁷⁰ and can physically crosslink to form a hydrogel network.

Bovine collagen I is used in studies presented in this work. At low temperatures and low pH, collagen is soluble⁶⁴ and has a low viscosity. Raising the temperature to 25 °C – 37 °C at neutral pH permits the collagen to form insoluble fibrils and physically gel to form a hydrogel⁶⁴. This process is used to encapsulate cells that are embedded at low temperature (5 °C) in pH neutral conditions and captured during gelation at 37 °C.

Collagen is used to produce gelatin by hydrolysis. Gelatin is then modified to contain the reactive methacrylate end groups^{71,66} as seen in Figure 2.6A. The methacrylate groups are capable of crosslinking using free radical polymerization initiated by a photoinitiator and light to form a covalently cross-linked GelMA network, Figure 2.6B. While the cell-loaded scaffold is forming a network, the surroundings are kept dry to avoid dissolving the scaffold. Advantages of using GelMA include rapid polymerization from seconds to minutes which prevents the hydrogel from drying out due to evaporation and minimizes the medium deprivation time during gelation.

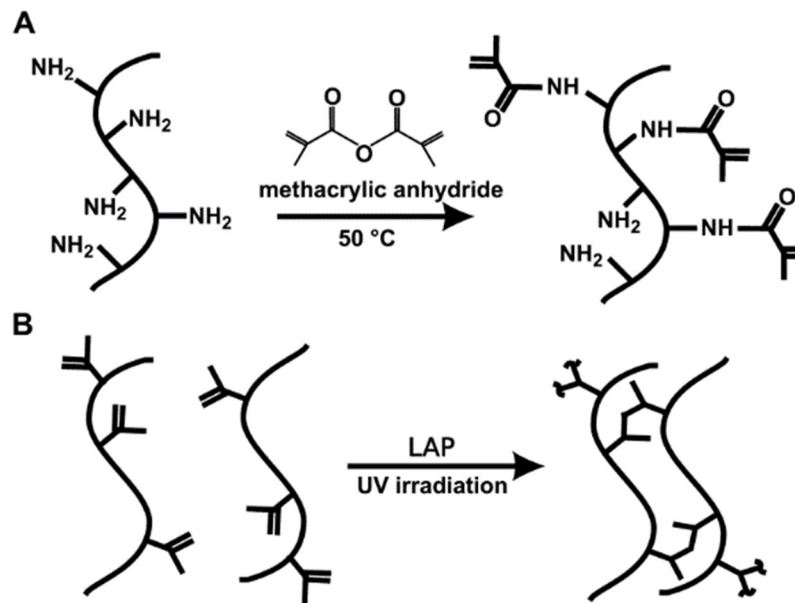


Figure 2.6| A) Gelatin hydrolyzed from collagen is methacrylated to form Gelatin methacrylate (GelMA). B) GelMA is cross-linked using a photoinitiator (e.g LAP) and UV irradiation; the number of GelMA molecules in each chain may vary. The sketched reaction occurs repeatedly to form a crosslinked network of GelMA molecules. Reprinted with permission from Nichol et al., 2008.⁶⁶

The cell binding motif RGD is inaccessible in collagen but is exposed and preserved during the formation of GelMA and is available for cell binding. RGD binding integrins are present in numerous cells including cardiomyocyte progenitors, skeletal myoblasts, and fibroblasts⁵⁷. There is therefore no need for further chemical modification of GelMA to promote cell binding in cases where cells recognize the RGD⁷² in the present conformation of the scaffold.

2.2.2.2. Fibrin

Fibrin hydrogels have great potential as a tissue engineering scaffold because of their mechanical properties that can be altered to have a stiffness resembling that of the natural muscle tissue⁷³.

The fibrin network is formed by polycondensation when the protease thrombin cleaves the glycoprotein fibrinogen in the central region of the molecule. The cleavage of fibrinogen removes fibrinopeptides and exposes the binding knobs A and B and thereby initiates the spontaneous reaction where knob A and B binds to hole A and B⁷⁴ as depicted in Figure 2.7. A fibrin network is formed when multiple monomers react together to form a network structure. Gelation times are controlled *in vitro* by varying the concentration of thrombin⁷⁵.

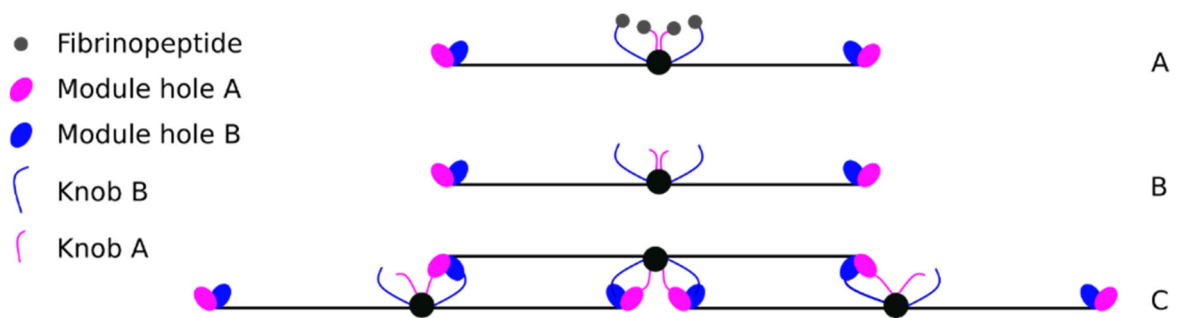


Figure 2.7| A) Simplified structure of the fibrinogen molecule. B) When thrombin cleaves the fibrinopeptides A and B from the fibrinogen molecule, a fibrin monomer is created with the binding Knobs A and B exposed. C) Knob A and B binds to module holes A and B in the distal ends of the fibrin monomer and a fibrin network is created when multiple monomers react together to form a network^{75,76}.

2.2.3. Common materials and fabrication techniques for tissue engineering platforms

In tissue engineering, one of the common main foci across the broad range of applications is how to use materials and design techniques to alter the shape and ultimately the function of mammalian cells. The soft, cell-loaded scaffold is used as the physical entrapment for uniform cell distribution and chemical interaction between material and cells whereas the surrounding molds comprised of stiffer materials are used as the shaping element, Figure 2.5. Incorporation of design features, such as microchannels for optimized diffusion of oxygen and nutrients, or designing mechanical cues for remodeling and reshaping the cell-loaded scaffold over time, aid in making the mold an important factor in cell and tissue maturation. By constructing the mold following design criteria known to affect cell development these can serve to have a profound role in tissue engineering. However, it requires an adequate production method to achieve such designs. A common prerequisite is the ability to produce the molds in biocompatible materials with aseptic working conditions or the possibility to sterilize after manufacturing.

Shaping the mold for seeding of the cell-loaded scaffolds can be achieved in various ways including, but not limited to, micro milling and laser cutting, casting and molding techniques, extrusion printing, and 3D printing. The three most common fabrication techniques used for molds in tissue engineering are different types of casting, molding, and 3D printing described in the following.

2.2.3.1. Casting and molding

Polydimethylsiloxane (PDMS) casting and injection molding as seen in Figure 2.8 is widely used to fabricate microfluidic chips and tissue forming platforms for biological applications due the cost efficiency. Although injection molding gives the opportunity to produce a high amount of

platforms in a short time PDMS casting is preferred for tissue forming purposes due to its flexible mechanical properties.

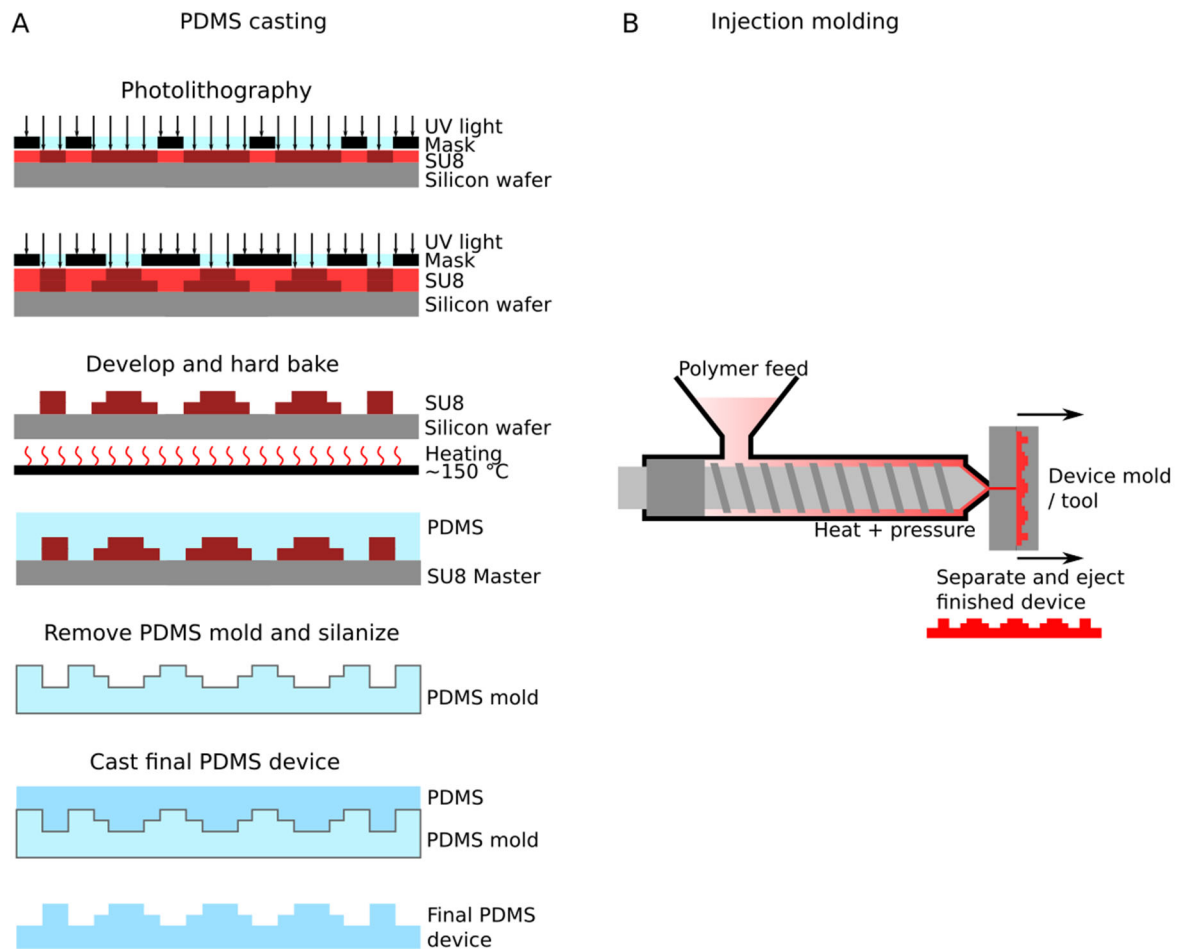


Figure 2.8| A) Polydimethylsiloxane (PDMS) casting procedure with an intermediate PDMS mold. The intermediate mold is softer and are used to create more delicate features that cannot be extracted from rigid molds. B) Injection molding process. The polymer is melted and extruded into the device mold where it is set. The finished device is then ejected. This molding methods makes it possible to produce a large amount of devices in a short time. Illustrations by courtesy of Louise Laub Busk.

PDMS casting involves a multistep process to produce a master replicate and is a fabrication technique that can be implemented in most places⁷⁷ and is cost efficient. Depending on the complexity of the designed structures it might involve several photolithography steps, making it a time consuming process involving an intermediate PDMS mold. To incorporate more geometrically advanced structures this extra step in the molding process is necessary to create a softer mold from where the structures can be removed

Despite the challenges of obtaining more advances geometric structures using this fabrication method, the flexibility of PDMS as an elastomer⁷⁸, makes it a favorable material for mold fabrication. Many tissue-formation platforms are also comprised of a set of assemblies using

both PDMS casting for cell-adhesive structures combined with molded or milled stiff polymer structures to obtain a finished assembly platform^{25,45}.

PDMS is relevant for biological assays as it is cell compatible and have tuneable mechanical properties⁷⁸ that can be adjusted by the ratio of monomer to cross-linker⁷⁷. PDMS is therefore a suitable choice for many biological applications and both academic and start-up companies' lab on a chip platforms are often build on cast PDMS devices^{77,78}. However, due to the hydrophobic nature and porosity, it is not a suitable material for drug screening purposes as it has shown undesirable adsorption and absorption of hydrophobic compounds^{78,79}, such as drug candidates.

2.2.3.2. Stereolithographic 3D printing

For tissue engineering, stereolithographic 3D printing is increasingly being used to fabricate advanced geometric structures using flexible cell compliant materials^{53,54,80,81}. Bioengineering platforms are produced with different kinds of 3D printing such as extrusion printing⁸² but are not described here as it is out of the scope of this thesis which focuses on stereolithography. Two different approaches to this technique will be described in this section.

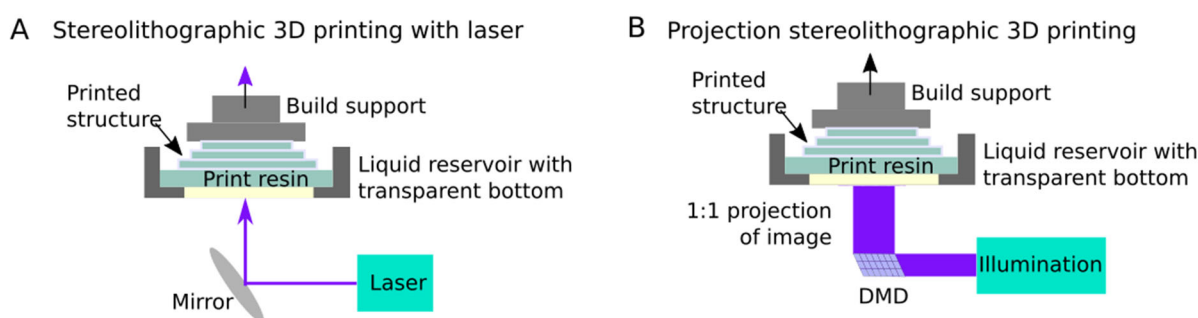


Figure 2.9| A) Stereolithographic 3D printing using laser. The object is created by moving the laser in the wanted pattern to polymerize the print resin in each layer. B) Stereolithographic 3D printing using DMD/projector illuminates the entire area thereby creating a 1:1 image to be polymerized. Each layer is thus created by one projection.

The process of stereolithographic 3D printing is based on light induced chemical polymerization of a liquid resin solution containing monomers, photoinitiator, and absorber. Solidification of the resin solution is spatially controlled by the light source in the XY plane. The light pattern is obtained by computer aided design (CAD) of a 3D object which is subsequently sliced into a Z-stack image series of XY slices which are later used to reproduce the 3D object. The profound difference in the two main stereolithographic processes shown in Figure 2.9 is the projection of the light into the resin containing reservoir (vat). Stereolithographic printing using steered laser beam, also referred to as SLA, scans the XY plane according to the sliced image pattern. A more recent stereolithographic method, using Digital Light Processing (DLP) projects the entire

XY plane at once and thereby cures each layer in one projection. After each layer, both methods use a digitally controlled stage to move the printed object in the Z direction to enable printing of subsequent layers thereby creating a 3D structure based on XY images from the 3D objects. The Z distance between sliced images can control the Z-resolution of the 3D printed objects with the drawback that a higher number of slices will increase the printing time (time to manufacture the 3D object).

Often poly(ethylene glycol) (PEG), poly(ethylene glycol) dimethacrylate (PEGDMA) or poly(ethylene glycol) diacrylate (PEGDA) are used as print materials due to tunable mechanical properties, resistance to nonspecific protein adsorption⁸³ (non-fouling property) and cell compatibility⁸⁴. The diffusive properties of the hydrogel network ensure that drug compounds can freely move in the network. Thereby it does not hamper the drug testing purpose as is the case for the PDMS. While PDMS casted devices retain their dimensions in water after casting, this is not the case for hydrogel based devices. The projection pattern is often created in a 1:1 scale. However, due to the hydrophilicity of PEGDA, swelling will occur after printing, resulting in increased dimensions of the printed structure in aqueous environments. Therefore, the design dimensions might require an offset to compensate for this prior to manufacturing.

2.3. Cells and tissue shaping: Methods to obtain functional muscle tissues

Stem cell differentiation has developed significantly over the last 2 decades, however, conventional cell culture methods using tissue culture treated polystyrene (TCPS) flasks and plates with planar 2D geometry are still used. Many important scientific discoveries have been made using this configuration and it is still a very robust and useful tool for many elementary biological investigations. However, culturing stem cells for differentiation requires a physiologically relevant environment that is critical to obtain a phenotype as close to the natural state as possible. The functional characteristics of the cells change with cell shape and conventional 2D cell culture methods therefore lack important features to mimic the *in vivo* situation including alteration to substrate stiffness and structural support. Improved maturation in 2D cultures grown on TCPS can be achieved by improving surface chemistry and stiffness by surface treatment with functional groups or thin sheets of soft polymeric materials. However, the cells still retain a simple 2D structure which limits their development potential.

2.3.1. Planar cell shaping

Obtaining the natural shape of developing stem cells have encouraged people to study methods to manipulate cell shape *in vitro*. By culturing cells in single cell chambers, Abadi et al.⁸⁵ successfully used human adult cardiomyocytes as a master replicate to shape molds for culturing and maturation of single iPSC derived cardiomyocytes. The molds are used to achieve more advanced mature cardiomyocytes for cell engrafting after heart failure using patient derived iPSC cells. Casting and molding using the desired adult cell as a master replicate

is one way to achieve a single cell mold. Others have used direct laser printing to study the direct relation between single cell shape and function⁸⁶. Single cell casting is similar to regular 2D culture as substrate rigidity and overall 3D shape does not ensure that the cells retain a normal phenotype. Using this culturing method deprives the cells from the natural chemical and physical environment sensing.

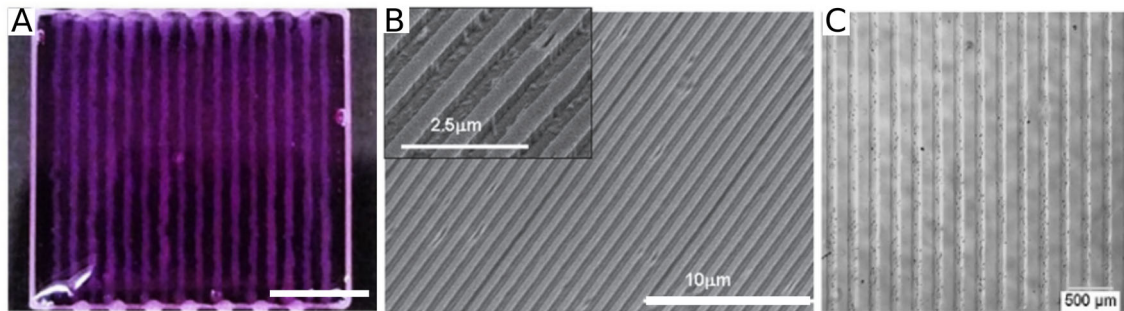


Figure 2.10| Grooves for directed cell growth and elongation produced by different manufacturing methods. (A) Custom made extrusion bioprinting “integrated tissue – organ printing” with cell-laden hydrogel. This technique can also be used to produce cardiac tissue patches (B) Fibronectin coated polystyrene surface made using hot embossing of polystyrene beads and a silicone mold. (C) Cell-laden 3D hydrogel micro patterned onto a PEG coated glass slide. Figures reprinted with permission^{52,67,87}. Scale bars A,C: 500 μm . Scale bar B: 10 μm and 2.5 μm .

In transitioning the cell culture constructs from 2D to 3D, micro-grooves have been widely used as a tool to direct cell growth and achieve a better organization, Figure 2.10. Several cell types such as fibroblasts and different muscle cell types have been modelled using this technique. By patterning or using micro-grooves, the cell-cell contacts can also be improved and reveal more physiologically relevant cell connections either distal between the cells inside the micro-grooves or by allowing connections between micro-grooves in specific regions with micro-channel connection between grooves. Micro-grooves have been used to study the influence of MMP activity on cell elongation⁶⁷ and improved cell-cell connections via gap junction protein connexin 43 (Cx43) in cardiomyocytes when using electrical stimulation⁴⁵. The micro-grooves show good functionality in studying specific stimuli dependent effects of both mechanical, electrical, chemical, and biological stimuli.

Cell loading into micro-grooves is most often achieved by pipetting an excess amount of cell-loaded scaffold material onto the microgroove area and spinning it down or by simply adding the solution followed by incubation directly. This loading method uses an excess amount of cells and, consequently, wastes them. In some cases, when micro-grooves are achieved by extrusion-based bioprinting, the fabrication process and cell loading process are combined, thus creating a faster process with the ability to produce many units with the same cell-loaded

mass. The bio-printing method shown in Figure 2.10A is also used to produce cardiac tissue patches where a functional read-out can be obtained during tissue contraction.

2.3.2. Advanced geometric and assembly based designs

Some organ models require the tissue to be mobile and therefore the micro-groove models are less suitable as they lack more advanced structures. In drug safety testing and drug screening, the ability to read-out contraction force and beating rate are key features that must be available from the design. Producing cardiac patches with contractile function using bioprinting (Figure 2.10A) offers read-out possibility but also uses a high amount of cells per construct if these were to be used for drug safety screening.

Achieving a functional optical read-out response has been shown using muscular thin films on micro-molded gelatin that also contains micro-grooves as shown in Figure 2.11. The gelatin is laser cut which makes it susceptible to bending when the attached sheet of cardiomyocytes contracts. The dimension of this technology being in the mm range and the possibility to have replicates within each construct makes the muscle thin films useful for functional analysis purposes⁸⁸. However, the method of filling includes a surplus of cell-suspension, making them economically unfavorable.

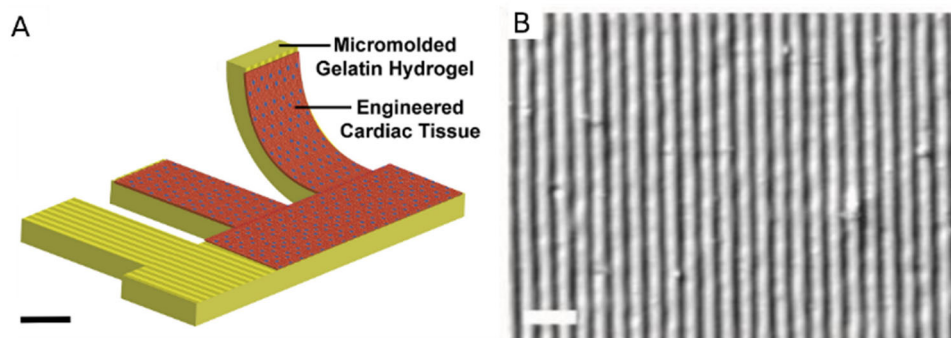


Figure 2.11| Muscular thin film formation with neonatal rat ventricular myocytes⁹⁰ (A). The substrate is formed using laser cut micro-molded gelatin with a groove structure⁸⁹ (B). The gelatin is pattern to form small cantilever strips that can bend as a result of cardiomyocyte contraction. Scale bar A: 1 mm. Scale bar B: 50 μ m. Figures are reprinted with permission^{89,90}.

Obtaining a mold that can provide a read-out of tissue function is often achieved by having vertical posts^{45,51,53,54,91–93}, Figure 2.12A-G, or a horizontally perpendicular stretched wire^{94,95}, Figure 2.12H,I. The horizontal, free-hanging tissues form around the posts or wires and are extended between two points thus creating a tissue strip. When the cells contract, they pull on the two attachment points, creating a movement that can be optically captured. Functionally-developed, engineered cardiac tissues were first developed as ring based constructs with advanced cardiac development of neonatal rat cardiomyocytes by Zimmermann et al.⁹⁶. These ring-shaped tissue constructs were stretched during differentiation and showed functional

response to electrical pacing and longitudinally aligned cells. Vandenburg et al.⁹² used cylindrical, vertical PDMS posts and investigated the effect of the posts' diameter on the ability of the tissue to bend the posts via force displacement evaluation. Many have since followed this approach with similar production techniques using different shapes and sizes of tissue constructs of various cell types including fibroblasts⁹³, skeletal muscle precursors⁹⁷, primary- and stem cell derived cardiomyocytes^{51,45}. All are based on the same principle: to have a functional read-out assay using flexible vertical posts and non-toxic materials such as PDMS or PEGDA. Cells are cultured in a soft scaffold material with ECM resemblance and muscle-mimicking stiffness. After days to weeks in culture, the cells contract the scaffold and form an engineered tissue. The ring-constructs by Zimmermann et al., showing the first functional *in vitro* engineered cardiac tissue, have also progressed into a post based system²⁵ (Figure 2.12E) and show both functionality^{21,98} and biological characteristics⁹⁹ that are superior to many other systems. However, both engineered tissues from the works shown in Figure 2.12B,D also show advanced functional characteristics^{45,50,100}.

Various design techniques have been used to create post-based tissue formation platforms from casting and molding of soft polymers such as PDMS, PEGDA and stiffer polycarbonate posts, Figure 2.12B-E,G. To achieve functional and mechanical cues at the top of the posts where the tissues can form around requires a time-consuming, multistep processes. Alternatively multi-part assemblies are produced that require different fabrication processes to produce various parts. The engineered cardiac tissue in Figure 2.12E uses an upside-down casting method that ensures positioning at the top of the posts. Digital light processing (DLP) and stereolithography (SLA) 3D printing using the soft polymer PEGDA seen in Figure 2.12A,F enable a faster single step process to produce mechanical cues for tissue entrapment positioning at the top of the posts. This saves time and gives a higher resolution with the potential to achieve more delicate structures. It is possible to produce the post-based design using PDMS molding without creating mechanical cues as seen in Figure 2.12D. This design, however, lacks the ability to control the vertical position of the tissue.

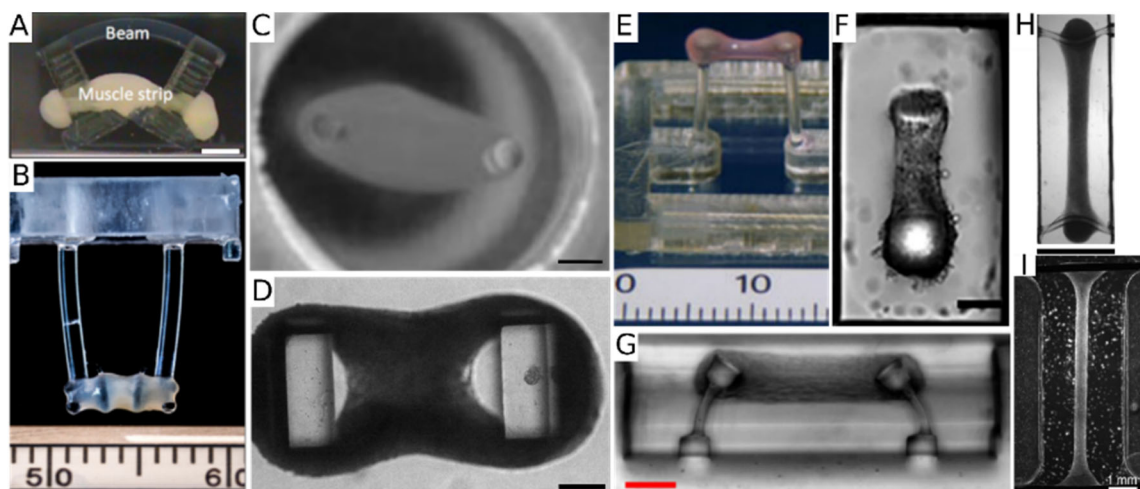


Figure 2.12| State of the art in tissue strip formation using vertical posts for functional read-out assays. (A) Cvetkovic et al. 2014⁵⁴ show the formation of an engineered muscle tissue using C2C12 mouse myoblasts encapsulated around PEGDA posts in a collagen/fibrin/matrigel scaffold. (B) Ronaldson-Bouchard et al. 2018⁴⁵ show advanced maturation of iPSC derived cardiomyocytes in a fibrin scaffold using electrical stimulation of the engineered muscle tissue formed around polycarbonate posts. (C) Vandenburg et. al 2008⁹² use PDMS to cast the mold and posts in a two-step molding process to produce caps on top of the posts. Primary mouse myoblasts were used to produce the tissue strips encapsulated in either collagen/matrigel or fibrin scaffold. (D) Mills et al.^{50,97,100} have several applications of their PDMS based muscle tissue composed of either C2C12 cells or iPSC derived cardiomyocytes embedded in a fibrin based scaffold. (E) In the protocol from Schaaf et. al. 2014⁵¹, a large size muscle tissue strip composed of neonatal rat heart cells in a fibrin scaffold is formed around silicone posts. Numerous investigations of drug response and cardiomyocyte maturation have been published by the same group^{21,98,101,102}. (F) Ma et al. 2019⁵³ have produced two sizes of PEGDA posts around which a tissue strip is formed of either neonatal mice ventricular cardiomyocytes or human iPSC derived CM's inside a collagen/fibrin scaffold. (G) Legant et al. 2009⁹³ show a small size (800 μm) tissue formation using fibroblasts embedded in a collagen scaffold using a PDMS mold containing micro-posts. (H) Zhao et al. 2019⁹⁴ show an engineered tissue with an atrial-like and a ventricular-like end composed of cardiomyocytes in an assembly chamber of polystyrene and POMaC wires to form an atrioventricular engineered cardiac tissue strip called a biowire. (I) Sidorov et al. 2017⁹⁵ use neonatal rat ventricular cells to produce a cardiac tissue strip in a PDMS casted mold. Scale bars A,B,C,E: 1 mm, D: 200 μm , F:500 μm , G: 100 μm Figures are reprinted with permission^{45,50,51,53,54,92–95}.

2.4. Maturation methods for engineered muscle tissues

To obtain relevant and reliable results for functional assays a more mature cell phenotype of the hiPSC derived cardiomyocytes are required. Immature cells are poor predictors of human adult cell behavior since they have different functional characteristics. Both Dennings et al.³⁵ and Yang et al.¹⁰³ have provided extensive comparison between human adult cardiomyocytes, hPSC derived cardiomyocytes, and immature cardiomyocytes. There is clear indication that even when classified as cardiomyocytes, stem cell derived counterparts are far from the adult cardiomyocytes in both appearance, function, and gene expression. For instance, adult human cardiomyocytes are rod shaped with an aspect ratio of 7:1 and has highly aligned sarcomere organization with a sarcomere length of 2.2 μm . Stem cell derived cardiomyocytes have a rounded shape with a 2:1 aspect ratio, disorganized sarcomeres, and sarcomere length of around 1.6 μm ³⁵. Further, adult cardiomyocytes demonstrate beating force orders of magnitudes higher and have conduction velocity at least four times that of stem cell derived cardiomyocytes³⁵.

For drug safety testing where resemblance of adult tissue physiology is important, the tissue must be composed of cells with a phenotypical composition comparable to that of natural heart tissue to have a similar response. This means that maturity is of key importance. Engineered tissues formed by embedding cells in a scaffold shaped by a mold mimics the *in vivo* environment in terms of stiffness and shape as described above. Incorporating biochemical factors into the scaffold or in the culture medium can also be used to achieve more mature cells as well as co-culturing with other cell types.

Different methods have been reported to achieve mature tissues beyond controlling the extracellular environment and adding medium supplements, Figure 2.13. The most promising are electrical stimulation and mechanical maturation using either passive auxotonic stretch or cyclic mechanical stretching^{20,104,105} as explained in the following sections.

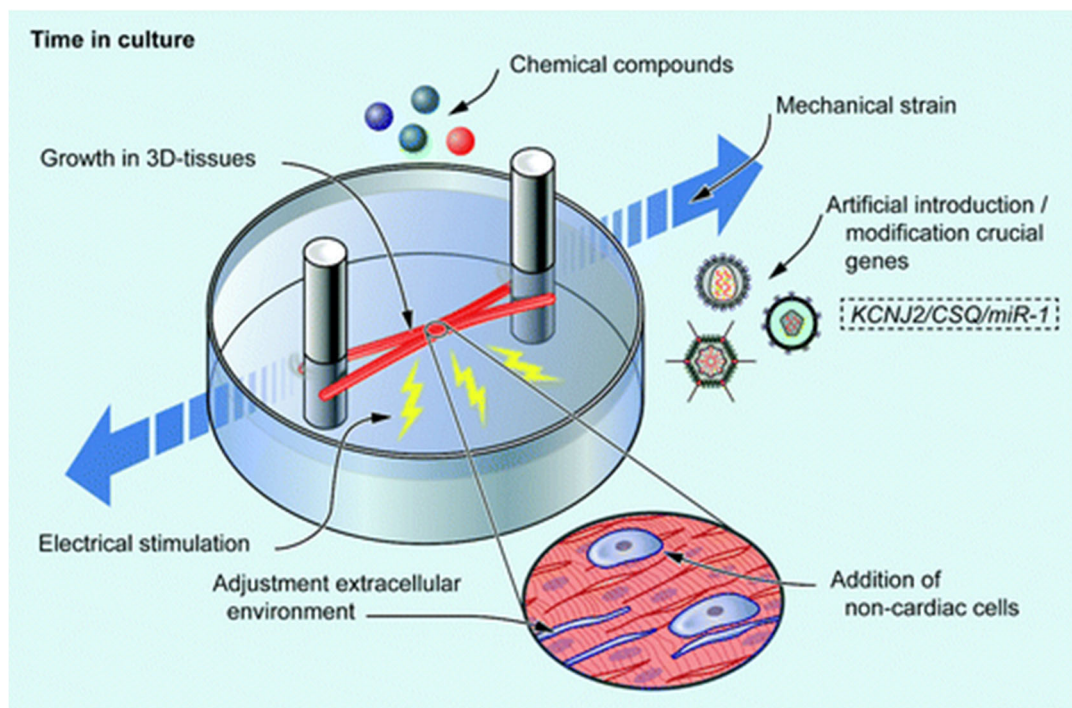


Figure 2.13| Overview of the different methods to achieve more mature cardiomyocytes differentiated from stem cells. Most protocols use a combination of stimuli to generate cardiomyocytes or engineered cardiac tissues with a more mature phenotype resembling that of the adult heart. Figure is reprinted with permission from Veerman et al.²⁰, published by Mary Ann Liebert, Inc.

2.4.1. Mechanical stimulation

In this thesis mechanical stimulation is defined as the mechanical interactions with the engineered muscle tissues from external stimuli not including the cell embedding scaffold which is described in section 2.2.1. External mechanical stimuli that alter the cell shape have been identified as a key drivers in normal heart development¹⁰⁶ and in skeletal muscle

development¹⁰⁷. Mechanical stretching has been used to obtain more mature cardiac muscle tissues as it has shown to align the cytoskeleton and form more aligned sarcomeres. This alignment will ultimately result in better force translation in the cell and contribute to a higher contraction force¹⁰⁸ due to more aligned unidirectional pulling, an indication of cardiac maturation.

Different methods have been applied to enforce mechanical stretching of muscle tissues. This section will treat passive static stretching and cyclic uniaxial stretching of engineered tissues that are extended between two points as seen in Figure 2.12. Three types of passive uniaxial tissue stretching with different modes of resistance at the anchor points have been described previously¹⁰⁹ as isometric, isotonic, and auxotonic stretching, Figure 2.14. In isometric stretching there is no length change of the tissue as the anchoring points are at fixed positions. The isotonic stretch provides a constant resistance as the anchor points move in response to tissue contraction to ensure constant load. Auxotonic stretch is when the tissue experiences increased resistance with increased contraction. This is the case when a tissue contraction causes bending of flexible posts.

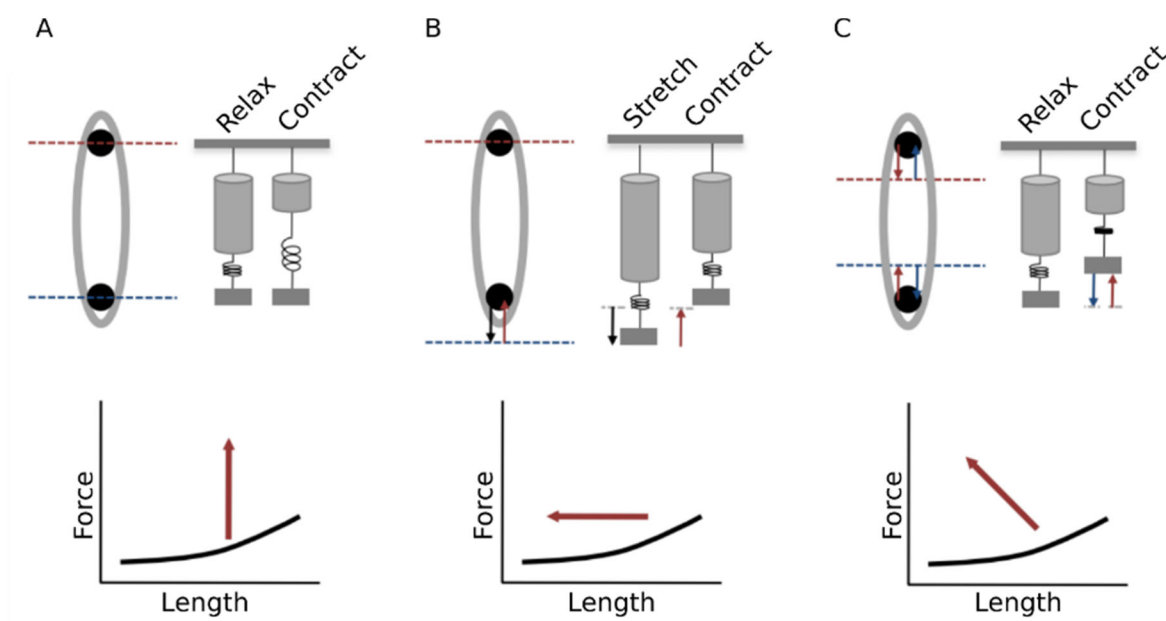


Figure 2.14 | Passive mechanical stretching of engineered cardiac tissues results in an improved sarcomeric organization, contractile force and biological phenotype compared to unstretched controls. The type of passive stretching, however, seems to influence the function. (A) Isometric stretching, where the tissue length remains constant and (B) Isotonic force, where the length changes with regards to the tissue contraction to ensure constant force seems to be less effective than (C) Auxotonic stretching where the length change is accompanied by an increased force acting on the tissue. The latter is achieved by introducing flexible posts as anchorpoints for the engineered tissue. Reprinted with permission from Liaw et al.¹⁰⁹.

Zimmermann et al.¹¹⁰ have shown that the auxotonic stretching is superior to both isometric and isotonic stretching. Auxotonic stretching mimics the *in vivo* physical response of the heart muscle by allowing the cells to change length while experiencing a restriction in movement. This indicates that the post-based tissue engineering as shown in Figure 2.12A-F is a good choice to improve tissue functionality using auxotonic stretching as a mean to achieve more mature cardiac tissues.

While passive stretch and elongation are widely used and have a positive influence on maturation of engineered tissues^{96,111}, cyclic stretch is less developed. Induced cyclic stretch has been used to stimulate natural heart rhythm and exercise cells to increase their functional apparatus and overall maturation levels¹¹². Cyclic strain can be implemented in many post-based tissue engineering designs, however, prior work in this area has focused mainly on planar¹¹² or ringbased constructs¹¹³. Other systems capable of stretching engineered tissue strips stretch only a single engineered tissue^{114,111}. Therefore, a basis exist for expanding this area using a multiassay platform in a stretch-compliant material.

2.4.2. Electrical stimulation

Coordinated beating of heart muscle cells is essential to obtain a physiologically relevant cardiac tissue. Immature cardiomyocytes beat individually if no cellular contacts are made to neighboring cells and engineered cardiac tissues will therefore not necessarily beat as a whole unit before cell-cell contacts are established. Propagation of the action potential between the cardiomyocytes happens through gap junctions in the intercalated discs. Formation of gap junctions in intercalated discs is therefore crucial for tissue development. Application of external electrical stimulation has been shown to increase the formation of the gap junction protein Cx43 in the distal regions of cardiomyocytes¹⁰¹. Thus suggesting that cell-cell connections are happening longitudinally to form a functional cardiac syncytium where signal propagation happens along the length of the tissue as a response of electrical stimulation. In addition, electrical stimulation, also termed electrical pacing, has been shown to increase cell length and improve cytoskeletal arrangement^{115–117} and calcium signaling¹¹⁸.

Electrical stimulation of engineered cardiac tissues serves two different purposes. Electrical stimulation can be used to improve maturity as described above. However, it is also a useful tool in the evaluation of drug response where both the tissue contraction force, but also the response to electrical pacing, can be measured to evaluate cardio-toxic effects. Lowered response to electrical pacing might indicate a disturbance in the electric propagation by ion channel inhibitions. The timing of electrical stimulation has been shown to be important²⁴, and might be the reason why electrical stimulation is mainly used for testing. Some groups, however, have shown continued electrical stimulation on engineered cardiac tissues with improved maturation as a result^{45,101}.

Enabling electrical pacing of engineered cardiac tissues is therefore of utmost importance for the use in cardiac safety screening to both achieve more mature cardiac tissues and measure cardio-toxic effects of pharmaceutical drugs.

2.5. Choosing the right strategy: Design, production methods, materials, and culture conditions used to produce cardiac tissues for drug safety screening

This Section outlines the requirements to be considered in the design based on the reviewed literature and design criteria selected to achieve engineered cardiac tissues in a cell seeding platform with optimal design and culture conditions.

2.5.1. Platform design criteria

In the previous sections, many aspects of designing a cell seeding platform for tissue formation have contributed to design criteria that must be fulfilled to obtain engineered cardiac tissues in a platform capable of inducing maturation and providing easy read-out for drug safety testing. The basic design criteria for platform design and production are listed below:

- 1) **Transport of oxygen and nutrients:** The design must either allow for transportation via channels, or the size of the tissues must be reduced to allow diffusion through the tissue thereby restricting the width to 200 μm if diffusion is equal from all sides¹¹⁹.
- 2) **Introducing auxotonic stretch:** To allow for mechanical stretching that has shown to be important for cell development of striated muscle cells, the design must have mechanical cues incorporated that allow the tissue to form in an elongated manner inducing auxotonic stretch on the tissues.
- 3) **Low cost:** Lowering the cost of production of each data-point obtained is possible by designing the platform in a fashion where the least amount of cells are used with a cost beneficial production method. Both size of the individual molds and seeding methods to avoid waste of cells reduce costs per platform.
- 4) **Read-out possibilities:** It must be possible to easily read-out a drug response on the tissue constructs. Introducing movable features to be captured optically or incorporating sensors are therefore important for the functionality of the platform.
- 5) **Maturation capability:** In addition to the introduction of auxotonic stretch it must be possible to further mature the tissues using either mechanical or electrical pacing. The material must be able to withstand both mechanical stretching and applied electrical fields. Mechanical stretching includes the option of stretching the tissue which entails having design features that move with mechanical stimulation (mechanical pacing). This will introduce a stretch in the tissue.
- 6) **Material:** The material must have a suitably scalable production method, be inexpensive, and enable delicate features to be incorporated in the design.

For the purposes of this work, the above criteria can be met by using stereolithographic 3D printing using the synthetic polymer PEGDA. Stereolithographic printing ensures a high degree of design flexibility and high resolution which meets design criteria 1, 2 and 3. Casting and stereolithographic 3D printing are the best manufacturing solutions to produce delicate features. Tissue size is expected to be a few hundred μm in width after compaction thereby allowing diffusion to the center of the tissue. Cardiac tissue *in vivo* has a distance between capillaries around 20 μm which is not achievable here, however sufficient oxygen diffusion have been showed in engineered tissues up to 100 μm ¹¹⁹. The manufacturing speed of each platform using stereolithographic 3D printing greatly exceeds that of casting thereby lowering production cost.

The choice of material for mold fabrication in this work is PEGDA M_n 700g/mol. Other suitable materials for stereolithographic 3D printing includes PEGDA of different molecular weight (MW) and other monomers or macromers with acrylate or methacrylate functionalities. Higher macromer concentration in the printing solution is expected to increase the reaction kinetics at the cost of lower final water content, which results in a stiffer base material. The difference in cost between PEGDA M_n 700g/mol and higher MW PEGDA is significant and apart from changing the swelling properties, described in section 3.2, changing to higher MW PEGDA would greatly increase production cost. Hence the choice of PEGDA M_n 700g/mol ensures low cost manufacturing in a flexible material that is electrically inert which meets design criteria 3 and 6. After manufacturing the PEGDA hydrogel will swell (see section 3.2) and consequently change the dimensions compared to the original design, which would not occur with non-water based materials. However, the open diffusion properties and the ability to change design freely compensates for the potential dimensional change which can be offset by design.

The mechanical properties of PEGDA can be controlled to be more elastic or brittle by modifying the polymer concentration. This makes PEGDA an ideal material for tissue engineering as many tissue engineering applications require the ability to strain or stretch the chip platform without damaging it ^{92,99,120–122}.

It is possible to manufacture a device with vertical posts that allows for bending during tissue movement and provides anchoring for auxotonic stretching of the tissues by combining the design complexity using stereolithographic 3D printing and the described PEGDA properties, thereby meeting design criteria 5. The post-based design is a system with the capability to do force measurements of engineered contractile tissues in a non-invasive and thus non-destructive way due to the possibility for optical read-out of flexible posts thereby meeting design criteria 4.

2.5.1.1. Summary

Using stereolithographic 3D printing with low MW PEGDA is a suitable choice for designing a cell seeding platform due to the estimated production requirements. Each acquired data-point

will be high value and production demands, with regards to the number of platforms needed, are low compared to traditional injection molding products. Compared to injection molding and other molding techniques, stereolithographic printing enables introduction of advanced geometric features that are critical in the design of a cell culture platform. In addition, the resolution makes it possible to produce small scale (approximately 1 mm) engineered tissues further lowering the cost of each data-point. The resolution of stereolithographic printing has a suitable accuracy (see section 3.2) for the size scale of the platforms needed.

2.5.2. Tissue formation and culture conditions

The ability of engineered tissues to form and remain intact throughout culture and test timeline is also termed “tissue robustness”. To obtain robust engineered tissues this work focuses on using materials and culture conditions that are compatible with the cell line in use. In order to obtain engineered tissues for use in drug safety screening the following criteria are set up:

- 1) **Tissue compliant scaffold materials:** In order for the cells to be encapsulated and maintain viability to form tissue constructs, the embedding scaffold material must be cell-compatible ensuring that the network formation happens under conditions that are in compliance with viable cell culturing conditions.
- 2) **Minimizing cost per tissue construct:** Drug safety testing and drug screening requires multiple tissue “*devices*” to be used. With large devices, the total cell numbers needed will be very high and accordingly so will the cost of drug testing or screening. A size restriction to make this an affordable technology must therefore be considered as a design criterion.
- 3) **Culture under tissue forming enhancing conditions:** Cell culturing must happen in a way that enables the cells to form intercellular connections in a physiological environment that promotes tissue formation.
- 4) **Enabling long term culture and drug testing:** Tissue formation has been described to happen over a period of days to weeks and hence the environment surrounding the tissues must support culture for weeks.

Scaffold materials used are forming a network in the temperature range from 4 °C – 37 °C in a timeline of less than 30 minutes which is consistent with regular cell handling procedures, maintaining a high cell viability, meeting criterion 1. Scaffolds are mixed to ensure that concentrations of components are similar to that of normal culture medium and have neutral pH. Scaffolds are chosen to match tissue stiffness of the natural environment and to contain available material ligands matching cell specific integrins with literature reported values and availability, meeting criteria 3 and 4. When network forming scaffolds are used, the cells can be embedded with close proximity in a 3D environment which supports tissue formation.

3D tissue models require a supply of nutrients and oxygen to be available via diffusion. Therefore, the culture of tissues inside diffusion open mold material is critical in the tissue

formation phase where the cell-loaded scaffold has not contracted to create space between the mold and the formed tissue. Using PEGDA as mold material therefore aids in the fulfillment of criteria 2 and 3. As the oxygen diffuses approximately 100 μm into the tissue¹¹⁹, tissue thickness must be less than 200 μm to ensure sufficient oxygen to the core. Forming tissues in this size range significantly lowers the cost per tissue due to low cell numbers being used compared to previously reported centimeter-sized tissue constructs. PEGDA mold production enables this.

2.5.3. Implementation strategy

As outlined in section 1.5, implementation and investigation of the above strategies are divided into two main chapters where the results of the design and production of the cell seeding platform as well as the tissue formation and characterization is presented.

Chapter 3 Design and manufacture of a multiassay cell seeding platform for tissue formation

Mainly focuses on the design of the stereolithographic 3D printing to manufacture a multiassay cell seeding platform that fulfills the criteria mentioned above. Testing and characterization of features are presented.

Chapter 4 Formation and characterization of engineered contractile tissues

Focuses on the results of using the 3D printed multiassay cell seeding platform for tissue formation. Different cell types are used to both show proof of concept, non-toxicity and function of the mechanical cues implemented in the platforms that aids the tissue formation and cell development.

Chapter 3

Design and manufacture of a multiassay cell seeding platform for tissue formation

A key part of tissue engineering is the design and manufacture of the cell seeding platform, as this defines the mechanical cues and environment felt by the cells, which will guide the development of engineered tissues. Chapter 2 presented a range of common fabrication methods which can be used for microfabrication processes, some of which has been previously applied in tissue engineering. The chapter also highlighted the benefits related to the three-dimensional freedom of 3D printing, which is limited in other fabrication methods. In this chapter, the application of 3D printing for designing and manufacturing of a cell seeding platform used to form engineered tissues is presented. The dimensional accuracy are evaluated and used to optimize designed structures. Mechanical properties of the printed structures are characterized in order to achieve a functional read-out analysis from the engineered tissues. Some of the work in this chapter also relates to the work presented in the journal paper attached in Appendix 2.

3.1. Introduction to the home-built stereolithographic 3D printer

In order to make delicate design features with more advanced geometric structures a home-built stereolithographic 3D printer was used to manufacture the cell seeding platforms presented in this work. The stereolithographic 3D printer (“the 3D printer”, Figure 3.1) makes use of a digital mirror device (DMD) to project light at 365 nm according to the full XY image projection stereolithographic approach described in section 2.2.3.2. The light is projected onto the printing resin contained in the vat above the projector, Figure 3.1A. The DMD pixel pattern is projected 1:1 onto the bottom of the printing vat. The light crosslinks the resin between the vat bottom and the print stage, which is moved up and down using a Z-stage. The DMD has a pixel size of 10.8 μm x 10.8 μm and 1920 pixels x 1080 pixels. The pixel size and the number of pixels impacts the XY resolution as well as the printing area which corresponding to a 20.736 mm x 11.664 mm rectangle. A schematic representation of the printer is seen in Figure 3.1B.

To create a 3D print, a computer aided design (CAD) is sliced into 2-dimensional XY images with a Z-layer distance of 20 μm or 25 μm . This distance impacts the Z-resolution. Each slice results in a digital image that is projected onto the resin-containing vat bottom using a high power LED emitting at 365 nm. This crosslinks the resin in the projected pattern. When one layer has been

exposed, the stage moves up to allow reflow of the print resin and positions back to the next Z-layer and the subsequent image is projected.

Prior to printing, a chemically modified coverglass, presenting methacrylate groups on the surface, is mounted on the stage, onto which the 3D print will be printed. The chemical modification ensures covalent bonding between the PEGDA print and the coverglass which prevents release of the print during printing and subsequent handling. The bottom layers of all designs are purposely overexposed to ensure strong adhesion between the methacrylated coverglass and the first layers of the PEGDA print. This results in a base PEGDA layer that are 100 μm – 200 μm tall in all printed designs. Subsequent layers are printed using a predetermined exposure time to optimize quality (Z-resolution and layer adhesion) of the print. Once the print is finished, the stage moves to a home position where the coverglass and PEGDA structure can be safely removed from the stage, Figure 3.1C.

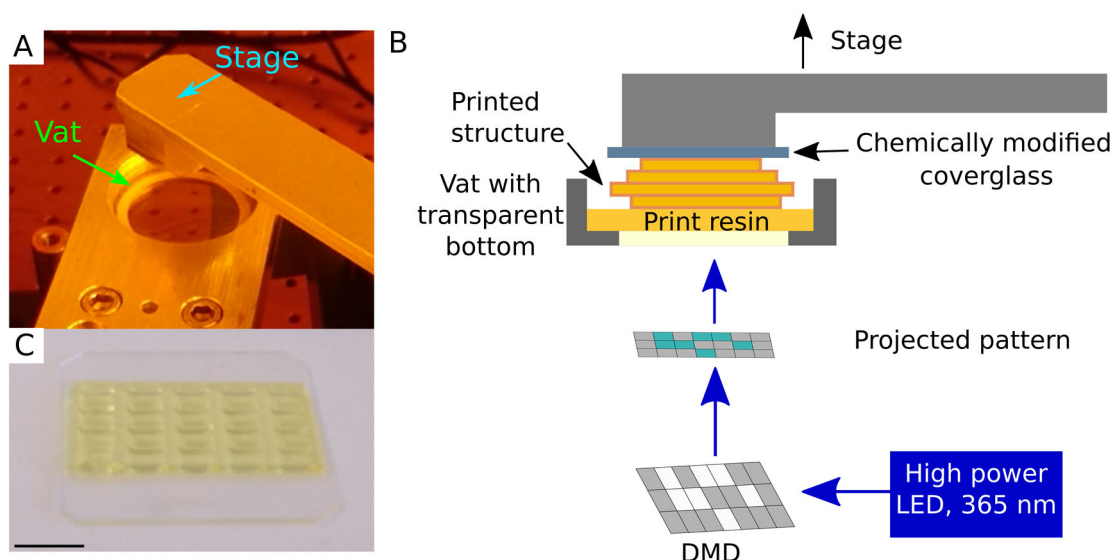


Figure 3.1 | The home-built stereolithographic 3D printer. A) A photograph of the vat and stage. B) A schematic representation of the stereolithographic process using the digital XY images projected onto the vat bottom to create a PEGDA network in the projected pattern from the DMD. Between exposure of each layer the stage moves up to allow reflow of the print resin before the next image is projected to form the new layer. C) Demounted coverglass with a printed PEGDA platform (footprint 10 mm x 20 mm). Scale bar: 5 mm.

3.1.1. Print resin

The print resin is composed of an aqueous solution of the polymer poly(ethylene glycol)-diacrylate M_n 700 g/mol (PEGDA) with the photoinitiator lithium phenyl-2,4,6-trimethylbenzoylphosphine (LAP), Figure 3.2A, and photo absorber quinoline yellow (QY), Figure 3.2B. A PEGDA network is formed by free radical polymerization as illustrated in Figure

3.2C. Previous work performed by other users of the 3D printer¹²³ has established recommended concentrations suitable for different printing resolutions. For each slicing thickness, the absorber concentration can be changed to achieve the best possible Z-resolution. Slicing thickness varies between 20 μm and 25 μm and the print resin can be altered to achieve better binding between layers by controlling the absorber concentration and the exposure time and thereby the light penetration depth. Compromising on the Z-resolution by lowering the absorber concentration and keeping the same slicing thickness can give a better layer-to-layer adherence, which is desirable in some cases where the Z-resolution is not critical. Details about the resin compositions in different designs can be found in the experimental section 3.8 for all design variants. Horizontal flow channel designs require a high spatial resolution in the Z-direction whereas high aspect ratio structures benefits more from a reduced Z-resolution that gives a more robust structure with a better layer-to-layer connection due to overexposure between layers.

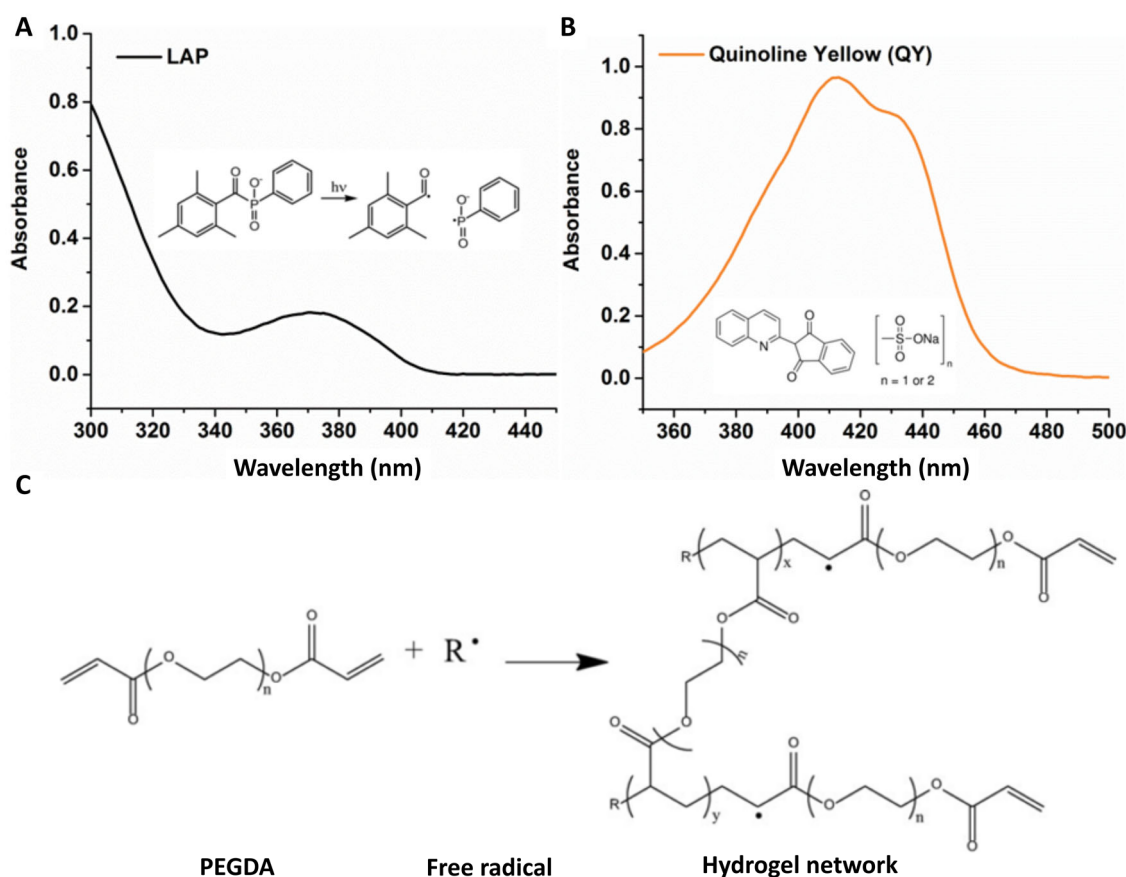


Figure 3.2| Components of the resin solution A) The UV absorption spectrum of the photoinitiator, LAP. B) The UV absorption spectrum of the photoabsorber, QY. C) The free radical polymerization of the PEGDA chain initiated by using a high power 365 nm LED. Reused with permission from R. Zhang¹²³.

3.2. Print resolution and the influence of swelling on design limitations

Stereolithographic 3D printing provides the ability to produce many different designs in a fast and reproducible manner. To ensure that the resolution of printed objects are obtained during printing and maintained afterwards, a range of design criteria that ensure optimal printing must be fulfilled. These criteria are set by testing the print resolution based on the exposure pattern of the printed object as well as the behavior after swelling. Possible resolution and swelling behavior is explained and investigated in this section.

3.2.1. Design resolution is dependent on light exposure pattern

For small structures (below 100 μm in X or Y direction), it is important that the design fits exactly with the mirrors of the DMD in order to achieve the highest possible print accuracy with respect to the highest theoretically possible resolution determined by the DMD pixel size. This requires that the design dimension must be a multiple of the pixel size. Based on camera-recordings, the projected image is well defined without any light refraction into neighboring pixels. The print resin starts to polymerize upon exposure and thereby the refractive index of the resin changes during printing. Due to the light refraction in the print resin from neighboring voxels, it is not possible to construct features down to the size of a few pixels with high accuracy. The light refraction causes the volume in the print resin corresponding to an “on” pixel (a voxel) to change the refractive index and hence scatter the light to neighboring voxels. This refraction causes a smear effect of the edges in the design.

The effect of the refraction of light can be illustrated by realizing that each pixel in the projected XY image is “on” or “off”. Features that are being exposed to light are visible via a pattern of “on” pixels from the DMD. The rest of the pixels are switched to an “off” position. Indentations are obtained by a set of “off” pixels surrounded by “on” pixels projected onto the resin containing vat. The corner voxel in the indentation will be exposed to scattered light from the three neighboring voxels as illustrated in Figure 3.3A. The opposite is true for extrusions that are produced with a pattern of “on” pixels surrounded by “off” pixels, Figure 3.3B. Both indentations and extrusions will be smaller than the designed dimensions due to this phenomenon.

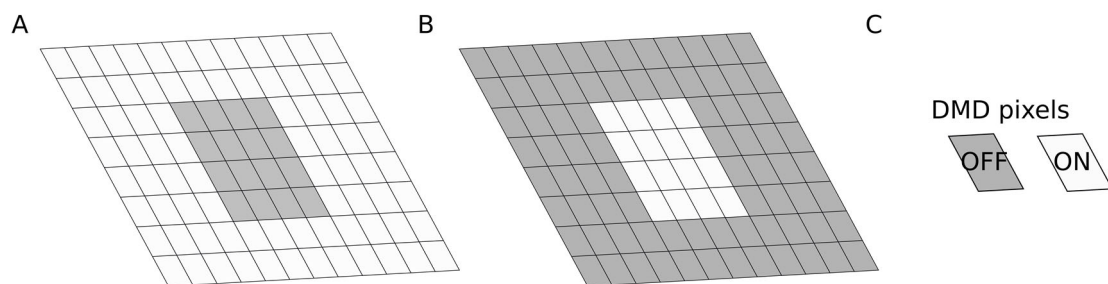


Figure 3.3| A) An indentation is printed as a result of “ON” pixels with an area of “OFF” pixels forming a square. A rounded effect of the corners is seen because the voxels corresponding to “OFF” pixels in the corners are exposed to some light due to refraction from neighboring voxels corresponding to “ON” pixels. B) A set of “ON” pixels creating a rectangular extrusion. The corners of the square will be underexposed as there are no refractive light exposure from surrounding voxels which results in rounded corners. The effect becomes more profound with decreasing feature sizes. C) Legends for “ON” and “OFF” DMD pixels.

To investigate the impact of neighboring voxel refraction, a set of indentations and extrusions is produced as rectangles with a width of 10.8 μm , 21.6 μm , 32.4 μm , 54 μm , and 108 μm . All samples are placed in deionized (DI) water at room temperature (RT) for 24 h before imaging in order to let them swell to equilibrium. The dimensions of the printed indentations and extrusions are then evaluated by light microscopy using 10x magnification.

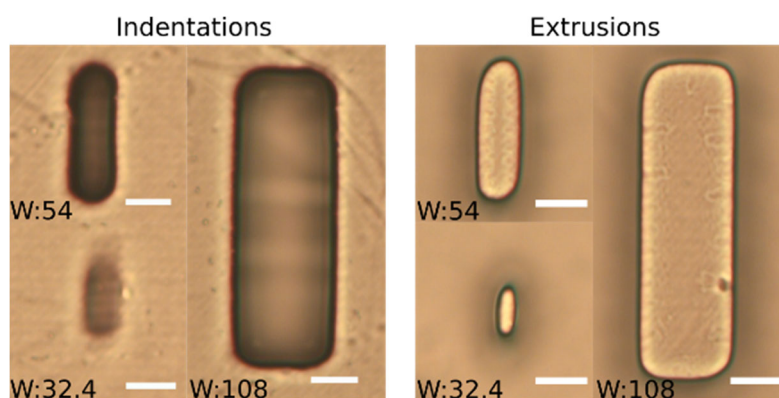


Figure 3.4| Micrographs showing prints of rectangular structures with dimensions as a multiple of the pixel size. The width of the rectangles are designed to be 10.8 μm , 21.6 μm , 32.4 μm , 54 μm and 108 μm , respectively. For printed structures below 32.4 μm , the structures cannot be resolved as they are insufficiently printed (not shown). The printed features are imaged after swelling to equilibrium in DI water for 24 h. Scale bar: 50 μm .

Figure 3.4 shows micrographs of both indentations and extrusions. For both indentations and extrusions, the rectangles below 32.4 μm in width are not visible after printing (not shown). Rectangles of 32.4 μm and 54 μm appear oval instead of rectangular in shape, and rectangles

with a width below 32.4 μm are insufficiently printed as seen in Figure 3.4. When the width is increased to 108 μm , all edges of the rectangle can be seen, and only corners appear rounded.

From these results it was concluded that it is possible to produce features with dimensions of approximately 50 μm and below; however, the length-to-width and height-to-width aspect ratios must be considered in order to achieve a robust design due to the fragile nature of high aspect ratio structures.

3.2.2. Effect of swelling

After printing, PEGDA will swell to equilibrium when placed in an aqueous solution. Swelling changes the dimensions of the PEGDA structures to various degrees depending on several factors such as the chain length between bonds in the network¹²⁴. High MW PEGDA will have a lower degree of crosslinking (longer chain length between network bonds), and low MW PEGDA will have a higher degree of crosslinking (shorter chain length between bonds). For networks of lower MW, the brittleness increases as a result of the shorter chain length between bonds. The more brittle nature provides more firm structures compared to high MW PEGDA structures, which are softer. However, it also increases the risk of notching and subsequent fracture. This study has used PEGDA solutions of low MW, M_n 700 g/mol, primarily at 200 mg/mL (20 %), therefore, the swelling behavior is assumed to be similar for all printed structures. Choosing a low MW PEGDA of 20 % w/v results in a low degree of swelling and is a good compromise between flexibility and robustness for the cell seeding platforms.

In the printed PEGDA network, the free energy of mixing and favorable PEGDA/water enthalpy drive the water into the PEGDA network and cause a stretch of the crosslinked chains. The stretched chains will counteract the swelling by generating an elastic retractive force against the stretch. When the two forces are in equilibrium, the hydrogel network is said to be in the volumetric equilibrium degree of swelling¹²⁵. The time it takes for this to happen can be found by measuring the weight change of the PEGDA network over time. For networks with a smaller pore size, the diffusion of water into the network is slow thus increasing the swelling time. Since the pore size is dependent on the chain length between crosslinks, low MW PEGDA networks will have a longer time to equilibrium compared to high MW PEGDA networks.

The equilibrium degree of swelling, Q , is described by the volume ratio between the swollen and dried polymer sample. For practicality, this can be found using the weight of the network using Eq. (1)⁴⁶, where V is volume and ρ is mass density. The equilibrium mass swelling ratio, q , is determined by $q = m_s/m_d$ where m_s and m_d is the mass of the swollen and dry polymer, respectively. The liquid polymer and solvent mass densities are ρ_{pol} and ρ_{sol} .

$$(1) \quad Q = \frac{V_s}{V_d} = 1 + \frac{\rho_{pol}}{\rho_{sol}}(q - 1)$$

To measure the equilibrium degree of swelling, five cylinders of 6 mm in diameter and 5 mm in height is printed. The cylinders are weighed immediately after printing and then every hour for 6 hours and again after overnight (O/N) in solution at RT to ensure full swelling. The samples are then dried at 60 °C for 8 hours¹²³ to determine the dry polymer weight.

Equilibrium volumetric swelling ratio is calculated from the mass of the wet and dry polymer using Eq. (1) and plotted in Figure 3.5. Equilibrium volumetric swelling is obtained after 3 hours for 20 % PEGDA (M_n 700 g/mol) with a relative change in volume of 9.2 % calculated from the change in equilibrium volumetric swelling ratio. The relatively small change in size means that designed print dimensions do not need to be corrected to obtain more precise print dimensions.

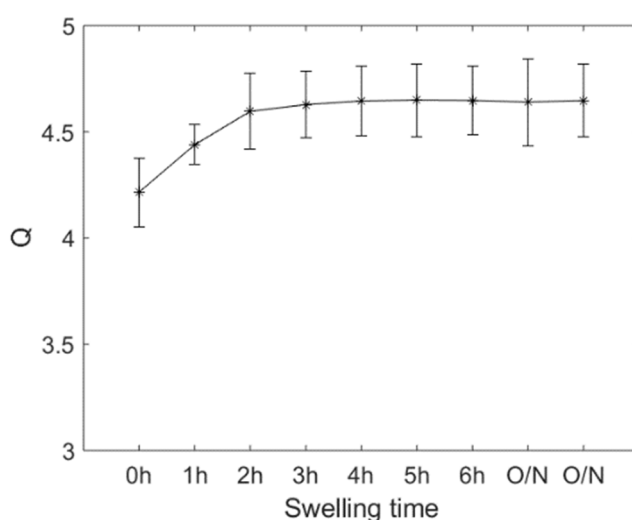


Figure 3.5| The equilibrium volumetric swelling ratio over time for cylinders of 20 % PEGDA (M_n 700 g/mol). The steady state is reached after 3 hours and the relative volumetric change is 9.2 %, giving only a small change in size from the designed dimensions of the printed structures. Error bars represent standard deviation ($n=5$). Adapted with permission from (Christensen et al., 2019, DOI: 10.1021/acs.biomac.9b01274) American Chemical Society.

To investigate the effect of subsequent swelling on printed design dimensions, indentations and extrusions in the shape of rectangles in multiples of 10, 20, or 30 times the pixel size are produced corresponding to 108 μm , 216 μm , and 324 μm . The width of the rectangles is measured at the center immediately after printing before they are placed in DI water until equilibrium swelling is reached. After swelling, the width is measured again, and the change in size from designed dimension to post swollen state is determined. Results are shown in Figure 3.6.

After printing, the dimensions are close to the designed dimensions for both indentations and extrusions. After swelling, the dimensions change as the network takes up water resulting in larger protrusions and smaller indentations. In general, there is a larger error in measured

dimensions from smaller structures. This is due to the measurement error being more profound in smaller structures. For extrusions, the dimensional change is considered negligible and no design changes are required based on these results. The cell seeding platform, described in sections 3.4, is constructed mostly on extrusion based designs and is hence considered to have dimensions close to the designed dimensions.

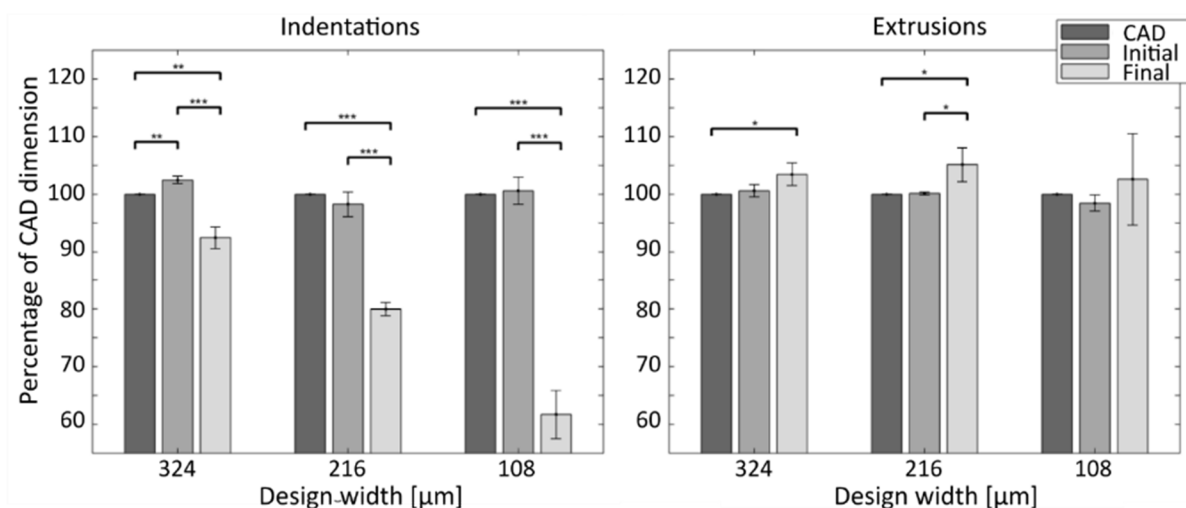


Figure 3.6 | Dimensional change from pristine print to swollen state is determined by measuring the dimensions of rectangles with 1:3 in width to length ratio produced in 20 % PEGDA immediately after printing and after swelling to equilibrium. The results are shown as relative change compared to the designed dimensions. Indentations change dimensions increasingly with smaller original design and must be evaluated during design phases to achieve visually apparent structures. After swelling protrusions are close to designed dimensions. Error bars show standard deviation ($n = 3$); $*p < 0.05$, $**p < 0.01$, $***p < 0.001$. Adapted with permission from (Christensen et al., 2019, DOI: 10.1021/acs.biomac.9b01274) American Chemical Society.

3.3. Mechanical stability of 3D printed PEGDA structures

The mechanical properties of PEGDA hydrogels, such as the shear modulus and stiffness of cylindrical posts, are determined to characterize force read-outs from subsequent tissue formation. The resistance to wear from mechanical stress caused by the contracting tissues is also examined, as parts of the printed structures will be subject to weeks of cyclic mechanical stress from bending.

3.3.1. Shear modulus

The composition of the hydrogel influences the mechanical strength and modulus of the printed structures. The shear modulus is determined by uniaxial compression, with a 50 N load cell, for cylinders composed of 20% PEGDA. Before compression test, the exact dimensions of the cylinders after swelling are obtained by optical measurement in air using a confocal

microscope. The cylinders are placed on the stage, and the focus is adjusted to the edge of the top surface and then readjusted to focus on the edge of the bottom of the cylinder. The difference in height is measured on the stage of the microscope, and the width and height of the sample is determined. Cylinders are then immersed in water to avoid drying of the hydrogel and compression test is performed on samples that are still wet.

Using the engineering stress, σ , plotted against the expression $\lambda - \lambda^{-2}$ with the extension ratio, λ , the shear modulus, G , can be determined for the linear region using Eq. (2)¹²⁴.

$$(2) \quad \sigma = G(\lambda - \lambda^{-2}), \quad \lambda = \varepsilon + 1 = \frac{L}{l}$$

The extension ratio is determined using the engineering strain, ε , calculated from the initial length, l , and the final length, L , of the tested cylinder. In Figure 3.7 the compressive stress found from uniaxial compression test is plotted against $-(\lambda - \lambda^{-2})$ for one of the samples. The negative of the expression is used as compression test and not tensile test is used. The slope of the linear fit in 0.2 – 0.8 of $-(\lambda - \lambda^{-2})$ is the shear modulus of the 20 % PEGDA cylinders. The shear modulus is found to be $G = 0.47 \text{ MPa} \pm 0.046 \text{ MPa}$.

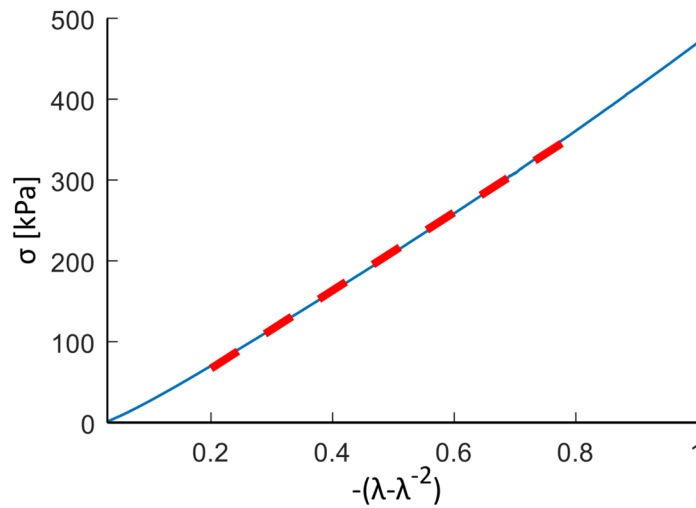


Figure 3.7| The shear modulus is found as the slope of the linear fit (red dashed line from 0.2 – 0.8 – $(\lambda - \lambda^{-2})$) in the plot of the measured stress from the uniaxial compression test plotted against $-(\lambda - \lambda^{-2})$ where λ is the extension ratio. The shear modulus is found to be $0.47 \text{ MPa} \pm 0.046 \text{ MPa}$ ($n = 15$).

3.3.2. Printability of microscale beams for fatigue testing

The cell seeding platform for tissue formation is based on a design with vertical posts to promote tissue formation and enable visual read-out. PEGDA platforms must be able to resist stress from cyclic mechanical stress exerted by the contraction of the cells or from applied mechanical pacing. A test beam is designed to mimic the size of mini-engineered tissue of

around 1 mm. This section focuses on explaining the design challenges and possible beam and support solutions to construct a horizontal beam, results from the test is shown in section 3.3.4.

Deflections of a 1000 μm long horizontal beam requires it to be unsupported in the full horizontal span in order to perform the deflection in the center of the beam. A horizontal beam with insufficient print-supports will either be narrowing in depth between the supports or the layers will be unable to adhere to each other as they are floating freely in between each layer. This happens because the nature of 3D printing relies on attachment to the previous layers. A beam of these dimensions that is supported at one end only (Figure 3.8A) will likely break as a result of the fluid shear that appears when moving to the next print layer. The first layer will only be 20 μm thick and 1000 μm in length. The beam has very low stiffness when only the first layer has been printed and is thus likely to curl away from its original position. This prevents contact, and thus adhesion, with the next printed layer giving rise to the brush like appearance (Figure 3.8B). The problem is reduced at the top of the beam (Figure 3.8C) because the previously printed layers increasingly support each other and eventually prevents the last printed layer from floating too far away from next layer to be printed. Consequently, adhesion between the layers is eventually possible and the brush appears denser at the top.

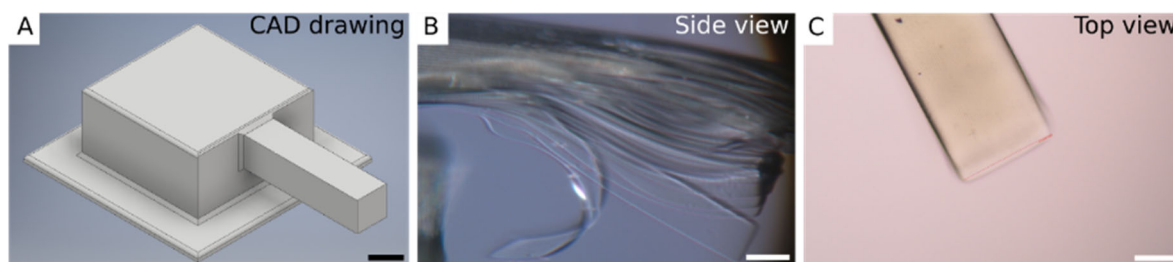


Figure 3.8| A) CAD drawing of an unsupported beam with one free end is designed. B) Micrograph of the beam after printing seen in sideview. The unsupported beam reveals a layered appearance where each print layer is a sheet of a well-defined PEGDA. However, adherence to the next layer is not achieved as the previous layer is not held in place but can float freely making the penetration depth insufficient to ensure gelation between the two layers. The layers get more attached with increasing print height as movement of subsequent layers is restricted by the previous layers resulting in more attachment between the final layers. C) Due to better attachment through the print, the top view does not necessarily reveal the missing attachment between layers. Scale bar black: 500 μm , scale bars white: 200 μm .

Support structures are necessary to enable printing of long free-hanging structures, such as a 1000 μm horizontal beam. However, as they are obviously not wanted in the final structure, it is desirable to use the lowest possible number of support structures. In order to determine the maximum horizontal distance between the vertical supports required to print a 1000 μm free-hanging horizontal beam, a range of support structure designs are tested as seen in Figure 3.9. A beam of length 1000 μm , width 100 μm , and thickness 100 μm is printed with different types of supports. The length between the two end posts is 800 μm . Beams with no support and

different support structures are designed both from directly below the beam and from the side as indicated in Figure 3.9A-E. Angled beam sections at the end of the beam are added as well (Figure 3.9F) to investigate design possibilities in the form of mechanical cues, optical markers and similar.

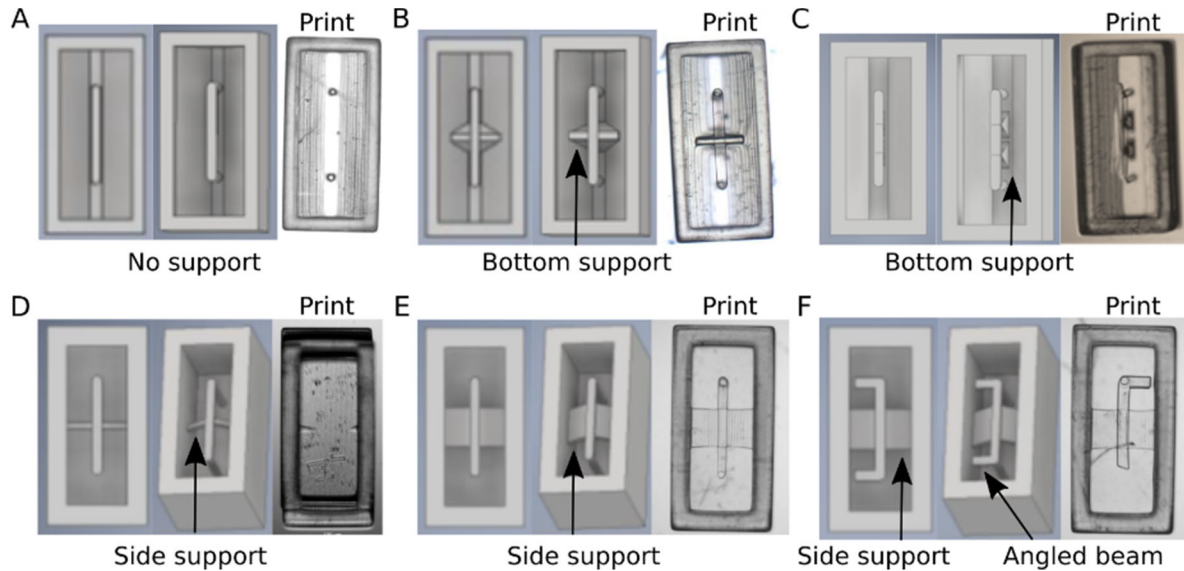


Figure 3.9| CAD design and micrographs of different support structures that are investigated to find the maximum distance between supports that is possible to produce. When the support structures are solid, the overhanging beam can be printed with only one support. Narrow and fragile supports or no support are not adequate to print the overhanging beam. In all designs, the length of the beam is 1 mm and the free overhanging distance with no supports is 800 μm in total.

Based on the results presented in Figure 3.9A, it is not possible to print an unsupported beam with a length of 800 μm . However, a single support structure placed at the center of the beam is enough to produce an intact beam when it is supported from the bottom (Figure 3.9B). One support is insufficient when the beam is supported from the side as the side support structures are too fragile (Figure 3.9D). Increasing the width of the side support structure results in intact support and beam (Figure 3.9E). Utilizing two support structures, each supporting the beam at a single point, also enables printing of the beam (Figure 3.9c). From the attempted options of support structures, it is found that 400 μm between supports is sufficient if the support itself is robust, however, for more fragile supports, the maximum distance between supports should be no more than 300 μm .

The beams are in risk of breaking during printing as the printed structure sticks to the bottom of the vat, which is covered by a non-stick film composed of fluorinated ethylene propylene. The adhesion of the PEGDA to this film is low, however, for delicate structures, the release might ruin the produced structures if the tensile stress is too high compared to structure stiffness. Supporting structures are in risk of breaking when the aspect ratio of the supporting

structure is high and the supported structure has a large surface area. This is due to the increase in surface area and thereby increased attachment between the structure and vat making the shear stress higher during release. An example where the surface area is increased and leading to print failure is seen in Figure 3.9F. One end of the beam is broken and one is intact showing that this design is on the border of possible aspect ratios for the supporting posts.

3.3.3. Production of an unsupported test beam

As described in section 3.3.2 it is not possible to print an unsupported beam with a horizontal span longer than 400 μm . However, if the support structures are designed so they can be removed from the structure after printing, it will result in a free hanging beam, Figure 3.10A. Manually removing support structures on a designed beam of length 800 μm , width 200 μm , and thickness 100 μm is not a straightforward process and might cause damage to other structures. Sacrificial supports that self-remove are consequently preferred. By designing an arch structure of narrow width with a high aspect ratio under the beam, it is possible to construct bearing supports that enable stable beam production. The cross-sectional area of the arch supports is 55 $\mu\text{m} \times 50 \mu\text{m}$ at the bottom and 100 $\mu\text{m} \times 50 \mu\text{m}$ below the beam in order to support the full width of the beam as seen in Figure 3.10B,C. The top part includes holes to weaken the attachment between support and beam.

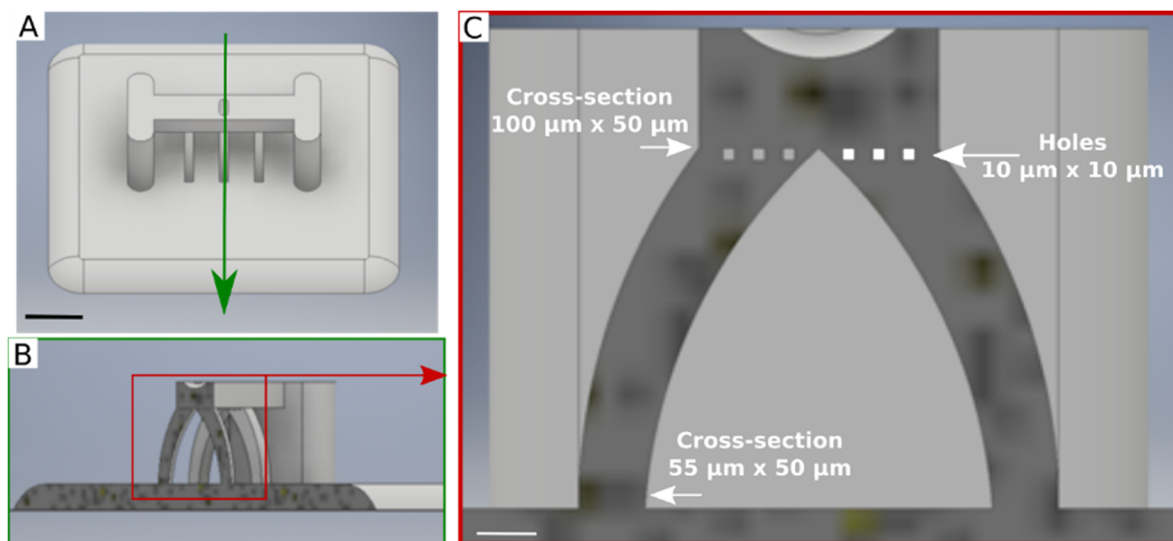


Figure 3.10| CAD drawing showing arching supports that create the possibility to construct a free hanging beam of length 800 μm by self-removal of the support structures during subsequent handling. Holes in the final layer of the support structures ensure a lower degree of attachment to the beam and no residues of the supports can be seen after detachment. Scale bar black: 200 μm , scale bar white: 50 μm .

The narrow supports are on the edge of the printable spectrum and cannot withstand the fluid shear experienced during removal of the print from the print solution and handling post-printing. This results in sacrificial supports and leaves no residues of the arch supports on the

beam post printing. Only the feet of the supports are visible in the bottom layer of the print as seen in Figure 3.11A. The aspect ratio of the supports is the key to achieving the sacrificial process as the shear will not break more robust supports as seen in Figure 3.11B. Here the width of the support structures is doubled and, as a result, they remain intact during printing. If supports are not sacrificial, subsequent manual removal is tedious and might cause damage to other structures during the removal process.

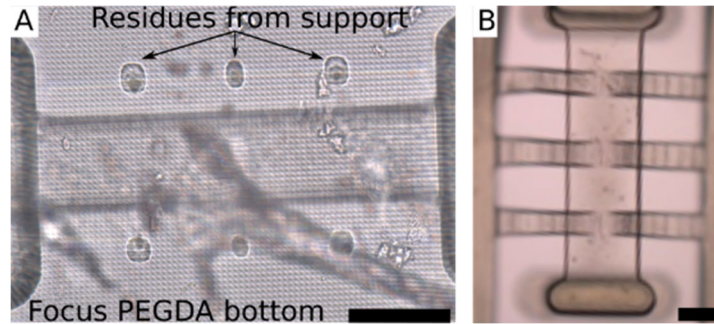


Figure 3.11| Micrographs of test beams. A) Post printing, the support structures have broken off and are only visible in the bottom substrate. These support residues have no influence on subsequent testing. Formation of support structures that do not break off is seen when the attachment to the beam is too strong or when they are not the right aspect ratio. Scale bar 200 μm . B) When the support structures are big enough to be robustly printed, they will not break off spontaneously and will need further handling in order to detach from the beam. Scale bar: 500 μm .

3.3.4. Fatigue test

The flexibility and robustness of the PEGDA beam is tested by its ability to withstand cyclic bending. Structures must be able to withstand such bending over an extended period of time during long-time culturing of 2-3 weeks. Cyclic bending with 0.5 – 2 Hz simulating natural cardiac contractions can potentially result in up to a million bends over a period of weeks. In order to test the ability of the delicate PEGDA structures to withstand wear and tear caused by up to a million bends, a test is set up to actuate a beam of PEGDA for 1.1 million times by displacing the center part of the beam by 220 μm as seen in Figure 3.12A. This is achieved by using a voltage controlled piezo actuator with a working range from 0 μm to 220 μm in vertical displacement in an aqueous environment. The optical read-out system captures the horizontal bending at no and full displacement, corresponding to top and bottom position of the actuator range. Before initiation, the pin is positioned at the surface of the beam in the center, marked by a small indentation in the printed beam.

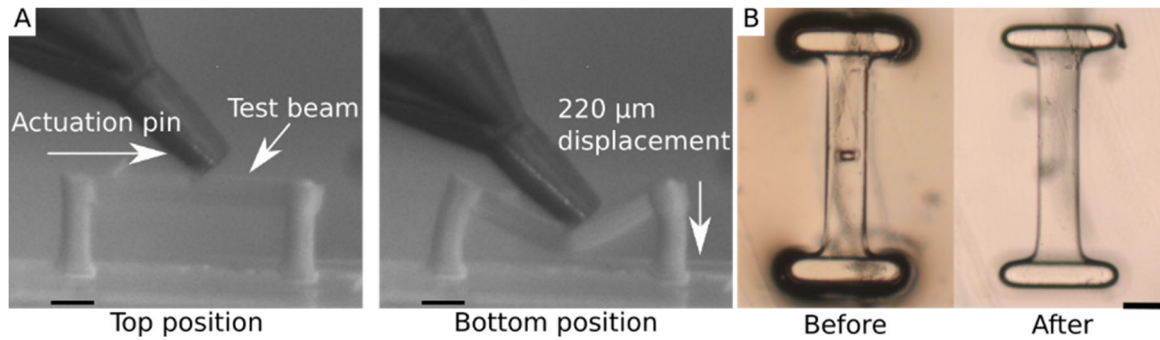


Figure 3.12 | Micrographs of the test beam. A) Top and bottom view during cyclic actuation of the PEGDA beam. Fatigue testing is performed by cyclic displacement of a horizontal PEGDA beam of 800 μm unsupported length, 100 μm in vertical cross-section and 200 μm wide. An actuator pin controlled by a piezo actuator is positioned at the surface of the PEGDA beam ("top position") before initiation of the test. A camera captures images from the side to visualize the resulting beam bending ("bottom position"). Displacement is performed 1.1 million times at 3 Hz. B) During testing, some wear is observed from abrasion of the actuator pin on the PEGDA beam. The indentation for optical adjustment of actuator pin position is worn off. Depth of the optical marker is 30 μm . Scale bars: 200 μm .

After 1.1 million cyclic vertical displacements of 220 μm , the beam is inspected in a bright field microscope to evaluate wear and tear. There is no tearing in form of ruptures or other visible impairments from the bending, suggesting that the material is capable of withstanding repetitive motions. Some wear is observed as the mark for central placement of the actuator pin can no longer be seen in the beam, Figure 3.12B. Abrasions from the metal pin seems to be uniform over the contact area and do not cause small ruptures that could lead to subsequent notching¹²⁶ and fracture of the PEGDA.

3.4. Designing a multiassay platform

Tissue formation happens spontaneously in most mold designs when there is an opposing force from the posts that can counteract the cells contraction and thereby make them form an elongated tissue expanded between two points (section 2.3.2). Compliant vertical posts are a suitable choice for engineered contractile tissue as optical tracking of the movement of the posts provides an easy way to observe tissue function. In this section, the design of a cell seeding multiassay platform with focus on manufacturing robustness and the ability to promote tissue formation is described.

3.4.1. Engineered tissue formation based on a vertical post design

The shape of the vertical post influences the tissue formation and read-out possibilities, and choosing the right design is essential for robust tissue formation and force read-out. In the design presented here, cylindrical posts are preferred as they result in reduced local stress

concentrations during tissue compaction compared to rectangular posts⁸¹. The ability of the posts to bend in response to tissue contraction depends on the stiffness of the post relative to the pulling strength of the tissue. The force exerted by cells in engineered tissues have been reported within a wide range (5 nN to 200 nN for single cells measurements and 0.08 mN/mm² to 4 mN/mm² for engineered tissues)^{35,127} and is the reason why estimation of suitable post dimensions based on tissue force can be challenging. To provide a visual output and avoid plastic deformation of the posts, it is estimated that the deflection should be 10 % to 20 % of the tissue length. To lower the cost per tissue, the length between posts is designed to be approximately 1 mm to minimize the number of cells used per tissue.

A suitable height and diameter of the posts is estimated to allow sufficient elastic bending of the posts to accommodate tissue shortening of 10 % to 20 %. Estimations are made based on previously reported flexible post designs⁹³, using the Euler-Bernoulli beam theory that relates the applied force with deflection of the post based on geometry according to Eq. (3), (4), and (5). A sketch of the principle is provided in Figure 3.13. The deflection, δ , and the Young's modulus of the material, E , are used to calculate the contraction force, F , using the length of the cylinder, L , and the position of the tissue, x . Post stiffness, k , can be found by knowing the force used to deflect the post a certain distance as seen in Eq.(4). The moment of inertia, I , is calculated based on the diameter, d , of the cylinder Eq. (5).

$$(3) \quad \delta = \frac{Fx^2}{6EI}(3L - x)$$

$$(4) \quad F = k\delta = \frac{6EI}{(3Lx^2 - x^3)}\delta$$

$$(5) \quad I_{circle} = \frac{\pi d^4}{64}$$

$$(6) \quad E = 2G(1 + \nu)$$

Based on the shear modulus, G , obtained in section 3.3.1, and a Poisson's ratio of $\nu = 0.5$ assuming an incompressible material¹²⁸, the Young's modulus is calculated according to Eq. (6). The starting point of the cylindrical post dimensions is estimated using this method to get the correct range of stiffness. However, exact dimensions are dependent on specific cell types and number of seeded cells and hence the post geometry is varied empirically as appropriate.

The position of the tissue around the post affects the extend of deflection. A higher tissue position on the post effectively makes it easier for the tissue to deflect the post, i.e. the same force results in a larger post deflection when applied higher on the post. This is illustrated in Figure 3.13. It is therefore advantageous to position the tissue at the top of the posts to ensure maximum deflection in response to the contraction force of the tissue.

Most designs presented in this work uses cylindrical posts with a height of $850\ \mu\text{m}$ and a diameter between $100\ \mu\text{m}$ and $200\ \mu\text{m}$ in order to allow a deflection corresponding to 10 % to 20 % assuming tissue position around the top of the post, where $x = L$.

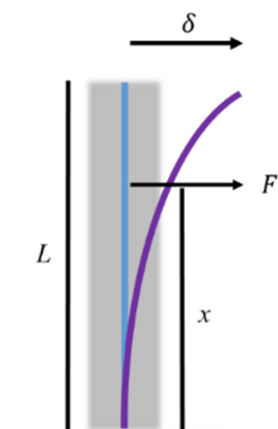


Figure 3.13| The principles of the Euler Bernoulli beam theory. The point of application a distance, x , from the fixed end of the post of length, L , determines the force, F , that must be applied to bend the post a distance, δ . Figure is adapted with permission from (Christensen et al., 2019, DOI: 10.1021/acs.biomac.9b01274) American Chemical Society.

3.4.2. Design of mechanical cues for vertical positioning of tissues

In order to calculate tissue contraction force accurately from post deflections, it is necessary to know where the tissue is anchored to the post (section 3.4.1). To ensure that this position does not vary between tissues, a mechanical cue in the form of an enlargement is added on the top of the posts. The mechanical cue will be encapsulated by the tissue during compaction and function as an anchor to fix the position of the tissue. The point of application of force from the tissue contraction will thereby be fixed at a constant vertical position on the post ensuring a constant correlation between post deflection and contraction force.

Designing the shape of the mechanical cue is not straightforward and must allow the post to be printed without breaking as the high aspect ratio of the post design makes it fragile during manufacturing. During each printing step, the print is attached to the bottom of the vat (explained in section 3.3.2). Moving the stage to the next print layer releases the print from the vat bottom by mechanically pulling it off the vat bottom and fragile structures are therefore at risk of breaking. The tensile force required to loosen the print from the vat scales directly with the area that is attached (i.e. the area that was printed in the last step). Consequently, when the area of attachment between the print and the vat bottom increases at the enlargement, the posts must be able to withstand a higher tensile stress during detachment. It is additionally important for all structures to have transitions when the geometry changes and to avoid changes with 90 degree angles as such points will be weak during printing. All mechanical cues

are therefore designed with a smooth transformation in width to avoid sharp edges and to improve the attachment between the cylindrical posts and the enlarged squared or rounded top cues. Three proposed designs are shown in Figure 3.14.

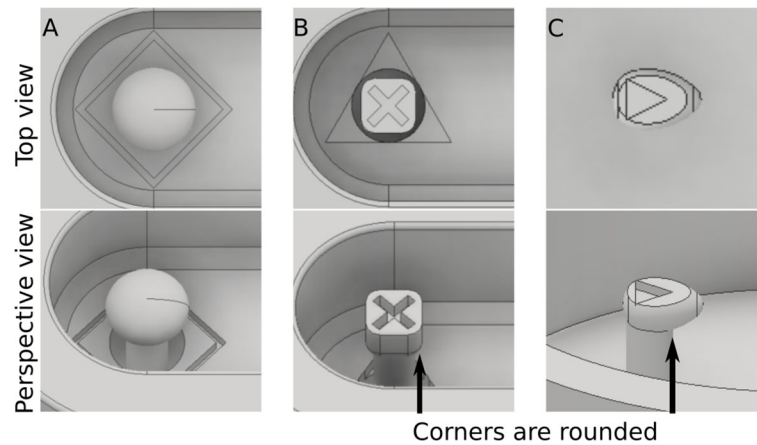


Figure 3.14| CAD drawings of mechanical cues on top of posts. All designs have the ability to fix the position of tissues at the top of the post by having an enlarged feature which can be encapsulated by the tissue during compaction. Round (A), square (B) and droplet shaped (C) mechanical cues are presented. Sharp edges are prevented by having round shape and rounded corners to reduce local stress concentrations.

Both round, droplet-shaped, and square top mechanical cues are designed with a transition region of stepwise change in the shape. This ensures printability and also avoids sharp corners and thereby reduces the stress on the tissue. Squared top mechanical cues shows a higher printability compared to round shapes whereas the droplet and square types are similar in robustness during printing. The difference in printability is likely due to the area differences and not shape-dependent. The squared and droplet based designs are used in future designs.

3.4.3. Elevated floor reduces seeding volume and assists tissue positioning

The performance of the tissue mold can be improved by elevating the floor of the PEGDA mold. This reduces the volume of the mold and makes it possible to seed fewer cells while still filling the molds to the top and embedding the mechanical cues. Thereby, elevating the floor accommodates tissue formation at the top of the posts rather than below the mechanical cue and maintains a low number of cells per tissue.

As the floor is raised and the height of the posts remains the same, a cavity inside the mold must be created around the posts to allow them to deflect. The distance between the post and the wall of the cavity must be large enough for the posts to deflect when the tissues are contracting. However, the void should not be filled with the cell-loaded scaffold. When excess water is removed from the MAP molds prior to cell seeding water remains inside the voids why filling of the void with cell-loaded scaffold is prevented, Figure 3.15.

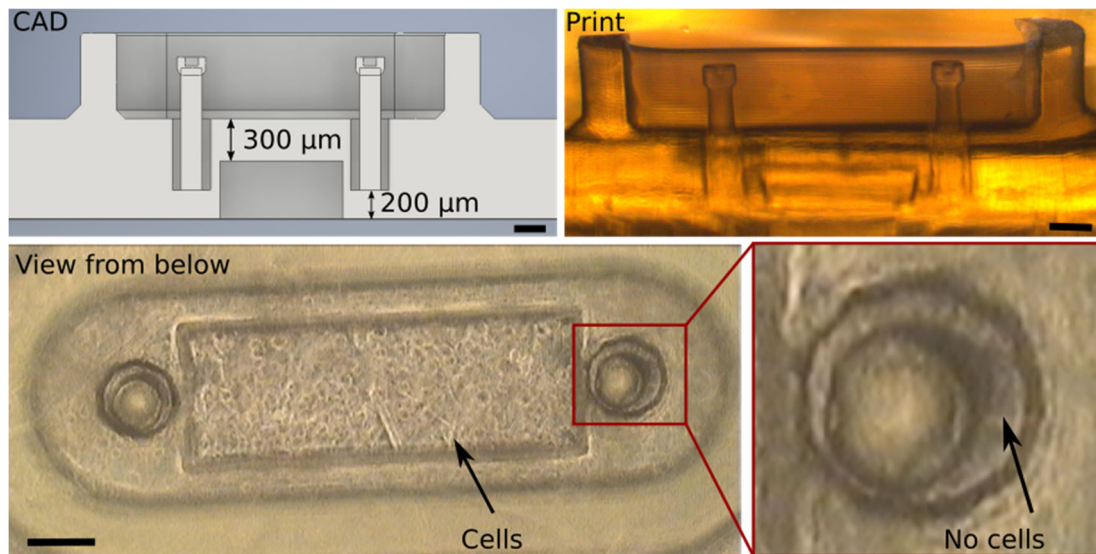


Figure 3.15| CAD drawing and micrographs showing mold design and cell position. The MAP mold is designed with an elevated floor that minimized the seeded volume while maintaining a filling level where the top mechanical cues are entrapped by the cell-loaded scaffold. Due to the elevated floor the posts are embedded in cavities to maintain the same height and thereby stiffness. The PEGDA layer below the walls of the well is 700 μm thick after the floor is elevated, which reduces visibility from below. A rectangular cavity in the bottom of the PEGDA layer enhances visualization in an inverted microscope, standard for cell culture laboratories and makes it possible to follow tissue formation. After cell seeding into the PEGDA chamber, inverted microscopy reveals that no cells are entrapped inside the cylindrical cavity around the post. Cells are more visible within the rectangle where the PEGDA layer is only 300 μm thick compared to 700 μm in the remaining part of the culture chamber. Scale bars: 200 μm .

Figure 3.15 shows a PEGDA mold with cell-loaded scaffold inside visualized by inverted microscopy. Cells are seen through the thin PEGDA layer in the central part of the mold floor. The central part is reduced in thickness to 300 μm to optimize visibility. In the cavity surrounding the posts, the PEGDA layer is 200 μm . No cells are seen inside the void, meaning that the no flow of cell seeded scaffold happens into the void during filling of the molds.

3.4.4. Optical markers for detection and calibration in a multiassay platform

Read-out of the tissue contraction is a key aspect for the PEGDA platform to be functional. To ease the read-out, an optical marker can be incorporated in the design. This marker can be an addition to the existing design such as a visible detection pin next to the tissue as depicted in Figure 3.9F where it is shown that an extension can be printed perpendicular to the tissue. Visual markers can also be embedded in the current design as either indentations or protrusions. Manufacturability is crucial for the visualization, as for example narrow structures in the CAD design may not look the same once printed as shown in Figure 3.4.

In order to track the movement of the posts via the optical markers, they must be visible after printing and provide optical contrast. This is achieved by making rectangular or triangular markers inside the perimeter of the cylindrical post as shown in Figure 3.16. A reference in the form of a square or a triangle can be created at the bottom of the mold (Figure 3.16B,C). However, it turned out that this feature was difficult to observe in the printed structure and therefore only the marker on top of the mechanical cue was maintained in subsequent designs. Of the optical markers in the top of the posts, both rectangles and triangles were produced (Figure 3.16C-F). Triangular markers are more visible than rectangular markers after printing and is therefore preferred. Automated visual recognition and detection is not considered in the design of the optical markers presented here.

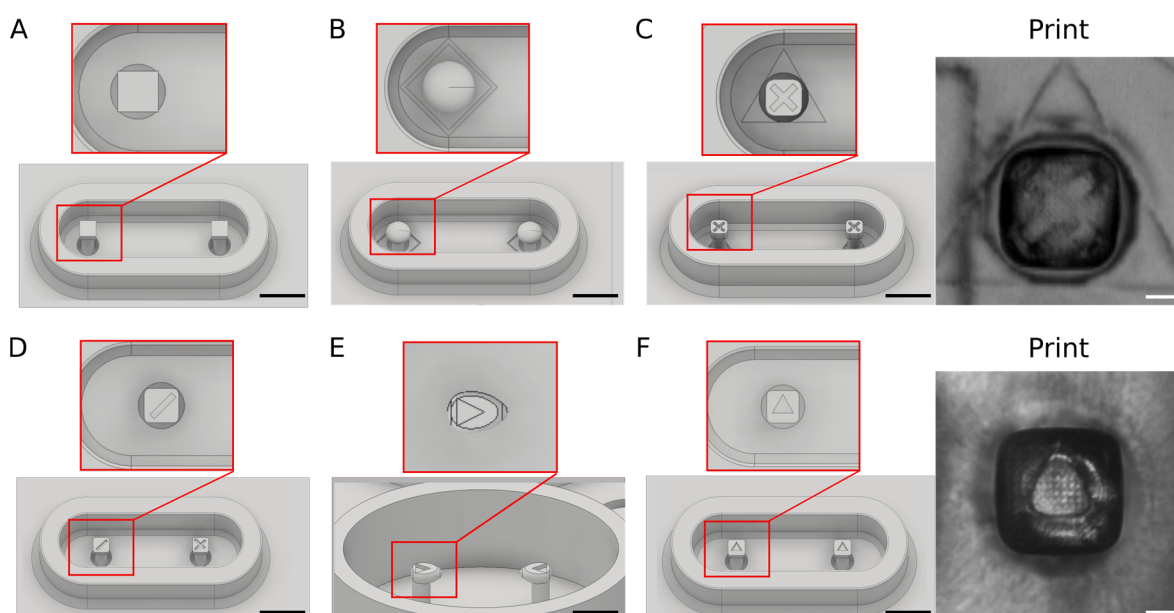


Figure 3.16 | Overview panel showing CAD drawings and micrographs of the optical cue designs incorporated in the mold and flexible PEGDA posts. A) No optical marker incorporated in the squared mechanical cue. B) Round mechanical cue with no optical marker and a squared reference marker in the PEGDA substrate below. C) Squared mechanical cue with cross embedded and a triangular reference marker in the PEGDA substrate. After printing the cross is vaguely visible in the top of the mechanical cue. D) On the top on one cue the cross is changed to a single rectangle to differ between left and right post. No reference marker is included in this design. E) A droplet-shaped mechanical cue with a triangular marker embedded. F) Triangular optical marker embedded in the top of the mechanical cue with no reference embedded in substrate below. After printing the optical marker is clearly visible, however with rounded corners. Scale bars: 500 μm .

Reproducibly printed platforms with stable posts are defined as having robust posts including mechanical cues on top, where 10 % or less is broken in each platform after printing. This can be achieved by using a resin composition containing 9 mg/mL absorber in combination with a slicing thickness of 25 μm which gives the best possible vertical print resolution¹²³. However,

for posts below 200 μm in diameter with heights of 850 μm and posts with droplet shaped mechanical cues, the threshold of a maximum 10 % broken posts cannot be achieved using these settings and hence another solution has to be used. Therefore, the print resin is adjusted to contain 9 mg/mL absorber with a slicing thickness of 20 μm which increases the bonding between layers. This composition ensures a reproducible production of the multiassay platforms with less than 10 % broken posts and is therefore preferred despite reduction in the vertical print resolution.

3.4.5. Characterization of flexible posts for functional read-out

As described in section 3.4.1, the tissue contraction causes the vertical posts to bend and this can be used to calculate the contractile force of the tissue from the length of displacement. A characterization of the post stiffness is therefore necessary to translate contraction distance into tissue contraction force. The factors that contribute to changing the stiffness of the posts are post diameter, geometry, and degree of crosslinking. Cylindrical posts are characterized in this section with different diameters and print settings that might influence the degree of crosslinking.

The stiffness of the posts is determined by mounting them horizontally on a high resolution scale and deflecting the free end 220 μm vertically. After deflection, the resulting weight change is converted to force and the stiffness, k , is calculated using Eq.(4).

It is investigated how different exposure times or design changes influence the stiffness of a post measuring 150 μm in diameter and 850 μm in height. Four designs are investigated produced with an exposure time of 2.2 s unless otherwise stated, Figure 3.17A. In design (i) a taper is added to the bottom of the post to prevent post breakage from a stress concentration point that would be created by having a 90° angle between the PEGDA substrate and the post. Design (iii) imitates the PEGDA MAP where the floor is elevated and the posts are embedded inside a cylindrical void. The region of the post inside the void might be thicker due to the overexposure from surrounding voxels and hence an increased stiffness would be expected. Design (ii) and (iv) explore the impact of increased exposure on post stiffness. Two cylindrical free standing posts with no taper and no embedding are produced using 2.2 s and 3 s exposure time. Results presented in Figure 3.17B do not show a difference in average means between the four different designs. The effect of the overexposure from light scattering of neighboring voxels inside the void seems to have little or no effect on the design as well as both exposure time and bottom taper does not notably change the stiffness of posts. For posts of 150 μm diameter it is hence concluded that within the range of changes tested here (changing the exposure time, adding a taper, or embedding the posts in a cylindrical void) have a negligible effect on post stiffness.

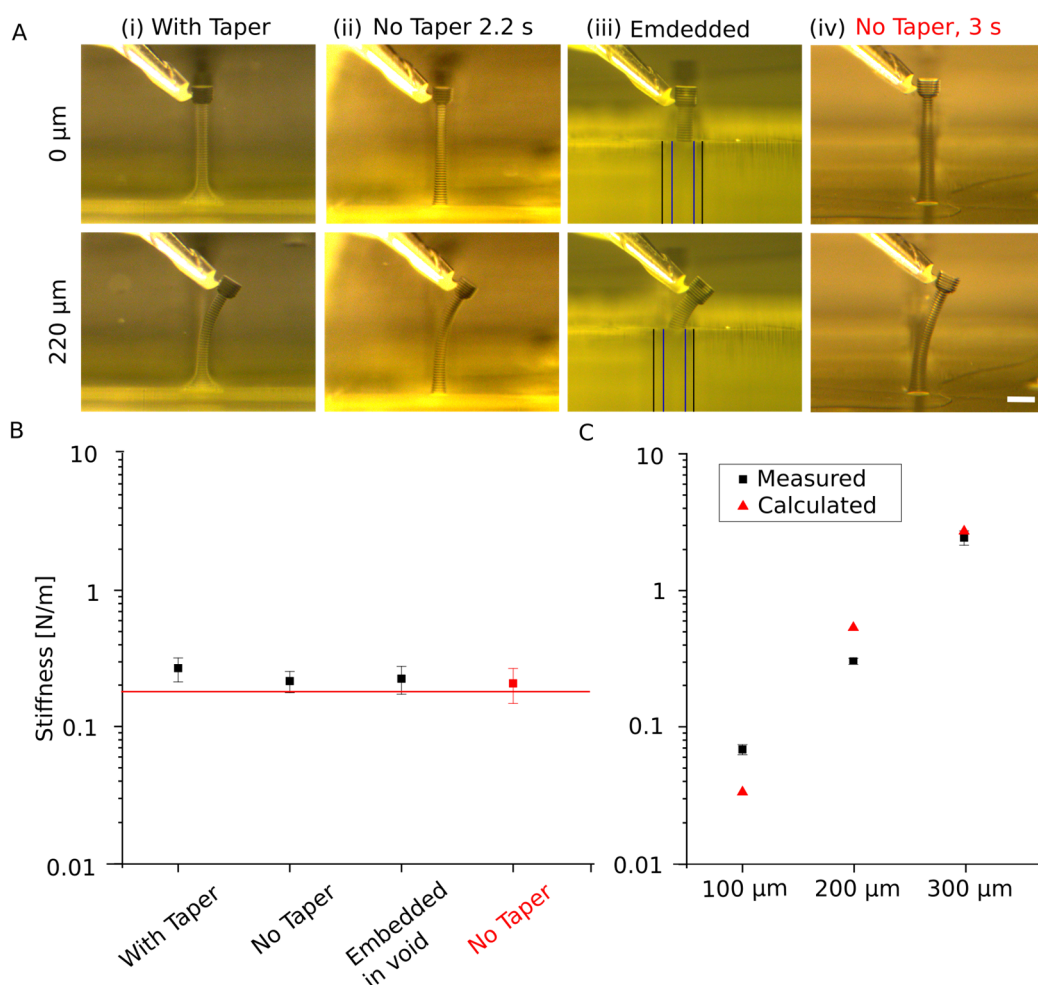


Figure 3.17 | A) Micrographs showing the deflection of four post designs all with a diameter of 150 μm and height 850 μm . (i) A taper is added in the bottom to make a softer transition from the PEGDA substrate and avoid 90° angles. (iii) Post embedded inside a cylindrical void in the PEGDA substrate. (ii),(iv) Free standing post with no taper produced with 2.2 s exposure time and 3 s exposure time respectively. Scale bar 200 μm . B) Stiffness in N/m of the four post designs described in A). The stiffness is similar for all four variations tested. The red label indicates a 3 s exposure with no taper, all other have been printed using 2.2 s exposure time. The horizontal red line is the theoretical stiffness based on post geometry and Young's modulus derived from measured shear modulus. Error bars represent standard deviation ($n=3$). C) Stiffness versus post diameter. All posts have a height of 850 μm . The measured stiffness (black square) is compared to the theoretical values (red triangle). Error bars represent standard deviation ($n=5$). Figure "C" is adapted with permission from (Christensen et al., 2019, DOI: 10.1021/acs.biomac.9b01274) American Chemical Society.

The stiffness of posts with diameters of 100 μm , 150 μm , 200 μm and 300 μm is determined. Figure 3.17C shows the increase in post stiffness that results from increasing the post diameter. In most cases the measured and theoretical value is similar, however for posts of 100 μm in diameter the measured stiffness is higher than the theoretical. This is likely due to difficulties in measuring the posts of this diameter leading to a higher uncertainty during measurements.

Increased crosslinking of the posts as a result of the compromised Z-resolution, from using 9 mg/mL QY concentration and 20 μm slicing thickness, is evaluated by investigating the change in height from designed CAD structure to swollen print. Micrographs of the posts are measured using the free software Fiji (imageJ). Little height change is observed due to the overexposure when evaluating the height of printed posts after swelling to equilibrium. The height of the posts is $98.2 \pm 1.4 \%$ of the designed height for posts printed with 5 s exposure time which is consistent with the expected design change due to swelling alone. The overexposure due to low absorber concentration is therefore not considered a risk to the final design of the MAPs produced. From the studies above, it can be seen that the major contribution to stiffness is the diameter of the posts.

3.5. Summary of the multiassay platform design

A single PEGDA platform can contain 20 identical molds to produce several tissues at the same time, under the same conditions. The printing time is the same when the z height remains unchanged due to the DMD based stereolithographic approach. Producing 20 molds at once is therefore more time efficient. The multiassay platform (MAP) allows for evaluation of multiple tissues at once and provides the ability to easily have several replicates in each experiment.

Each mold of the MAP is numbered for identification (Figure 3.18B) and the mold design is based on the conditions described in the above sections. The raised floor with cavity for the flexible posts (Figure 3.18F) and the wall defining the mold (Figure 3.18A) secures a minimal number of cells used while the mechanical cues ensures position of the tissues (Figure 3.18D). The flexible posts (Figure 3.18C) ensures the possibility for functional read-out and the optical marker on the top (Figure 3.18E) provides optical contrast in order to track the post deflection. In order to calibrate the position of the entire platform, an optical marker is embedded (Figure 3.18G). The positions of other features on the platform relative to this marker are predetermined and does not change between platforms. Thereby, the accuracy of the print position on the coverglass and the positioning of the platform inside culture chambers are not critical for optical read-out.

Manufacturing time of the MAPs are fast compared to casting methods and are determined by the number of printed layers and hence the platform height. The height of the MAP shown in Figure 3.18 is 1.77 mm and hence the printing time for a single platform with 20 parallel molds for tissue formation is around 15 min with the exact printing time depending on the slicing thickness and exposure time.

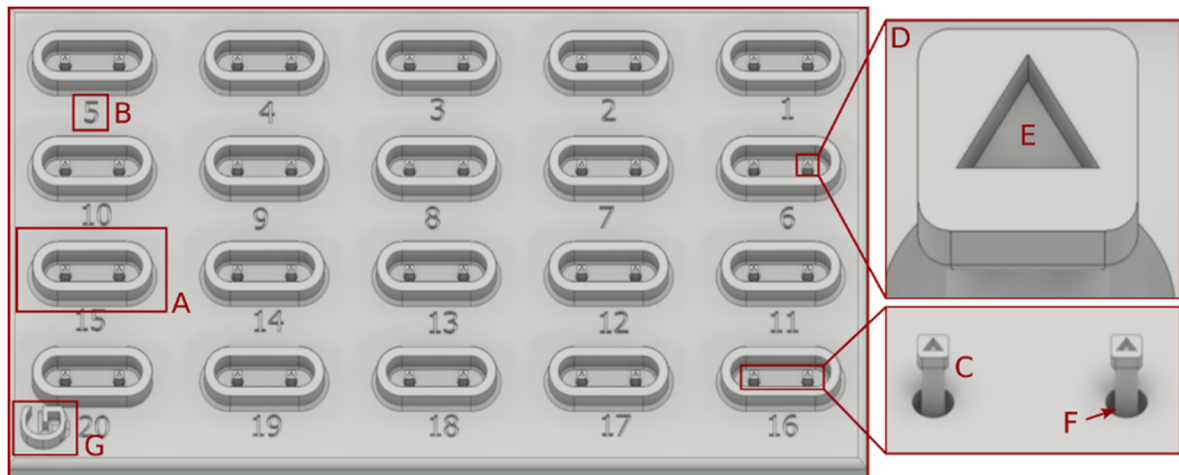


Figure 3.18| CAD drawing of a MAP design that are characterized by having multiple cell seeding chambers for tissue formation on each platform. The chambers are created by having a stadium shaped PEGDA wall forming boundaries for the cell-loaded scaffold (A). All chambers are numbered for convenience during culturing and handling (B). The molds contain 2 vertical posts, spaced 1 mm apart (C), with mechanical cues on top to create anchoring points for the tissue during formation (D) and a visual marker for optical tracking (E). The posts function as mechanical resistance to shape the cell-loaded scaffold between the two posts and as optical force sensors during contraction. Cylindrical voids are created into the PEGDA substrate to create an elevated floor and enhance tissue position around mechanical cues while maintaining the height of the posts (F). An optical marker for calibration of the platform position is placed in the lower left corner and shaped as a “G” to differ in appearance from other features on the platform (G). The full footprint of the platform measures 10 mm x 20 mm.

3.5.1. Design variability between PEGDA MAPs

In this work, the MAP design shown in Figure 3.18 is used for cell testing for many different purposes. Other MAP designs are also tested, which varies the post shape as well as the mold shape. Figure 3.19, shows an overview of the different MAP designs evaluated in this study. The shape of the mold is either stadium-shaped as seen in Figure 3.19A or oval as seen in Figure 3.19A,B. cylindrical posts are chosen in designs shown in Figure 3.19A,B where a mechanical cue is also introduced at the top of the posts. Rectangular posts are chosen in Figure 3.19C which is adapted from Mills et al.⁵⁰

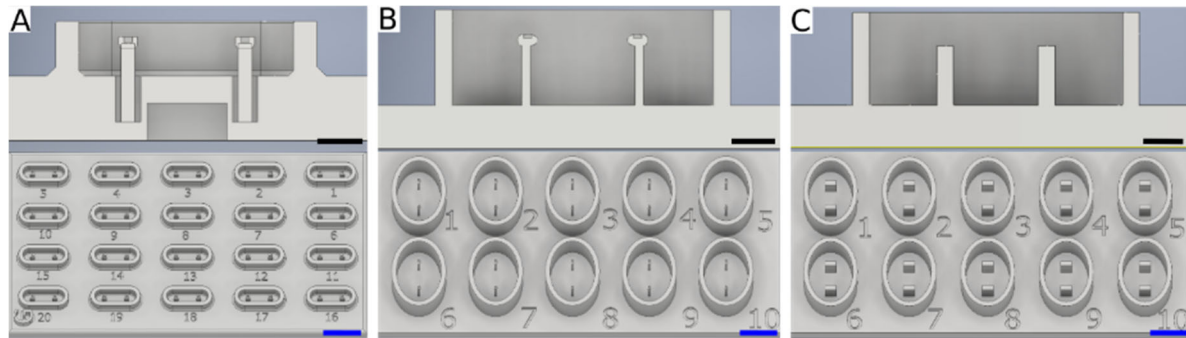


Figure 3.19 | Cad drawings of MAP designs used to generate engineered tissues shown as a full platform and cross-section of a single mold. A) Stadium-shaped mold and cylindrical posts with triangular markers embedded in top mechanical cue. B) Oval mold with cylindrical posts and droplet-shaped mechanical cues with triangular optical marker. C) Oval mold with rectangular posts. No mechanical cues or optical markers. Design of the mold shape in “B” and “C” as well as the post shape in “C” is adapted from Mills et al.⁵⁰. Scale bars black: 500 μm . Scale bars blue: 2 mm.

3.6. Cell loading into PEGDA based multiassay platforms

Tissues are formed in the MAPs by dispensing a liquid scaffold material mixed with cells into the cell seeding chambers. Filling each mold in a MAP requires precision as the free space in the surface of the molds are as small as 1000 μm x 700 μm . Furthermore, cell-loading into the platform must happen without damaging the sidewalls or the posts inside. This section focuses on the ability to fill the platforms uniformly with volumes down to 0.5-1.5 μL of cell-loaded scaffold using both a manual and an automatic approach. The cell loading must occur without overfilling the molds or in other ways anchoring the cell-loaded scaffold to undesirable structures on the platform. Due to the light curing properties of GelMA, parts of this section also focuses on a build-in solution for gelation of cell-loaded GelMA in the process.

3.6.1. Manual cell seeding

The interior volume of a single mold on a MAP is reduced down to 0.5 μL depending on the design. Manual filling of these molds therefore requires low volume dispensing together with temperature control to regulate the viscosity of the scaffolds while ensuring aseptic conditions. Molds must be adequately filled and require a confined droplet of the cell-loaded scaffold of uniform volume to ensure an equal number of cells in each tissue. If the volume is too low, the number of cells might be insufficient for tissue formation. Volumes that exceed the capacity of the molds will result in an overflow, leaving cell-loaded scaffold between molds, which is a waste of cells and risk impeding the tissue formation due to scaffold anchorage in unwanted structures.

Manual filling can be achieved by forming a droplet of cell-loaded scaffold at the pipette tip that can be deposited at the top of the mold. In this case, the scaffold material must have a low enough viscosity to allow the liquid to spread into the mold including the areas around the posts. Depending on the scaffold used, this means that the solution must either be cooled to 4 °C to prevent gelation (fibrin, collagen) or heated to 37 °C (GelMA) to lower the viscosity prior to pipetting. For temperature-controlled gelation of scaffolds (fibrin and collagen), curing is performed by transferring the cell-loaded MAPs to 37 °C for 30 min. GelMA scaffolds only requires UV light and photoinitiator for the gelation to occur via free radical polymerization as described below.

3.6.1.1. Light-cured scaffold

For this work GelMA is used at a concentration of 5 % w/v. GelMA must be warmed to above 30 °C to lower the viscosity sufficiently to allow for cell embedding and pipetting, as seen in Figure 3.20. GelMA crosslinks by free radical polymerization initiated by light at a wavelength of 365 nm that cleaves the photoinitiator, LAP, creating free radicals. A custom-built light box with heating and 365 nm LEDs is used to ensure optimized gelling of the molds. The heating reduces the viscosity of the GelMA and ensures that deposited GelMA will distribute inside the wells. The integrated LED ensures gelation of the cell-loaded scaffold without manual handling before gelation, which reduces the risk of spilling.

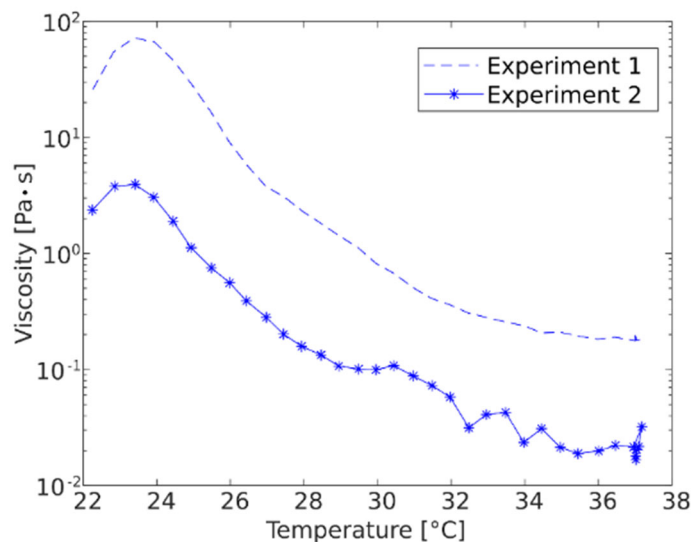


Figure 3.20| The viscosity of 5 % GelMA changes rapidly with temperature. At room temperature, the viscosity is too high to allow mixing with cells and pipetting. For temperatures above 30 °C the viscosity allows pipetting and mixing, hence the cell-loaded GelMA scaffold must be heated to above 30 °C during cell seeding to allow the solution to disperse into the well. The different curves correspond to two separate measurements.

The light intensity and time required to solidify GelMA sufficiently is optimized by using different exposure times and evaluating subsequent dissolution in cell culture medium. For sufficient gelation with no subsequent dissolution, the exposure time is set to 30 s at an intensity of 4.8 mW/cm^2 when exposing through a $200 \mu\text{m}$ thick PEGDA bottom layer. Increasing the thickness of the PEGDA substrate below the designed MAP will require an increased exposure time to ensure complete gelation of the GelMA scaffold.

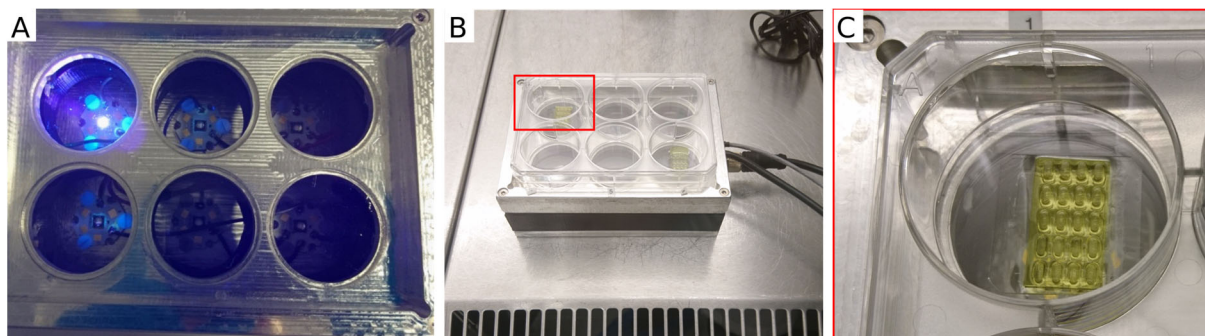


Figure 3.21| (A),(B) Custom-built heating and light exposure box capable of gelling 6 wells separately. (A) An LED is turned on showing the blue light emitted at 365 nm. (B), (C) A PEGDA MAP with 20 molds is shown inside the 6 well plate. The exposure to 365 nm light ensures gelation of the cell-loaded molds before manual handling of the plate and avoids spill. The light-heating box is placed inside a LAF bench to ensure aseptic working conditions.

3.6.2. Automatic cell seeding based on a modified dispensing system

An automatic filling method is desired over a manual method to overcome the variance that can occur from manual filling. A pipetting robot is made that can deposit sub- μL droplets based on a I&J7100 Fisnar Robot, a glue robot made to create custom patterns of lines and droplets,. The robot is controlled by Fisnar DSPE501A-LF dispensing unit by air-pressure. By controlling the air pressure, it is possible to create droplets of deionized (DI) water down to $803 \pm 95 \text{ nL}$ measured by depositing droplets onto a polystyrene (PS) surface weighed before and after droplet deposition.

The robot was modified to include a holder for a rectangular 8-well plate containing inserts to hold the coverglasses with the 3D printed MAPs in place. A custom-built controller is used to heat an aluminum syringe holder to 37°C and can turn on the 365 nm LED via the output channel on the robot. Both the aluminum syringe holder and the LED are additions to the original robot design. The LED is encapsulated in a black PLA box in order to collimate the light to the MAP (Figure 3.22). The robots' included teach pendant (Figure 3.22 yellow) is used to program the filling of 20 molds sequentially. The built in calibration cue shown in Figure 3.18G is used to calibrate the position of the MAP before filling also using the included teach pendant.

The tested platforms contain 20 molds and all tests are performed using 5 % GelMA solution containing 2 μm fluorescent beads. In the majority of operations, a fraction of the molds (range: 0 % to 50 %) are not adequately filled and are either overflowed or contain too little material.

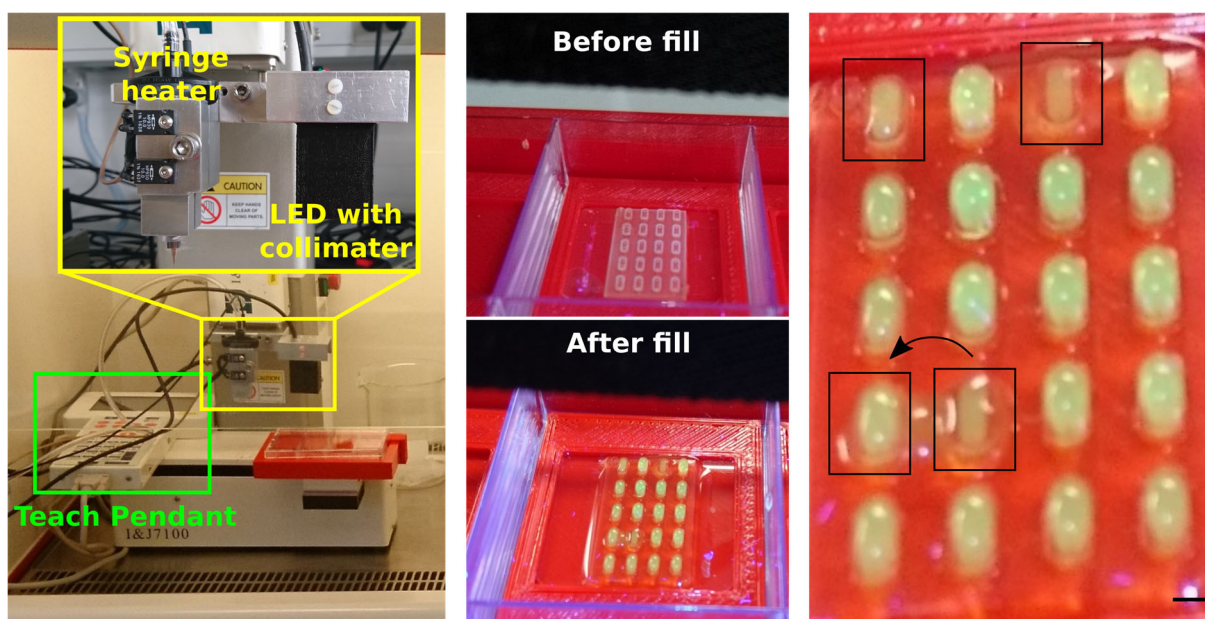


Figure 3.22| Automatic dispensing robot obtained by modification of an I&J7100 Fisnar glue robot. On the left, the unit is seen inside a LAF bench. The teaching pendant is used to program the dispensing of scaffold, and to calibrate the start position before each operation. A heating unit is mounted to pre-heat the dispensed GelMA to 37 °C and a 365 nm light emitting diode is mounted to solidify the GelMA after dispensing. A MAP is seen before and after dispensing of 37 °C pre-heated GelMA into the molds. Overflowing is observed in 4/20 molds marked with black boxes. In this case the 4th well have overflowed due to the spillage from the neighboring well (arrow). Scale bar: 1 mm.

It is estimated that each adequately filled mold contains 1.5-2 μL GelMA solution and hence there is a large degree of excess volume compared to the volume of the well which is approximately 0.5 μL . The surface tension and affinity of GelMA and PEGDA to adhere to each other ensures that the dispensed GelMA solution is confined inside the mold borders and only a few wells are overflowed as seen in Figure 3.22(right). To avoid overflow and to make a better filling level compared to well volume the pressure settings can be changed to reduce the dispensed volume. It is possible to dispense between 0.5 μL and 1 μL into each mold, however, the resulting volumes are less accurate and there is a bigger deviation within each operation which makes this an unsuitable solution.

Figure 3.23 shows that the fluorescent beads encapsulated in 5 % GelMA are confined inside the PEGDA molds with varying filling degree. Filling with approximately 0.5 μL and 1.5 μL shows that the bead-loaded GelMA is contained inside the molds, Figure 3.23A,B. When the molds overflow, the GelMA forms a sheet between adjacent molds (Figure 3.23C). Insufficient

pressure control results in either overfilling of the molds (Figure 3.23C) when the pressure is too low, or bubble formation if the pressure is too high (Figure 3.23D). If bubbles occur, they are formed inside the syringe before dispensing due to air being sucked back into the syringe. Due to insufficient control using the dispensing robot, manual seeding is preferred in the work presented in Chapter 4 to avoid wasting high value cells.

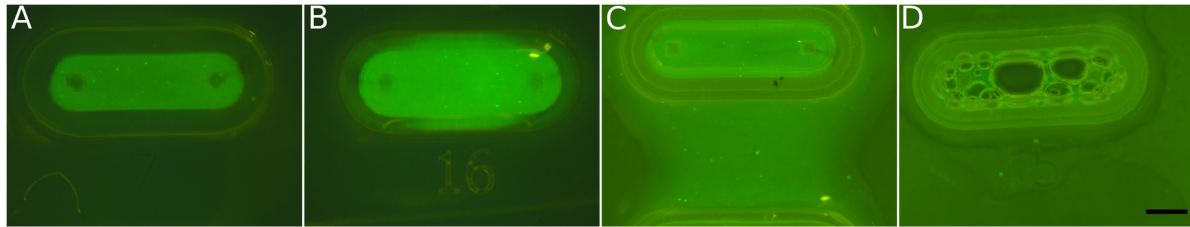


Figure 3.23| Fluorescence micrographs of different filling degrees of PEGDA MAPs with approximately 0.5 μ L to 2 μ L preheated 5 % GelMA. A) The mold is filled without droplet forming on top of the mold sides. Approximately 0.5 μ L is loaded into the mold. B) Droplet formation is seen inside the mold without overflow. Approximately 1.5 μ L is loaded into the mold. C) Overflow of the mold results in GelMA deposition between two adjacent molds. Approximately 2-3 μ L is loaded into the mold. D) High pressure results in bubble formation inside the syringe and hence dispensing of bubbles into the molds. Volume unknown. Scale bar: 500 μ m.

3.7. Conclusions

A cell seeding multiassay platform has been produced using stereolithographic 3D printing. Small features acting as mechanical cues to promote tissue formation have been successfully incorporated into the design and are characterized, enabling an optical force read-out of tissue contraction force. Mechanical properties and wear resistance have been investigated to adequately design a PEGDA MAP. Cell compatibility have been confirmed using already published designs and an automatic filling method has been suggested, including incorporated calibration markers for position calibration during filling. The proposed platforms fulfil the design criteria and seems to be a promising tool for engineered tissue formation.

3.8. Experimental details

Experimental details and materials and methods for the above described findings and processes are explained in this section.

3.8.1. 3D printing using a home-built stereolithographic printer

All PEGDA structures are manufactured by projection stereolithography using a custom-built high-resolution 3D printer¹²⁹ built by professor Niels Bent Larsen. Projected light from a high

power LED projects the light onto a DMD and the light is reflected onto the vat containing the print resin. The projected image is projected 1:1. Image projections are controlled by a custom Matlab (MathWorks) code that times the image projection via the LED and DMD and controls the Z-stage movement.

The print resin is an aqueous solution based on Milli-Q water (MQ, Merck-Millipore) composed of the polymer poly(ethylene glycol)-diacrylate M_n 700 g/mol (PEGDA, 455008, Sigma-Aldrich), the photoinitiator lithium phenyl-2,4,6-trimethylbenzoylphosphine (LAP, from Allevi or 900889, Sigma-Aldrich), and the photoabsorber quinoline yellow (QY, 309052, Sigma-Aldrich). The PEGDA solution presented in this chapter is 200 mg/mL (20 % w/v). The absorber concentration varies between 9 mg/mL and 12 mg/mL depending on the structures printed, as indicated in the specific experimental sections. All print resins are prepared using 5 mg/mL LAP. After mixing, the resin solution is left at RT for minimum 30 min in order to degas and avoid bubbles during printing.

All 3D designs are drawn using computer aided design (CAD) in Autodesk Inventor Professional. CAD drawings are converted to digital image sequences by slicing in the z-direction in 20 or 25 μ m thick slices using the open source Slic3r software (www.slic3r.org). Digital images projected onto the print vat are exposed for 2.2 s to 5 s depending on the design. Initial layers (approximately 100 μ m) are overexposed to ensure adequate attachment of the 3D structure to the cover glass. The first image is exposed for 10 s and the stage is moved up 5 μ m before exposing the same image for another 10 s. This is done 4 times for the first 3 images, and twice for the following 2 images with 5 s exposure time and 10 μ m between each layer. After the overexposure, another 100 μ m base layer of PEGDA is printed using the desired exposure time.

After printing, the stage is removed from the printer and the coverglass is demounted. Coverglass and 3D printed features are transferred to DI water immediately to avoid drying. DI water is exchanged 3 times over at least 24 h to wash out residuals of the print solution. For cell seeding molds, DI water is exchanged to PBS to exchange the water content in the PEGDA MAPs with saline water before cell preparations.

Table 3.1 | Overview of slicing thickness, absorber concentration and exposure times used in results presented in Chapter 3.

Design	Slicing thickness	QY concentration	Exposure time
Stereolithographic 3D printing (sections 3.2 as well as 3.3.2, 3.3.3, and 3.3.4)			
Print resolution and swelling	20 μ m	12 mg/mL	3 s
Free hanging structures	20 μ m	12 mg/mL	3 s

Mechanical characterization (sections 3.3.1 and 3.4.5)			
Free posts $\varnothing 100\ \mu\text{m}$, $200\ \mu\text{m}$, $300\ \mu\text{m}$	$20\ \mu\text{m}$	9 mg/mL	5 s
Free posts $\varnothing 150\ \mu\text{m}$	$20\ \mu\text{m}$	9 mg/mL	2.2s and 3 s
Cylinders mechanical test and swelling	$20\ \mu\text{m}$	9 mg/mL	5 s

3.8.2. Coverglass treatment

Square coverglasses of 22 mm x 22 mm and 0.4 mm thickness (#4 Menzel-Gläser) are pretreated by coating them on one side with a methacrylate layer allow chemical crosslinking of the printed PEGDA solution and the glass surface. Cleaning in oxygen plasma for 10 min removes any organic residues on the surface. Coverglasses are soaked for 10 min in an ethanol solution of 2 % v/v 3-(trimethoxysilyl) propyl methacrylate (Sigma-Aldrich) with pH adjusted to 5 by acetic acid. Hereafter they are rinsed, first with pure ethanol 3 times and then with MQ water 3 times. The coverglasses are heated on a heater plate at 150 °C for 20 min

3.8.3. Constructing small features – Spatial resolution

To test the printability of small-size features, a block of 5 mm x 5 mm x 1 mm is designed with rectangles of 1:3 in width to length ranging from $10.8\ \mu\text{m}$ to $108\ \mu\text{m}$ in width in multiples of $10.8\ \mu\text{m}$. The protrusion or indentation height of all rectangles is $100\ \mu\text{m}$ and the slicing thickness is set to $20\ \mu\text{m}$. Print resin contains 20 % w/v PEGDA, 5 mg/mL LAP and 9 mg/mL QY. The width of the rectangles is imaged before and after swelling by light microscopy using a Zeiss Axioskop 40 with 10x magnification. The dimensions are determined using Fiji/ImageJ.

3.8.4. Fatigue test

A print resin of 20 % w/v PEGDA, 12 mg/mL QY, and 5 mg/mL LAP is used to print the structures with a layer thickness of $20\ \mu\text{m}$. Brightfield microscopy is used to investigate successful printing. A beam of dimensions $L \times W \times H = 1000\ \mu\text{m} \times 200\ \mu\text{m} \times 100\ \mu\text{m}$ is deflected 1.1 million times using a voltage controlled (KPZ101 - K-Cube Piezo Controller, Thorlabs) piezo-actuator (PK2FSF1 - Amplified Piezoelectric Actuator, Thorlabs). The controller is steered by a custom Matlab (MathWorks) code that navigates the controller between 0 V and 75 V to get minimum ($0\ \mu\text{m}$) and maximum ($220\ \mu\text{m}$) displacement. An image is acquired at specific time points in top and bottom position using a custom camera setup also controlled by the Matlab code. The PEGDA beam sample is immersed in MQ water inside a PMMA holder sealed with parafilm to reduce evaporation during the test. Optical investigation of the sample is performed by brightfield microscopy before and after testing to observe damages to the material.

3.8.5. Determining the swelling of printed PEGDA hydrogels

Cylinders, 6 mm in diameter and 5 mm in height, are printed in 20 % w/v PEGDA with 9 mg/mL QY and 5 mg/mL LAP. Slicing thickness is 20 μm . Immediately after printing, the cylinders are weighed and immersed in MQ water. The weight change is measured over 16 hours during which the MQ water is exchanged twice. Cylinders are then dried for 8 hours at 60 °C and lastly the dry weight is obtained. The equilibrium volumetric swelling degree is calculated based on the swollen and dry state of the cylinders. Dimensional change due to swelling are determined by constructing rectangles of 108 μm , 216 μm , and 324 μm using the procedure described in section 3.8.3.

3.8.6. Compression modulus analysis of printed PEGDA hydrogels

Uniaxial compression of cylinders, 6 mm in diameter and 5 mm in height, is performed using an Instron 5967 (Instron, MA) with a 50 N load cell. Before performing the measurement, the samples are brought to equilibrium swelling. The height and width of the samples are measured optically in a confocal microscope for precise read-out from the microscope stage. The samples are then placed wet between two parallel plates at room temperature. A compression rate of 0.5 mm/min is used to perform the uniaxial compression. Shear modulus is determined by the linear region of the slope when plotting the engineering stress against $-\lambda-\lambda^2$.

3.8.7. Automatic dispensing

Dispensing down to $\sim 0.9 \mu\text{L}$ can be accomplished by adjusting the pressure control on the I&J7100 dispensing robot (Fisnar). 10 droplets are deposited into a petri dish with a known weight. The weight after droplet deposition is noted and mean droplet volume is calculated. Pressure is adjusted until sub-microliter droplets are obtained and the settings are noted. All droplets are placed by contact-deposition on the petri dish. For automatic filling of a MAP, a 5 % GelMA solution is mixed with 0.02 % green fluorescent microbeads with 2 μm in diameter (FluoSpheres, Thermo Fisher Scientific) and loaded into the syringe of the robot. A custom code for filling of 20 molds is used via the integrated teach pendant. Position of the MAP is calibrated by the optical marker prior to droplet contact-deposition into PEGDA MAP molds. Fluorescent-bead loaded GelMA is crosslinked by free radical polymerization using 5 mg/mL LAP illuminated for 120 s (365 nm, 8.3 mW/cm²) and visualized by a Zeiss Axioskop 40 fluorescent microscope.

3.8.8. Characterization of bendable posts

PEGDA posts are positioned horizontally in a bath of MQ water on a high resolution scale and the tip of the actuator pin is positioned in the center of the top mechanical cue. The scale is tared and a voltage controlled piezo actuator is used to displace the top of the post 220 μm . The resulting weight change is recorded. Testing time is approximately 20 s in total and the evaporation is measured to be less than 5 mg. Weight change due to water displacement of the actuator pin is measured before each deflection measurement. The resulting weight change is

used to calculate the actuation force. The stiffness of the post is calculated using the Euler-Bernoulli beam theory, Eq.(4), from the calculated actuator force and the length of displacement.

3.8.9. Optimization of gelation time

3.8.9.1. Light-heater box

GelMA is cross-linked by free radical polymerization using the photoinitiator LAP exposed to 365 nm light. In both the custom light-heater box and in the automatic dispensing robot, a 365 nm LED is used to initiate the free radical polymerization. The time to solidify 2 μ L of GelMA sufficiently to encapsulate live cells is critical to avoid dissolution. Droplets of 2 μ L 5 % w/v GelMA are deposited on a standard tissue culture 6-well plate (Nunc) with 3 droplets inside each well. The 6-well plate is placed in the light-heater box and the LED are turned on for 10 s, 20 s, 30 s, 40 s, 50 s, or 60 s for well 1-6 respectively. DMEM (Sigma-Aldrich) with 10 % FBS and 1 % P/S is added to each well after light exposure and the well plate is incubated at 37 °C. Droplet integrity is evaluated after 24 h of incubation. Intact droplets correspond to sufficient light exposure times. The lowest amount of light exposure resulting in fully intact GelMA droplets is chosen as the ideal light exposure times.

3.8.9.2. Automatic dispensing robot

1-2 μ L 5 % GelMA droplets with fluorescent beads are deposited inside the molds of a PEGDA MAP and the light exposure is varied from 30 s to 2 min between different wells. DMEM (Sigma-Aldrich) with 10 % FBS and 1 % P/S is added to each well after light exposure and the well plate is incubated at 37 °C. Similar to the light-heater box, the droplet integrity is evaluated after 24 h of incubation. Intact droplets correspond to sufficient light exposure times. The lowest amount of light exposure, resulting in fully intact GelMA droplets is chosen for the subsequent light exposure time.

The Inverse Square Law (see Eq.(7)) states that the light intensity, I , is proportional to the inverse of the distance, d , squared.

$$(7) \quad I \propto \frac{1}{d^2}$$

That implies that since the light source is approximately double the distance from the light source in the dispensing robot compared to the manual light/heat box, the intensity of the light is approximately 1/4th. This is also consistent with observations on gelation times. In order to crosslink GelMA enough to restrain the cells and keep it from dissolving in the medium at 37°C, a light exposure time of 20 s to 30 s is needed in the manual light box when the GelMA is placed directly on PS with no PEGDA between. For the robot, where light is not blocked by PEGDA

between cell-loaded GelMA, an exposure time of 1.5 min to 2 min is required to crosslink the GelMA enough to keep it from dissolving.

3.8.9.3. Determining the effect of LEDs in the light-heater box and automatic dispensing robot

The intensity of the light is compared between the light box used for manual pipetting and the light on the Fisnar robot. Both use LEDs of the same type.

In order to estimate the difference in gelling time it is of interest to find and compare the intensity between the two setups used for manual and automatic pipetting, respectively. The light intensity is measured by a Thorlabs PM100 power and energy meter with the Thorlabs S142C Sphere photodiode power sensor.

The sensor is positioned where the sample would normally be placed. In the light box, there is a physical restriction due to sensor geometry that means the sensor is 0.5 cm further away from the light source. A well-plate is placed in the light box before the measurement is performed.

In all measurements the background light is first measured three times before the light is switched on and measured. In the light box, two different measurements are performed, with and without a sample placed in the well. For the Fisnar setup, the light source is placed above the sample and is therefore not restricted by the PEGDA; the sensor is placed in the same position as a sample would be.

In the light box, three different LEDs are measured. For each LEDs, the measurement has been performed three times and the background measurement is subtracted from the mean. The light intensity that reaches the GelMA solution is lowered significantly by the presence of a PEGDA sample as expected (Table 3.2) and confirms the effectiveness of having the light source on top of the sample to avoid restriction of the light path by PEGDA layers. The illumination power stated in the experimental section is for the “no PEGDA” measurement as the PEGDA constructs vary in thickness. The light-heater box has been updated during the course of the experiments why an updated value is included and used for subsequent experiments.

Table 3.2| Measurements of light intensity for the light-heater box with and without a PEGDA construct and for the dispensing robot.

Light-Heater box, no PEGDA	Light-Heater box, with PEGDA	Fisnar I&J700 Robot
$4.8 \pm 0.6 \text{ mW/cm}^2$	$0.4 \pm 0.1 \text{ mW/cm}^2$	$8.3 \pm 0.0 \text{ mW/cm}^2$
Updated: $15.9 \pm 2.1 \text{ mW/cm}^2$		

Chapter 4

Formation and characterization of engineered contractile tissues

Obtaining mature engineered cardiac tissues that can be used for functional drug safety screening requires multiple optimization steps of both scaffold and cell concentrations as well as changes to the platform surface to accompany scaffold-PEGDA compatibility. This chapter describes the optimization work performed for cell-scaffold concentrations, PEGDA-scaffold interactions, general cell viability, and -performance inside the PEGDA MAPs. Different cell types are used to perform optimization and characterization. Initial PEGDA-scaffold interactions and basic abilities to form an engineered tissue (“a tissue”) using the presented MAP design, are performed using 3T3 mouse fibroblasts. Further optimization and cell viability studies are performed using the C2C12 mouse myoblast cell line with differentiation capabilities. Finally, the formation of engineered cardiac tissues and their development inside PEGDA MAPs is performed using hiPSC derived cardiomyocyte progenitor cells.

4.1. Defining and quantifying engineered tissues in PEGDA MAPs

The formation of a successful engineered tissue can be described using various definitions or measures. Evaluating the tissues during the time of culture is difficult without destroying them. A tissue compaction ratio (TCR) is introduced, Eq.(8), to have a quantitative measure of tissue formation, based on the cells performance to contract the scaffold. The tissue compaction ratio describes how much a tissue has compacted based on the total volume of cells and scaffold seeded to final compacted state.

$$(8) \quad TCR = \frac{V_{seeded} - V_{measured}}{V_{seeded} - V_{cells}}$$

The tissue compaction ratio describes how much the tissue have compacted from V_{seeded} to $V_{measured}$. V_{seeded} is the total volume of cell-loaded scaffold dispensed into each MAP mold. $V_{measured}$ is the volume of the tissue during the course of tissue compaction and V_{cells} is the calculated volume comprised of all dispensed cells. V_{cells} is also the final minimum volume that can be reached upon full tissue compaction without taking the volume of scaffold material into account.

Figure 4.1 describes the tissue quantification method. A fully compacted tissue will be similar in size to the volume of the total number of cells seeded, while a cell loaded-scaffold which

have not compacted will be equal to the volume of the seeded volume. The difference between the seeded volume and the volume of the seeded cells corresponds to the volume of scaffold material. The TCR is therefore a measure of the cells ability to compact the scaffold. As TCR indirectly evaluates the cell viability and performance without measuring the cell yield, it is important to state that this measure can only be used after visual inspection of the tissue where cell morphology is evaluated. Thus, TCR is only applied for tissues that are expected to contain healthy living cells. TCR should not be used as a conclusive measure but as a method of comparing between tissues composed of the same cell type.

To calculate the TCR, experimental results are used to estimate a fully compacted tissue. Based on top- and sideview of the tissues formed, it is found that a tissue from a stadium-shaped PEGDA MAP, can be evaluated as a rectangular box with height, h , length, L and width, w . Cross-sectional images of the tissues have not been obtained to confirm the shape, that are likely best modelled as either a rectangle, as done in this work, or a circle. In this work the available sideview micrographs from 2 tissues are used to estimate that the height of the tissues can be calculated as $h = 0.9 w$ as seen in Figure 4.1A. Therefore a 2D image of the tissues can be used to estimate the volume, Figure 4.1B. Sideview of formed engineered tissues are only available at the end of the experiment why the ratio between height and width are based solely on this timepoint.

During experimental work presented in this chapter micrographs of cell-counting chambers with cardiomyocyte progenitor cells have been obtained and are used to determine that the diameter of cardiomyocyte progenitor cells vary greatly in size. The diameter of cardiomyocytes in suspension is measured to be between $7\text{ }\mu\text{m}$ and $25\text{ }\mu\text{m}$ with a mean diameter of $13.5\text{ }\mu\text{m} \pm 6.8\text{ }\mu\text{m}$ giving a relative uncertainty in diameter of 150 %. The mean cell diameter is thus a rough estimate given the variation in cell dimensions. Despite the significant variation in size, the mean diameter is used to calculate the theoretical volume of a fully compacted volume of cells, V_{cells} .

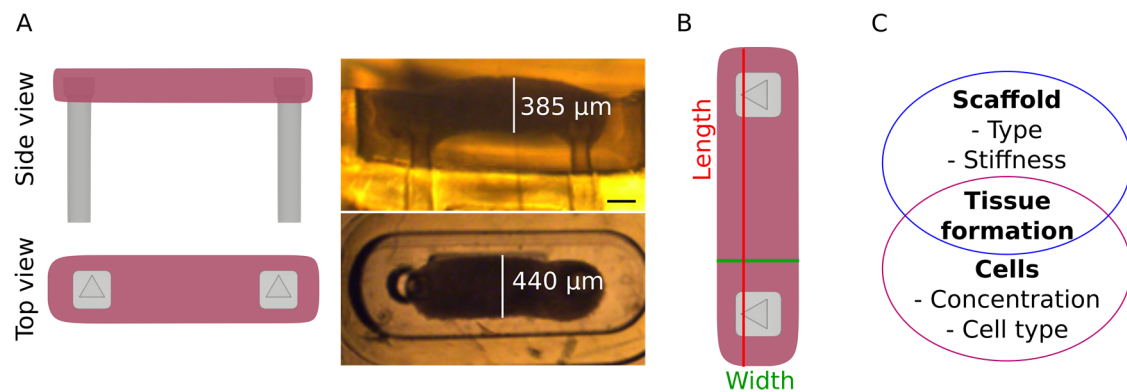


Figure 4.1| A) Schematic overview of a full tissue formation using the PEGDA MAP molds based on experimental results. B) The shape of a compacted tissue can be modelled as a simple rectangular box where $h = 0.9 w$, thus making it possible to estimate the volume based on a 2D top view image of the tissue. Calculating the volume of the seeded cells reveals the minimum size of a tissue with 100 % viable cells. The measured volume of the tissue compared to the volume of seeded cells can be used to estimate the tissue compaction ratio (TCR). The possible compaction range is based on the difference between the seeded volume, including scaffold and cells, and the volume of the seeded cells alone. TCR should not be used as a conclusive measure but as a method of comparing between tissues. C) A successful tissue formation not only depends on cell seeding density (concentration of cells in the cell seeding scaffold) but also on scaffold type and stiffness. The seeding density needed to obtain a successful tissue can vary between different cell types. Drawings are not to scale.

Tissue formation is influenced by several factors of which cell and scaffold type and concentration are the main contributors, Figure 4.1C. The affinity for the cells to connect to different scaffold materials varies between cell lines, depending on cell type and origin. Therefore, the compatibility between specific cells and scaffolds must be considered.

Varying the cell seeding density and thereby the cell concentration influences the tissue formation by changing the spacing between the cells inside the scaffold. Cells in close proximity to each other will be able to form connections to neighboring cells. Having a high cell concentration means investing more cells for each tissue and thereby increases the cost per engineered tissue. An optimal cell concentration will result in a compacted tissue where the cells are able to form cell-cell contacts without having an excess amount of cells. For different scaffold materials, the needed cell concentration can vary due to difference in the mechanical and biochemical properties. Cells must be able to modify the scaffold material to contract and form a tissue.

4.2. Tissue formation using 3T3 Swiss Albino fibroblasts

Tissue formation using MAPs is optimized using the 3T3 Swiss Albino fibroblast cell line. Fibroblasts are relevant to use as a model cell line to create contracting tissues that are not

beating, as these are naturally contracting cells and have previously been used to show proof of concept in tissue engineered devices¹³⁰. They are not limited to contract in 2D structures but also show a substrate-dependent contraction when embedded in a 3D conformation¹³¹.

In this section, fibroblasts are used to optimize tissue formation inside PEGDA MAPs. The contractile behavior of 3T3 cells is used to evaluate the tissue forming properties as a response to the shape and mechanical properties of the PEGDA MAP containing flexible posts.

Results in this section are partly generated in collaboration with master student Maria Ludvigsen as indicated in figure captions.

4.2.1. Optimizing cell- and scaffold concentrations

The scaffold material GelMA is used to encapsulate fibroblasts inside the PEGDA MAPs. 3T3 fibroblasts contain RGD binding integrins and hence fibroblasts will naturally be able to bind to and contract GelMA to form an engineered tissue.

Optimal working concentrations of both cells and GelMA are explored by forming droplets of 3 %, 5 %, and 10 % GelMA with encapsulated cells on a tissue culture polystyrene (TCPS) surface. The cell concentrations are varied between 2×10^6 cells/mL to 32×10^6 cells/mL. The cell-loaded GelMA droplets are cross-linked by free radical polymerization and cultured for 3 days. Breakdown or dissolution of the GelMA scaffold is evaluated together with the cells' ability to remodel the scaffold.

Scaffolds are used to encapsulate the cells and allow the cells to form intercellular connections but should not be a significant part of the engineered tissue after tissue formation. Results show that 3 % GelMA is not able to fixate the cells as it disintegrates over a short time course of 3 days. GelMA concentrations of 5 % and 10 % show cells primarily inside the droplets with cells migrating out near the edges of the droplet. Therefore, the lowest possible scaffold concentration has been chosen and 5 % GelMA is used in subsequent testing.

4.2.2. Forming a fibroblast tissue strip

Tissue formation inside the single MAP molds occurs spontaneously due to cell-scaffold interactions. During loading of the molds, the cell-loaded scaffold surrounds the vertical posts. As the cells contract, the mechanical cue becomes entrapped in the scaffold and the contractile force of the cells result in a tissue strip between the two posts. However, the affinity of the GelMA scaffold to adhere to the PEGDA walls must be overcome by the contraction force of the cells to properly form a tissue.

During GelMA network formation, the methacrylate groups from the GelMA and the acrylate groups in the surface of the PEGDA molds can create covalent bonds and thereby complicate tissue formation, Figure 4.2. Removing excess water from the PEGDA molds before cell loading is necessary for optimal filling of the wells but it also removes the excess water that would

otherwise prevent or decrease direct GelMA to PEGDA contact at the sides and bottom of the MAP mold. Partially contracted tissues are observed even after 2 weeks of culturing as seen in the top image of Figure 4.3B. This suggests that the cells are unable to contract the scaffold sufficiently due to bonding between GelMA and PEGDA.

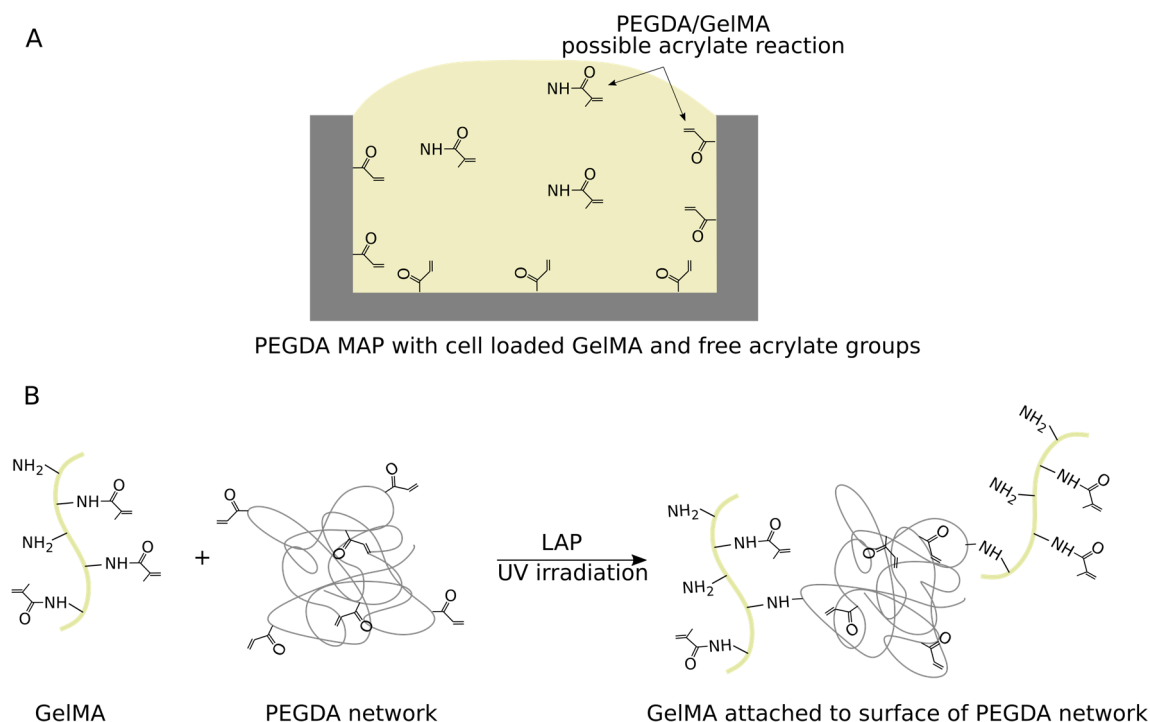


Figure 4.2| When the cell-loaded GelMA is introduced into the PEGDA MAP molds (A) and subsequently exposed to UV irradiation, using LAP as photoinitiator, the acrylate groups remaining in the PEGDA mold can react with the methacrylates in the GelMA scaffolds (B) thereby causing a covalent binding between the mold and the scaffold which can prevent subsequent tissue formation.

Preventing attachment between GelMA and PEGDA during light-curing can be attained by terminating the active acrylate groups in the PEGDA before cell loading. A treatment with 5 mg/mL LAP for 30 min using UV-A illumination functions as termination of free unreacted acrylate groups and as a post-curing of the PEGDA by solidifying any unreacted print resin left in the network. Before the treatment is performed, the residual print solution is washed out by leaving the printed PEGDA in water for 24 h with exchange of the water at least 2 times. The washing steps ensure that the treatment including UV-A illumination minimizes further network formation of PEGDA and mainly functions as a surface treatment as residual print resin has been exchanged with water. Therefore the treatment is termed “surface treatment” although it affects the whole bulk PEGDA structures.

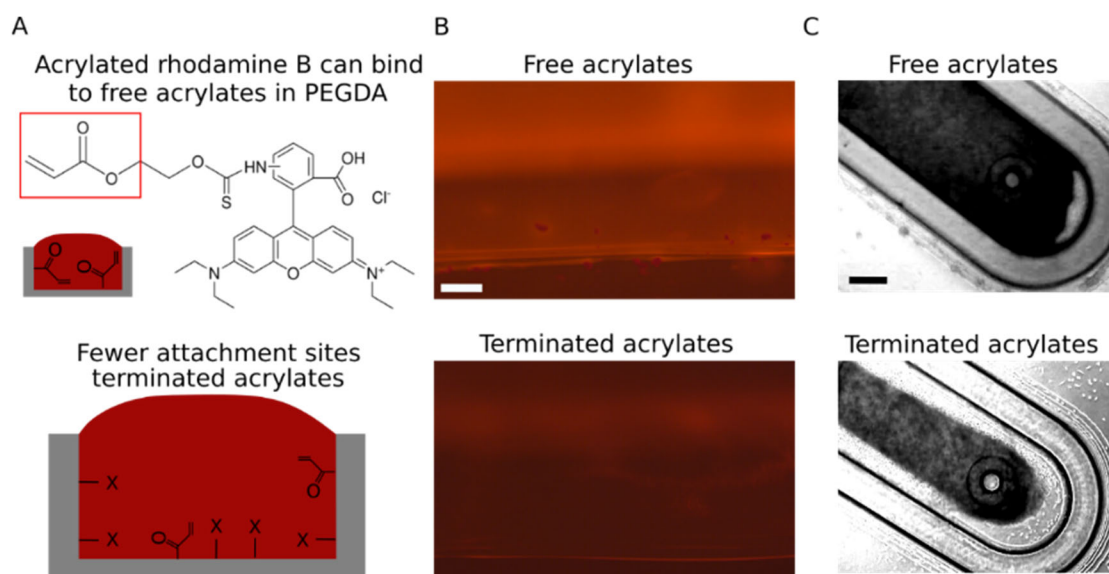


Figure 4.3| A) Testing the effect of acrylate termination in printed PEGDA is investigated by binding acrylated rhodamine B to a block of PEGDA with and without terminated acrylate groups using UV-A illumination and LAP as a photoinitiator. When PEGDA have free acrylate groups in the surface the acrylated rhodamine B binds to the surface and can easily be detected by fluorescent microscopy. B) The surface treated PEGDA block with terminated acrylates shows a decrease in rhodamine B attachment, indicating a reduced number of active acrylate groups after surface treatment compared to the untreated PEGDA with free acrylate groups. C) Micrographs of 3T3 tissues shows that attachment of cell-loaded GelMA to the PEGDA mold is no longer observed after surface treatment. The surface treatment terminates remaining acrylates in the PEGDA and thereby leaves fewer acrylates available for attachment during gelation of the GelMA scaffold. Scale bars: 250 μm . Micrographs in “C” recorded by Maria Ludvigsen.

Investigating the effect of surface group termination is performed by binding the fluorescent rhodamine B to unreacted acrylate groups in PEGDA. Acrylated rhodamine B is bound by UV-A illumination using LAP as a photoinitiator. To observe the difference in free acrylate groups before and after acrylate termination, Rhodamine B is bound to a surface treated PEGDA block with terminated acrylates as well as non treated PEGDA block with free acrylates, Figure 4.3A,B. Rhodamine B is used as it can be detected with fluorescence microscopy.

The printed PEGDA block is submerged in a solution of LAP (5 mg/mL) to terminate the unreacted acrylate groups by binding with the radical LAP byproduct. The block and solution is exposed with UV-A illumination for 30 min (330-380 nm, 18mW/cm²). Afterwards the block is transferred to a solution of LAP (10 mg/mL) and rhodamine B (20 mg/mL) and set to react for 2 min using UV-A illumination. If the rhodamine B does not attach to the surface, this indicates that there are no unreacted acrylates on the PEGDA surface. A non-treated PEGDA block is also submerged in a solution of LAP and rhodamine B followed by UV-A illumination for 2 min to

observe the difference in binding. As seen in Figure 4.3B, the amount of bound rhodamine B is greatly reduced for the surface treated block compared to the untreated block. This indicates that fewer unreacted acrylate groups are present on the surface treated block. By terminating acrylate groups, the tissue formation is greatly improved as the fibroblasts are able to remodel the scaffold and release it from the PEGDA surface, forming a defined tissue, Figure 4.3C.

Using the 3T3 Swiss Albino fibroblasts cell line, it is possible to show spontaneous tissue formation inside PEGDA MAP molds for at least 2 weeks of culture. However, as the fibroblast cell line is not contact inhibited¹³², the cells are continuously dividing with a doubling time of around 24 h. Tissues are consequently expanding inside the MAP mold, Figure 4.4. Tissue expansion is measured by the surface area of the tissue seen in Figure 4.4. After 7 days of culturing, the tissue has expanded by approximately 30 % from day 1 and after 12 days, the tissues have expanded by approximately 60 % from initial contraction at day 1. The expansion of the tissues makes this cell line an unsuitable choice for long-term culture testing.

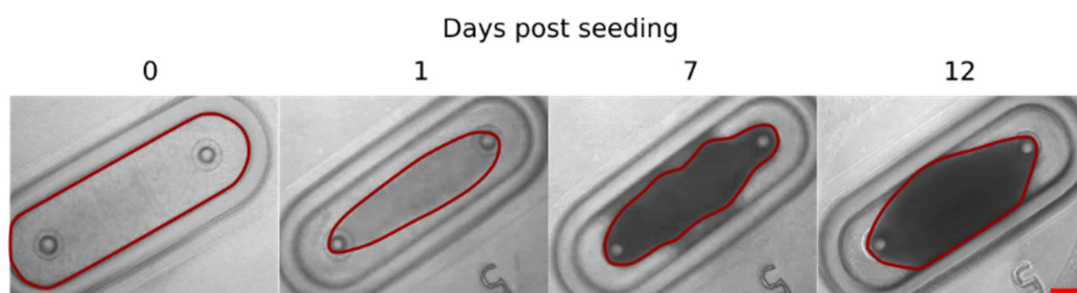


Figure 4.4| Micrographs showing that 3T3 fibroblasts remodel the GelMA scaffold to form a tissue within 24 h. However, as the cells keep proliferating inside the tissue due to a lack of contact inhibition, the tissue expands in size over time. This cell line is therefore unsuitable for further optimization of tissue formation inside the PEGDA MAP molds. The red line indicates the edge of the cell-loaded GelMA scaffold, defining the 3T3 fibroblast tissue. Scale bar: 250 μm . Micrographs recorded by Maria Ludvigsen.

4.3. Tissue formation using C2C12 mouse myoblasts

Myoblasts are a contractive cell type with the ability to differentiate and fuse to form myotubes. The C2C12 cell line originates from adult C3H mouse leg muscle and can be used to study cell differentiation *in vitro*¹³³. Differentiation of the C2C12 cell line is initiated via close cellular contact with inhibited growth arrest³³ when the serum concentration is lowered¹³⁴ (2 % FBS is used). Unless modified to contain the $\alpha 2\beta 1$ integrin, C2C12 cells do not bind to native collagen or 2D configurations of gelatin⁴⁹. C212 cells contain $\alpha v\beta 3$ and $\alpha 5\beta 1$ integrins that bind to fibrin but not to natural collagen¹³⁵. The 2D configuration of cell-loaded gelatin scaffolds to PS surfaces is believed to result in conformational changes that affect the ability of the cells to recognize the RGD binding motif. In 3D configurations, however, RGD is recognizable which

allows unmodified C2C12 cells with $\alpha v\beta 3$ and $\alpha 5\beta 1$ gelatin binding integrins to attach to the RGD motif. Using fibrin or the modified gelatin, GelMA, in a 3D configuration should therefore allow C2C12 cell binding.

The aim of this section is to show the tissue forming properties of this cell line using PEGDA MAPs and to investigate how changes in design features in the mold influences tissue formation. Development and alignment of the C2C12 cell line is characterized and compared to 2D cell encapsulation by using auxotonic stretching, induced by the flexible PEGDA posts in the MAP molds.

4.3.1. C2C12 tissue formation and differentiation in GelMA scaffolds

Initial experiments investigating cell seeding density and scaffold concentration experiments show that the protocol from 3T3 fibroblasts can be directly transferred to C2C12 myoblasts without changing the cell seeding density or GelMA concentration. A cell-loaded scaffold is loaded into the MAP and tissue formation is tracked over a period of 8 days. Tissue compaction is initiated after addition of the C2C12 differentiation medium with a low serum concentration. Compaction of the cell-loaded scaffold is observed from day 4 of culture and progresses until day 6 where complete tissue formation is achieved as seen in Figure 4.5A. After 8 days of culture, tissue viability is evaluated using a live/dead assay. The C2C12 cells cease to proliferate after differentiation and hence no tissue expansion can be observed unlike the 3T3 fibroblast tissues. Deflection of the posts is visible after tissue compaction as seen in Figure 4.5A. No deflection of the posts is observed for 3T3 fibroblasts in Figure 4.4, indicating a higher contraction force of the C2C12 compared to the 3T3 fibroblasts tissues. Micrographs reveal a deflection around 200 μm based on visibility of the mechanical cue in the distal region of the posts as seen in Figure 4.5A, marked with a blue square on top of the deflected posts.

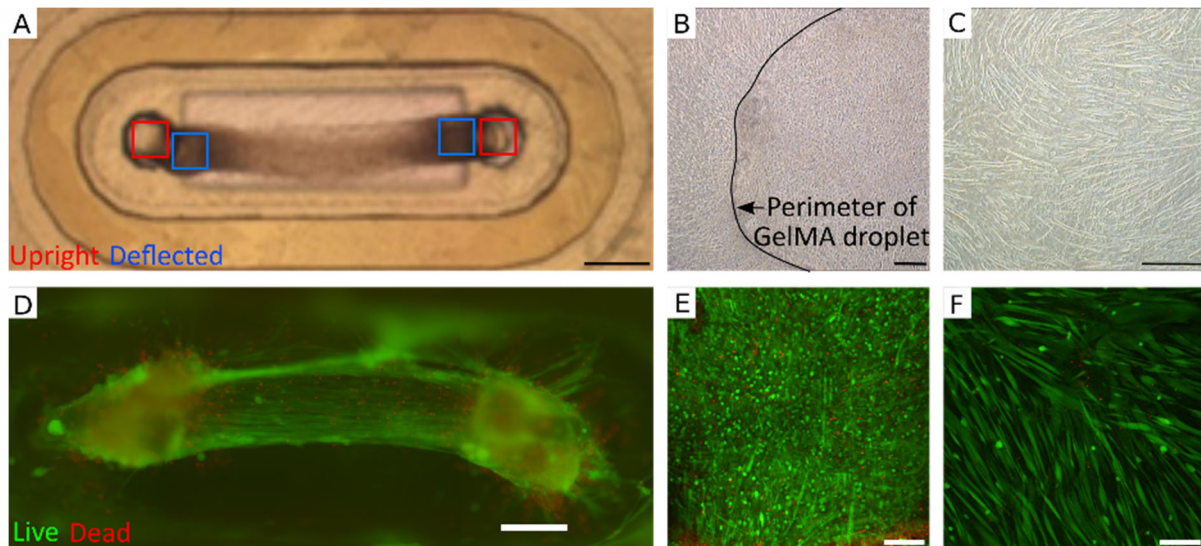


Figure 4.5 | A) Micrograph reveals a well-defined compacted tissue at 6 days after seeding. The contraction force of the C2C12 cells results in deflection of the posts as indicated by red and blue squares corresponding to the position on the top of the post in upright (non-deflected) and deflected posts respectively. B) A droplet of the cell-loaded GelMA is cultured on TCPS. Micrograph shows that cells are observed outside the perimeter of the GelMA droplet. This suggests that the cells are proliferating and able to move outside the scaffold. C) Micrographs of C2C12 cells cultured in 2D on TCPS shows that cells differentiate and align with neighboring cells when cultured on a rigid 2D surface. D-F) Confocal fluorescence micrographs of a live/dead assay of the three culture formats. D) On day 8 after seeding of mouse myoblasts to form an engineered muscle tissue the live/dead staining reveals mostly live cells with a few dead cells around the posts. E) Unstructured, unaligned, cells are observed inside the GelMA droplet with cell viability comparable to the tissue construct. F) In the 2D culture, mostly live cells are observed, spontaneously aligned next to neighboring cells. Scale bars black: 250 μm. Scale bars white: 200 μm.

Alignment and viability of the C2C12 cells is evaluated on a 2D TCPS surface, inside a GelMA droplet, and in an engineered tissue formed with a PEGDA MAP, seen in Figure 4.4. Cell viability evaluation at day 8 of culture is performed by staining with Calcein-AM and propidium iodide (PI). Similar viability is observed in all three configurations, indicating that all tested environments are suited for cell culture. Inside the tissue, few dead cells are observed around the posts, similar to the amount of dead cells in the droplet, Figure 4.5D,E. Cell alignment inside the tissue and on the 2D TCPS surface shows unidirectional cell alignment (Figure 4.5D,F) whereas cells cultured inside the droplet show rounded form or randomized cell elongation (Figure 4.5E). The unidirectional alignment of C2C12 cells is lost inside the GelMA droplet and might be due to unavailability of cell binding motifs⁴⁹ in this configuration of GelMA. When culturing C2C12 cells inside MAP molds, a 3D conformation is achieved. The 3D conformation, together with auxotonic stretching between the posts, result in unidirectional elongation of the cells.

In the perimeter around the GelMA droplet cultured on TCPS, cells can be seen that have migrated out of the GelMA, Figure 4.5B. This suggests a higher proliferation rate than seen in the MAP mold where cells are not observed outside the platforms.

In summary, shaping of the cell-loaded scaffold is important to obtain a tissue-like structure. These results indicate that the auxotonic stretch provided by the compliant PEGDA posts results in elongated cells inside the scaffold which is also observed in 2D but not in the scaffold alone. Cells grown inside the MAP mold forms a well-defined engineered muscle tissue with less cell proliferation than in the scaffold alone indicating that differentiation is initiated.

4.3.1.1. Characterization of C2C12 tissues by immunostaining

Cell differentiation is evaluated by sarcomeric f-actin and nucleus staining in cryosections of tissues formed inside MAP molds. Figure 4.6 shows a cryosection of a C2C12 tissue at day 3 after seeding, constructed of 1.5 μ L cell-loaded scaffold containing 10×10^6 cells/mL. The tissue is cultured inside a MAP with 1 mm spacing between the posts. A tissue has formed around the mechanical cues at the top of the posts, that deflect as a result of the contracted tissue seen in Figure 4.6A. Cells are multinucleated and show uniform elongation after 3 days of culturing inside PEGDA MAPs suggesting differentiation into myotubes, Figure 4.6B. The tissue measures 170 μ m in cross-section and hence allows diffusion of oxygen to the tissue core. As a result, cells are compacted throughout the cross-sectional area.

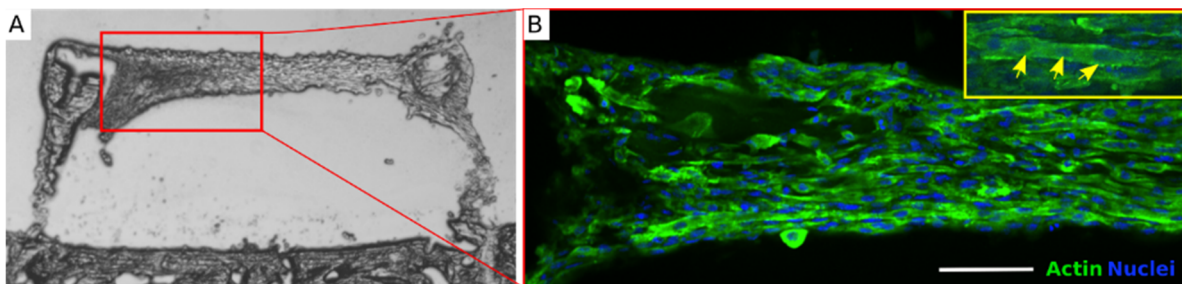


Figure 4.6| A) Micrograph of a cryosectioned MAP mold with a C2C12 tissue at day 3 after seeding. Tissue slices verify tissue positioning at the mechanical cues as expected. B) Staining for f-actin and nuclei in 3 day old C2C12 tissues shows elongated and multinucleated cells (yellow arrows) indicating a differentiation beyond myoblast level. Cryosectioning and immunostaining are performed by Ayzel Kiziltay. Scale bar: 100 μ m.

4.3.2. Design dependent tissue formation

Culturing of contractile tissues inside PEGDA MAPs requires intact molds with all features robustly printed. In cases where the mechanical cues of the posts are broken off in the printing process, the tissue forms during a similar timeline but slips off the defective post after 1-2 days, Figure 4.7.

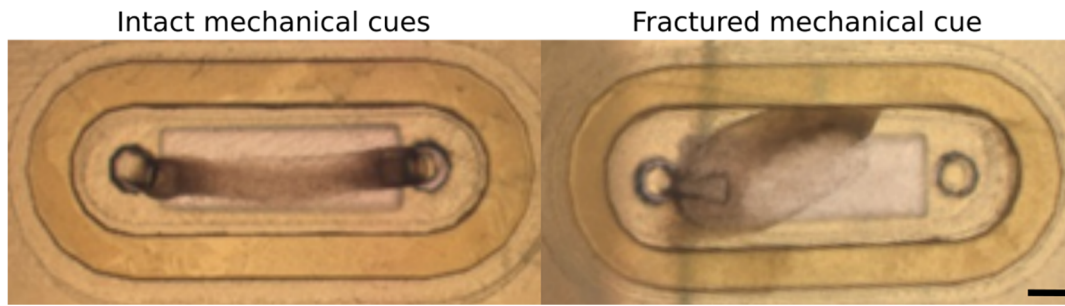


Figure 4.7 | Micrographs shows that intact mechanical cues are critical for long-lasting tissues. If the posts are not intact after printing, the formed tissues can slip off the posts during contraction. Thereby losing the effect of the auxotonic stretching and read-out possibility. Scale bar: 200 μm .

After printing, the molds are inspected to investigate if the posts and mold walls are intact. An optimized printing procedure with a better layer-to-layer printing based on a lower absorber concentration, described in section 3.4.4, ensures that less than 10 % of the posts are broken after printing and thereby ensures robust tissue formation.

Reproducibility of tissue formation can be evaluated based on uniformity between tissues as well as the compaction and shape of a single tissue. Using the simple post-based MAP with both stadium-shaped and oval molds results in equal tissue formation between tissues inside the MAP as seen in Figure 4.8. Tissues formed in oval molds are comprised of 3.5×10^6 cells encapsulated in a fibrin scaffold whereas tissues formed in the stadium-shaped molds consist of 1.5×10^6 cells encapsulated in a GelMA scaffold. The lower number of cells in the stadium-shaped molds gives the ability to use fewer cells while still obtaining uniform tissues. Both designs result in uniform tissues, capable of bending the PEGDA posts upon contraction.

Obtaining contractile tissues inside PEGDA MAP in both oval and stadium-shaped designs result in unidirectional elongation of multinucleated cells inside the tissues (Figure 4.8 and Christensen et al., 2019⁸¹). Hence, the PEGDA MAPs show the ability to culture contractile tissues that facilitate functional read-out by bending of the flexible PEGDA posts.

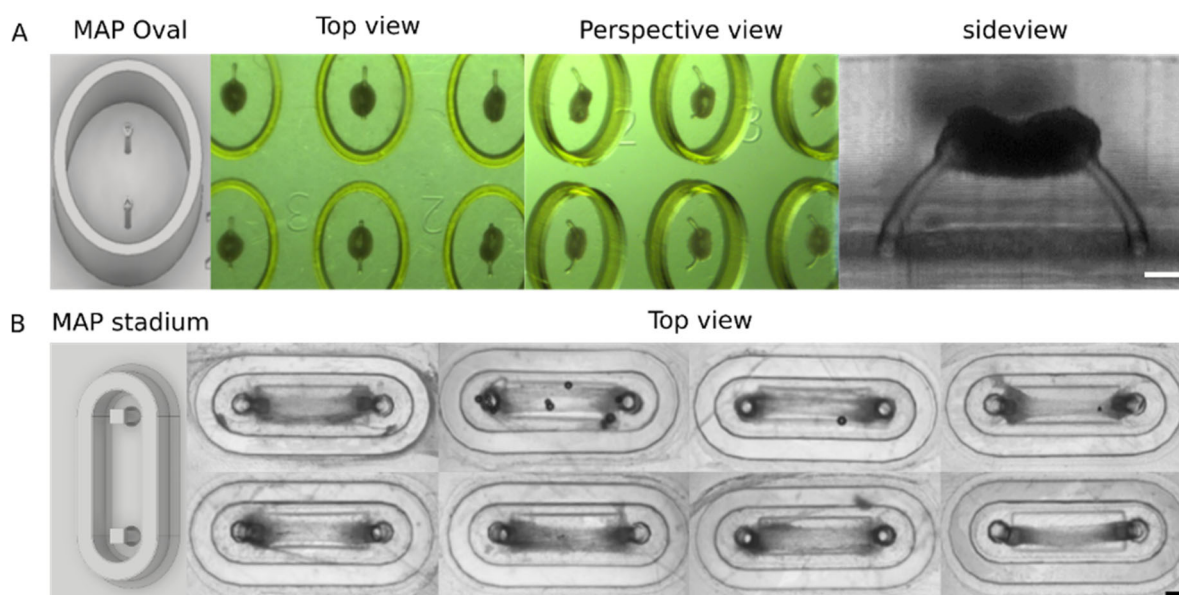


Figure 4.8| Micrographs showing uniform tissue formations in two designs of PEGDA MAPs. A) Oval molds of 50 % (w/v) PEGDA. C2C12 tissues are imaged at day 5 after seeding encapsulated in a fibrin scaffold. B) Stadium-shape 20 % (w/v) PEGDA molds. C2C12 tissues are imaged at day 6 after seeding encapsulated in a 5 % (w/v) GelMA scaffold. Scale bars: 200 μm . The sideview micrograph in “A” is adapted with permission from (Christensen et al., 2019, DOI: 10.1021/acs.biomac.9b01274) American Chemical Society.

4.4. Cardiac tissue formation in three types of cell-loaded scaffolds

Both cell concentration and scaffold composition highly influence the ability to form a tissue inside the PEGDA mold as described in section 4.1. As the cells are known to dedifferentiate when they are taken out of their 3D environment²⁴ and likewise differentiate better when in a 3D environment. Therefore the aim of this work is to find a scaffold where the cardiomyocyte progenitor cells will be able to remodel the scaffold and form a tissue in a timescale of up to one week. Over an extended culture time, cell-cell connections are formed, and degradation of the scaffold material will not result in a damaged tissue. When designing the correct ratio between scaffold materials and seeded cells, a compromise is made between scaffold robustness against degradation and cell remodeling. A scaffold that is too stiff prohibits the cells from reshaping the scaffold, resulting in aggregation of the cells in small clusters inside the scaffold. Aggregated cells are often viable in this conformation, however, the functionality of the tissue is lost. Resistance to remodeling of the scaffold could lead to dedifferentiation¹³⁶ of the seeded cells and hence become a set-back to the differentiation timeline. Contrary, if the scaffold is too soft or degrades rapidly, tissue formation will be incomplete or insufficient. This section describes the tissue formation properties of different combinations of scaffold materials and cell seeding concentrations. Characterization of the formed tissues is presented in subsequent sections. Cardiomyocyte progenitor cells are provided by our collaborator at

Instituto de Biologia Experimental e Tecnológica (iBET) in Portugal who developed the differentiation protocol from hiPSCs to cardiomyocytes.

4.4.1. Cardiac tissue formation and culturing using a 30 days differentiation protocol

GelMA, fibrin, and collagen are tested as seeding scaffolds to form tissues with cardiomyocyte progenitor cells. Two cell seeding densities and scaffold concentrations are tested in order to investigate the effect of scaffold stiffness and cell seeding density on cardiac tissue formation. A 30-days differentiation protocol and two different MAP designs are used. Differentiation is performed using the protocol developed by iBET which achieves cardiomyocytes at day 15 and further mature them until day 30, Figure 4.9. Differentiation is performed in 2D culture until day 10. Cells are seeded into PEGDA MAP molds at day 10 of differentiation when they are cardiomyocyte progenitors. The cells are kept in culture until day 30 to evaluate the tissue formation. Tissues are evaluated as described in section 4.1. Cardiac tissues will start beating synchronized and uniformly. A delay can be observed from one part of the tissue to another due to low conduction velocity in immature tissues. When the cells form connections via intercalated discs, they will start beating spontaneously at an earlier timepoint and, as the cells mature, the contraction happens with increased force.

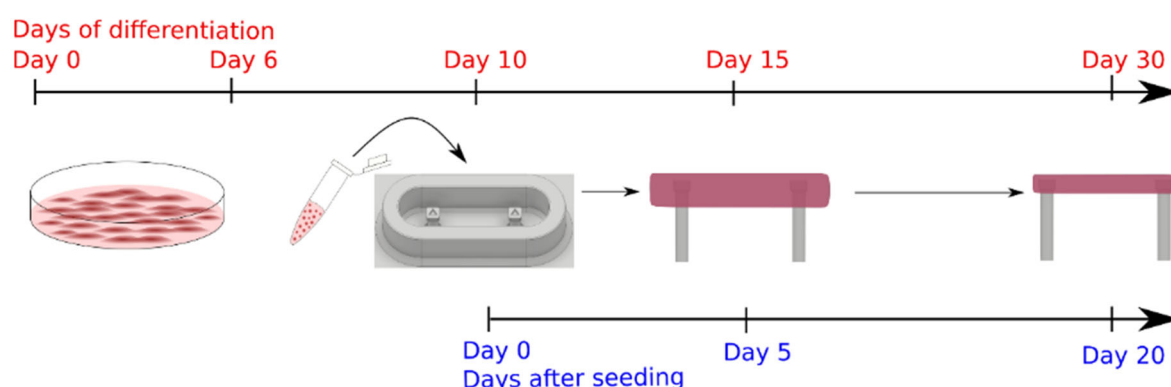


Figure 4.9 | Differentiation of cardiomyocytes from hiPSC derived stem cells and cardiac tissue formation using PEGDA MAP molds. Cell differentiation is initiated at day 0 using standard 2D culture methods. At day 6, the iPSC derived cells have reached the cardiomyocyte progenitor stage and start beating. At day 10 of differentiation, cells are seeded into PEGDA MAP molds using a hydrogel scaffold. Tissue formation happens between day 10 and 15 of the differentiation. Tissue compaction and maturation happens during the following two weeks of culture.

4.4.2. Effect of scaffold stiffness and cell seeding density on cardiac tissue formation

Collagen, GelMA, and Fibrin are all assessed as candidates to form cardiac tissues with different concentrations of cardiac progenitor cells. Both collagen, one of the natural ECM components of the heart, and fibrin hydrogels have previously been used to form engineered cardiac

tissues^{50,51}. Here, GelMA is introduced as well due to its rapid gelation time. Fast gelation is advantageous to prevent drying of both the hydrogel scaffold and PEGDA mold during gelation of the scaffold.

4.4.2.1. The effect of cell seeding densities on the ability to form engineered cardiac tissues

Cell seeding densities needed to form a tissue varies between cell types. Finding the optimal cell seeding density can be tricky and requires some optimization. Based on the C2C12 cell concentration used for tissue formation, a range of different cell seeding concentrations is tested. From this pre-test, two cell concentrations are tested in the three different cell seeding scaffolds and two different PEGDA MAP designs. The stadium-shaped MAP with cylindrical posts and the oval MAP with rectangular posts, similar to the one presented by Mills et al.⁵⁰, are used. The “low” and “high” cell concentration corresponds to 15×10^6 cells/mL and 30×10^6 cells/mL respectively.

For the fibrin and GelMA scaffolds, the cell seeding density alone can improve tissue formation capacity as seen in Figure 4.10. By using a high cell concentration, tissue formation is seen at day 15 whereas the low cell concentration does not result in any tissue formation. A low cell concentration with both fibrin and GelMA reveals cell clustering inside the scaffold as a result of the space between cells being too large. The spacing makes it difficult for the cells to adhere to each other across the network and therefore the cells aggregate with their nearest neighbors, resulting in aggregation rather than tissue formation. Conclusively, a high cell seeding concentration is found to be the best choice to form a well-defined, lasting tissue.

Figure 4.10 shows that increasing the cell seeding density in the collagen scaffold does not improve the tissue formation properties, indicating that the stiffness of the material is too high for the cells to remodel and form a tissue. This results in cell aggregates forming inside the gel scaffold 5 days after seeding (differentiation day 15) and a longer timespan before a tissue formation is observed. At the end of the differentiation, the formed tissues consist of aggregated cells with some scaffold material remaining in the perimeter of the PEGDA mold. The collagen scaffold is contracted in the center of the MAP molds with a large number of cells and scaffold surrounding it. The same is observed for both MAP designs. Hence, an incomplete tissue formation is seen using the collagen scaffold at both low and high cell concentration.

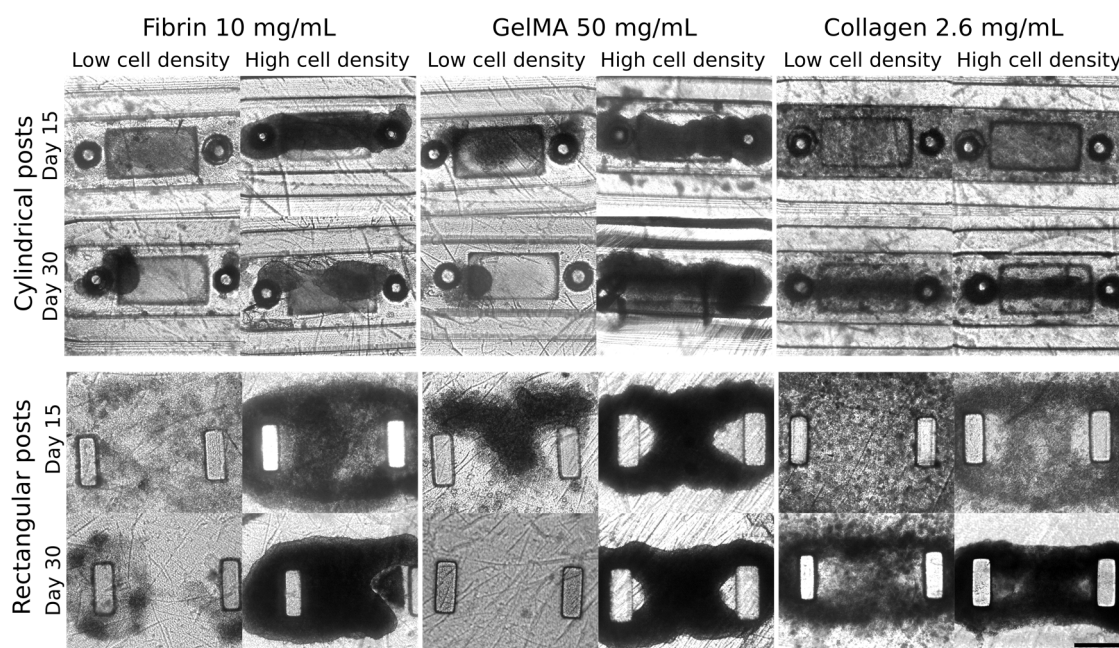


Figure 4.10| Micrographs of engineered cardiac tissues at day 15 and day 30 of differentiation in three scaffolds with two different cell seeding densities and in molds with different post geometries. Low cell density corresponds to 15×10^6 cells/mL and high cell density is 30×10^6 cells/mL. Day 15 and day 30 are days of differentiation. Cells are seeded into the MAPs at day 10 of differentiation. For all three scaffolds tested, the low cell density is insufficient to form a tissue construct. For fibrin and GelMA, the cells aggregate locally, and a tissue is not observed whereas the collagen encapsulated cells form a tissue after three weeks in culture. The high cell density results in a well-defined tissue for both fibrin and GelMA. In the collagen scaffold, an incomplete tissue formation is observed after three weeks in culture. Scale bar: 500 μm .

4.4.2.2. Type and concentration of the scaffold influences tissue formation

The GelMA and fibrin scaffolds are tested at two concentrations with a cell seeding density of 30×10^6 cells/mL to evaluate how the scaffold stiffness affects the tissue formation properties. The results are compared to the collagen scaffold in Figure 4.11. The GelMA scaffold is loaded with 10 $\mu\text{g/mL}$ fibronectin to enhance cell binding properties as initial tests showed low binding to GelMA alone. Seeding cardiomyocyte progenitor cells on fibronectin coated 2D surface showed high binding affinity and therefore the RGD containing fibronectin⁴⁶ is added to the GelMA scaffold to improve cell binding. Using a GelMA concentration of 100 mg/mL results in aggregation inside the mold similar to that observed in collagen at day 15. In contrast to collagen, where the cells are able to start remodeling the collagen scaffold over two subsequent weeks of culturing, no remodeling is observed for a GelMA concentration of 100 mg/mL. Reducing the GelMA concentration to 50 mg/mL drastically changes the tissue formation process. The GelMA 50 mg/mL and the two fibrin concentrations share a similar timeline for

scaffold remodeling and tissue formation. A well-defined tissue is formed by the remodeling of the scaffold by the cells after 2 – 5 days in culture, similar to the tissue formation process previously reported in literature^{50,51,96}. On day 30 of differentiation, the low concentration 5 mg/mL fibrin tissue is broken whereas both 10 mg/mL fibrin and 50 mg/mL GelMA reveal intact tissues of relevant size and shape. Spontaneous beating with synchronized contraction of the formed tissue is observed 3 days after seeding in the 50 mg/mL GelMA, suggesting that cell-cell connections have been formed. In the fibrin and collagen-based tissues, spontaneous beating is observed 5 days after seeding. Spontaneous synchronized beating is observed throughout the culture time in compacted and well-defined tissues. For combinations that result in aggregated tissues, individual clusters are beating spontaneously without simultaneous contractions suggesting that insufficient cell-contacts have been formed between clusters.

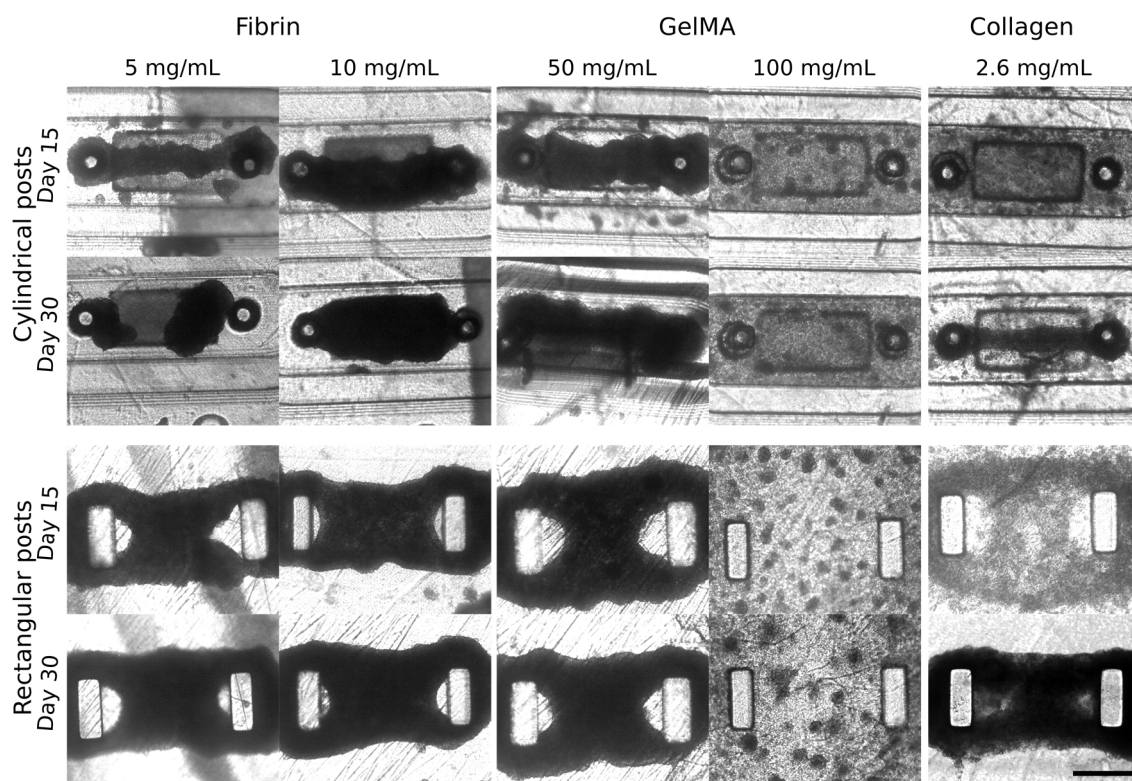


Figure 4.11| Micrographs of engineered cardiac tissues. Three different scaffold materials are tested to promote tissue formation of cardiomyocyte progenitor cells in two different MAP designs. Two concentrations of GelMA and fibrin are tested to identify the better conditions for tissue formation. The cell concentration is 30×10^6 cells/mL. Fibrin 10 mg/mL and GelMA 50 mg/mL result in uniform tissue formation with tissues that start spontaneous, synchronized beating upon tissue formation within 5 days of culture. Collagen 2.6 mg/mL results on cell aggregates that results in a slow compaction. At the end of experiment cell aggregates and uncontracted collagen are still observed outside of the formed tissues. Scale bar: 500 μ m. Micrographs of GelMA 50 mg/mL and collagen are from the same experiment as presented in Figure 4.10.

It is valuable to obtain tissue formation in a time span of 1 week or less to limit both the culture time and, more importantly, inhibit any dedifferentiation associated with keeping the cells in a scaffold that limits their ability to stretch and form connections to one another^{137,136}. For all tested scaffolds, a concentration that is too low will result in rapid disintegration of the scaffold with encapsulated cells and thereby a lack of tissue formation or tissue failure. In order to avoid dedifferentiating the cells, the softer scaffolds fibrin 10 mg/mL and GelMA 50 mg/mL are considered relevant candidates for tissue formation using this cell line. Cardiomyocytes developed from another cell line might function differently in the tested scaffolds. For each cardiomyocyte source the scaffolds should therefore be considered. The results of tissue formation, depicted in Figure 4.10 and Figure 4.11, show that GelMA 50 mg/mL and fibrin 10 mg/mL function equally well; the fibrin 10 mg/mL scaffold is chosen for subsequent experiments. Fibrin is chosen over GelMA to enable comparison with studies in the literature where fibrin has been widely used as a cell-seeding scaffold for cardiac tissue engineering.

4.4.2.3. Quality of engineered cardiac tissues based on macroscopic tissue morphology

Tissue formation is compared between MAPs with the stadium shaped mold design with cylindrical posts and the oval mold design with rectangular posts, Figure 4.11. Comparing the shape of the tissues reveals that the macroscopic tissue morphology is similar between tissues formed in the same shape of MAP with different scaffolds. However, there is a distinct difference in tissue shape between the two mold designs. In the stadium-shaped molds, the tissues form in a thin rectangular shape and fully surround the posts with no gaps. In the oval design with rectangular posts, tissues form a wider rectangle and gaps are seen in the vicinity of the posts. Gaps forming in the tissues result in a thinning of the tissue around the corner of the posts. During tissue maturation, the tissue force is expected to increase thus resulting in a higher tensile stress. Thinning might therefore lead to necking and ultimately failure of the tissues¹³⁸. Therefore, cylindrical posts should be used to avoid gaps.

4.5. Maturation methods for Cardiac tissues

Obtaining a mature cardiac tissue is not a straightforward, automatic process. Many studies show that stem cell derived cardiomyocytes remain in an immature state at the end of the differentiation. Additional maturation procedures must therefore be implemented to achieve a higher degree of maturation as described in section 2.4. Previous studies using mechanical or electrical pacing suggest that both methods can increase maturation in engineered cardiac tissues^{45,112}. Due to the time constraints of building a mechanical pacing setup, an electrical pacing unit using commercial electrodes is used as a mean of maturation in this work and is described in section 4.5.2. A brief summary of the work performed on mechanical stimulation is described in section 4.5.1.

4.5.1. Cyclic mechanical stimulation of PEGDA MAPs

Building a mechanical actuation setup includes both actuation setup and customized design of the PEGDA MAP. Within the PolyCell group at DTU Health Technology, several ways to achieve mechanical actuation of cardiac tissues formed inside stadium-shaped molds of the PEGDA MAP have been investigated. The work has been led by Christian Pless (microactuator) and Christoffer von Halling Laier (multiple-tissue actuator). My contribution to this work was to assist in the design development and discussions around concept of cyclic mechanical actuation based on background knowledge. A detailed description of the contribution can be seen in “List of contributions”.

Work performed by C. Pless¹³⁹ shows the proof of concept for cyclic mechanical actuation using the stadium-shaped MAP design by actuating a single post using a topology optimized microactuator. An applied deflection of the microactuator results in an increased deflection output which is capable of deflecting the post and achieving 20 % tissue strain. This work demonstrates the possibility of performing cyclic mechanical actuation of tissues formed inside PEGDA MAPs. However, upscaling of this device to allow maturation of multiple tissues seems to be challenging as the displacement potential decreases when the design is changed to include deflection of multiple posts to stretch multiple tissues in parallel.

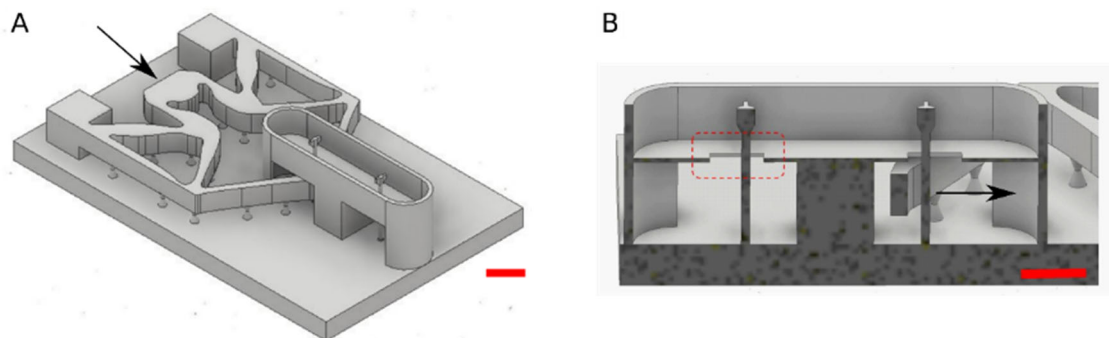


Figure 4.12| CAD drawing of the microactuator developed by C. Pless. The microactuator can actuate one post by applying a displacement at the point of application shown by the arrow in A). The actuator pulls in the post shown in B) thereby increasing the distance between the posts. This will elongate the formed engineered tissue. This mechanism has been shown to effectively actuate one post. However, due to a loss of output displacement when upscaling to actuate multiple tissues, this design was not further developed. Scale bars: 500 μm . Adapted with permission from C. Pless¹³⁹.

Unpublished work led by C. von Halling Laier shows another approach to achieve cyclic mechanical actuation inside standard cell culture well plates. This model uses custom designed well-plate inserts (“the inserts”) that can simultaneously actuate all tissues within a single MAP. Actuation is achieved by introducing a built-in actuator on the PEGDA MAP design that is activated by the designed inserts that pushes on the PEGDA actuator upon external stimulation,

thus keeping a sterile environment inside the wells. This set-up can achieve simultaneous stimulation of 6 wells each containing 9 cardiac tissues and has the ability to be expanded to include multiple well plates.

Due to the time constraint on this project, the cyclic mechanical actuation methods were not implemented to mature cardiac tissues in the presented PEGDA MAPs in the work presented in this thesis.

4.5.2. Parameter optimization of the custom-built electrical stimulation system

Electrical pacing is applied to engineered cardiac tissues at day 5-7 after seeding when tissue compaction has taken place. Electrical pacing is then continued throughout the culture time. The electrical stimulation pacing system (“the pacing system”) is built and characterized by Peder Skafte-Pedersen and Jens Henneke, Sophion Bioscience A/S. The PC based control software was made by Torben Trindkær Nielsen. My contribution to this work has been to evaluate the cell-toxicity in the final system as well as defining the settings used to stimulate cardiac tissues inside PEGDA MAPs based on preliminary testing which had determined the voltage and pulse-duration intervals.

The custom-built electrical pacing unit (Figure 4.13 blue rectangle) is connected to a commercial carbon electrode lid from IonOptix fitting an 8 well plate system (Figure 4.13 red rectangle). The pacing system is built on the open-source electronics platform Arduino Due, and further contains an amplifier and multiplexer to control the pulse length, frequency and voltage. A PC is used as pacing and video controller and allows simultaneous control of pacing stimulation and video recording to view tissue response. All recordings are performed inside an incubator at 37 °C and 5 % CO₂.

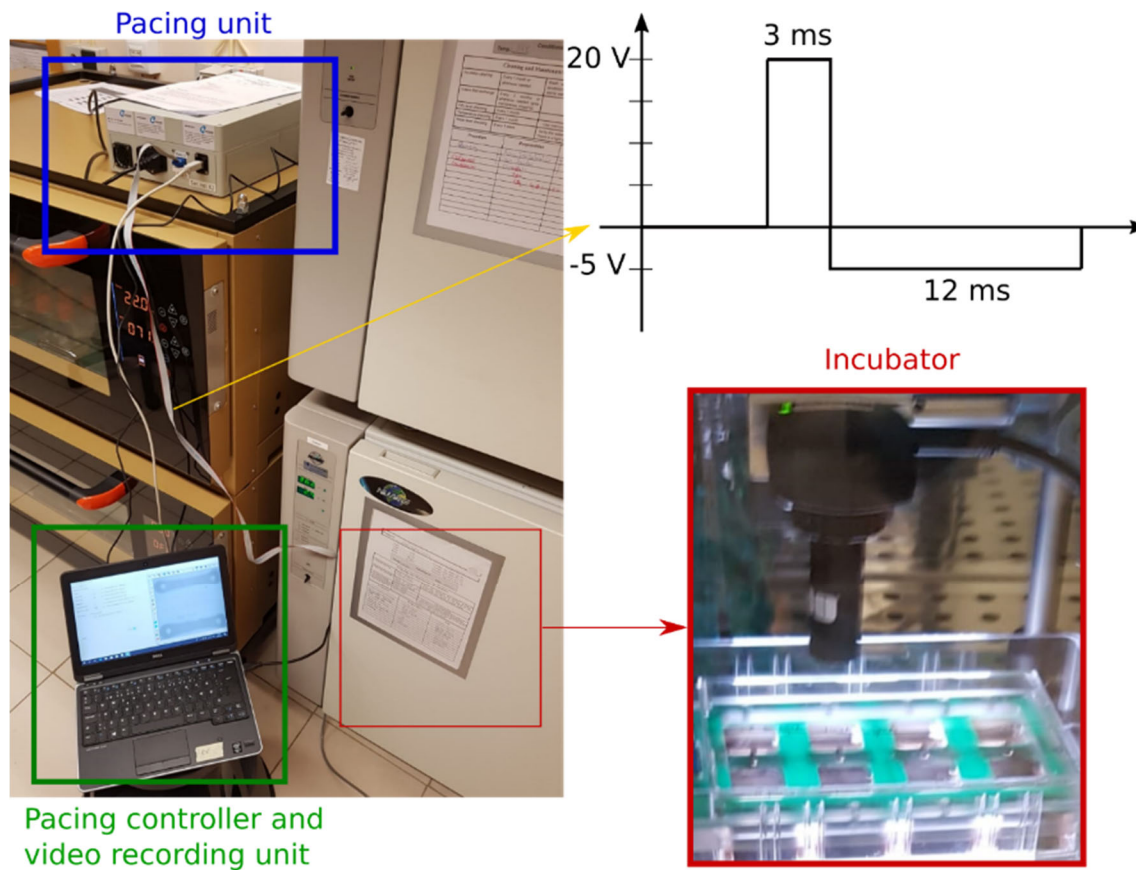


Figure 4.13| Culture setup using electrical pacing of engineered cardiac tissues. Continuous electrical pacing is performed inside an incubator at 37 °C. A custom-built pacing unit applies a biphasic pulse of 3 ms with a positive pulse of 6.7 V/cm followed by a negative reversing pulse of 1.7 V/cm for 12 ms. A camera setup captures the tissue response and is used to record videos and images of tissues every second day throughout the culturing time.

A range of voltage, pulse, and frequency settings are investigated to evaluate the tissue contraction response, to the electric pacing. At day 5 after seeding, compacted cardiac tissues are visualized through a camera setup inside an incubator at 37 °C. Expected parameter settings are based on literature values with electric fields in the range from 3 V/cm¹¹⁹ to 6.6 V/cm¹¹⁸ and pulse duration from 2 ms to 5 ms^{45,118,119} at 0.5 Hz to 6 Hz pacing. The voltage is changed between 15 V (5 V/cm) to 20 V (6.7 V/cm) with pulse durations of 2 ms to 5 ms at 0.5 Hz and 1 Hz. If the tissues contract as a response to the electric pacing, the applied setting is noted as “functional”. The minimum required amplitude and duration needed to stimulate tissue contraction are found to be 20 V (6.7 V/cm) with a 3 ms pulse duration at 0.5 Hz and 1 Hz pacing frequency. Therefore, this is chosen as the set-point for tissue stimulation for all subsequent experiments with engineered cardiac tissues with a frequency of 1 Hz.

The electrochemical effect of electrical pacing is investigated using a monophasic pulse and a biphasic pulse as displayed in Figure 4.14. A squared biphasic pulse with slow reversion has previously been reported to minimize the electrochemical reactions occurring at the electrode-

electrolyte interphase²⁴. It is therefore expected that a biphasic pulse will introduce less cytotoxicity. The electrochemical effect is measured by pH (medium color change or pH strips) and odor change in culture medium without cells. A significant difference is found between pacing with biphasic and monophasic pulses as elaborated below.

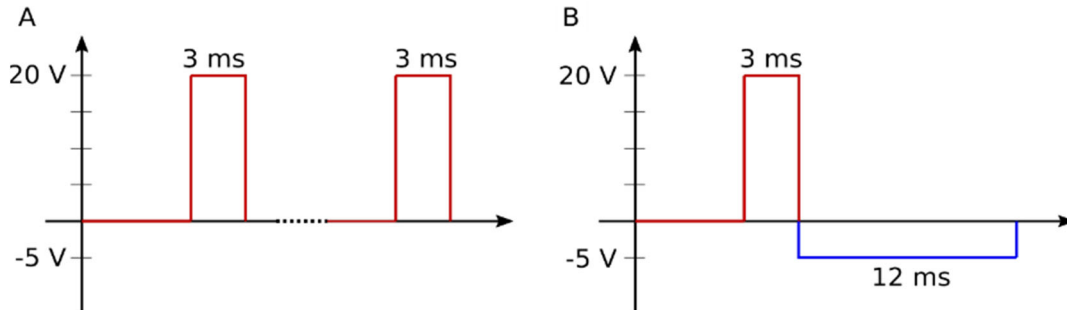


Figure 4.14| Schematic of the electric stimulation pulses used to test cytotoxicity and to stimulate engineered tissues. The electric fieldstrength of the 20 V pulse is 6.6 V/cm and 1.7 V/cm for the 5 V pulse. A) A monophasic pulse 20 V and 3 ms in duration. B) Biphasic pulse with stimulating pulse of 20 V and 3 ms duration followed by a slow reversing pulse of - 5 V for 12 ms.

When using monophasic pulses, there is a pronounced change in medium color from stimulation in both Dulbecco's Modified Eagle Medium (DMEM) and Roswell Park Memorial Institute medium (RPMI) for 42 min and 40 min, respectively, as seen in Figure 4.15A,B. Change in medium color clearly indicates undesirable electrochemical reactions at the electrode-medium interface. After minutes of pacing at a frequency of 20 Hz, visible bubbles are forming around the electrodes, Figure 4.15C. A chlorine odor is released, indicating electrolysis of the medium. During the test, significant condensation is formed under the lid of the paced well-plate suggesting an increase in temperature, Figure 4.15D, which was not measured during this test. The electrochemical reactions that leave chemical residues in the medium and the production of gas from electrolysis can be toxic to cells^{101,140}. These effects must therefore be avoided to the best extent to culture engineered cardiac tissues with continued electrical pacing. No testing to determine explicit electrochemical reactions has been done in this work.

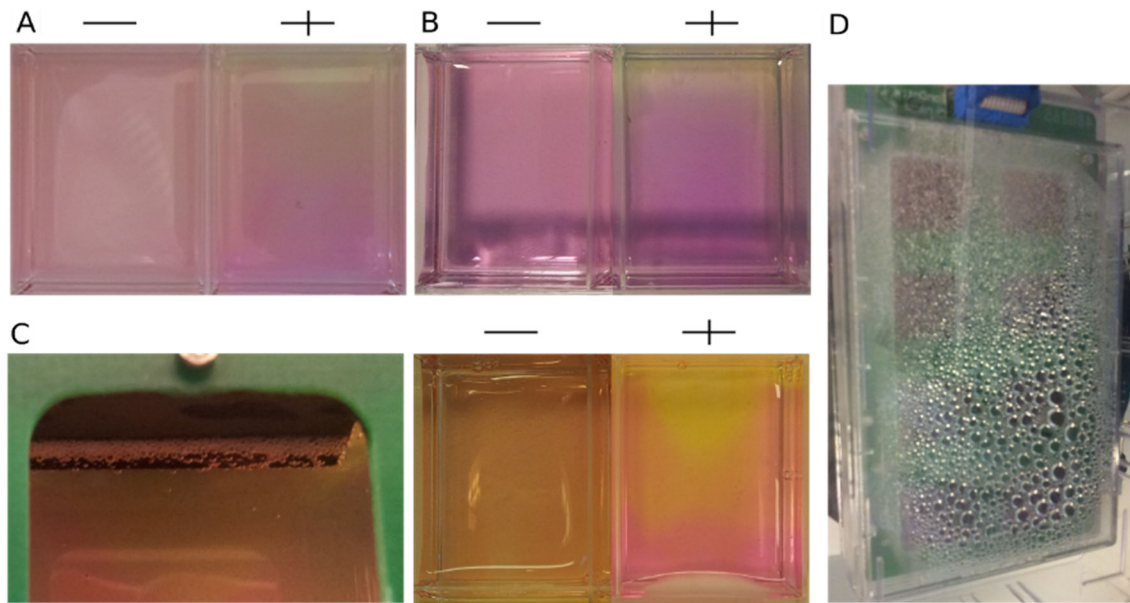


Figure 4.15 | Pictures of electrochemical and thermal effects observed during stimulation with a monophasic pulse of 20 V (6.7 V/cm) for 3 ms at 6.66 Hz and 20 Hz. Unpaced (-) and paced (+) wells are compared. A) The right well shows the visible medium color change from electrical stimulation using a monophasic pulse at 20 V, 3ms for 42 min at 6.66 Hz. Left well is unpaced control (DMEM) and shows no sign of change in color. B) The monophasic pulse is applied to the right well at 20 V, 3 ms for 40 min at 6.66 Hz (RPMI). The left well is an unpaced control where no change is seen. C) DMEM paced with 20 V and 3 ms for 28 min at 20 Hz. Bubbles forming around the electrodes are visible a few minutes into the test (DMEM) and is a clear indicator of the electrochemical effect. On the right a distinct color change is seen in the paced well compared to the unpaced. D) Pacing with a frequency of 20 Hz results in condensation and indicate an increase in temperature. Tests and photos by Peder Skafte-Pedersen.

The effect on medium color, pH, and temperature is investigated using the biphasic pulse with slow reversal pulse shown in Figure 4.14B. The tests are performed in RPMI medium. Applying the biphasic pulse with a pacing frequency of 20 Hz for 38 min does not result in change of medium color or gas production as seen in Figure 4.16A. The lack of detection indicates that the net electrochemical reactions around the electrode-medium interphases are minimized due to reversed reactions using the biphasic settings. Despite the reduction of detectable chemical effects, the carbon electrodes are exchanged every 48 hours during tissue pacing to rinse out any toxic compounds that may have accumulated inside the electrode. Rinsing is performed in a sterile environment by immersing the electrodes in sterile water for 2 x 24 hours following the manufacturer's instruction. The temperature are monitored over 48 h while continuously stimulating with the biphasic pulse at 1 Hz. Temperature is measured in paced wells and unpaced wells in the same well-plate. No difference is observed between paced and unpaced wells, however changing to 20 Hz increases the temperature which is

expected from the results seen in Figure 4.15. After 2 h of pacing at 20 Hz using the biphasic pulse the temperature in the paced wells are measured to be 40 °C

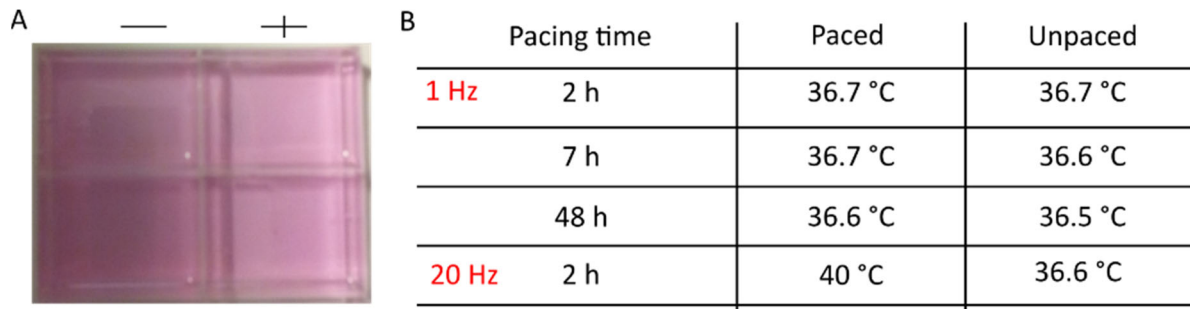


Figure 4.16| A) Picture of unpaced (-) and paced (+) RPMI. After electrical stimulation for 38 min with a biphasic pulse of positive 6.7 V/cm for 3 ms and negative 1.7 V/cm for 12 ms at 20 Hz, no change in medium color or odor is observed (+) compared to unpaced control (-). Unpaced well appears darker due to shadow in picture. B) The table summarizes the results of applying the same biphasic pulse as described in (A) for 48 h at a pacing frequency of 1 Hz. Temperature is monitored over time. No increase in temperature is observed in paced wells compared to unpaced wells. Changing the pacing frequency to 20 Hz results in a temperature increase to 40 °C in the paced wells. Test in A) performed by Peder Skafte-Pedersen.

4.5.3. Investigation of cell toxicity induced by continuous electrical pacing

Toxicity effect of the biphasic electrical stimulation on cells is tested using C2C12 mouse myoblasts in both 2D and 3D tissue cultures. Unpaced controls are kept under identical culture conditions. Engineered C2C12 tissues are prepared using the previously described protocol with fibrin as the scaffold material. After tissue formation, MAPs are moved to the pacing system and paced for 5 consecutive days using a biphasic pulse at 1 Hz with a stimulation pulse of 6.7 V/cm for 3 ms followed by a slow reversal pulse at 1.7 V/cm for 12 ms as shown in Figure 4.14B. The carbon electrode pacing lid is changed to a new sterile lid every 48 hours. Electrodes are cleaned for 2 x 24 h by immersion in MQ water under sterile conditions to remove any toxic electrochemical residues according to the manufacturer's instructions. Cell viability of the paced and unpaced tissues is evaluated by live/dead staining. Figure 4.17 shows the viability staining of the tissues. During handling of the tissues they are detached from the posts and therefore spherical in shape as they are no longer extended between the posts. Confocal fluorescence micrographs are presented from the same vertical depth in the tissues. Similar levels of live and dead cells in both paced and unpaced tissues indicate that pacing for 5 days has not affected the level of cell death. A 2D layer of C2C12 cells also shows similar morphology after 5 days in culture, with and without pacing.

Based on these results, it can be concluded that this setup can be used for electrical pacing of engineered tissues without introducing substantial cytotoxic effects.

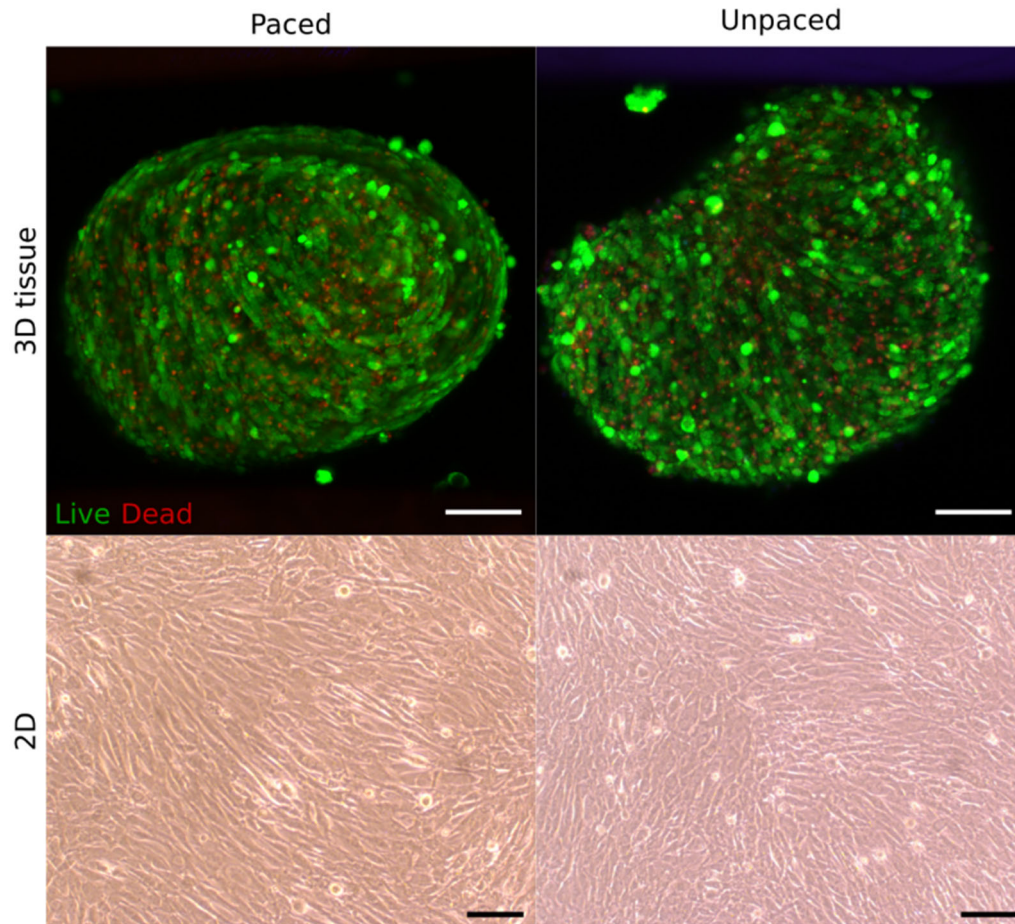


Figure 4.17| Confocal fluorescence micrographs of 3D engineered tissues and phase-contrast micrographs of 2D cells is presented to evaluate cytotoxicity. The cytotoxic effect of continuous electrical pacing is evaluated by culturing C2C12 mouse myoblasts in 2D or as engineered tissues in 3D. Continuous pacing at 1 Hz with a biphasic electrical pulse of 6.7 V/cm for 3 ms followed by -1.7 V/cm for 12 ms. 3D tissues) During handling and staining, the C2C12 engineered tissues are released from PEGDA MAP molds and, as a result, curl up to form a spherical structure. Presented confocal fluorescence micrographs are from the center of the tissues at the same confocal depth in both tissues and are thus directly comparable. 2D) Phase-contrast micrographs of 2D cells shows attached cells with high confluency indicating that the cells are viable. Color difference between paced and unpaced are due to different illumination Scale bars: 100 μ m.

4.6. Characterization of engineered cardiac tissues in PEGDA MAPs

This section aims to investigate cardiac tissue maturity based on cellular development in electrically paced cardiac tissues formed in stadium-shaped PEGDA MAPs of two different sizes. Two different sizes of the stadium-shaped PEGDA MAP are prepared to investigate if mold size, and hence tissue size, influences tissue formation, development, and function.

Please note that experiments in this section are comprised mostly of results from 1-2 experiments due to time restrictions. They can therefore not be statistically evaluated for robustness but are discussed based on the indicative behavior of the preliminary results obtained. Experiments were performed in collaboration with Marta Paiva from the Instituto de Biologia Experimental e Tecnológica (iBET) in Portugal during my external stay and repeated by me at Sophion Bioscience A/S afterwards. Results have been evaluated and prepared by me. See the section “List of collaborations” for details on contributions.

4.6.1. Shape and viability of electrically paced cardiac tissues of different sizes

The stadium-shaped MAP with a 1 mm spacing of posts (mini-MAP) is compared to an upscaled version that has 5 mm between the posts (Large-MAP). Many cardiac tissues presented in literature are in the centimeter range^{25,95,141} and the large MAP hence resembles those engineered tissues. Cardiac progenitor cells are seeded into the molds at day 10 of differentiation and electrical pacing is applied 7 days after seeding corresponding to day 17 of differentiation (Figure 4.9), and is continuous throughout the culture time until day 30 of differentiation.

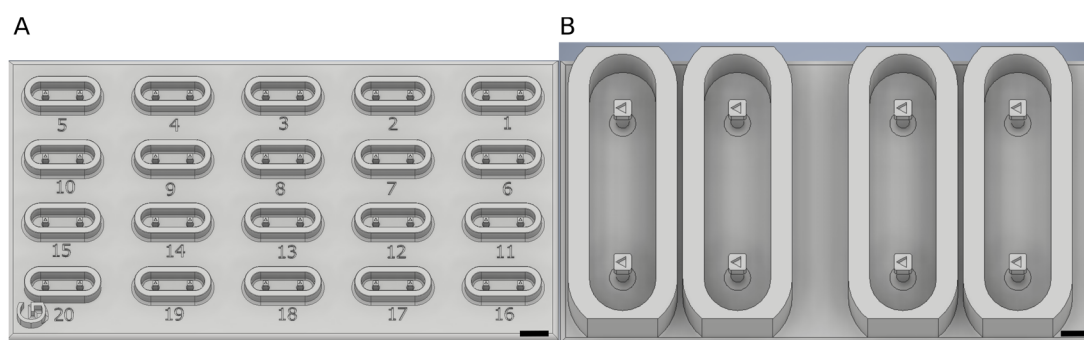


Figure 4.18| CAD drawings of stadium-shaped PEGDA MAPs in two different sizes. Both are used to investigate the maturation of cardiac tissues developed from hiPSC-CM progenitor cells seeded at day 10 of differentiation and cultured for 20 days while being electrically paced for 12 days after tissue formation. A) A mini-tissue sized mold with 1 mm distance between the vertical posts corresponding to the size range as previously reported cardiac tissues^{50,138}. B) Increasing the lateral dimensions of the mold in “A” by a factor of 5, results in a large-size stadium-shaped PEGDA mold, comparable in size to previously described engineered cardiac tissues^{25,95,141}. Scale bars: 1 mm.

Mini-tissues are observed to form between day 13 and 21 of differentiation and large-tissues form between day 19 and day 26 of differentiation. Both types beat spontaneously and synchronously and respond to pacing, indicating that they have developed cell-cell connections. At day 30 of differentiation, both types have formed compacted tissues positioned at the top of the posts around the mechanical cues, Figure 4.19A,B. Visual inspection from the top and side view shows compacted cells that have formed a uniform compaction of the tissue

where cells are not aggregating in smaller clusters. The macroscopic inspection of the tissues indicates that the seeded cells have worked together to form a well-functioning cardiac tissue. To evaluate the tissue on a cellular level, a viability stain using calcein-AM (live cells, green) and propidium iodide (PI) (dead cells, red) has been performed at day 30 of differentiation.

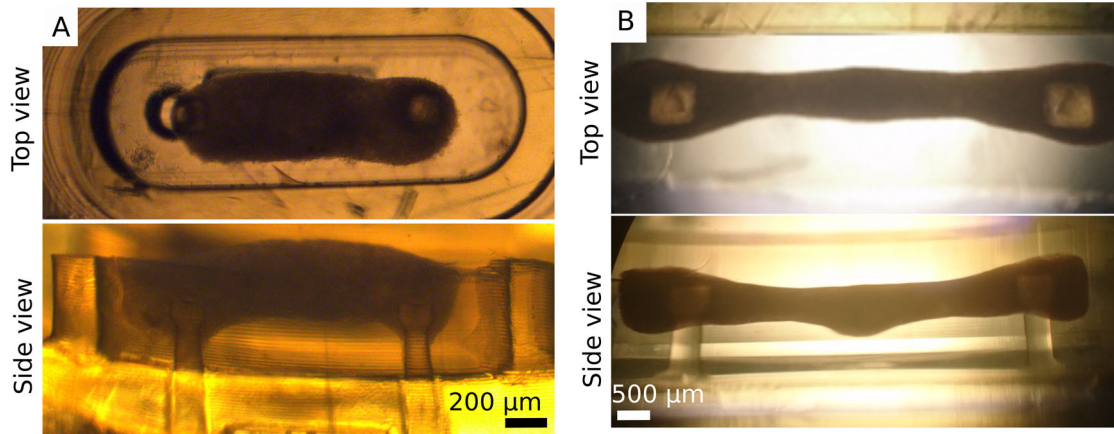


Figure 4.19| Micrographs of compacted cardiomyocyte tissues at day 30 of differentiation in top view and sideview. A) Mini size tissue and B) large-tissue. The engineered cardiac tissues are suspended between the two posts without being stretched. Upon contraction the tissue shortens and hence deflects the posts which applies auxotonic stretching to the tissues.

Live/dead staining of the compacted large-tissues shows clustering of dead cells that are evenly distributed throughout the tissue, Figure 4.20A. However, mostly live cells are present. The thickness of the tissue hinders full visibility to the tissue core. Diffusion distances to the tissue core is more than 100 μm , giving a diffusion distance above the critical distance of diffusion described for engineered tissues¹¹⁹. This could mean that the core of the tissue has a higher cell death than the live/dead staining reveals. Figure 4.20B shows live/dead staining of a mini-tissue with a live/dead pattern similar to that of the larger tissue. Mostly live cells appear with areas of dead cells inside.

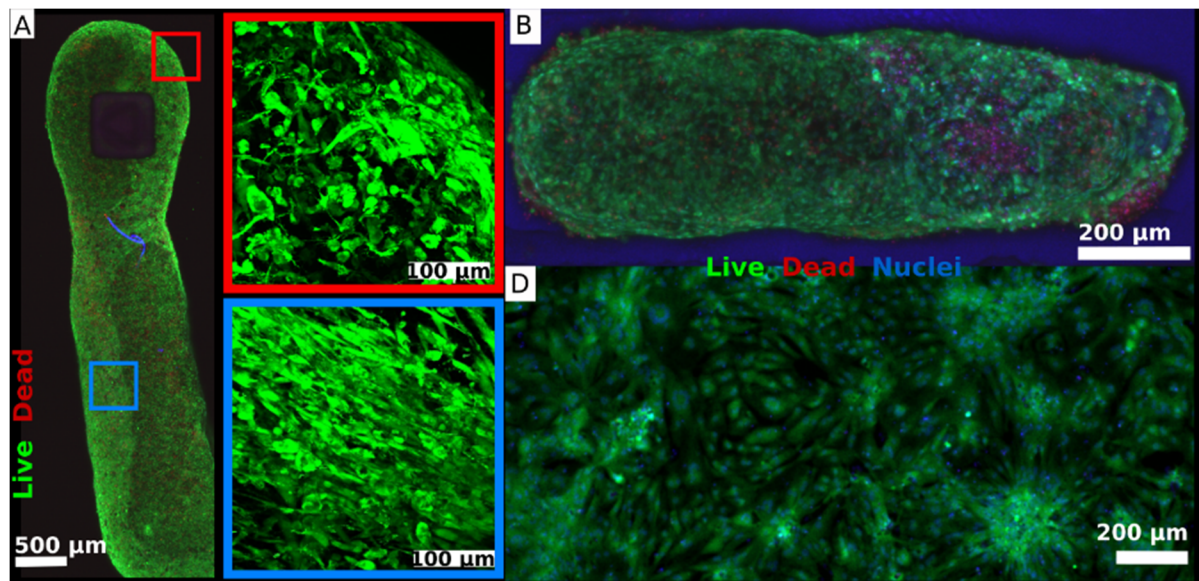


Figure 4.20| Confocal fluorescence microscopy of live/dead staining at day 30 of differentiation using calcein-AM (green) and PI (red). Nuclei are counterstained with Hoechst 34580 (blue) for mini-tissues and 2D cultures. A) Large-tissues show mostly live cells with aggregates of dead cells inside. Enlargement of the edge (red box) and center (blue box) regions show uniaxially elongated cells in the center part expanded between the two flexible posts. Randomized alignment is seen on the edges of the tissue with no stretch elongation (live stain only). B) Mini-tissue at Day 30 of differentiation showing mostly live cells with areas of dead cells near the center of the tissue. C) Live/dead staining of a 2D control. Mostly live cells with cells arranged in attached aggregates. No unidirectional alignment is seen.

The auxotonic stretch that happens during contraction of the tissues being suspended between the two posts results in aligned cells inside the formed cardiac tissues as seen in the blue box of Figure 4.20A. During relaxation engineered cardiac tissues are not stretched between the posts but simply suspended between them. Upon contraction the tissue shortens and the posts deflect causing auxotonic stretching of the tissue. Alignment is seen in the mid-section of the tissues whereas the end shows more randomized cellular structures apparent from the red box Figure 4.20A. This is in correspondence with expected findings described in literature from stretching of engineered tissues between two points¹⁴². Uniaxial alignment of the cells ensure uniaxial force translation in the tissue and thereby a higher contraction force, measured by the movement of the posts. Unidirectional alignment of cells has previously shown to be essential for cardiac tissue maturation into more mature physiologically relevant models^{25,111,143}. Alignment of the hiPSC-CM does not occur spontaneously in 2D as seen in Figure 4.20C.

Engineered cardiac tissues are cryo-sectioned into 20 µm thick slices and immunostained against α -actinin and myosin. Figure 4.21 shows a large-size MAP with defined sarcomere structures and a dense tissue of cells apparent from the density of nuclei. The staining for myosin only reveals an unspecific pattern and should be optimized for further analysis.

However, the striated appearance shown for staining of α -actinin suggests that cardiomyocytes are developing well-defined sarcomeres and are hence maturing inside the PEGDA MAP.

In summary the engineered cardiac tissues are showing synchronized beating, they respond to pacing, show alignment of the cells with defined sarcomeres and have live cells evenly distributed. These results hence suggest that culturing cardiac tissues inside the PEGDA MAPs supports maturation of *in vitro* cardiac tissues and suggests that mini-size and large-size tissues are comparable.

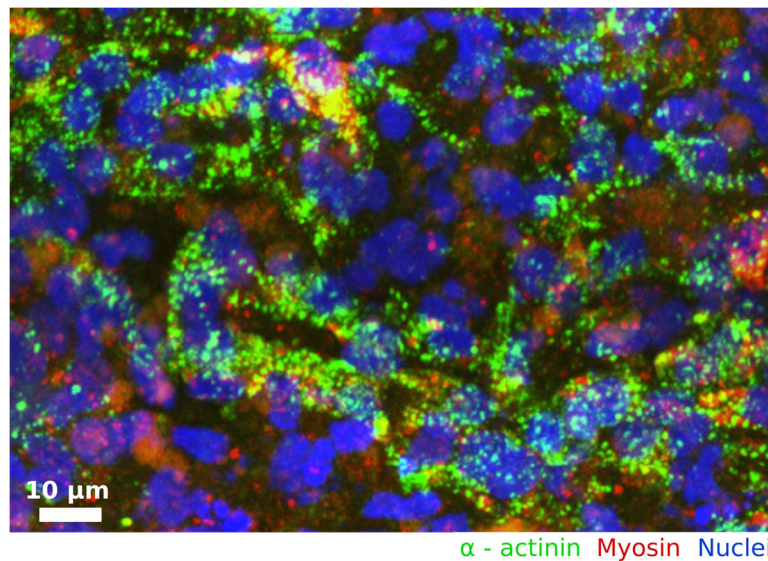


Figure 4.21| Confocal fluorescence micrograph of immunostaining for α -actinin (green) and myosin (red) of a large size engineered cardiac tissue cultured inside a PEGDA MAP for 20 days with 2 weeks of electrical stimulation reveals defined α -actinin in the sarcomeres. Nuclei are counterstained in blue (Hoechst 33342).

4.6.2. Assessment of engineered cardiac tissue maturation using gene expression

Investigating the structural and functional development of the cultured cardiac tissues is assessed by gene expression analysis using quantitative real time PCR (qRT-PCR). The structural genes TNNI1 and TNNI3, encoding for the cardiac troponin I (cTnI) in its immature (TNNI1) and mature (TNNI3) form, are investigated together with the myosin heavy chain immature (MYH6) and mature (MYH7) form. Different ion-channels are also investigated for signs of increased expression over time suggesting more developed cardiomyocytes. Figure 4.22A shows the comparison between cardiac mini-tissues and large-tissue at day 30 of differentiation, normalized to tissues of respective size at day 15 of differentiation. The same behavior is observed for both tissue sizes. Both upregulation of MYH7 and downregulation of MYH6 indicate structural development of the cardiac tissues in agreement with results in Figure 4.20A, that showed elongated aligned cells and with reported finding in literature^{116,144}.

However, for the cTnI, the TNNI1 is upregulated and TNNI3 is downregulated which is unexpected for more mature cardiomyocytes when comparing to literature findings¹⁴⁴.

Comparing an electrically paced large-tissue with an unpaced large-tissue, Figure 4.22B, shows that the structural MYH and ion channels expression are regulated comparably between the paced and unpaced cardiac tissues. The cTnI's (TNNI1 and TNNI3) shows opposite behavior between the two conditions. However, the ratio between the structural MYH7/6 as well as the expression level for the ion channels, show the same regulation pattern. The ratio between mature and immature MYH7/MYH6 and TNNI3/TNNI1 is indicated for easy comparison between the upregulations towards more mature phenotype or reduced maturity.

As overexpression¹⁴⁵ or modification¹⁴⁶ of TNNI1 has previously been described to have a role in increased risk of arrhythmia due to increased sensitivity to Ca^{2+} , these findings might indicate that while electrical pacing has been shown to improve maturity, in some cases⁴⁵, it might also alter the properties of cardiomyocytes. More experiments are needed in order to confirm these findings. However, results shown in Figure 4.22A,B indicate that using electrical pacing as mean of maturation is not a straight forward process.

There are an upregulation of both sodium (SCN5A, $\text{Na}_v1.5$), potassium (KCQN1, $\text{K}_v1.7$) and calcium (CACNAC1, $\text{Ca}_v1.2$) channels in both small-size and large-size tissues, Figure 4.22A. All channels that are important for normal electrophysiological function of the cardiomyocytes¹⁴⁷. However the same trend is not seen in Figure 4.22B where the calcium channel is not upregulated. The same regulation trend is seen for both tissues examined in Figure 4.22B, including the hERG channel (KCNH2, $\text{K}_v11.1$). According to literature upregulation of these genes should be observed in engineered cardiac tissues^{21,45} during culture. Due to the inconsistencies between the experiments shown in Figure 4.22A and Figure 4.22B the development of channel expression is inconclusive and more experiments are needed. Both results, shown in Figure 4.22A and Figure 4.22B, are from single experiments and hence cannot be used to draw conclusions. Comparing results from the two experiments shows a trend towards more mature tissues during culture for 15 days using the PEGDA MAPs.

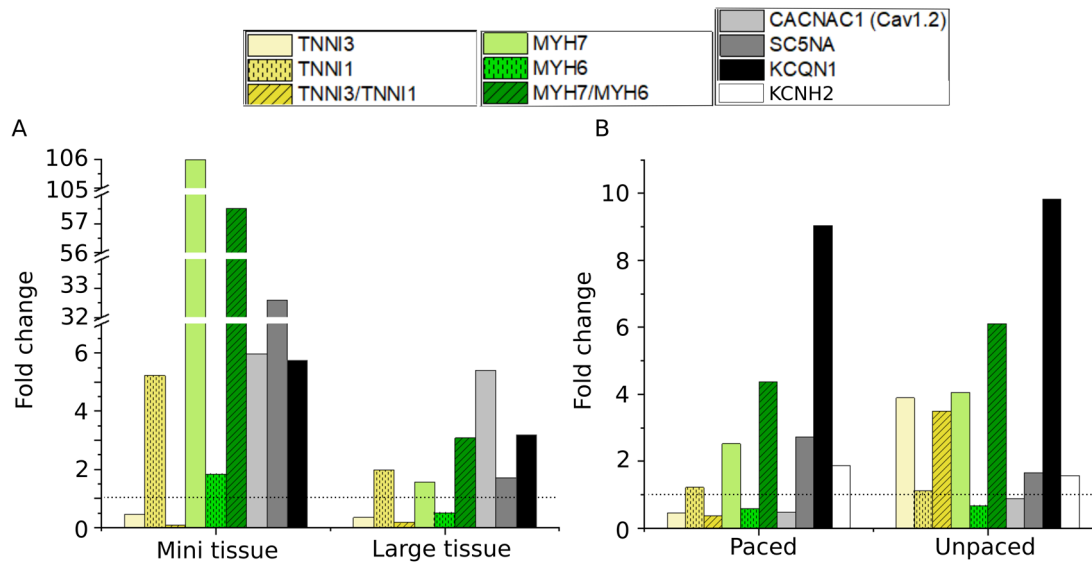


Figure 4.22 | Gene expression analysis comparing selected structural and ion channel genes in engineered cardiac tissues at day 30 of differentiation compared to day 15. A) Comparing mini-tissues and large-tissues at day 30 of differentiation. Same trend in upregulation and downregulation can be seen although the mini-tissues are upregulated considerably more. The KCNH2 is not included due to measurement error from these samples. B) Large-tissues at day 30 of differentiation comparing culturing with applied electrical stimulation (paced) or without (unpaced). Mini-tissues are not available for analysis in the experiment summarized in B), why only large-tissues are compared. Horizontal dotted line indicate no fold change, values above indicates upregulation, values below indicates downregulation.

4.6.3. Characterization of tissue contraction force in electrically paced cardiac tissues

Tissue contraction force is measured on three to five replicates within the same experiment. The force exerted by the cells that is used to deflect the posts is calculated using the Euler-Bernoulli beam theory, explained in section 3.4.1. A camera and lens are used to capture the movement of electrically stimulated engineered cardiac tissues every second day. Custom tracking software based on Lucas-Kanade tracking is developed by Torben Trindkær Nielsen at Sophion Bioscience A/S and used for contraction analysis of the obtained videos, Figure 4.23. The distance between the posts is measured to calculate the post deflection and thereby the contraction force of the cells based on the known stiffness of the posts. Calculated contraction force of the tissues is normalized to the cross-sectional area of the tissue. The cross-sectional area is estimated to be rectangular and calculated from the measured width of the tissue using $h = 0.9w$ based on measured width and height of obtained tissues described in section 4.1. Results can be seen in Figure 4.24.

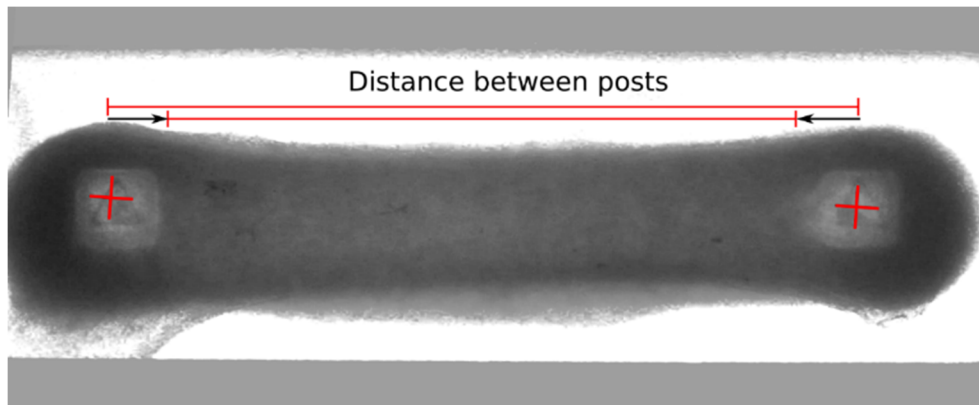


Figure 4.23| Micrograph from the tracked image sequence using the tracking-software. Two markers are tracked, one on top of each post. Using optical tracking, the variation in post distance during the contraction and relaxation of beating engineered cardiac tissues is found by calculating the distance between the two markers. Tissue contraction force is calculated using Euler-Bernoulli beam theory and post stiffness measurements. Engineered cardiac tissues are electrically paced throughout the culture time from tissue compaction. Tracking videos are obtained of electrically paced tissues with a framerate of 8.77 fps.

The contraction force increases over time in correspondence with previous findings, which showed more aligned and elongated cells as effect of time in culture inside the PEGDA MAPs, Figure 4.20A. Mini-tissues and large-tissues display contraction forces per cross-sectional area in the same range. However they follow different timelines of tissue formation and compaction as also indicated by TCR marked in red on the bar graphs, Figure 4.24. Mini-tissues are formed 3 to 11 days after seeding whereas large-tissues form 9 to 16 days after seeding. This indicates that the cell can compact the scaffold in the mini-tissues with more ease compared to large-tissues. Tissue formation time affects the timeline for engineered tissues readiness for drug safety testing with longer culturing times also leading to more handling and ultimately higher cost. Therefore the faster tissue compaction is preferred.

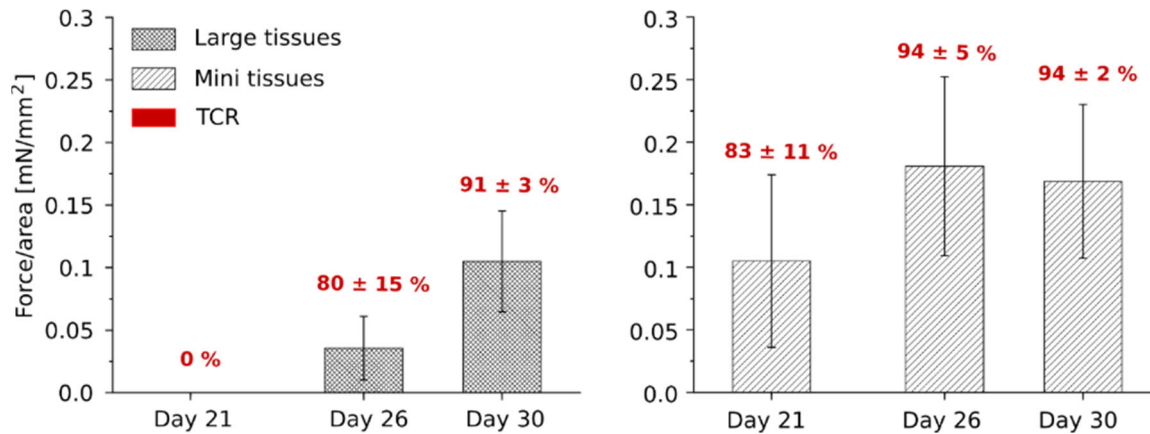


Figure 4.24 | Contraction force for paced cardiac tissues, normalized to cross-sectional area of the tissue. The area is estimated to be a rectangle of $h = 0.9 w$. TCR is measured and indicated in red on the bars. At day 21 of the differentiation, day 11 after seeding, no tissue formation is observed in large-tissues. For both large- and mini-tissues, the force develops over time and increases when tissues are compacting. Replicates from 1 experiment; $n = 3$ for large-tissues and $n = 5$ for mini-tissues. Bars represent the mean contraction force and the error bars are one standard deviation.

The timeline of tissue formation can be seen by comparing two tissues of the same size that form at different timepoints. Two large-tissues are compared where tissue compaction is initiated at day 19 of differentiation and day 26 of differentiation. Tissue formation time influences the force development as seen in Figure 4.25A where the force development for large-tissues are compared at day 30 of differentiation. Both tissues increase their contractile force over time, and are compacted to have approximately the same cross-sectional area at day 30 of differentiation (1.13 mm^2 and 1.15 mm^2 respectively). The tissue formed at day 19 shows a higher force development at day 30 of differentiation suggesting that time of tissue formation is an important factor in functional tissue development. Mini-tissues are comparable to the large-size tissues formed at the same time point. This result fits with the hypothesis that the cardiomyocytes develop and form more cell-cell connections in compacted tissues. An example of a contraction plot for a mini-tissue is seen in Figure 4.25B, also showing that contractions are similar in small-size and large-size tissues. Before engineered cardiac tissues can be used for drug safety screening the tissues must have developed into functional tissues. A longer time in culture will therefore result in more handling and consequently a higher price per tissue. Therefore tissue compaction time is seen as an important parameter for development of engineered cardiac tissues.

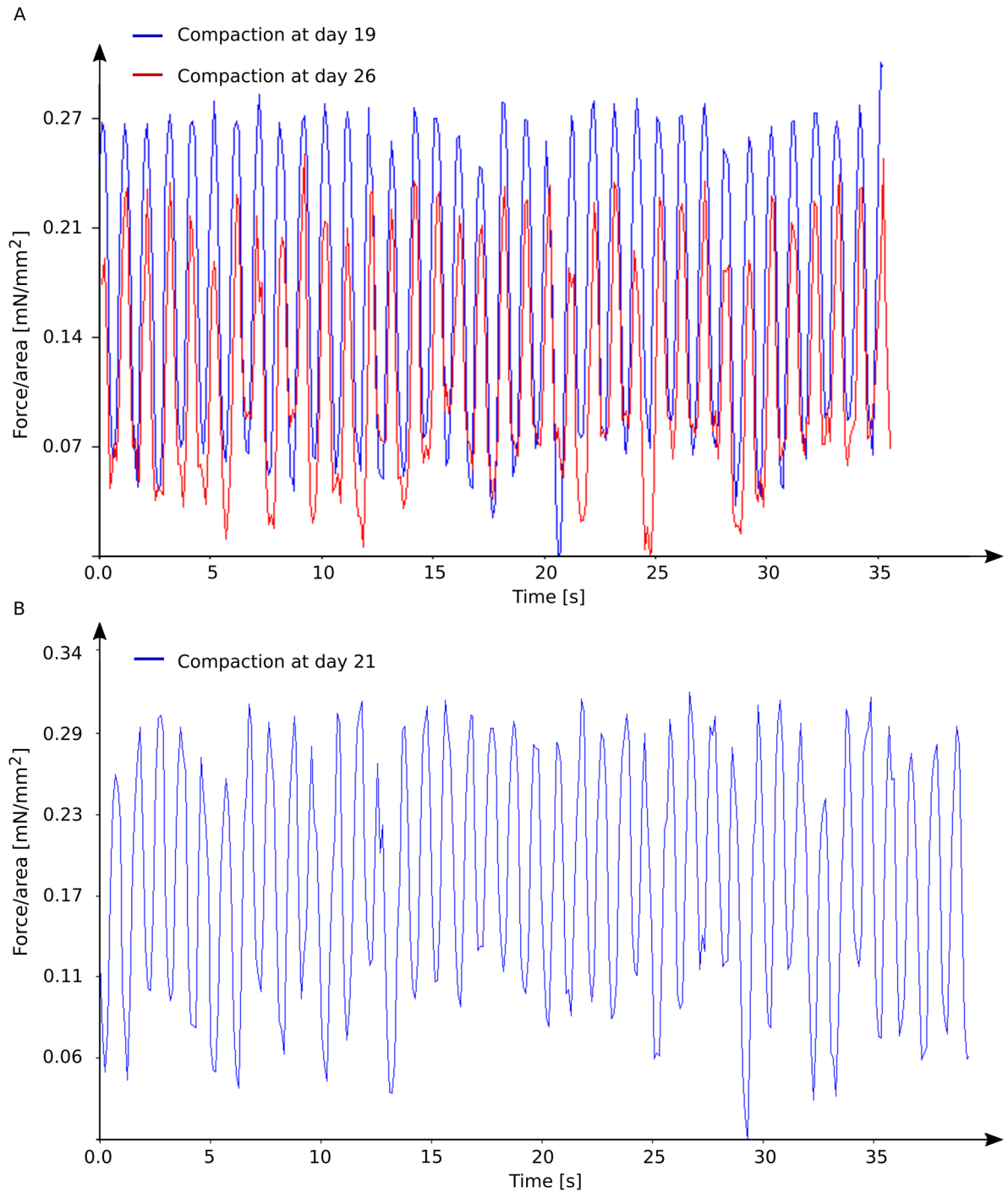


Figure 4.25| A) Overlapping contraction force plot for two large-tissues at day 30 of differentiation. The blue graph indicates contraction from tissue formed at day 19 of differentiation and red graph indicates the contraction from tissue formed at day 26 of differentiation. The mean contraction force for the tissue depicted by the blue graph is 0.21 ± 0.02 mN/mm² and for the red graph is 0.17 ± 0.02 mN/mm² measured by the mean peak-to-peak contraction force. B) Contraction force plot of a representative mini-tissue at day 30 of differentiation showing a similar contraction pattern to the large-tissues. The mean contraction force is 0.20 ± 0.03 mN/mm².

4.6.4. Functional tissue development depends on the environment

Using the contraction analysis software developed by Torben Trindkær Nielsen at Sophion Bioscience A/S, it was possible to measure the tissue contraction of cardiac tissues formed in the stadium shaped MAPs using the three scaffolds shown in Figure 4.11. Contraction force is normalized to cross-sectional area. As shown in Figure 4.11 the tissues formed in collagen consists of a denser packed area of cells in the center of the mold with collagen and cells still being present at the perimeter of the wells. The cross-sectional area of the collagen tissue is estimated based on the dense region of cells in the center of the tissues.

Measurements of tissue contraction revealed that, apart from forming tissues at an earlier time point, the scaffold of GelMA 50 mg/mL seems to provide a basis for higher contraction forces of the cardiac tissues compared to tissues formed in collagen and fibrin scaffolds, Figure 4.26. This suggests that culturing cardiac tissues formed in a GelMA scaffold might be interesting to explore further. Recordings of the tissue contractions are performed at room temperature on spontaneously beating tissues as these tissues were not electrically stimulated. At room temperature, the beat rate of cardiac cells slows down over time which makes the recordings more uncertain than temperature-controlled measurements. All tissues are recorded immediately after extraction from 37 °C and hence comparison can be made between the three scaffolds.

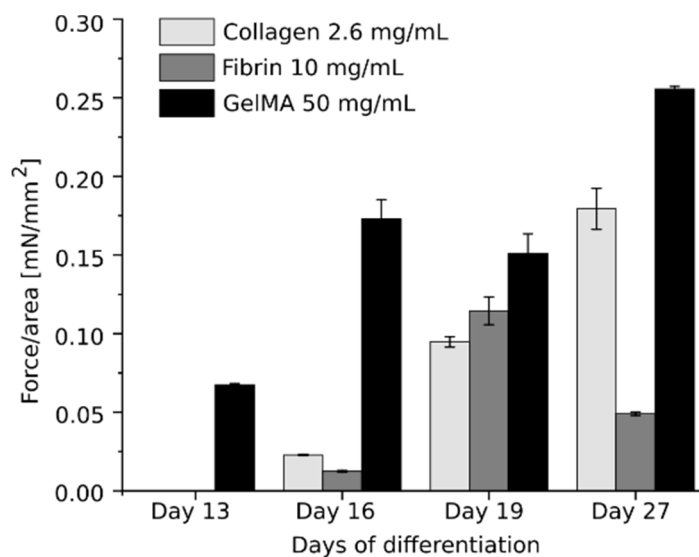


Figure 4.26| Contraction force measurements normalized to cross-sectional area of stadium-shaped tissues formed in different scaffold materials with 45000 cells seeded per tissue corresponding to the “high” cell concentration. Contraction is measured on spontaneously beating tissues at 4 time points from initial tissue compaction and onset of spontaneous beating to termination of experiment. Bars represent the mean of contractions, normalized to the cross-sectional area of the tissue. Error bars represent the standard deviation for the variation of contractions within the same tissue during 20 s to 30 s of spontaneous beating.

4.7. Conclusions

Obtaining engineered contractile tissues inside PEGDA MAPs of molds with different shapes and post designs is possible using the three contractile cell types of mouse and human origin. The designed MAP effectively ensures self-forming tissues with unidirectionally aligned cells and providing auxotonic resistance via the flexible posts. Electrical stimulation of engineered cardiac tissues in different size scales can be performed over 2 weeks of culture, however, the effect of the electrical pacing on tissue development has not been conclusively determined. It is possible to optically track the movement of the posts and thereby determine the contractile force of the cells inside the engineered cardiac tissues. Results presented here indicates that tissues of different sizes have comparable functionality and viability. Contraction force and time for initial tissue compaction seem to be correlated and thus indicates that rapid tissue formation over a few days is favorable for cardiac tissue development and should be assessed as a key parameter for functional formation of engineered cardiac tissues for drug screening purposes to lower the cost of production.

4.8. Experimental details

Experimental details on standard cell culture of 3T3 cells and C2C12 cells, 3D stereolithographic printing, cover glass preparation, optimization of GelMA gelling time, preparation of 3D printed PEGDA molds and live/dead staining are explained in section 3.8. Any deviations to these procedures are incorporated in relevant sections below.

4.8.1. Print settings used for producing PEGDA MAPs

All PEGDA MAPs are produced as described in section 3.8.1. The details of the printing slice thickness, absorber concentration and exposure time for all PEGDA MAPs used in Chapter 4 can be found in Table 4.1.

Table 4.1| Overview of the 3D print slicing thickness, absorber concentration and exposure times used in results presented in Chapter 4.

Design	Slicing thickness	QY concentration	Exposure time
3T3 tissues (section 4.2)			
Stadium shaped PEGDA molds	20 μm	12 mg/mL	3 s
C2C12 tissues (section 4.3)			
Stadium shaped PEGDA molds	25 μm	9 mg/mL	3 s
Oval shaped PEGDA molds	20 μm	9 mg/mL	5 s
Scaffold and cell concentration tests for cardiac tissues (section 4.4)			
Stadium shaped PEGDA molds	20 μm	9 mg/mL	3 s
Oval shaped PEGDA molds	20 μm	9 mg/mL	3 s
Electrically paced cardiac tissues stadium shape (section 4.6)			
Mini-size PEGDA molds	20 μm	9 mg/mL	2.2 s
Large PEGDA molds	20 μm	9 mg/mL	3 s

4.8.2. Surface treatment of PEGDA MAPs

Rhodamine-B labelling on 3D printed PEGDA is performed by using a 20 $\mu\text{g/mL}$ acryloxyethyl thiocarbamoyl rhodamine B (Sigma-Aldrich) solution with 10 mg/mL lithium phenyl-2,4,6-trimethylbenzoylphosphinate (LAP, from Allevi or 900889, Sigma-Aldrich). The solution is added to cover a 3D printed PEGDA block with no surface treatment and UV-A illuminated (330-380 nm, 18 mW/cm²) for 2 min. Another PEGDA block is covered by a solution of 5 mg/mL LAP and UV-A illuminated (330-380 nm, 18 mW/cm²) for 30 min followed by the same Rhodamine-B labelling for 2 min. The two PEGDA blocks are moved to PBS and investigated using a florescent Zeiss Axioskop 40 microscope.

Subsequent surface treatment of PEGDA MAPs is performed by covering the PEGDA block with a 5 mg/mL LAP solution in PBS followed by UV-A illumination (330-380 nm, 18 mW/cm²) for 30 min. The platforms are moved to new sterile well plates and washed with sterile PBS for at least 2 x 2 h to prepare for sterilization and cell seeding.

4.8.3. Preparation of 3D printed PEGDA molds for cell seeding

Sterilization is performed by immersion in 70 % ethanol diluted in MQ water for 10 min, followed by UV-C exposure (254 nm, Mini UV Sterilization Cabinet, Cleaver Scientific) for 10 min under aseptic conditions. PEGDA molds are washed with sterile PBS 3 times after ethanol immersion. At least 2 hours prior to cell seeding, the PBS is exchanged to remove any ethanol residues. Prior to cell loading, the PEGDA molds are gently dried using sterile lint free paper to remove excess water from the mold.

4.8.4. Preparation and gelation of cell seeding scaffolds

4.8.4.1. GelMA

200 mg/mL sterile GelMA (Allevi) is diluted to a final concentration of 50 mg/mL (5 % w/v) or 100 mg/mL (10 % w/v) in cell culture media appropriate for the cell type encapsulated. Photoinitiator LAP is added at a final concentration of 5 mg/mL. For seeding of cardiac progenitor cells, 10 µg/mL fibronectin (F1056, Sigma-Aldrich) is added to the solution. Prepared GelMA solution is mixed with a cell pellet to achieve the desired cell concentration. After dispensing the cell-loaded GelMA into PEGDA MAPs, the GelMA scaffold is crosslinked by using either the light heater box described in section 3.6.1.1 with 20 s exposure time (365 nm, 15 mW/cm²) or by using the automatic dispensing robot described in section 3.6.2 with 120 s exposure time (365 nm, 8.3 mW/cm²).

4.8.4.2. Fibrin

10 mg/mL or 5 mg/mL fibrinogen (F8630, Sigma-Aldrich) containing 0.5 µg/mL aprotinin (A1153, Sigma-Aldrich), 20% (v/v) Matrigel (354277, Corning), and 1.4 % (v/v) 10x medium (RPMI: Sigma R1145, DMEM: Sigma D2429) is mixed to prepare the cell-loading mastermix. The solution should be kept at a temperature below 5 °C to allow subsequent mixing without gelation. Cells are mixed with the mastermix solution in the desired concentration. The cell-mastermix solution is mixed with thrombin (T7513, Sigma-Aldrich) to give a final concentration of 3 U/mL. Mixing with thrombin is performed immediately prior to dispensing as the solution solidifies upon mixing with thrombin. Cell-loaded fibrin scaffold is allowed to fully gel in the PEGDA MAP for 30 min at 37 °C before addition of medium.

4.8.4.3. Collagen

A final concentration of 2.6 mg/mL bovine collagen I (Purecol 5005) with 4.2 mg/mL NaCl (S5886, Sigma), 6.9 mg/mL sucrose (S1888, Sigma), and 1.8 mg/mL NaHCO₃ is prepared and mixed to contain 8 % v/w Matrigel. The pH of the solution is between 7.2 and 7.4. The collagen solution is mixed with cells to obtain the desired cell concentration and allowed to gel for 30 min at 37 °C before addition of medium.

4.8.5. Cell culture of 3T3 cells

3T3 Swiss Albino fibroblasts (ECACC 85022108) are cultured in DMEM high glucose (Sigma-Aldrich) with 10 % FBS (Sigma-Aldrich) and 1 % P/S (Sigma-Aldrich). Cells are split when reaching confluency approximately every third day and reseeded at 1/3 concentration.

4.8.6. Cell culture of C2C12 cells

C2C12 mouse myoblasts (C3H muscle myoblast, 91031101, Sigma-Aldrich) are grown in DMEM high glucose (Sigma-Aldrich) with 10 % FBS (Sigma-Aldrich) and 1 % P/S (Sigma-Aldrich). Cells are split before reaching 80 % confluency and reseeded at 10×10^3 cells/cm². Differentiation medium consists of DMEM high glucose (Sigma-Aldrich) with 2 % FBS and 1 % P/S. Differentiation medium is added 2 days after seeding when differentiation is desired.

4.8.7. Determining cell concentration of 3T3 fibroblasts encapsulated in GelMA

GelMA concentrations of 3, 5, and 10 % (w/v) are tested with 2, 4, 8, 16, and 32×10^6 cells/mL to evaluate suitable cell seeding concentrations in PEGDA MAPs. Cells are encapsulated in GelMA and 50 μ L is seeded inside a standard tissue culture 96-well plate. Gelation is performed by 2 min of UV-A illumination (330-380 nm, 18 mW/cm²) and thereafter cultured with 150 μ L culture medium. Cell aggregation and growth are evaluated over 3 days.

4.8.8. Seeding of 3T3 fibroblasts and C2C12 mouse myoblasts

3T3 fibroblasts or C2C12 mouse myoblasts are encapsulated with 16×10^6 cells/mL in 5 % GelMA. 1.5 μ L cell-loaded GelMA is seeded into the stadium shaped PEGDA molds and gelled using the light-heater box with 20 s exposure time (365 nm, 15 mW/cm²). Medium is added until the cell-loaded MAPs are covered and incubated at 37 °C, 5 % CO₂.

Encapsulating C2C12 mouse myoblasts in a fibrin gel are done by mixing 16×10^6 cells/mL in 10 mg/mL fibrinogen mastermix solution. 1.5 μ L cell-mastermix with thrombin is seeded into the stadium shaped PEGDA molds. After 30 min of incubation at 37 °C, DMEM high glucose with 10 % FBS and 1 % P/S is added to the wells until the platforms are covered. 2 days after seeding, the medium is changed to DMEM high glucose with 2 % FBS and 1 % P/S.

4.8.9. 2D culture and harvesting of cardiomyocyte progenitor cells

Cardiomyocyte progenitor cells derived from hiPSC are received at day 8-9 of differentiation. Prior to shipping the cells, our collaborators at iBET have determined the cardiomyocyte positive cells by flow cytometry to determine cardiac troponin T positive cells to be 79 % - 93 % corresponding to values reported in literature⁹⁹. Cells are cultured in Matrigel (354277, Corning) coated standard tissue culture well plates. Culture medium consists of RPMI 1640 (11530586, Fisher Scientific) with 2 % (v/v) B-27 supplement (15360284, Fisher Scientific). Medium is changed every 2-3 days. Prior to harvesting, 5 μ M of Y27632 (Y0503, Sigma-Aldrich)

is added to the culture medium and incubated for 1 h. TrypLE select (11598846, Fisher Scientific) is used for cell harvesting. Cells are spun down using 180 g for 3 min and medium is gently aspirated to avoid disturbing the cell pellet. Time in suspension is minimized during cell harvest, encapsulation, and seeding and does not exceed 45 min.

4.8.10. Seeding of cardiomyocyte progenitors into PEGDA MAPs

Cells are encapsulated in the respective scaffold and gelation is achieved dependent on the scaffold type as described in section 4.8.4. The cell-loaded scaffold is pipetted into MAP molds after removal of excess fluid using lint free paper. Manual pipetting is used for seeding to better control the seeded volume. Table 4.2 summarizes seeded volumes of cell-loaded scaffold into each mold of varying size and shape.

Table 4.2 | Volume of cell suspension in each PEGDA MAP type platform.

MAP type	Volume seeded (for 1 mold)	Number of cells (15 x 10 ⁶ cells/mL)	Number of cells (30 x 10 ⁶ cells/mL)
Mini-size stadium shaped	1.5 µL	22,500 cells	45,000 cells
Large stadium shaped	80 µL	NA	2,400,000 cells
Mini-size oval shaped	3.5 µL	52,500 cells	105,000 cells

4.8.11. 3D culture of cardiomyocytes inside PEGDA MAPs

After gelation of the cell-loaded fibrin scaffold inside PEGDA MAPs a culture medium RPMI 1640 (11530586, Fisher Scientific) with 2 % (v/v) B-27 supplement (15360284, Fisher Scientific) containing 33 µg/mL aprotinin (A1153, Sigma-Aldrich) is added to inhibit scaffold degradation. Culture medium RPMI 1640 (11530586, Fisher Scientific) with 2 % (v/v) B-27 supplement (15360284, Fisher Scientific) without protease inhibitor is added to GelMA and collagen containing MAPs. After seeding of cardiomyocyte progenitors, the MAPs are left untouched for 3 days to allow tissue formation without introducing fluid shear from handling. From day 3 after seeding, medium without protease inhibitor is changed every 2-3 days throughout culture time by exchanging 2/3 of the medium each time.

4.8.12. Electrical stimulation of engineered cardiac tissues

Electrical stimulation is applied for from day 7 after seeding and continued throughout the entire culture time. MAPs are transferred to sterile 8-well plates (Nunc 167064). Carbon electrode lids (IonOptix C-Dish CLD8WB) are fitted and connected to the custom-built pacing unit. Wells contains 4 mL of culture medium for mini-size MAP and 5.5 mL for large MAPs. Electrical stimulation of 6.7 V/cm with a pulse length of 3 ms is used to pace the engineered cardiac tissues at 1 Hz with a slow reversing pulse of 1.7 V/cm² for 12 ms. Carbon electrode lids are exchanged to a new sterile lid every second day to avoid cytotoxic effects from

electrochemical residues inside carbon electrodes. The lids are washed by immersion in sterile water for 2 x 24 h according to the manufacturer's protocol.

4.8.13. Tests of electrical pacing unit

The tests described here are solely tests performed on the finished pacing unit. Preliminary test and validation that relates to the manufacture of the pacing unit are performed by engineers at Sophion Bioscience A/S and is not reported here.

4.8.13.1. Parameters used to obtain contractile response of engineered cardiac tissues

Cardiomyocyte progenitor cells are seeded into mini-size and large-size stadium shaped molds in a 10 mg/mL fibrin scaffold. On day 5 after seeding, the tissues that have formed are used to assess the voltage and pulse duration needed for the tissues to respond to electrical pacing. Table 4.3 summarizes all settings tested with an indication of tissue response to pacing. Engineered tissues are cultured in standard culture medium and the test is performed in this. The applied voltage must be at 6.7 V/cm in order to obtain a contraction of the engineered cardiac tissue.

Table 4.3 | Engineered cardiac tissue response to electrical pacing (Yes/No) at a range of applied voltages and pulse durations at 0.5 Hz and 1 Hz pacing frequency.

0.5 Hz	Voltage (V/cm)			1 Hz	Voltage (V/cm)		
Pulse duration	5	5.7	6.7	Pulse duration	5	5.7	6.7
2 ms	No	No	No	2 ms	No	No	No
3 ms	No	No	Yes	3 ms	No	No	Yes
4 ms	No	No	Yes	4 ms	No	No	Yes
5 ms	No	No	Yes	5 ms	No	No	Yes

4.8.13.2. Parameter optimization to minimize electrochemical effects

To investigate the electrochemical effects of pacing with 6.7 V/cm and 3 ms pulse a test is performed with and without a slow reversing pulse under an exhaust. In DMEM 6 mL/well an electrical monophasic pulse of 3 ms, 6 V/cm is applied with a frequency of 6.66 Hz for 42 min or 20 Hz for 28 min. In RPMI, a monophasic pulse of 3 ms, 6 V/cm is applied with a frequency of 6.66 Hz for 40 min. In all experiments 2 – 4 wells are paced and an equal number of wells are left unpaced for control. After testing, the medium is observed for color-change and bubble formation indicating electrochemical effects. At the end of testing photographs are taken of the medium in both paced and unpaced wells. The exhaust is removed and the odor of chlorine are noted if present. pH is measured in wells where no distinct color change is seen (pH strips, Merck Universal indicator pH 0 – 14).

Electrochemical effects of pacing with biphasic pulse of 6.7 V/cm and 3 ms pulse and a slow reversing pulse of 1.7 V/cm and 12 ms is investigated by applying the stimuli to RPMI medium for 38 min at 20 Hz and observing changes to medium color and odor. Temperature is measured over 48 h of applying the biphasic pulse at 1 Hz and for 2 h at 20 Hz.

4.8.13.3. Cytotoxicity test

C2C12 mouse myoblasts are encapsulated in a fibrin scaffold and seeded into mini-size stadium shaped MAPs. On the same day, C2C12 cells are seeded into a non-surface treated nunc 8-well plate. 2 days after seeding tissues have formed, and the MAPs are transferred to empty wells in the nunc 8-well plate. A sterile carbon electrode lid (IonOptix, C-Dish CLD8WB) is used and electrical pacing is initiated at 1 Hz using a pulse of 6.7 V/cm for 3 ms and a slow reversing pulse of 1.7 V/cm for 12 ms. Pacing is performed for 5 days in differentiation medium (section 4.8.6) with the carbon electrode lid replaced every 48 h. Cytotoxicity is evaluated by micrographs of the 2D culture and live/dead staining of the engineered tissues using the protocol described in section 4.8.16.

4.8.14. Contraction analysis

During electrical stimulation, the iDS camera software uEye is used to capture videos with a camera (Edmund Optix, EO-3212 LE) and 1x lens mounted on a custom-built three-axis setup to control position and focus. Videos are obtained with a framerate of 8.77 fps. Captured videos are analyzed using the custom built C++ based analysis software using Lucas Kanade tracking (Software developed by Torben Trindkær Nielsen at Sophion Bioscience A/S). Features for optical tracking are manually located by selecting a region of interest (ROI) on the top of each post and an analysis is performed based on mean position from 4 points within each selected ROI. Post deflection is calculated from the distance in pixels between the two points. Deflection distance in μm is calculated based on pixel size and subsequently translated to force using Euler-Bernoulli beam theory and known post stiffness. Posts from mini-size stadium shaped MAPs have a stiffness of 0.22 N/m (± 0.05 N/m) and posts from large stadium shaped MAPs have a stiffness of 1.9 N/m (± 0.24 N/m) determined as described in section 3.8.8. Contraction force is normalized to force per cross-sectional area. The cross-sectional area are assumed to be rectangular and estimated by measuring the width of the tissue in three places and assuming $h = 0.9w$. The mean tissue width is used.

4.8.15. Quantitative real-time polymerase chain reaction (qRT-PCR)

Engineered tissues are extracted from the PEGDA MAPs by gentle pipetting to avoid PEGDA residues in the extracted RNA. High Pure RNA isolation Kit (Roche) is used to extract RNA. Using the provided lysis buffer, it is necessary to pipette the tissues until full dissolution is obtained and RNA extraction can then be achieved using the manufacturer's protocol. RNA

concentration is measured by spectrophotometry using a Nanodrop 2000 spectrophotometer (Thermo Fisher).

cDNA is prepared using Transcriptor High Fidelity cDNA Synthesis Kit (Roche) for 50 ng RNA. RNA and Anchored-oligo(dT)₁₈ primer are denatured by heating for 10 min at 65 °C (Biometra T3 Thermocycler) and mixed with Transcriptor High Fidelity Reverse Transcriptase Reaction Buffer, Protector RNase Inhibitor and Deoxynucleotide Mix, Dithiothreitol (DTT) and Transcriptor High Fidelity Reverse Transcriptase following manufacturer's protocol. The mix is incubated at 55 °C for 30 min followed by 85 °C for 5 min (Biometra T3 Thermocycler).

Gene expressions are quantified by qRT-PCR using TaqMan (Thermo Fisher) primers listed in Table 4.4 and LightCycler 480 Probes Master (Roche) on a LightCycler® 480 Instrument. Briefly, a 10 µL reaction is prepared by mixing 2.5 µL of cDNA with 2 µL PCR grade water, 0.5 µL TaqMan Gene Expression Assays (20x) and 5 µL TaqMan Universal Master mix (2x). The LightCycler program is as follows: 10 min preincubation at 95 °C followed by 40 cycles of amplification with 15 s of denaturation at 95 °C and 1 min for annealing at 60 °C. Extensions follows for 5 min at 72 °C.

All compared samples are prepared simultaneously in a 384 well plate in triplicates and prepared with no direct light. Results from the cycle threshold (CT) are normalized using the $\Delta\Delta CT$ method, assuming full reaction efficiency, with the housekeeping genes glyceraldehyde-3-phosphate dehydrogenase (GAPDH) and ribosomal protein lateral stalk subunit P0 (RPLP0). For both mini-size and large- cardiac tissues, day 15 tissues are used as reference samples. Mini-size and large-tissues are from one experiment and are analyzed from one cycle-run. Large-tissues paced and unpaced are likewise from one experiment and prepared from one cycle-run. Statistical data are therefore not available.

Table 4.4 | Target genes and primer identification (TaqMan, Thermo Fisher)

Target	Primer identification
GADPH	Hs99999905
RPLP0	Hs99999902
MYH6	Hs01101425
MYH7	Hs01110632
TNNI1	Hs00913333
TNNI3	Hs00165957
SCN5A	Hs00165693
CACNA1C	Hs00167681
KCQN1	Hs00923522
KCNH2	Hs04234270

4.8.16. Live/dead staining

Cell viability is evaluated by confocal imaging on a Zeiss LSM700 with either a 10x, 0.25NA, or 5x, 0.13NA, epiplan neofluar objective. Fibrin encapsulated tissues are stained for 1 h with 2 $\mu\text{g}/\mu\text{L}$ Calcein AM (15560597, Fisher Scientific), 4 $\mu\text{g}/\text{mL}$ propidium iodide (PI; 81845, Sigma-Aldrich), and 2 $\mu\text{g}/\text{mL}$ Hoechst34580 (H21486, Invitrogen). After incubation, tissues are washed in pure DMEM high glucose medium. Excitation is performed at 405 nm, 488 nm, and 555 nm for Hoechst 34580, calcein AM, and PI, respectively.

4.8.17. Immunohistochemistry

Mouse myoblast tissues are handled as previously described (see appendix 2)⁸¹. Engineered cardiac tissues are cryopreserved by fixation in 4 % PFA for 30 min followed by washing for 2 x 30 min. Dehydration is performed gradually by submerging in 1 % PEG (MW 10000 g/mol) (0263, Roth) at 4 °C for minimum 6 h followed by 10 % PEG (MW 10000 g/mol) at 4 °C for minimum 12 h. Samples are placed in metal cryo-molds and covered in Tissue-Tek OCT medium (4583, Sakura) and incubated for 1 h at RT. Samples are frozen by placing the metal cryo-molds in isopentane chilled on liquid nitrogen. The isopentane does not come into contact with the OCT medium. Immediately after freezing the samples are transferred to -80 °C until cryosectioning is performed. Samples are sliced in 20 μm thick slices using a cryostat (Leica 3050) at -20 °C.

Immunostaining is performed to analyze cardiac tissue specific antigens α -actinin, and myosin light chain. For this purpose, sections on slides are first permeabilized and blocked in 0.2 % Triton X-100, 2 % BSA (A9647, Sigma) and 5 % horse serum solution in PBS for 1 h. Slices are then incubated with primary antibodies of mouse monoclonal anti- α -actinin (1:200, A7811, Sigma) and rabbit polyclonal anti-myosin (1:100, ab79935, abcam) O/N at 4 °C, followed by incubation with secondary antibodies of anti-mouse IgG and anti-rabbit IgG for 2 hours at RT in dark. Then, nuclei are counterstained with Hoechst 33342 (2 $\mu\text{g}/\text{mL}$ in PBS, Fisher Scientific) for 10 min and the slices are immediately covered with a cover slip in antifade mounting medium (H-1000, Vectashield) and sealed with nail polish. The slices are analyzed by using a CSU-W1 spinning disc confocal microscope (Nikon Ti2/Yokogawa) using 60x objective with immersion oil with excitation at 405, 488, and 560 nm for Hoechst 33342, FITC and rhodamine, respectively.

Chapter 5

Discussion

5.1. Development of a microenvironment to promote tissue formation

The presented stereolithographic 3D printing method enables fast and reproducible production of mechanical micro-features to enhance tissue formation in a manner that cannot be achieved by conventional casting and molding techniques using cell-compliant, flexible materials. Fixed position of the tissues, at uniform height, ensures reliable force read-outs based on a horizontal view of the post displacement that cannot be achieved using posts without mechanical cues for tissue positioning. Side views of engineered muscle tissues confirm the positioning around the mechanical cues. Using casting methods, the production of delicate features to secure tissue position has also been reported in previous works^{45,130} but requires extensive preparation time for each platform when tissue positioning is not secured by up-side down encapsulation around the posts as seen in some work²⁵. The reusability of the flexible, casted molds for production of delicate structures and the success of recovery for extraction of the platform from the molds have not been reported. However, the production time per platform, even with reuse of casting molds, exceeds that of 3D printing using projection stereolithography. Other tissue engineering platforms for drug safety screening that rely on stereolithographic printing⁵³ do not take advantage of the design flexibility offered and hence do not control tissue positioning. Using SLA single-tissue platforms, “bio-bots” have been developed⁵⁴ that form tissues between enlargements, using free-floating locomotion for read-out. While this technology demonstrates functionality response and can be used to study functional behavior, it is unsuitable for upscaling for use in drug safety screening.

The mold and scaffold material interactions are important in the tissue formation process to allow the scaffold to be compacted by contraction of the cells. Due to the acrylate bonding between the PEGDA mold and the scaffold material GelMA, a post-treatment of the PEGDA mold is required to prevent a chemical interaction between mold and scaffold. Post-treatment of the cell seeding molds was not previously described in literature for PDMS and hard plastic molds. The addition of post-treatment steps extends the preparation process of the mold for cell culture and hence total manufacturing time, thereby reducing the fabrication advantage to other methods when using GelMA as a scaffold material. However, post-treatment can be performed in parallel for many platforms and the overall process is therefore estimated to be superior in fabrication time compared to traditional casting methods.

One of the critical aspects of tissue formation is to promote cell-cell formations to adequately construct an *in vitro* tissue instead of a fixed mass of single cells embedded in a scaffold material

with defined shape. Tissue formation and cell elongation are obtained by the auxotonic resistance of the flexible posts as seen from the C2C12 mouse myoblast tissue where cells elongate unidirectionally between the posts. Cells are allowed to elongate and fuse together to form myotubes thus confirming the effect of the designed posts to aid in tissue formation. Similar results have been shown for myoblast differentiation using human myoblasts encapsulated in a fibrin scaffold¹⁴⁸, also using the flexible post approach. The shape of the posts seems to influence the tissue shape, with cylindrical posts achieving narrow engineered tissues with uniaxially aligned cells^{81,102}, and rectangular posts result in wider tissues with cell elongation being more diagonal between opposite post corners^{53,54,97}. While both post geometries result in viable, functional engineered muscle tissues, cylindrical posts appear to result in thinner tissues without thinning around corners due to local stresses.

5.2. Characterization of device functionality

Engineered muscle tissues consisting of either mouse myoblasts or hiPSC derived cardiac progenitor cells show the ability to form around the posts as described previously and deflect the posts upon contraction. Cells develop inside the PEGDA MAP to form cell-cell contacts, thereby giving a functional muscle tissue. Similar results have been described for human myoblast differentiation in a fibrin scaffold, also using flexible posts¹⁴⁸. A functional device with functional response analysis, based on post deflection from tissue contractions relies on trustworthy post stiffness determination. The stiffness is highly dependent on size and geometry as apparent from the Euler-Bernoulli beam theory. Stiffnesses of posts in this work are determined and are consistent with literature values of flexible posts comparable in size. The stiffness of the cylindrical PEGDA posts of 150 μm in diameter and 850 μm in height are found to be 0.2 N/m, while posts of 500 μm in diameter and 2.2 mm in height have a stiffness of 2 N/m. For comparison, rectangular PDMS posts of $W \times D \times H = 200 \mu\text{m} \times 500 \mu\text{m} \times 700 \mu\text{m}$ have been reported to have a stiffness of 14 N/m⁵⁰ whereas rectangular PDMS posts of $W \times D \times H = 163 \mu\text{m} \times 33.2 \mu\text{m} \times 199 \mu\text{m}$ have a stiffness of 0.4 N/m⁹³.

Determination of the degree of swelling and shear modulus has only been determined for one exposure time, slicing thickness, and absorber concentration. Changes to any of the parameters will lead to a change in the network formation within each layer or between layers. In this work the designed dimensioned was not offset prior to printing to obtain dimensions desired dimension as has been described for similar work using 40 % PEGDA MW 700 g/mol⁵³.

The mechanical characteristics of the PEGDA hydrogel may change when the print settings are varied which has been done in experiments presented in this work. However, a change in overall mechanical properties will also change the stiffness as it is directly dependent on the mechanical properties. Within the print settings used in the presented work, the 20 % w/v PEGDA hydrogels are similar in mechanical properties which is seen from the post stiffness measurements. Posts with the same diameters produced with minor modifications to geometry

or print settings are similar in stiffness and close to the expected theoretical value. These results are also consistent with previous reported values of the shear modulus of 20 % w/v PEGDA with MW 700 g/mol. However¹²⁹, changing the print parameters more drastically will likely lead to more significant changes in the stiffness and swelling behavior. In such cases, more mechanical measurements should be performed in order to assess the changes to the network formation. This work shows that the biggest influence on stiffness of cylindrical posts is the post diameter.

5.3. Development of engineered cardiac tissues

Achieving mature cardiac tissues in a short timescale of weeks is advantageous both for cost and laboratory space. In previous studies, it was determined that culturing cardiomyocytes in engineered cardiac tissues is advantageous over 2D culturing as this technique obtains a higher maturity level in a shorter timespan¹⁴⁹. Results from the work presented in this thesis have shown that it is possible to achieve engineered cardiac tissues with increasing functional characteristics over time, measured by increased contraction force. Contraction force are normalized to cross-sectional area of the tissues, with the assumption of a rectangular cross-section that has also been used previously⁵³. The contractile forces found for both mini and large size engineered cardiac tissues are in the same range as reported in literature^{35,41}. Reported values span over a wide range and are reported in both force per cell and force per cross-sectional area. However, it seems that the size of the tissues does not influence the contractile force when normalized to cross-sectional area. The tissues can therefore be produced down to mm size without compromising functionality. Hence, usability of engineered cardiac tissues for drug safety screening increases due to lower cost per tissue.

The maturation level of the engineered cardiac tissues presented in this study is based on the ability to develop a higher degree of maturation inside PEGDA MAPs. Maturity is measured based on improved expression of cardiac markers, development of cell-cell connections seen by synchronous beating of the tissues, responsiveness to pacing, and cellular alignment from initial tissue formation at day 15 of differentiation. The results from these experiments show that engineered cardiac tissues are able to improve cardiac characteristics over time in culture which is also reported in literature¹⁰². The state of maturity is inconclusive due to the lack of statistical data. However, results suggest that by pursuing this mold design and culture tissues will be comparable to other engineered cardiac tissues presented in literature in terms of presence and upregulation of structural markers⁵³ and contractile response³⁵. Immunostaining of an engineered cardiac tissue shows the formation of sarcomere units of the cardiac tissue after 2 weeks of culture. The response to electrical pacing together with simultaneous contractions of unpaced tissues indicate the development towards more mature tissues containing cell-cell connections. The maturity of presented cardiac tissues at this time is not comparable to some of the more advanced maturation of engineered cardiac tissues that have been presented^{45,102}. However, these results suggest that this method can be used for further

maturation of cardiac tissues. The cellular alignment of cardiomyocytes can aid the development of a functional *in vitro* syncytium with unidirectional force development which in turn benefits the visual read-out of post displacement.

As a method to evaluate the tissue formation properties, the tissue compaction ratio (TCR) has been introduced to offer a quantitative measure of the formed tissues. The TCR is non-invasive and can be used to evaluate tissue status during culture. TCR is based on the assumption of full cell-to-cell compaction without including scaffold material or potential proliferation of non-cardiomyocytes inside the tissues. Despite the uncertainties associated with these assumptions, the TCR has shown to be a valuable measure of the state of the tissue formation and correlates well with prediction of tissue contraction force.

5.4. Improving robustness of engineered tissues

The ability of engineered tissues to form and remain intact is important for usability. Robustness of the engineered tissues has not been studied to the full extent, although scaffold optimization and cell seeding densities have been investigated to obtain engineered tissues that are well-defined and can be cultured for 30 days. Previous studies have shown that using co-culture of fibroblasts and endothelial cells^{95,111,150,151} enhances cardiac tissue formation. During prolonged culture times, the scaffold of the engineered tissues will degrade and poses a risk for the tissue robustness⁴². The scaffold material will degrade due to proteolytic activity of enzymes secreted by the cells. Therefore a proteolytic inhibitor is often used in tissue engineering^{73,102}, including this work, to slow down the degradation process. Co-culture of fibroblasts has been shown to improve initial tissue formation as they assist in scaffold remodeling^{95,111} and to help improve cardiac viability by counteracting the effects from delayed scaffold remodeling. Further, co-culturing with fibroblasts can improve tissue strength due to the secretion of ECM components¹¹¹. Improving tissue robustness by seeding of cardiac bodies by pre-culturing cardiomyocytes in aggregates has been shown to improve tissue strength and reduce necking compared to seeding single cells¹¹¹. Future studies using PEGDA MAPs could benefit from using co-culture of cardiac fibroblasts as well as using cardiac bodies for cell seeding instead of single cells to both improve scaffold remodeling, tissue compaction, and sustainability.

Culture time of engineered cardiac tissues is dependent on the ability to achieve mature tissues. Previously reported times to achieve mature cardiomyocytes vary greatly and extend up to 8 months of culture⁹⁴, why it is relevant to consider the maturity level needed to show relevant functional response and to consider the robustness of tissues over long-term cultures. In literature, a guide-wire has been introduced where the tissue forms around a surgical wire¹⁴¹. This design is not based on the flexible post approach but rather uses a horizontally expanded wire to guide the tissue formation and support tissue structure. This design type might have an advantage over the flexible post design with regard to scaffold degradation because the wire

functions as a mechanical support inside the tissues. One of the challenges of engineered tissue formation using post-based designs is robustness of the tissues and ability to resist the tensile stress and avoid breaking¹³⁸. In this work, the possibility of incorporating additional design features to promote tissue support during long-term culture has been assessed by fabricating micro features down to 30 μm to function as non-degradable support during long-term tissue culture (results are shown in Appendix 1). It is shown that micro-features for tissue support during long term culture can be produced using the presented stereolithographic 3D printing method. However, these designs have not been adequately tested. More work is needed in this field to fully assess the possibilities of incorporating flexible structures inside tissues while maintaining the flexible post functionality.

5.5. Readiness level and competitor evaluation

Obtaining engineered cardiac tissues for cardiac safety screening is a growing field and many similar construct designs have been presented in recent years. A common property of the engineered cardiac tissues presented in literature is their responsiveness to known proarrhythmic drugs measured under electrical stimulation^{21,45,94,100,152}. Existing commercial products that resemble the intended application of use for engineered cardiac tissues are based on planar fluidic systems^{153–156}. Commercial fluidic systems are largely compliant with existing laboratory systems and therefore have an advantage in terms of their user readiness level. Despite the similarity in intended use for commercial products, the technology significantly differs from engineered tissues and hence these systems lack the 3D functionality, why comparison against other engineered cardiac tissues described in literature is more relevant. Table 5.1 describes the most profound advantages and disadvantages to current systems described in the literature.

The usefulness of engineered cardiac tissues compared to their commercial microfluidic organ-on-a-chip counterparts relies on the user-friendliness which again depends on the full system availability. This work focuses primarily on the formation of engineered cardiac tissues by engineering a mechanical microenvironment that promotes tissue formation. However, usefulness also relies on complementary equipment for use in functional read-out and analysis. Whether a final end-user product adds value to the end user depends on the readiness level achieved. If the user-friendliness of the system is low, it will have low value at the end-user site. Despite low technological readiness levels, engineered cardiac tissues will still be applicable for use, however, the market model will differ accordingly. A low technological readiness level will result in more end-user training required or in using the engineered tissues as an in-house service instead of commercialization of the product. To obtain a user-friendly product the engineered cardiac tissue must enable easy read-out to optimize the interface with surrounding analysis systems and achieve an efficient, user-friendly system. Having an easily accessible

optical read-out possibility, as the one in the presented PEGDA MAPs, allows such integrations and hence facilitates the way to market for engineered cardiac tissues.

Table 5.1| Summary of advantages and disadvantages between the proposed engineered cardiac tissue design presented in this work and literature equivalents.

	Advantages	Disadvantages
Tissues in PEGDA MAPs	<p><u>Low cost</u> manufacturing due to a reduced number of cells and inexpensive materials.</p> <p><u>Controlled positioning</u> of engineered tissues results in higher accuracy of the calculated force from displacement read-out.</p> <p><u>Scalable</u> to industrial needs.</p>	<p><u>No demonstration</u> of drug response analysis.</p> <p>Current biological characterization is <u>missing statistical significance</u> and the culture method needs optimization.</p>
Tissues reported in literature ^{21,45,100}	<p>Some has shown <u>advanced maturation</u> and functional characteristics</p> <p><u>Response to selected drugs</u> shows promising results with expected properties.</p>	<p>High number of expensive cells <u>increasing the cost</u> per data-point.</p> <p>Material choice or production methods can prove <u>challenging</u> for industrial use and upscaling.</p>

Chapter 6

Conclusions and outlook

6.1. Conclusions

The aim of this work has been to develop a multiassay platform (MAP) for cell seeding with microenvironments based on a novel fabrication method using a compliant non-toxic material. MAPs should promote tissue formation and allow maturation of engineered cardiac tissues and are intended for use in cardiac drug safety screening to assess risks of adverse effects of pharmaceutical agents in preclinical testing.

In summary, this work has successfully resulted in the design and production of a multiassay platform using stereolithographic 3D printing in the synthetic polymer PEGDA. Stereolithographic printing offers fast and reproducible manufacturing of the platforms compared to conventional casting techniques making it suitable for industrial purposes. Developed MAPs contain vertical flexible posts with mechanical cues on top that promote *in vitro* tissue formation positioned at a fixed vertical height and ensure reproducibility. Optical markers and calibration features have been incorporated into the MAPs with designs down to 30 μm although feature sizes of 50 μm and above shows better geometrical print accuracy. Constructed features are tested initially after printing as well as after swelling and compared to the designed dimensions to assess the ability of the stereolithographic printer to produce delicate features with high precision. Both indentations and protrusions have been investigated. In summary, swollen dimensions are more robust in extrusions and support the designed approach to use mainly protrusion based features.

By simultaneously producing up to 20 molds for cell seeding the stereolithographic approach shows the ability to produce tissue culture units in quantities that are suitable for use in drug safety screening to provide more data-points without increasing time to manufacture. The ability to automatically seed cell-loaded scaffold into the molds suggests that this setup can minimize manual handling and thereby increases the ability to use this technology in an industrial setting. The size of the molds has been designed to produce tissues down to 1 mm in length and thereby limit the costs per tissue from a reduced number of cells which makes this technology inexpensive compared to competitor products and thus desirable to use.

PEGDA MAPs are designed to allow a simple read-out of post deflection by capturing images in a top-view. Mechanical properties of the flexible posts are determined to facilitate subsequent read-out possibilities by optically measuring the deflection from a 2D view of the top of the posts. Stiffness of the posts has a low variation and can be used to calculate the resulting

contraction force of the tissues using the Euler-Bernoulli beam theory. Degree of deflection is closely correlated to the geometry and size of the posts. Thereby the stiffness can be modified without major design changes and enables this design to be used for cells with various contraction forces.

Quantification of the tissue formation has been assessed by introducing the tissue compaction ratio (TCR) which uses the size of a tissue, calculated from a 2D image, to correlate the degree of contraction with the cells' ability to remodel the scaffold. The TCR has shown a correspondence with the contraction force with a higher tissue compaction ratio also showing a higher force read-out for the tissue in scope. Contraction force seems to be dependent on the time of tissue formation after seeding and the scaffold material used, indicating that choosing the right scaffold is a key element of cardiac tissue formation.

Engineered tissues contain healthy viable cells that are capable of growing or developing dependent on the cell type used. C2C12 mouse myoblasts cultured inside PEGDA MAPs shows formation of multinucleated myotubes uniaxially elongated between the flexible posts. Culture of hiPSC-derived cardiomyocyte progenitor cells for 2 weeks in PEGDA MAPs reveals viable cells with a uniaxial elongation and overall improved cardiac genetic characteristics at day 30 compared to day 15 of differentiation. Defined cytoskeletal structures with immunofluorescence micrographs showing visible striations indicate development of organized sarcomeres. Spontaneous beating of the tissues shows synchronized cells indicating cell-cell connections. The contraction force of the engineered cardiac tissues can be determined by optical read-out of post displacement during electrical stimulation thus enabling functional analysis of the cardiac tissues, which can also be used for subsequent drug testing to detect inhibition of electrical conductive properties.

In summary, this work shows the possibility to produce a cell seeding platform with micro features that promote formation of engineered contractile tissues using a novel fabrication method based on stereolithographic 3D printing in a compliant synthetic hydrogel material. Seeding of cardiomyocyte progenitor cell-loaded hydrogel scaffolds with muscle mimicking stiffness results in the formation of engineered cardiac tissues. Upon extended culturing time it is possible to show improved biological development by upregulation of cardiac specific genes and improved functional characteristics measured by contraction force that are determined by the tissues' ability to deflect the integrated flexible posts. Deflection can be easily determined by optical read-out hence confirming the suitable response analysis of the platform.

6.2. Outlook

The presented work around formation of engineered cardiac tissues explores a rapidly developing field where the technology for formation of molds is still developing and the characterization methods of achieved cardiac tissues are still not well defined.

6.2.1. Validation of cardiac tissues by functional and biological characterization

This work has shown the possibility of achieving engineered cardiac tissues by producing a platform that enables simultaneous formation of up to 20 tissues in parallel. Obtaining information on drug testing and biological assessment is a key aspect of evaluating engineered cardiac tissues. Future work should therefore focus on obtaining more data for statistical significance on the biological assessment including contraction force read-out, gene expression, cellular connections, and structural evaluation using immunostaining and electron microscopy.

Functionality of the engineered cardiac tissues by evaluating tissue response on exposure to known torsadogenic and non-torsadogenic drugs is a natural continuation of the work presented here. Such testing is essential in order to conclude on the usability of the proposed design to result in a testing platform for drug safety screening. Hence, it is crucial that future work on this system includes drug-testing with said drug types.

6.2.2. Engineered cardiac tissue formation

Most reported engineered tissues are initially embedded in the hydrogels fibrin or collagen, which have also been used in this study. As seen in Figure 4.26, the GelMA scaffold with fibronectin seems to be a promising candidate to form engineered cardiac tissues with a substantial contraction force which will aid in achieving a functional optical read-out. The GelMA scaffold was not further investigated. Future studies to optimize and characterize engineered cardiac tissues in PEGDA MAPs could benefit from the inclusion of GelMA as a cell seeding scaffold. Both fibrin and collagen protocols include the use of matrigel which is known for its ability to alter differentiation of stem cells¹⁵⁷. Further, due to the animal origin, matrigel constitutes an obstacle for regulatory approval. GelMA can be produced from human collagen and can be used without the use of matrigel which makes it an obvious candidate for further study of engineered cardiac tissues. Seeding and handling of engineered tissues will benefit from using GelMA due to the light-initiated fast gelation. As fibrin and collagen uses 30 min for gelation prior to addition of culture medium there is a risk that the PEGDA MAPs dries out in the areas not covered by aqueous medium leading to micro fractures in the network. As gelation of GelMA happens within seconds to minutes, culture medium can be directly added with no prior incubation. Independently of the seeding scaffold used, it is valuable to investigate the degradation-rate of the scaffold to avoid premature degradation and ensure adequately formed cell-cell connections.

6.2.3. Maturation of engineered cardiac tissues

Although previous studies have successfully shown promising results by using a variety of pacing modes⁴⁵, it is also well-known that electrical pacing can be harmful to cardiomyocytes^{24,119}. Using electrical stimulation of cardiomyocytes to induce higher degree of

maturation in engineered cardiac tissues must be carefully considered. While engineered tissues cultured in PEGDA MAPs are functional after 2 weeks of electrical stimulation, further studies are needed to fully understand the effect of long-term pacing of cardiomyocytes. Mechanical stimulation has been used by introducing auxotonic stretch. It has also been demonstrated that it is possible to make a cyclic mechanical actuator to exercise engineered muscle tissues; however, this has not been implemented. Others have shown that using cyclic mechanical actuation obtains similar maturation degrees when used on its own compared to using mechanical and electrical stimulation in combination¹¹³. Due to the risk of compromising cardiomyocyte viability when using electrical stimulation, cyclic mechanical actuation might be suitable for maturation of engineered tissues in PEGDA MAPs.

The physical stimulation methods to obtain a higher maturation degree may also be combined with metabolic maturation which has shown to increase cardiomyocyte maturation on its own³⁶. A combination of physical and chemical maturation might be the key to obtain functional maturation without risk of damaging the engineered tissues by electrochemical effects or overstretching the cells.

6.2.4. Potential applications

The use of stereolithographic printing is becoming a more popular method for production of molds and other support-structures needed in tissue engineering^{53,54,129} to determine the shape of the resulting tissues. The ability to design a wide range of structures for different purposes makes the proposed technique useable for a wide range of applications not exclusively for muscle cells although the specific proposed design has been optimized for contractile cells types. The flexible posts can easily be modified in stiffness and used to study the dependence of stiffness on muscle tissue development. Such design flexibility opens the possibility for this system to be used not only for drug safety testing but also for studying on muscle tissues based on patient derived cells or stem cells to gain knowledge in specific patient disease as well as disease models.

References

- (1) Stockbridge, N.; Morganroth, J.; Shah, R. R.; Garnett, C. Dealing with Global Safety Issues: Was the Response to QT-Liability of Non-Cardiac Drugs Well Coordinated? *Drug Saf.* **2013**, *36* (3), 167–182. <https://doi.org/10.1007/s40264-013-0016-z>.
- (2) Fermini, B.; Hancox, J. C.; Abi-Gerges, N.; Bridgland-Taylor, M.; Chaudhary, K. W.; Colatsky, T.; Correll, K.; Crumb, W.; Damiano, B.; Erdemli, G.; et al. A New Perspective in the Field of Cardiac Safety Testing through the Comprehensive In Vitro Proarrhythmia Assay Paradigm. *J. Biomol. Screen.* **2016**, *21* (1), 1–11. <https://doi.org/10.1177/1087057115594589>.
- (3) Dowden, H.; Munro, J. Trends in Clinical Success Rates and Therapeutic Focus. *Nat. Rev. Drug Discov.* **2019**, *18* (7), 495–496. <https://doi.org/10.1038/d41573-019-00074-z>.
- (4) Cook, D.; Brown, D.; Alexander, R.; March, R.; Morgan, P.; Satterthwaite, G.; Pangalos, M. N. Lessons Learned from the Fate of AstraZeneca’s Drug Pipeline: A Five-Dimensional Framework. *Nat. Rev. Drug Discov.* **2014**, *13* (6), 419–431. <https://doi.org/10.1038/nrd4309>.
- (5) Smietana, K.; Siatkowski, M.; Møller, M. Trends in Clinical Success Rates. *Nat. Rev. Drug Discov.* **2016**, *15* (6), 379–380. <https://doi.org/10.1038/nrd.2016.85>.
- (6) ICH Official web site : ICH <https://www.ich.org/page/safety-guidelines> (accessed Jan 22, 2020).
- (7) ICH Official web site : ICH <https://www.ich.org/page/efficacy-guidelines> (accessed Jan 22, 2020).
- (8) Gintant, G.; Sager, P. T.; Stockbridge, N. Evolution of Strategies to Improve Preclinical Cardiac Safety Testing. *Nat. Rev. Drug Discov.* **2016**, *15* (7), 457–471. <https://doi.org/10.1038/nrd.2015.34>.
- (9) Organ on Chip Market By Type and Industry Analysis - 2023 <https://www.alliedmarketresearch.com/organ-on-chip-market> (accessed Feb 2, 2020).
- (10) Shah, M.; Akar, F. G.; Tomaselli, G. F. Molecular Basis of Arrhythmias. *Circulation* **2005**, *112* (16), 2517–2529. <https://doi.org/10.1161/CIRCULATIONAHA.104.494476>.
- (11) Neher, E.; Sakmann, B. Single-Channel Currents Recorded from Membrane of Denervated Frog Muscle Fibres. *Nature* **1976**, *260* (5554), 799–802. <https://doi.org/10.1038/260799a0>.
- (12) El-Sherif, N.; Turitto, G. Torsade de Pointes. *Curr. Opin. Cardiol.* **2003**, *18* (1), 6–13. <https://doi.org/10.1097/00001573-200301000-00002>.
- (13) Hocini, M.; Shah, A. J.; McKelvie-Sebileau, P.; Haïssaguerre, M. Ventricular Fibrillation. In *Cardiac Electrophysiology: From Cell to Bedside: Seventh Edition*; Elsevier, 2018; pp 1263–1269. <https://doi.org/10.1016/B978-0-323-44733-1.00129-2>.
- (14) Kramer, J.; Obejero-Paz, C. A.; Myatt, G.; Kuryshev, Y. A.; Bruening-Wright, A.; Verducci, J. S.; Brown, A. M. MICE Models: Superior to the HERG Model in Predicting Torsade de

- Pointes. *Sci. Rep.* **2013**, 3 (1), 2100. <https://doi.org/10.1038/srep02100>.
- (15) Ando, H.; Yoshinaga, T.; Yamamoto, W.; Asakura, K.; Uda, T.; Taniguchi, T.; Ojima, A.; Osada, T.; Hayashi, S.; Kasai, C.; et al. A New Paradigm for Drug-Induced Torsadogenic Risk Assessment Using Human IPS Cell-Derived Cardiomyocytes. *J. Pharmacol. Toxicol. Methods* **2017**, 84, 111–127. <https://doi.org/10.1016/j.vascn.2016.12.003>.
- (16) Vaz, R.; Klabunde, T. *Antitargets: Prediction and Prevention of Drug Side Effects (Methods and Principles in Medicinal Chemistry)*; Vaz, R., Klabunde, T., Eds.; Wiley-VCH, 2008; Vol. 38.
- (17) Sager, P. T.; Gintant, G.; Turner, J. R.; Pettit, S.; Stockbridge, N. Rechanneling the Cardiac Proarrhythmia Safety Paradigm: A Meeting Report from the Cardiac Safety Research Consortium. *Am. Heart J.* **2014**, 167 (3), 292–300. <https://doi.org/10.1016/j.ahj.2013.11.004>.
- (18) Hoekstra, M.; Mummery, C. L.; Wilde, A. A. M.; Bezzina, C. R.; Verkerk, A. O. Induced Pluripotent Stem Cell Derived Cardiomyocytes as Models for Cardiac Arrhythmias. *Front. Physiol.* **2012**, 3. <https://doi.org/10.3389/fphys.2012.00346>.
- (19) Mummery, C. L.; Sala, L.; Bellin, M. Themed Section: New Insights into Cardiotoxicity Caused by Chemotherapeutic Agents Integrating Cardiomyocytes from Human Pluripotent Stem Cells in Safety Pharmacology: Has the Time Come? *Br. J. Pharmacol.* **2017**, 174, 3749–3765. <https://doi.org/10.1111/bph.13577>.
- (20) Veerman, C. C.; Kosmidis, G.; Mummery, C. L.; Casini, S.; Verkerk, A. O.; Bellin, M. Immaturity of Human Stem-Cell-Derived Cardiomyocytes in Culture: Fatal Flaw or Soluble Problem? *Stem Cells Dev.* **2015**, 24 (9), 1035–1052. <https://doi.org/10.1089/scd.2014.0533>.
- (21) Lemoine, M. D.; Krause, T.; Koivumäki, J. T.; Prondzynski, M.; Schulze, M. L.; Girdauskas, E.; Willems, S.; Hansen, A.; Eschenhagen, T.; Christ, T. Human Induced Pluripotent Stem Cell-Derived Engineered Heart Tissue as a Sensitive Test System for QT Prolongation and Arrhythmic Triggers. *Circ. Arrhythmia Electrophysiol.* **2018**, 11 (7). <https://doi.org/10.1161/CIRCEP.117.006035>.
- (22) Goversen, B.; van der Heyden, M. A. G.; van Veen, T. A. B.; de Boer, T. P. The Immature Electrophysiological Phenotype of iPSC-CMs Still Hampers in Vitro Drug Screening: Special Focus on I K1. *Pharmacol. Ther.* **2018**, 183, 127–136. <https://doi.org/10.1016/j.pharmthera.2017.10.001>.
- (23) Edmondson, R.; Broglie, J. J.; Adcock, A. F.; Yang, L. Three-Dimensional Cell Culture Systems and Their Applications in Drug Discovery and Cell-Based Biosensors. *Assay Drug Dev. Technol.* **2014**, 12 (4), 207–218. <https://doi.org/10.1089/adt.2014.573>.
- (24) Tandon, N.; Cannizzaro, C.; Chao, P. H. G.; Maidhof, R.; Marsano, A.; Au, H. T. H.; Radisic, M.; Vunjak-Novakovic, G. Electrical Stimulation Systems for Cardiac Tissue Engineering. *Nat. Protoc.* **2009**, 4 (2), 155–173. <https://doi.org/10.1038/nprot.2008.183>.
- (25) Hansen, A.; Eder, A.; Bönstrup, M.; Flato, M.; Mewe, M.; Schaaf, S.; Aksehirlioglu, B.; Schwörer, A.; Uebeler, J.; Eschenhagen, T. Development of a Drug Screening Platform Based on Engineered Heart Tissue. *Circ. Res.* **2010**, 107 (1), 35–44.

<https://doi.org/10.1161/CIRCRESAHA.109.211458>.

- (26) Eschenhagen, T.; Eder, A.; Vollert, I.; Hansen, A. Physiological Aspects of Cardiac Tissue Engineering. *Am. J. Physiol. Circ. Physiol.* **2012**, *303* (2), H133–H143. <https://doi.org/10.1152/ajpheart.00007.2012>.
- (27) Eder, A.; Vollert, I.; Hansen, A.; Eschenhagen, T. Human Engineered Heart Tissue as a Model System for Drug Testing. *Adv. Drug Deliv. Rev.* **2016**, *96*, 214–224. <https://doi.org/10.1016/j.addr.2015.05.010>.
- (28) Geneser, F. *Histology*, 1st ed.; Munksgaard Danmark, 2011.
- (29) 10.2 Skeletal Muscle | Anatomy and Physiology <https://opentextbc.ca/anatomyandphysiology/chapter/10-2-skeletal-muscle/> (accessed Jan 27, 2020).
- (30) Openstax College. 10.7 Cardiac Muscle Tissue – Anatomy and Physiology <https://opentextbc.ca/anatomyandphysiology/chapter/10-7-cardiac-muscle-tissue/> (accessed Jan 27, 2020).
- (31) Alberts, B.; Jonson, A.; Lewis, J.; Raff, M.; Roberts, K.; Walter, P. *Molecular Biology of The Cell*, 5th ed.; Garland Science, 2008.
- (32) Boonen, K. J. M.; Langelaan, M. L. P.; Polak, R. B.; van der Schaft, D. W. J.; Baaijens, F. P. T.; Post, M. J. Effects of a Combined Mechanical Stimulation Protocol: Value for Skeletal Muscle Tissue Engineering. *J. Biomech.* **2010**, *43* (8), 1514–1521. <https://doi.org/10.1016/j.jbiomech.2010.01.039>.
- (33) Tanaka, K.; Sato, K.; Yoshida, T.; Fukuda, T.; Hanamura, K.; Kojima, N.; Shirao, T.; Yanagawa, T.; Watanabe, H. Evidence for Cell Density Affecting C2C12 Myogenesis: Possible Regulation of Myogenesis by Cell-Cell Communication. *Muscle and Nerve* **2011**, *44* (6), 968–977. <https://doi.org/10.1002/mus.22224>.
- (34) Yamamoto, D. L.; Csikasz, R. I.; Li, Y.; Sharma, G.; Hjort, K.; Karlsson, R.; Bengtsson, T. Myotube Formation on Micro-Patterned Glass: Intracellular Organization and Protein Distribution in C2C12 Skeletal Muscle Cells. *J. Histochem. Cytochem.* **2008**, *56* (10), 881–892. <https://doi.org/10.1369/jhc.2008.951228>.
- (35) Denning, C.; Borgdorff, V.; Crutchley, J.; Firth, K. S. A.; George, V.; Kalra, S.; Kondrashov, A.; Hoang, M. D.; Mosqueira, D.; Patel, A.; et al. Cardiomyocytes from Human Pluripotent Stem Cells: From Laboratory Curiosity to Industrial Biomedical Platform. *Biochim. Biophys. Acta - Mol. Cell Res.* **2016**, *1863* (7), 1728–1748. <https://doi.org/10.1016/j.bbamcr.2015.10.014>.
- (36) Correia, C.; Koshkin, A.; Duarte, P.; Hu, D.; Teixeira, A.; Domian, I.; Serra, M.; Alves, P. M. Distinct Carbon Sources Affect Structural and Functional Maturation of Cardiomyocytes Derived from Human Pluripotent Stem Cells. *Sci. Rep.* **2017**, *7* (1). <https://doi.org/10.1038/s41598-017-08713-4>.
- (37) Jeziorowska, D.; Korniat, A.; Salem, J. E.; Fish, K.; Hulot, J. S. Generating Patient-Specific Induced Pluripotent Stem Cells-Derived Cardiomyocytes for the Treatment of Cardiac Diseases. *Expert Opin. Biol. Ther.* **2015**, *15* (10), 1399–1409. <https://doi.org/10.1517/14712598.2015.1064109>.

-
- (38) Engler, A. J.; Griffin, M. A.; Sen, S.; Bönnemann, C. G.; Sweeney, H. L.; Discher, D. E. Myotubes Differentiate Optimally on Substrates with Tissue-like Stiffness: Pathological Implications for Soft or Stiff Microenvironments. *J. Cell Biol.* **2004**, *166* (6), 877–887. <https://doi.org/10.1083/jcb.200405004>.
- (39) Shih, Y. R. V.; Tseng, K. F.; Lai, H. Y.; Lin, C. H.; Lee, O. K. Matrix Stiffness Regulation of Integrin-Mediated Mechanotransduction during Osteogenic Differentiation of Human Mesenchymal Stem Cells. *J. Bone Miner. Res.* **2011**, *26* (4), 730–738. <https://doi.org/10.1002/jbmr.278>.
- (40) Rodriguez, M. L.; Beussman, K. M.; Chun, K. S.; Walzer, M. S.; Yang, X.; Murry, C. E.; Sniadecki, N. J. Substrate Stiffness, Cell Anisotropy, and Cell-Cell Contact Contribute to Enhanced Structural and Calcium Handling Properties of Human Embryonic Stem Cell-Derived Cardiomyocytes. *ACS Biomater. Sci. Eng.* **2019**, *5* (8), 3876–3888. <https://doi.org/10.1021/acsbiomaterials.8b01256>.
- (41) Zhang, W.; Kong, C. W.; Tong, M. H.; Chooi, W. H.; Huang, N.; Li, R. A.; Chan, B. P. Maturation of Human Embryonic Stem Cell-Derived Cardiomyocytes (HESC-CMs) in 3D Collagen Matrix: Effects of Niche Cell Supplementation and Mechanical Stimulation. *Acta Biomater.* **2017**, *49*, 204–217. <https://doi.org/10.1016/j.actbio.2016.11.058>.
- (42) Lee, S.; Serpooshan, V.; Tong, X.; Venkatraman, S.; Lee, M.; Lee, J.; Chirikian, O.; Wu, J. C.; Wu, S. M.; Yang, F. Contractile Force Generation by 3D hiPSC-Derived Cardiac Tissues Is Enhanced by Rapid Establishment of Cellular Interconnection in Matrix with Muscle-Mimicking Stiffness. *Biomaterials* **2017**, *131*, 111–120. <https://doi.org/10.1016/j.biomaterials.2017.03.039>.
- (43) Leonard, A.; Bertero, A.; Powers, J. D.; Beussman, K. M.; Bhandari, S.; Regnier, M.; Murry, C. E.; Sniadecki, N. J. Afterload Promotes Maturation of Human Induced Pluripotent Stem Cell Derived Cardiomyocytes in Engineered Heart Tissues. *J. Mol. Cell. Cardiol.* **2018**, *118*, 147–158. <https://doi.org/10.1016/j.yjmcc.2018.03.016>.
- (44) Aubin, H.; Nichol, J. W.; Hutson, C. B.; Bae, H.; Sieminski, A. L.; Cropek, D. M.; Akhyari, P.; Khademhosseini, A. Directed 3D Cell Alignment and Elongation in Microengineered Hydrogels. *Biomaterials* **2010**, *31*, 6941–6951. <https://doi.org/10.1016/j.biomaterials.2010.05.056>.
- (45) Ronaldson-Bouchard, K.; Ma, S. P.; Yeager, K.; Chen, T.; Song, L.; Sirabella, D.; Morikawa, K.; Teles, D.; Yazawa, M.; Vunjak-Novakovic, G. Advanced Maturation of Human Cardiac Tissue Grown from Pluripotent Stem Cells. *Nature* **2018**, *556* (7700), 239–243. <https://doi.org/10.1038/s41586-018-0016-3>.
- (46) Caliari, S. R.; Burdick, J. A. A Practical Guide to Hydrogels for Cell Culture. *Nat. Methods* **2016**, *13* (5), 405–414. <https://doi.org/10.1038/nmeth.3839>.
- (47) Larsen, E. K. U.; Mikkelsen, M. B. L.; Larsen, N. B. Facile Photoimmobilization of Proteins onto Low-Binding PEG-Coated Polymer Surfaces. *Biomacromolecules* **2014**, *15* (3), 894–899. <https://doi.org/10.1021/bm401745a>.
- (48) Tallawi, M.; Rosellini, E.; Barbani, N.; Cascone, M. G.; Rai, R.; Saint-Pierre, G.; Boccaccini, A. R. Strategies for the Chemical and Biological Functionalization of Scaffolds for Cardiac Tissue Engineering: A Review. *J. R. Soc. Interface* **2015**, *12* (108), 20150254.

<https://doi.org/10.1098/rsif.2015.0254>.

- (49) Davidenko, N.; Schuster, C. F.; Bax, D. V.; Farndale, R. W.; Hamaia, S.; Best, S. M.; Cameron, R. E. Evaluation of Cell Binding to Collagen and Gelatin: A Study of the Effect of 2D and 3D Architecture and Surface Chemistry. *J. Mater. Sci. Mater. Med.* **2016**, *27* (10), 148. <https://doi.org/10.1007/s10856-016-5763-9>.
- (50) Mills, R. J.; Titmarsh, D. M.; Koenig, X.; Parker, B. L.; Ryall, J. G.; Quaife-Ryan, G. A.; Voges, H. K.; Hodson, M. P.; Ferguson, C.; Drowley, L.; et al. Functional Screening in Human Cardiac Organoids Reveals a Metabolic Mechanism for Cardiomyocyte Cell Cycle Arrest. *Proc. Natl. Acad. Sci. U. S. A.* **2017**, *114* (40), E8372–E8381. <https://doi.org/10.1073/pnas.1707316114>.
- (51) Schaaf, S.; Eder, A.; Vollert, I.; Stöhr, A.; Hansen, A.; Eschenhagen, T. Generation of Strip-Format Fibrin-Based Engineered Heart Tissue (EHT). In *Methods in Molecular Biology*; 2014; Vol. 1181, pp 121–129. https://doi.org/10.1007/978-1-4939-1047-2_11.
- (52) Wang, Z.; Lee, S. J.; Cheng, H.-J.; Yoo, J. J.; Atala, A. 3D Bioprinted Functional and Contractile Cardiac Tissue Constructs. *Acta Biomater.* **2018**, *70*, 48–56. <https://doi.org/10.1016/j.actbio.2018.02.007>.
- (53) Ma, X.; Dewan, S.; Liu, J.; Tang, M.; Miller, K. L.; Yu, C.; Lawrence, N.; McCulloch, A. D.; Chen, S. 3D Printed Micro-Scale Force Gauge Arrays to Improve Human Cardiac Tissue Maturation and Enable High Throughput Drug Testing. *Acta Biomater.* **2019**, *95*, 319–327. <https://doi.org/10.1016/j.actbio.2018.12.026>.
- (54) Cvetkovic, C.; Raman, R.; Chan, V.; Williams, B. J.; Tolish, M.; Bajaj, P.; Sakar, M. S.; Asada, H. H.; Saif, M. T. A.; Bashir, R. Three-Dimensionally Printed Biological Machines Powered by Skeletal Muscle. *Proc. Natl. Acad. Sci. U. S. A.* **2014**, *111* (28), 10125–10130. <https://doi.org/10.1073/pnas.1401577111>.
- (55) Maitra, N.; Flink, I. L.; Bahl, J. J.; Morkin, E. Expression of α and β Integrins during Terminal Differentiation of Cardiomyocytes. *Cardiovasc. Res.* **2000**, *47* (4), 715–725. [https://doi.org/10.1016/S0008-6363\(00\)00140-1](https://doi.org/10.1016/S0008-6363(00)00140-1).
- (56) Ross, R. S.; Borg, T. K. Integrins and the Myocardium. *Circ. Res.* **2001**, *88* (11), 1112–1119. <https://doi.org/10.1161/hh1101.091862>.
- (57) Barczyk, M.; Carracedo, S.; Gullberg, D. Integrins. *Cell Tissue Res.* **2010**, *339* (1), 269–280. <https://doi.org/10.1007/s00441-009-0834-6>.
- (58) Wu, X.; Sun, Z.; Foskett, A.; Trzeciakowski, J. P.; Meininger, G. A.; Muthuchamy, M. Cardiomyocyte Contractile Status Is Associated with Differences in Fibronectin and Integrin Interactions. *Am J Physiol Hear. Circ Physiol* **2010**, *298*, 2071–2081. <https://doi.org/10.1152/ajpheart.01156.2009.-Integrins>.
- (59) Seetharaman, S.; Etienne-Manneville, S. Integrin Diversity Brings Specificity in Mechanotransduction. *Biol. Cell* **2018**, *110* (3), 49–64. <https://doi.org/10.1111/boc.201700060>.
- (60) Gun'ko, V.; Savina, I.; Mikhlovsky, S. Properties of Water Bound in Hydrogels. *Gels* **2017**, *3* (4), 37. <https://doi.org/10.3390/gels3040037>.

-
- (61) Richbourg, N. R.; Peppas, N. A.; Sikavitsas, V. I. Tuning the Biomimetic Behavior of Scaffolds for Regenerative Medicine through Surface Modifications. *J. Tissue Eng. Regen. Med.* **2019**, *13* (8), 1275–1293. <https://doi.org/10.1002/term.2859>.
- (62) Kim, C.; Young, J. L.; Holle, A. W.; Jeong, K.; Major, L. G.; Jeong, J. H.; Aman, Z. M.; Han, D. W.; Hwang, Y.; Spatz, J. P.; et al. Stem Cell Mechanosensation on Gelatin Methacryloyl (GelMA) Stiffness Gradient Hydrogels. *Ann. Biomed. Eng.* **2020**, *48* (2), 893–902. <https://doi.org/10.1007/s10439-019-02428-5>.
- (63) Khodabukus, A.; Baar, K. Regulating Fibrinolysis to Engineer Skeletal Muscle. *Tissue Eng. Part C* **2009**, *15* (3), 501–511. <https://doi.org/10.1089=ten.tec.2008.0286>.
- (64) Yunoki, S.; Ohyabu, Y.; Hatayama, H. Temperature-Responsive Gelation of Type I Collagen Solutions Involving Fibril Formation and Genipin Crosslinking as a Potential Injectable Hydrogel. *Int. J. Biomater.* **2013**, *2013*, 1–14. <https://doi.org/10.1155/2013/620765>.
- (65) Wilson, J. L.; McDevitt, T. C. Biofunctional Hydrogels for Three-Dimensional Stem Cell Culture. In *Biology and Engineering of Stem Cell Niches*; Elsevier, 2017; pp 345–362. <https://doi.org/10.1016/B978-0-12-802734-9.00022-6>.
- (66) Nichol, J. W.; Koshy, S. T.; Bae, H.; Hwang, C. M.; Yamanlar, S.; Khademhosseini, A. Cell-Laden Microengineered Gelatin Methacrylate Hydrogels. *Biomaterials* **2010**, *31* (21), 5536–5544. <https://doi.org/10.1016/j.biomaterials.2010.03.064>.
- (67) Aubin, H.; Nichol, J. W.; Hutson, C. B.; Bae, H.; Sieminski, A. L.; Cropek, D. M.; Akhyari, P.; Khademhosseini, A. Directed 3D Cell Alignment and Elongation in Microengineered Hydrogels. *Biomaterials* **2010**, *31* (27), 6941–6951. <https://doi.org/10.1016/j.biomaterials.2010.05.056>.
- (68) Gillies, A. R.; Lieber, R. L. Structure and Function of the Skeletal Muscle Extracellular Matrix. *Muscle Nerve* **2011**, *44* (3), n/a-n/a. <https://doi.org/10.1002/mus.22094>.
- (69) Hinderer, S.; Schenke-Layland, K. Cardiac Fibrosis – A Short Review of Causes and Therapeutic Strategies. *Adv. Drug Deliv. Rev.* **2019**, *146*, 77–82. <https://doi.org/10.1016/j.addr.2019.05.011>.
- (70) Pawelec, K. M.; Best, S. M.; Cameron, R. E. Collagen: A Network for Regenerative Medicine. *J. Mater. Chem. B* **2016**, *4* (40), 6484–6496. <https://doi.org/10.1039/c6tb00807k>.
- (71) Kolesky, D. B.; Truby, R. L.; Gladman, A. S.; Busbee, T. A.; Homan, K. A.; Lewis, J. A. 3D Bioprinting of Vascularized, Heterogeneous Cell-Laden Tissue Constructs. *Adv. Mater.* **2014**, *26* (19), 3124–3130. <https://doi.org/10.1002/adma.201305506>.
- (72) García, A. J.; Vega, M. D.; Boettiger, D. Modulation of Cell Proliferation and Differentiation through Substrate-Dependent Changes in Fibronectin Conformation. *Mol. Biol. Cell* **1999**, *10* (3), 785–798. <https://doi.org/10.1091/MBC.10.3.785>.
- (73) Khodabukus, A.; Baar, K. Regulating Fibrinolysis to Engineer Skeletal Muscle from the C2C12 Cell Line. *Tissue Eng. Part C Methods* **2009**, *15* (3), 501–511. <https://doi.org/10.1089/ten.tec.2008.0286>.

-
- (74) Weisel, J. W. Fibrinogen and Fibrin. *Adv. Protein Chem.* **2005**, *70*, 247–299. [https://doi.org/10.1016/S0065-3233\(05\)70008-5](https://doi.org/10.1016/S0065-3233(05)70008-5).
- (75) Janmey, P. A.; Winer, J. P.; Weisel, J. W. Fibrin Gels and Their Clinical and Bioengineering Applications. *J. R. Soc. Interface* **2009**, *6* (30), 1–10. <https://doi.org/10.1098/rsif.2008.0327>.
- (76) Weisel, J. W.; Litvinov, R. I. Fibrin Formation, Structure and Properties. *Subcell. Biochem.* **2017**, *82*, 405–456. https://doi.org/10.1007/978-3-319-49674-0_13.
- (77) Friend, J.; Yeo, L. Fabrication of Microfluidic Devices Using Polydimethylsiloxane. *Biomicrofluidics* **2010**, *4* (2). <https://doi.org/10.1063/1.3259624>.
- (78) Li, N.; Schwartz, M.; Ionescu-Zanetti, C. PDMS Compound Adsorption in Context. *J. Biomol. Screen.* **2009**, *14* (2), 194–202. <https://doi.org/10.1177/1087057108327326>.
- (79) van Meer, B. J.; de Vries, H.; Firth, K. S. A.; van Weerd, J.; Tertoolen, L. G. J.; Karperien, H. B. J.; Jonkheijm, P.; Denning, C.; IJzerman, A. P.; Mummery, C. L. Small Molecule Absorption by PDMS in the Context of Drug Response Bioassays. *Biochem. Biophys. Res. Commun.* **2017**, *482* (2), 323–328. <https://doi.org/10.1016/j.bbrc.2016.11.062>.
- (80) Raman, R.; Bhaduri, B.; Mir, M.; Shkumatov, A.; Lee, M. K.; Popescu, G.; Kong, H.; Bashir, R. High-Resolution Projection Microstereolithography for Patterning of Neovasculature. *Adv. Healthc. Mater.* **2016**, *5* (5), 610–619. <https://doi.org/10.1002/adhm.201500721>.
- (81) Christensen, R. K.; von Halling Laier, C.; Kiziltay, A.; Wilson, S.; Larsen, N. B. 3D Printed Hydrogel Multiassay Platforms for Robust Generation of Engineered Contractile Tissues. *Biomacromolecules* **2020**, *21* (2), 356–365. <https://doi.org/10.1021/acs.biomac.9b01274>.
- (82) Huang, Y.; Zhang, X.-F.; Gao, G.; Yonezawa, T.; Cui, X. 3D Bioprinting and the Current Applications in Tissue Engineering. *Biotechnol. J.* **2017**, *12* (8), 1600734. <https://doi.org/10.1002/biot.201600734>.
- (83) Rogers, C. I.; Pagaduan, J. V.; Nordin, G. P.; Woolley, A. T. Single-Monomer Formulation of Polymerized Polyethylene Glycol Diacrylate as a Nonadsorptive Material for Microfluidics. *Anal. Chem.* **2011**, *83* (16), 6418–6425. <https://doi.org/10.1021/ac201539h>.
- (84) Choi, J. R.; Yong, K. W.; Choi, J. Y.; Cowie, A. C. Recent Advances in Photo-Crosslinkable Hydrogels for Biomedical Applications. *Biotechniques* **2019**, *66* (1), 40–53. <https://doi.org/10.2144/btn-2018-0083>.
- (85) Abadi, P. P. S. S.; Garbern, J. C.; Behzadi, S.; Hill, M. J.; Tresback, J. S.; Heydari, T.; Ejtehadi, M. R.; Ahmed, N.; Copley, E.; Aghaverdi, H.; et al. Engineering of Mature Human Induced Pluripotent Stem Cell-Derived Cardiomyocytes Using Substrates with Multiscale Topography. *Adv. Funct. Mater.* **2018**, *28* (19), 1707378. <https://doi.org/10.1002/adfm.201707378>.
- (86) Silbernagel, N.; Körner, A.; Balitzki, J.; Jaggy, M.; Bertels, S.; Richter, B.; Hippler, M.; Hellwig, A.; Hecker, M.; Bastmeyer, M.; et al. Shaping the Heart: Structural and Functional Maturation of iPSC-Cardiomyocytes in 3D-Micro-Scaffolds. *Biomaterials* **2020**, *227*, 119551. <https://doi.org/10.1016/j.biomaterials.2019.119551>.

-
- (87) Heidi Au, H. T.; Cui, B.; Chu, Z. E.; Veres, T.; Radisic, M. Cell Culture Chips for Simultaneous Application of Topographical and Electrical Cues Enhance Phenotype of Cardiomyocytes. *Lab Chip* **2009**, 9 (4), 564–575. <https://doi.org/10.1039/b810034a>.
- (88) Lind, J. U.; Busbee, T. A.; Valentine, A. D.; Pasqualini, F. S.; Yuan, H.; Yadid, M.; Park, S.-J.; Kotikian, A.; Nesmith, A. P.; Campbell, P. H.; et al. Instrumented Cardiac Microphysiological Devices via Multimaterial Three-Dimensional Printing. *Nat. Mater.* **2017**, 16 (3), 303–308. <https://doi.org/10.1038/nmat4782>.
- (89) Nawroth, J. C.; Scudder, L. L.; Halvorson, R. T.; Tresback, J.; Ferrier, J. P.; Sheehy, S. P.; Cho, A.; Kannan, S.; Sunyovszki, I.; Goss, J. A.; et al. Automated Fabrication of Photopatterned Gelatin Hydrogels for Organ-on-Chips Applications. *Biofabrication* **2018**, 10 (2), 025004. <https://doi.org/10.1088/1758-5090/aa96de>.
- (90) McCain, M. L.; Agarwal, A.; Nesmith, H. W.; Nesmith, A. P.; Parker, K. K. Micromolded Gelatin Hydrogels for Extended Culture of Engineered Cardiac Tissues. *Biomaterials* **2014**, 35 (21), 5462–5471. <https://doi.org/10.1016/j.biomaterials.2014.03.052>.
- (91) Pinera, P. P.; Palasz, A.; Raman, R.; Cvetkovic, C.; Kong, H.; Bashir, R.; Dabbous, H.; Gapinske, M.; Grant, L.; Seo, Y. Damage, Healing, and Remodeling in Optogenetic Skeletal Muscle Bioactuators. *Adv. Healthc. Mater.* **2017**, 6 (12), 1700030. <https://doi.org/10.1002/adhm.201700030>.
- (92) Vandeburgh, H.; Shansky, J.; Benesch-Lee, F.; Barbata, V.; Reid, J.; Thorrez, L.; Valentini, R.; Crawford, G. Drug-Screening Platform Based on the Contractility of Tissue-Engineered Muscle. *Muscle Nerve* **2008**, 37 (4), 438–447. <https://doi.org/10.1002/mus.20931>.
- (93) Legant, W. R.; Pathak, A.; Yang, M. T.; Deshpande, V. S.; McMeeking, R. M.; Chen, C. S. Microfabricated Tissue Gauges to Measure and Manipulate Forces from 3D Microtissues. *Proc. Natl. Acad. Sci. U. S. A.* **2009**, 106 (25), 10097–10102. <https://doi.org/10.1073/pnas.0900174106>.
- (94) Zhao, Y.; Rafatian, N.; Feric, N. T.; Cox, B. J.; Aschar-Sobbi, R.; Wang, E. Y.; Aggarwal, P.; Zhang, B.; Conant, G.; Ronaldson-Bouchard, K.; et al. A Platform for Generation of Chamber-Specific Cardiac Tissues and Disease Modeling. *Cell* **2019**, 176 (4), 913–927.e18. <https://doi.org/10.1016/j.cell.2018.11.042>.
- (95) Sidorov, V. Y.; Samson, P. C.; Sidorova, T. N.; Davidson, J. M.; Lim, C. C.; Wikswo, J. P. I-Wire Heart-on-a-Chip I: Three-Dimensional Cardiac Tissue Constructs for Physiology and Pharmacology. *Acta Biomater.* **2017**, 48, 68–78. <https://doi.org/10.1016/j.actbio.2016.11.009>.
- (96) Zimmermann, W.-H.; Schneiderbanger, K.; Schubert, P.; Didié, M.; Münzel, F.; Heubach, J. F.; Kostin, S.; Neuhuber, W. L.; Eschenhagen, T. Tissue Engineering of a Differentiated Cardiac Muscle Construct. *Circ. Res.* **2002**, 90 (2), 223–230.
- (97) Mills, R. J.; Parker, B. L.; Monnot, P.; Needham, E. ; Vivien, C. J.; Ferguson, C.; Parton, R. G.; James, D. E.; Porrello, E. R.; Hudson, J. E. Development of a Human Skeletal Micro Muscle Platform with Pacing Capabilities. *Biomaterials* **2019**, 198, 217–227. <https://doi.org/10.1016/j.biomaterials.2018.11.030>.
- (98) Lemoine, M. D.; Mannhardt, I.; Breckwoldt, K.; Prondzynski, M.; Flenner, F.; Ulmer, B.;

-
- Hirt, M. N.; Neuber, C.; Horváth, A.; Kloth, B.; et al. Human iPSC-Derived Cardiomyocytes Cultured in 3D Engineered Heart Tissue Show Physiological Upstroke Velocity and Sodium Current Density. *Sci. Rep.* **2017**, *7* (1), 5464. <https://doi.org/10.1038/s41598-017-05600-w>.
- (99) Ulmer, B. M.; Stoehr, A.; Schulze, M. L.; Patel, S.; Gucek, M.; Mannhardt, I.; Funcke, S.; Murphy, E.; Eschenhagen, T.; Hansen, A. Contractile Work Contributes to Maturation of Energy Metabolism in HiPSC-Derived Cardiomyocytes. *Stem Cell Reports* **2018**, *10* (3), 834–847. <https://doi.org/10.1016/j.stemcr.2018.01.039>.
- (100) Mills, R. J.; Parker, B. L.; Quaife-Ryan, G. A.; Voges, H. K.; Needham, E. J.; Bornot, A.; Ding, M.; Andersson, H.; Polla, M.; Elliott, D. A.; et al. Drug Screening in Human PSC-Cardiac Organoids Identifies Pro-Proliferative Compounds Acting via the Mevalonate Pathway. *Cell Stem Cell* **2019**, *24* (6), 895–907.e6. <https://doi.org/10.1016/j.STEM.2019.03.009>.
- (101) Hirt, M. N.; Boeddinghaus, J.; Mitchell, A.; Schaaf, S.; Börnchen, C.; Müller, C.; Schulz, H.; Hubner, N.; Stenzig, J.; Stoehr, A.; et al. Functional Improvement and Maturation of Rat and Human Engineered Heart Tissue by Chronic Electrical Stimulation. *J. Mol. Cell. Cardiol.* **2014**, *74*, 151–161. <https://doi.org/10.1016/j.yjmcc.2014.05.009>.
- (102) Mannhardt, I.; Breckwoldt, K.; Letuffe-Brenière, D.; Schaaf, S.; Schulz, H.; Neuber, C.; Benzin, A.; Werner, T.; Eder, A.; Schulze, T.; et al. Human Engineered Heart Tissue: Analysis of Contractile Force. *Stem Cell Reports* **2016**, *7* (1), 29–42. <https://doi.org/10.1016/j.stemcr.2016.04.011>.
- (103) Yang, X.; Pabon, L.; Murry, C. E. Engineering Adolescence. *Circ. Res.* **2014**, *114* (3), 511–523. <https://doi.org/10.1161/CIRCRESAHA.114.300558>.
- (104) Ghafar-Zadeh, E.; Waldeisen, J. R.; Lee, L. P. Engineered Approaches to the Stem Cell Microenvironment for Cardiac Tissue Regeneration. *Lab Chip* **2011**, *11* (18), 3031. <https://doi.org/10.1039/c1lc20284g>.
- (105) Stoppel, W. L.; Kaplan, D. L.; Black, L. D. Electrical and Mechanical Stimulation of Cardiac Cells and Tissue Constructs. *Adv. Drug Deliv. Rev.* **2016**, *96*, 135–155. <https://doi.org/10.1016/j.addr.2015.07.009>.
- (106) Farouz, Y.; Chen, Y.; Terzic, A.; Menasché, P. Concise Review: Growing Hearts in the Right Place: On the Design of Biomimetic Materials for Cardiac Stem Cell Differentiation. *Stem Cells* **2015**, *33* (4), 1021–1035. <https://doi.org/10.1002/stem.1929>.
- (107) Passey, S.; Martin, N.; Player, D.; Lewis, M. P. Stretching Skeletal Muscle in Vitro: Does It Replicate in Vivo Physiology? *Biotechnol. Lett.* **2011**, *33* (8), 1513–1521. <https://doi.org/10.1007/s10529-011-0610-z>.
- (108) Feinberg, A. W.; Alford, P. W.; Jin, H.; Ripplinger, C. M.; Werdich, A. A.; Sheehy, S. P.; Grosberg, A.; Parker, K. K. Controlling the Contractile Strength of Engineered Cardiac Muscle by Hierarchical Tissue Architecture. *Biomaterials* **2012**, *33* (23), 5732–5741. <https://doi.org/10.1016/j.biomaterials.2012.04.043>.
- (109) Liaw, N. Y.; Zimmermann, W.-H. Mechanical Stimulation in the Engineering of Heart Muscle. *Adv. Drug Deliv. Rev.* **2016**, *96*, 156–160. <https://doi.org/10.1016/j.addr.2015.09.001>.

-
- (110) Zimmermann, W. H.; Melnychenko, I.; Wasmeier, G.; Didié, M.; Naito, H.; Nixdorff, U.; Hess, A.; Budinsky, L.; Brune, K.; Michaelis, B.; et al. Engineered Heart Tissue Grafts Improve Systolic and Diastolic Function in Infarcted Rat Hearts. *Nat. Med.* **2006**, *12* (4), 452–458. <https://doi.org/10.1038/nm1394>.
- (111) Kensah, G.; Lara, A. R.; Dahlmann, J.; Zweigerdt, R.; Schwanke, K.; Hegermann, J.; Skvorc, D.; Gawol, A.; Azizian, A.; Wagner, S.; et al. Murine and Human Pluripotent Stem Cell-Derived Cardiac Bodies Form Contractile Myocardial Tissue in Vitro. *Eur. Heart J.* **2013**, *34* (15), 1134–1146. <https://doi.org/10.1093/eurheartj/ehs349>.
- (112) Marsano, A.; Conficconi, C.; Lemme, M.; Occhetta, P.; Gaudiello, E.; Votta, E.; Cerino, G.; Redaelli, A.; Rasponi, M. Beating Heart on a Chip: A Novel Microfluidic Platform to Generate Functional 3D Cardiac Microtissues. *Lab Chip* **2016**, *16* (3), 599–610. <https://doi.org/10.1039/c5lc01356a>.
- (113) Morgan, K. Y.; Black, L. D. Mimicking Isovolumic Contraction with Combined Electromechanical Stimulation Improves the Development of Engineered Cardiac Constructs. *Tissue Eng. - Part A* **2014**, *20* (11–12). <https://doi.org/10.1089/ten.tea.2013.0355>.
- (114) Subramanian, G.; Elsaadany, M.; Bialorucki, C.; Yildirim-Ayan, E. Creating Homogenous Strain Distribution within 3D Cell-Encapsulated Constructs Using a Simple and Cost-Effective Uniaxial Tensile Bioreactor: Design and Validation Study. *Biotechnol. Bioeng.* **2017**, *114* (8). <https://doi.org/10.1002/bit.26304>.
- (115) Pavesi, A.; Adriani, G.; Rasponi, M.; Zervantonakis, I. K.; Fiore, G. B.; Kamm, R. D. Controlled Electromechanical Cell Stimulation On-a-Chip. *Sci. Rep.* **2015**, *5* (1), 11800. <https://doi.org/10.1038/srep11800>.
- (116) Hernández, D.; Millard, R.; Sivakumaran, P.; Wong, R. C. B.; Crombie, D. E.; Hewitt, A. W.; Liang, H.; Hung, S. S. C.; Pébay, A.; Shepherd, R. K.; et al. Electrical Stimulation Promotes Cardiac Differentiation of Human Induced Pluripotent Stem Cells. *Stem Cells Int.* **2016**, *2016*, 1–12. <https://doi.org/10.1155/2016/1718041>.
- (117) Adams, S. D.; Ashok, A.; Kanwar, R. K.; Kanwar, J. R.; Kouzani, A. Z. Integrated 3D Printed Scaffolds and Electrical Stimulation for Enhancing Primary Human Cardiomyocyte Cultures. *Bioprinting* **2017**, *6*, 18–24. <https://doi.org/10.1016/J.BPRINT.2017.04.003>.
- (118) Chan, Y. C.; Ting, S.; Lee, Y. K.; Ng, K. M.; Zhang, J.; Chen, Z.; Siu, C. W.; Oh, S. K. W.; Tse, H. F. Electrical Stimulation Promotes Maturation of Cardiomyocytes Derived from Human Embryonic Stem Cells. *J. Cardiovasc. Transl. Res.* **2013**, *6* (6), 989–999. <https://doi.org/10.1007/s12265-013-9510-z>.
- (119) Tandon, N.; Marsano, A.; Maidhof, R.; Wan, L.; Park, H.; Vunjak-Novakovic, G. Optimization of Electrical Stimulation Parameters for Cardiac Tissue Engineering. *J. Tissue Eng. Regen. Med.* **2011**, *5* (6), e115–e125. <https://doi.org/10.1002/term.377>.
- (120) Lux, M.; Andrée, B.; Horvath, T.; Nosko, A.; Manikowski, D.; Hilfiker-Kleiner, D.; Haverich, A.; Hilfiker, A. In Vitro Maturation of Large-Scale Cardiac Patches Based on a Perfusable Starter Matrix by Cyclic Mechanical Stimulation. *Acta Biomater.* **2016**, *30*, 177–187. <https://doi.org/10.1016/J.ACTBIO.2015.11.006>.

-
- (121) Gaio, N.; van Meer, B.; Quirós Solano, W.; Bergers, L.; van de Stolpe, A.; Mummery, C.; Sarro, P.; Dekker, R. Cytostretch, an Organ-on-Chip Platform. *Micromachines* **2016**, *7* (7), 120. <https://doi.org/10.3390/mi7070120>.
- (122) Liao, I.-C.; Liu, J. B.; Bursac, N.; Leong, K. W. Effect of Electromechanical Stimulation on the Maturation of Myotubes on Aligned Electrospun Fibers. *Cell. Mol. Bioeng.* **2008**, *1* (2–3), 133–145. <https://doi.org/10.1007/s12195-008-0021-y>.
- (123) Zhang, R. Stereolithographic Hydrogel Printing of 3D Microfluidic Cell Culture Chips, Technical University of Denmark, 2017.
- (124) Treloar, L. R. G. *The Physics of Rubber Elasticity*, 3rd ed.; Clarendon Oxford, 1975.
- (125) Holback, H.; Yeo, Y.; Park, K. Hydrogel Swelling Behavior and Its Biomedical Applications. In *Biomedical Hydrogels*; Elsevier, 2011; pp 3–24. <https://doi.org/10.1533/9780857091383.1.3>.
- (126) Yamaguchi, T.; Sato, R.; Sawae, Y. Propagation of Fatigue Cracks in Friction of Brittle Hydrogels. *Gels* **2018**, *4* (2), 53. <https://doi.org/10.3390/gels4020053>.
- (127) Zhang, D.; Shadrin, I. Y.; Lam, J.; Xian, H.-Q.; Snodgrass, H. R.; Bursac, N. Tissue-Engineered Cardiac Patch for Advanced Functional Maturation of Human ESC-Derived Cardiomyocytes. *Biomaterials* **2013**, *34* (23), 5813–5820. <https://doi.org/10.1016/j.biomaterials.2013.04.026>.
- (128) Kapnisi, M.; Mansfield, C.; Marijon, C.; Guex, A. G.; Perbellini, F.; Bardi, I.; Humphrey, E. J.; Puetzer, J. L.; Mawad, D.; Koutsogeorgis, D. C.; et al. Auxetic Cardiac Patches with Tunable Mechanical and Conductive Properties toward Treating Myocardial Infarction. *Adv. Funct. Mater.* **2018**, *28* (21). <https://doi.org/10.1002/adfm.201800618>.
- (129) Zhang, R.; Larsen, N. B. Stereolithographic Hydrogel Printing of 3D Culture Chips with Biofunctionalized Complex 3D Perfusion Networks. *Lab Chip* **2017**, *17*, 4273–4282. <https://doi.org/10.1039/c7lc00926g>.
- (130) Borochin, M. A.; Margulies, K. B.; Zandstra, P. W.; Boudou, T.; Radisic, M.; Thavandiran, N.; Epstein, J. A.; Mu, A.; Chen, C. S.; Legant, W. R. A Microfabricated Platform to Measure and Manipulate the Mechanics of Engineered Cardiac Microtissues. *Tissue Eng. Part A* **2011**, *18* (9–10), 910–919. <https://doi.org/10.1089/ten.tea.2011.0341>.
- (131) Grinnell, F. Mini-Review on the Cellular Mechanisms of Disease Fibroblasts, Myofibroblasts, and Wound Contraction. *J. Cell Biol.* **1994**, *124*, 401–404.
- (132) European Collection of Authenticated Cell Cultures. ECACC General Cell Collection: 3T3 Swiss Albino https://www.phe-culturecollections.org.uk/products/celllines/generalcell/detail.jsp?refId=85022108&collection=ecacc_gc (accessed Feb 23, 2020).
- (133) C2C12 Cell Line from mouse C3H muscle myoblast | Sigma-Aldrich https://www.sigmaaldrich.com/catalog/product/sigma/cb_91031101?lang=en®ion=DK&gclid=EAlaIQobChMlo-WuuLvE5wIVTYGyCh0cywllEAAYASAAEgleD_D_BwE (accessed Feb 9, 2020).
- (134) Yoshida, N.; Yoshida, S.; Koishi, K.; Masuda, K.; Nabeshima, Y. Cell Heterogeneity upon

- Myogenic Differentiation: Down-Regulation of MyoD and Myf-5 Generates 'Reserve Cells.' *J. Cell Sci.* **1998**, *111* (6), 769–779.
- (135) Reyhani, V.; Seddigh, P.; Guss, B.; Gustafsson, R.; Rask, L.; Rubin, K. Fibrin Binds to Collagen and Provides a Bridge for $\text{AV}\beta 3$ Integrin-Dependent Contraction of Collagen Gels. *Biochem. J.* **2014**, *462* (1), 113–123. <https://doi.org/10.1042/BJ20140201>.
- (136) Szibor, M.; Pöling, J.; Warnecke, H.; Kubin, T.; Braun, T. Remodeling and Dedifferentiation of Adult Cardiomyocytes during Disease and Regeneration. *Cell. Mol. Life Sci.* **2014**, *71* (10), 1907–1916. <https://doi.org/10.1007/s00018-013-1535-6>.
- (137) Pandey, P.; Hawkes, W.; Hu, J.; Megone, W. V.; Gautrot, J.; Anilkumar, N.; Zhang, M.; Hirvonen, L.; Cox, S.; Ehler, E.; et al. Cardiomyocytes Sense Matrix Rigidity through a Combination of Muscle and Non-Muscle Myosin Contractions. *Dev. Cell* **2018**, *44* (3), 326–336.e3. <https://doi.org/10.1016/J.DEVCEL.2017.12.024>.
- (138) Wang, H.; Svoronos, A. A.; Boudou, T.; Sakar, M. S.; Schell, J. Y.; Morgan, J. R.; Chen, C. S.; Shenoy, V. B. Necking and Failure of Constrained 3D Microtissues Induced by Cellular Tension. *Proc. Natl. Acad. Sci. U. S. A.* **2013**, *110* (52), 20923–20928. <https://doi.org/10.1073/pnas.1313662110>.
- (139) Pless, C. J. 3D Printed Microactuators for Cell Stimulation, Technical University of Denmark, 2019.
- (140) Plonsey, R.; Barr, R. C. Electrical Stimulation of Excitable Tissue. In *Bioelectricity*; Plonsey, R., Barr, R. C., Eds.; Springer US: Boston, MA, 2000; pp 179–216. https://doi.org/10.1007/978-1-4757-3152-1_7.
- (141) Nunes, S. S.; Miklas, J. W.; Liu, J.; Aschar-Sobbi, R.; Xiao, Y.; Zhang, B.; Jiang, J.; Massé, S.; Gagliardi, M.; Hsieh, A.; et al. Biowire: A Platform for Maturation of Human Pluripotent Stem Cell-Derived Cardiomyocytes. *Nat. Methods* **2013**, *10* (8), 781–787. <https://doi.org/10.1038/nmeth.2524>.
- (142) Thavandiran, N.; Dubois, N.; Mikryukov, A.; Masse, S.; Beca, B.; Simmons, C. A.; Deshpande, V. S.; McGarry, J. P.; Chen, C. S.; Nanthakumar, K.; et al. Design and Formulation of Functional Pluripotent Stem Cell-Derived Cardiac Microtissues. *Proc. Natl. Acad. Sci.* **2013**, *110* (49), E4698–E4707. <https://doi.org/10.1073/pnas.1311120110>.
- (143) Papadaki, M.; Bursac, N.; Langer, R.; Merok, J.; Vunjak-Novakovic, G.; Freed, L. E. Tissue Engineering of Functional Cardiac Muscle: Molecular, Structural, and Electrophysiological Studies. *Am. J. Physiol. - Hear. Circ. Physiol.* **2001**, *280* (1 49-1). <https://doi.org/10.1152/ajpheart.2001.280.1.h168>.
- (144) Murphy, J. F.; Mayourian, J.; Stillitano, F.; Munawar, S.; Broughton, K. M.; Agullo-Pascual, E.; Sussman, M. A.; Hajjar, R. J.; Costa, K. D.; Turnbull, I. C. Adult Human Cardiac Stem Cell Supplementation Effectively Increases Contractile Function and Maturation in Human Engineered Cardiac Tissues. *Stem Cell Res. Ther.* **2019**, *10* (1), 373. <https://doi.org/10.1186/s13287-019-1486-4>.
- (145) McCauley, M. D.; Wehrens, X. H. T. Animal Models of Arrhythmogenic Cardiomyopathy. *Dis. Model. Mech.* **2009**, *2* (11–12), 563–570. <https://doi.org/10.1242/dmm.002840>.

-
- (146) Shafaattalab, S.; Li, A. Y.; Lin, E.; Stevens, C. M.; Dewar, L. J.; Lynn, F. C.; Sanatani, S.; Laksman, Z.; Morin, R. D.; van Petegem, F.; et al. In Vitro Analyses of Suspected Arrhythmogenic Thin Filament Variants as a Cause of Sudden Cardiac Death in Infants. *Proc. Natl. Acad. Sci. U. S. A.* **2019**, *116* (14), 6969–6974. <https://doi.org/10.1073/pnas.1819023116>.
- (147) Grant, A. O. Cardiac Ion Channels. *Circ. Arrhythm. Electrophysiol.* **2009**, *2* (2), 185–194. <https://doi.org/10.1161/CIRCEP.108.789081>.
- (148) Chiron, S.; Tomczak, C.; Duperray, A.; Lainé, J.; Bonne, G.; Eder, A.; Hansen, A.; Eschenhagen, T.; Verdier, C.; Coirault, C. Complex Interactions between Human Myoblasts and the Surrounding 3D Fibrin-Based Matrix. *PLoS One* **2012**, *7* (4), e36173. <https://doi.org/10.1371/journal.pone.0036173>.
- (149) Tiburcy, M.; Hudson, J. E.; Balfanz, P.; Schlick, S.; Meyer, T.; Liao, M. L. C.; Levent, E.; Raad, F.; Zeidler, S.; Wingender, E.; et al. Defined Engineered Human Myocardium with Advanced Maturation for Applications in Heart Failure Modeling and Repair. *Circulation* **2017**, *135* (19), 1832–1847. <https://doi.org/10.1161/CIRCULATIONAHA.116.024145>.
- (150) Nugraha, B.; Buono, M. F.; von Boehmer, L.; Hoerstrup, S. P.; Emmert, M. Y. Human Cardiac Organoids for Disease Modeling. *Clin. Pharmacol. Ther.* **2019**, *105* (1), 79–85. <https://doi.org/10.1002/cpt.1286>.
- (151) Giacomelli, E.; Bellin, M.; Sala, L.; van Meer, B. J.; Tertoolen, L. G. J.; Orlova, V. V.; Mummery, C. L. Three-Dimensional Cardiac Microtissues Composed of Cardiomyocytes and Endothelial Cells Co-Differentiated from Human Pluripotent Stem Cells. *Development* **2017**, *144* (6), 1008–1017. <https://doi.org/10.1242/dev.143438>.
- (152) Sun, X.; Nunes, S. S. Biowire Platform for Maturation of Human Pluripotent Stem Cell-Derived Cardiomyocytes. *Methods* **2016**, *101*, 21–26. <https://doi.org/10.1016/j.ymeth.2015.11.005>.
- (153) Nortis Bio <https://www.nortisbio.com/> (accessed Feb 14, 2020).
- (154) Technology — Emulate <https://www.emulatebio.com/our-technology> (accessed Feb 14, 2020).
- (155) Technology | Mimetas <https://mimetas.com/page/technology> (accessed Feb 14, 2020).
- (156) Technology | TissUse GmbH <https://www.tissuse.com/en/technology/> (accessed Feb 14, 2020).
- (157) Prokhorova, T. A.; Harkness, L. M.; Frandsen, U.; Ditzel, N.; Schröder, H. D.; Burns, J. S.; Kassem, M. Teratoma Formation by Human Embryonic Stem Cells Is Site Dependent and Enhanced by the Presence of Matrigel. *Stem Cells Dev.* **2009**, *18* (1). <https://doi.org/10.1089/scd.2007.0266>.

Appendix 1

Design features to promote scaffold entrapment and tissue robustness

Different design changes are evaluated to discover if any additional support structures can enhance tissue formation while retaining the functional read-out possibility. Variations in the post based design are seen in Figure A.1. In Figure A.1A, supports are added to the post top and only 1 post can be deflected by tissue contraction. The idea is to support tissue formation without breaking the tissues due to print imperfections. Posts and supports are all cylindrical with 100 μm in diameter. One post is fixed and the other can be used for tracking of movement during tissue contraction.

In Figure A.1B,C guidewires of width 30 μm are printed between the posts to ensure support inside the tissue during long term culturing when the scaffold material is degraded. Guide wires are printed by addition of self-removing supports as described in section 3.3.3 and designed to be as thin as possible to allow deflection of the posts.

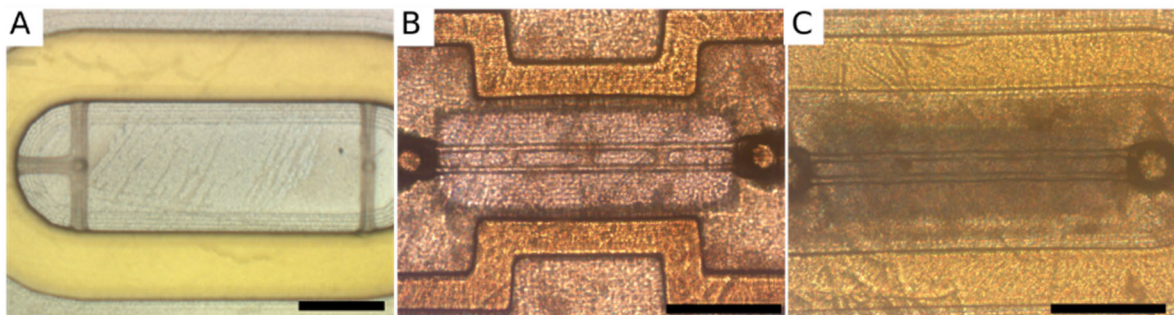


Figure A.1| Changing the design of the MAP mold to increase post-printing and tissue robustness includes mechanical support structures attached to the free distal ends. Neither of the solutions results in an improvement in tissue formation. A) Introducing a string based design with 1 end free B),C) Addition of thin supporting guide structures in the stadium shaped MAP (B) or dogbone shaped MAP (C). Scale bars: 500 μm .

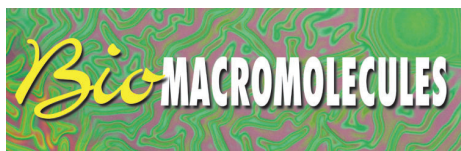
Appendix 2

Peer reviewed journal paper

This appendix contains the peer reviewed, published, journal paper with the title: *“3D Printed Hydrogel Multiassay Platforms for Robust Generation of Engineered Contractile Tissues”*.

It is published in ACS Biomacromolecules online on 20th of December 2019 and reprinted in this thesis with permission from the publisher.

Details on my contributions to the paper can be found in “List of collaborations”.

Cite This: *Biomacromolecules* 2020, 21, 356–365

pubs.acs.org/Biomac

<https://pubs.acs.org/articlesonrequest/AOR-qK5hbCxHd5VKjC6gs8UH>

3D Printed Hydrogel Multiassay Platforms for Robust Generation of Engineered Contractile Tissues

Rie Kjær Christensen,^{†,‡} Christoffer von Halling Laier,[†] Aysel Kiziltay,^{†,§} Sandra Wilson,[‡] and Niels Bent Larsen^{*,†}

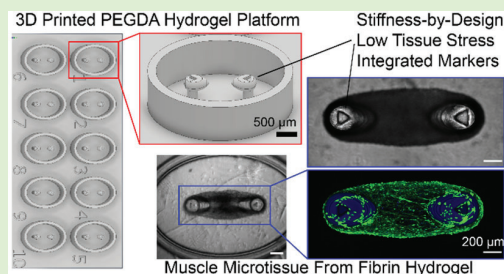
[†]Department of Health Technology, DTU Health Tech, Technical University of Denmark, Ørstedes Plads 345C, 2800 Kgs. Lyngby, Denmark

[‡]Sophion Bioscience A/S, Baltorpvej 154, 2750 Ballerup, Denmark

Supporting Information

ABSTRACT: We present a method for reproducible manufacture of multiassay platforms with tunable mechanical properties for muscle tissue strip analysis. The platforms result from stereolithographic 3D printing of low protein-binding poly(ethylene glycol) diacrylate (PEGDA) hydrogels. Contractile microtissues have previously been engineered by immobilizing suspended cells in a confined hydrogel matrix with embedded anchoring cantilevers to facilitate muscle tissue strip formation. The 3D shape and mechanical properties of the confinement and the embedded cantilevers are critical for the tissue robustness. High-resolution 3D printing of PEGDA hydrogels offers full design freedom to engineer cantilever stiffness, while minimizing unwanted cell attachment.

We demonstrate the applicability by generating suspended muscle tissue strips from C2C12 mouse myoblasts in a compliant fibrin-based hydrogel matrix. The full design freedom allows for new platform geometries that reduce local stress in the matrix and tissue, thus, reducing the risk of tissue fracture.



INTRODUCTION

Hydrogel materials made from biological or synthetic macromolecules are widely applied in the life science area, including in analytics and advanced cell culture. Hydrogels offer tunable protein and cell adhesion properties, widely variable mechanical properties, and controllable diffusivity of dissolved compounds. Hydrogel materials have traditionally been cast into their targeted final 3D shape, which limits the attainable design freedom. The recent emergence of 3D printing methods enables direct and fast manufacture of highly complex 3D shapes. Major 3D printing methods for hydrogels include mechanical extrusion of polymer solutions (including cell-laden hydrogels used in bioprinting)¹ and spatially selective photochemical cross-linking (stereolithography)² of macromolecules.

Engineering of miniaturized tissue-like 3D cell aggregates, for example contractile muscle tissue strips, is a key application of hydrogel 3D printing. Here, we explore the use of high-resolution stereolithographic 3D printing of a synthetic polymer—poly(ethylene glycol) diacrylate (PEGDA), into a force sensing and cell seeding hydrogel unit supporting the formation of contractile microtissues from a suspension of muscle cells in a biological polymer hydrogel (fibrinogen/Matrigel). Free-form 3D microshaping of the synthetic hydrogel parts enables broad tuning of the force responsiveness as well as guidance of the microtissue formed into a well-defined 3D shape with low residual stress. The combination of a low cell-adherent 3D printed PEGDA hydrogel mold and a

high cell-adherent fibrin hydrogel as cell matrix supports the robust formation of stable contractile microtissues needed for their applications, for example in drug development and safety screening. Our previous work on photochemically anchored poly(ethylene glycol) (PEG)³ and PEGDA⁴ hydrogel coatings demonstrated their ability to limit nonspecific adsorption of proteins, DNA, and small lipophilic drug molecules, which is essential for their use in drug testing devices. This is a significant advantage over previously published device solutions^{5–9} using poly(dimethylsiloxane) (PDMS) that is known to absorb and deplete dissolved lipophilic compounds.¹⁰

Engineered muscle tissue strips (MTS) are of broad interest in application areas such as drug screening, individualized medicine, disease modeling, and tissue grafts. As a result, methods to obtain a mature and robust muscle tissue have been explored during the past decade.^{11–19} A shift in tissue culture platform design from 2D cantilevers with adherent cells^{20–22} toward free hanging tissues between cantilever beams has been pursued as this 3D conformation seems to have a positive effect in both tissue formation and maturation.^{23–26} Producing a physiologically relevant 3D

Special Issue: Advances in Functional Polymers for Medicine

Received: September 15, 2019

Revised: November 1, 2019

Published: December 20, 2019

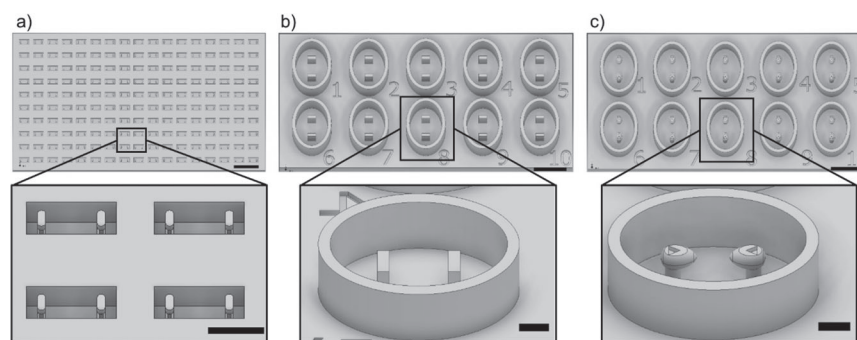


Figure 1. Multiassay platform (MAP) designs containing wells with integrated cantilevers for tissue formation. (a) Microwell MAP (MICROMAP) with 170 micro wells using rectangular cantilevers. (b) Mini-well MAP (MINIMAP) with 10 mini-wells using rectangular cantilevers. (c) Low residual Stress MAP (LOWSTRESSMAP) with 10 mini-wells using circular cantilevers with a cantilever end engineered to minimize local stress in the forming muscle microtissue. The LOWSTRESSMAP design additionally includes a 3D triangular micromarker at the cantilever end to facilitate automated optical tracking of the cantilever end displacement. Scale bars 2 mm (top row) and 500 μm (bottom row).

environment will promote cell differentiation and tissue formation compared to standard 2D or matrix encapsulation as it mechanically directs the cells to elongate and form better cell–cell connections.^{5,27–30}

A main challenge in contractile microtissue engineering is the robustness of the constructed tissues against “necking” behavior leading to subsequent failure.³¹ Previous studies have shown the importance of cantilever stiffness and matrix composition on the robustness of the engineered tissue.^{24,31–33} However, the effects of geometrical features of the cantilever itself have not been extensively studied, likely due to the limited 3D design freedom of conventional molding approaches. Here, we present a fast method for producing tissue formation platforms using synthetic PEGDA hydrogels to generate muscle microtissues. We employ a custom-built stereolithographic 3D printer to reproducibly manufacture tissue culturing platforms with microstructures for optical tracking and for promotion of tissue formation in designs that cannot be obtained by conventional molding or 3D printing methods. This allows for a broader design spectrum and gives the possibility to further explore the mechanically induced tissue-differentiation possibilities. The introduction of optical markers further enables accurate contraction analysis valuable in upscaling for industrial use.

MATERIALS AND METHODS

Stereolithographic 3D Printing and Printing Solution Composition. 3D structures made from poly(ethylene glycol)-diacrylate M_n 700 $\text{g}\cdot\text{mol}^{-1}$ (PEGDA, 455008, Sigma-Aldrich) hydrogels are obtained by projection stereolithography using a previously described custom-built high resolution 3D printer.² The printer uses one-to-one projection of dynamic images displayed on a Digital Mirror Device (DMD) with a pixel pitch of 10.8 μm in both lateral dimensions. The aqueous printing solutions contain 5 mg/mL photoinitiator (lithium phenyl-2,4,6-trimethylbenzoylphosphine, LAP, Allevi or 900889, Sigma-Aldrich) and 9 mg/mL photoabsorber (quinoline yellow, QY, 309052, Sigma-Aldrich) dissolved in ultrapure Milli-Q water (MQ, Merck-Millipore) with either 200 mg/mL PEGDA (“20% PEGDA”) or 500 mg/mL PEGDA (“50% PEGDA”). The solution components are mixed at room temperature and degassed for 30 min to avoid bubbles that would interfere with the initiator light and cause deformations in the 3D printed object.

Computer aided design (CAD) structures are drawn using Autodesk Inventor Professional with dimensions fitting a multiple of the pixel pitch (10.8 μm) of the printer’s DMD. This secures the best possible dimension accuracy of the printed subject compared to the CAD design dimensions. The CAD structure is sliced with a

thickness of 20 μm using the open source Slic3r software (www.slic3r.org). The sliced structure is 3D printed with 365 nm light with an intensity of 20 mW/cm^2 using 3 or 5 s of light exposure for 50% PEGDA and 20% PEGDA, respectively. The structure is 3D printed on a surface treated glass coverslip (22 \times 22 mm #4, Menzel-Gläser). The surface treatment provides a methacrylate layer on the coverslip to enable chemical cross-linking between the print and the glass cover slide.²

Analysis of the Relative Degree of Swelling and Dimensional Change. The dimensional stability of the 3D printed materials is assessed by measuring the time-dependent swelling of printed circular PEGDA cylinders immersed in water and by microscopy analysis of rectangular PEGDA blocks having rectangular indentations or protrusions at their surface. Circular cylinders of diameter 6 mm and height 5 mm are printed in 20% PEGDA and 50% PEGDA. The printed cylinders are weighed immediately after printing. The cylinders are then placed in MQ water and weighed every hour for 6 h. The MQ water is exchanged twice and cylinders are left in MQ water for a total of 16 h before the weight is determined again. Cylinders are dried at 60 $^{\circ}\text{C}$ for 8 h and the weight is monitored every second hour to obtain the stable dry weight. The equilibrium volumetric swelling ratio, Q , is determined for five cylinders of 20% PEGDA and of 50% PEGDA using eq 1, where V is volume, ρ is mass density, $q = m_s/m_d$ is the equilibrium mass swelling ratio, and m is the mass. Subscripts s and d indicate the swollen and dry polymer, respectively, while ρ_{pol} and ρ_{sol} are the polymer and solvent mass densities.

$$Q = 1 + \frac{\rho_{\text{pol}}}{\rho_{\text{sol}}}(q - 1) = \frac{V_s}{V_d} \quad (1)$$

The dimensional change after swelling is determined by printing 4 \times 5 \times 1 mm^3 blocks of 20% PEGDA and 50% PEGDA having rectangular surface indentations and protrusions with widths of 108 to 324 μm and a 1:3 width to length aspect ratio. The widths are designed to be multiples of the DMD’s 10.8 μm pixel pitch to achieve the highest possible spatial resolution. The depths of indentations and heights of protrusions are 100 μm for all surface features. The samples are imaged by microscopy immediately after printing and after equilibrium swelling in MQ water. The dimensions of the structures are determined using the FIJI/imageJ software package.³⁴

Compression Modulus Analysis. Circular cylinders of diameter 6 mm and height 5 mm are printed in 20% PEGDA and 50% PEGDA and left in MQ water overnight to reach their equilibrium swelling ratio. The dimensions of the swollen cylinders are determined, and the shear modulus is measured in a uniaxial compression test using an Instron 5967 (Instron, MA). Samples are placed wet between two parallel plates and compressed at a rate of 0.5 mm/min at room temperature until sample failure. The shear modulus (G) is determined by plotting the engineering stress (σ) against the $\lambda - \lambda^{-2}$

ratio according to eq 2, where λ is the extension ratio. Linear regression is performed in the linear region of $\lambda-\lambda^{-2}$ (0.2 to 0.6 for 50% PEGDA and 0.2 to 0.8 for 20% PEGDA) to determine G .³⁵

$$\sigma = G\left(\lambda - \frac{1}{\lambda^2}\right) \quad (2)$$

Cantilever Stiffness Analysis. Cantilevers of designed length 850 μm and diameters of 100, 200, and 300 μm are printed in 20% PEGDA and in 50% PEGDA. The printed cantilevers are placed horizontally in an aqueous environment with one end at a fixed height on a scale. A piezoelectric actuator is used to displace the free end of the cantilever vertically by 220 μm (Supporting Information, Figure S1). The measured weight increase on the scale is used to calculate the actuation force. The stiffness, k , is determined using eq 4 derived from the Euler–Bernoulli beam theory. F , E , and I are the force, Young's modulus, and moment of inertia, respectively. L , x , and δ denote the length of the cantilever, distance from the fixed end to the point of force application, and the vertical displacement, respectively.

$$F = k \cdot \delta = \frac{6EI}{3Lx^2 - x^3} \delta \quad (4)$$

The moment of inertia for a circular cylinder is given by eq 5, where d is the cylinder diameter.

$$I = \frac{\pi d^4}{64} \quad (5)$$

Five independent samples are analyzed for each condition, except for 100 μm diameter cantilevers in 20% PEGDA, where only three samples are analyzed due to inconsistent printing.

Preparation of Multiassay Platforms. Three different Multiassay Platforms (MAP) are produced for generating Muscle Tissue Strips (MTS). Two designs are selected from previously investigated cell seeding platforms with the use of vertical cantilevers reported by Legant et al.²⁴ and by Mills et al.^{13,25} (Figure 1a,b). The third design (Figure 1c) is developed to minimize stress concentrations around the vertical cantilevers to promote a more robust MTS formation. 3D printed MAPs are washed in phosphate buffered saline (PBS) for at least 24 h after printing. The liquid is exchanged two times to wash out any residual print solution from the cross-linked PEGDA network. Sterilization is performed by immersing the printed MAPs in 70% v/v ethanol/water for 10 min followed by UV–C exposure (254 nm) for 15 min (Mini UV Sterilization Cabinet, Cleaver Scientific). The MAPs are stored sterile in PBS until use to ensure exchange of water to PBS prior to cell culture. Before seeding cells into the MAPs, the PBS is removed and the platforms are blotted dry with sterile lint free paper to make sure the wells are empty.

Cell Seeding and Cell Culture. C2C12 mouse myoblasts (C3H muscle myoblast, 91031101, Sigma-Aldrich) are used at passages 5 to 8. Cells are kept in culture using growth medium composed of DMEM high glucose (Sigma-Aldrich) with 10% fetal bovine serum (FBS; Sigma-Aldrich) and 1% penicillin/streptomycin (P/S, Sigma-Aldrich). Tissue formation is initiated by casting cells suspended at 10×10^6 cells/mL in a solution of 10 mg/mL fibrinogen (F8630, Sigma-Aldrich), 0.5 $\mu\text{g/mL}$ aprotinin (A1153, Sigma-Aldrich), 20% (v/v) Matrigel (354277, Corning), and 3 U/mL thrombin (T7513, Sigma-Aldrich) in growth medium into the prepared MAPs. The solution is kept on ice to prevent gelation until casting. The larger MAP wells (“MINIMAP”, Figure 1b; “LOWSTRESSMAP”, Figure 1c) are filled individually with 3.5 μL of the cell suspension. The smaller MAP wells (“MICROMAP”, Figure 1a) are filled in a two-step process. First, 200 μL of cell suspension is loaded on top of all wells of the MAP. Second, the MAP is spun in a centrifuge at 200 g for 10 s to force the suspension into the wells, similar to the process used in the work by Legant et al.²⁴

The loaded MAPs are incubated at 37 $^\circ\text{C}$ for 30 min to let the fibrin matrix form before growth medium is added. After 2 days in culture, the medium is changed to DMEM high glucose with 2% FBS and 1% P/S to enhance the fusion of myoblasts to myotubes.³⁶

Medium change is conducted every 2–3 days throughout the culture time.

Optical Tracking of Tissue Formation. The wells of a LOWSTRESSMAP printed in 50% PEGDA and with a cantilever diameter of 100 μm are imaged from day 1 after seeding until full tissue formation. Tissue contraction is monitored using a custom-made stage incubator mounted on a Motic stereomicroscope. Images are recorded every 5 min. A custom-made tracking software is used to track the optical markers on the cantilever tops in the acquired image sequences.

Viability Staining. Staining is performed by incubating for 1 h at 37 $^\circ\text{C}$ with 2 $\mu\text{g/mL}$ Calcein AM (15560597, Fisher Scientific), 4 $\mu\text{g/mL}$ propidium iodide (81845, Sigma-Aldrich), and 2 $\mu\text{g/mL}$ Hoechst 34580 (H21486, Invitrogen). Samples are then washed with medium before confocal imaging on a Zeiss LSM700 using a Zeiss 10 \times /0.3NA Epiplan Neofluar objective with an excitation at 405, 488, and 555 nm for Hoechst 34580, calcein AM, and propidium iodide, respectively. The recorded z-stacks are collapsed to a 2D image in FIJI/ImageJ by maximum intensity projection.

Cryopreservation and Immunohistochemistry. Cell-laden MAPs are fixed in 4% paraformaldehyde (PFA) for 30 min, washed in PBS and cryo protected by incubation at room temperature in a 10 mg/mL solution of poly(ethylene glycol) M_n 10 kg $\cdot\text{mol}^{-1}$ (PEG10k, 92897, Sigma-Aldrich) for 6–8 h followed by incubation in 100 mg/mL PEG10k overnight at 4 $^\circ\text{C}$. The samples are gently dried to remove excess PEG10k and transferred into embedding medium (Tissue-Tek OCT Compound, Leica) before being snap-frozen on isopentane chilled on liquid nitrogen and stored at -80 $^\circ\text{C}$. For immunohistochemistry, 10 to 20 μm thick sections are cut at -25 $^\circ\text{C}$ using a cryo microtome (Leica 3050) and dried.

For α -actinin labeling, cryo sections on glass slides are first washed with PBS to remove excess OCT and then permeabilized in 0.2% Triton X-100 for 5 min and blocked in blocking buffer (2% w/v BSA and 5% v/v horse serum in PBS) for 1 h at room temperature (RT). The sections are then incubated for 2 h at RT in blocking buffer with 1:200 monoclonal anti- α -actinin (sarcomeric) IgG produced in mouse (A7811, Sigma-Aldrich). They are subsequently washed twice with PBS and incubated for 2 h at RT in the dark with 2 $\mu\text{g/mL}$ polyclonal FITC-conjugated goat F(ab')₂ antimouse IgG (H+L) (SAB4600388, Sigma-Aldrich) in blocking buffer. Afterward, sections are stained with 2 $\mu\text{g/mL}$ Hoechst 34580 for 15 min and washed 3 times with PBS. The sections are imaged with a Nikon Ti2/Yokogawa CSU-W1 spinning disc confocal microscope using a Nikon Plan Apo λ 20 \times /0.75 NA objective with excitation at 405 and 488 nm for Hoechst 34580 and FITC, respectively. The resulting image stacks are processed using FIJI/ImageJ.

RESULTS AND DISCUSSION

Design and Manufacture of Multiassay Platforms (MAPs). Controlling the cellular orientation and the mechanical environment are key factors to achieve better and more robust translation from single cells to tissue. Various MAP designs using similar design concepts have been reported over the past decade.^{24,26,13,25} All have shown aligned growth of contractile cells, including fibroblasts, myotubes, and cardiomyocytes.³⁷ However, previous reports mostly use low throughput manufacturing methods. The authors also observe tissue damage and failure due to high internal stresses in the formed tissues. Most research has employed rectangular cantilevers that are likely to induce large tensile stress in the seeded cell-laden matrix hydrogel during initial hydrogel compaction and subsequent tissue formation. The stress is predicted to be maximum along the center line of the microtissue suspended between the cantilevers.³¹ The full design freedom offered by stereolithographic 3D printing can be exploited to integrate tissue guide structures that reduces the intermittent and final stress. Another key design aspect is

the microtissue size, with smaller sizes needing fewer cells per tissue but also likely complicating the seeding procedure due to the tiny matrix volumes used. Large tissues are easier to handle but may suffer from core cell death and propensity for tissue failure due to insufficient oxygen and nutrient diffusion to the tissue core. We investigate both design parameters by using stereolithographic 3D printing of PEGDA to functionally reproduce two formerly published rectangular PDMS cantilever designs of different sizes as baseline for evaluating a new design overcoming the residual stress limitations of the rectangular cantilever format.

One design reported by Legant et al.²⁴ uses micro-sized cantilevers and tissues ("MICROMAP"; Figure 1a), while the other design reported by Mills et al.²⁵ employs mesosized cantilevers and tissues ("MINIMAP"; Figure 1b). Both MAP designs have showed successful tissue formation using contractile cells. We also introduce a new MAP format, LOWSTRESSMAP, designed to lower the stress concentrations in the formed tissues around the edges of the cantilever end (Figure 1c). A droplet shaped enlargement with soft edges to reduce local stresses (referred to as "biomechanical cue") is added at the top of a cylindrical cantilever to guide the location of the tissue formed. It is shaped with rounded edges to reduce stress concentrations and secure the tissue from slipping off the cantilevers. Printing times are 8 min for the 170-well MICROMAP design and 17 min for the 10-well MINIMAP and LOWSTRESSMAP designs. All MAPs are fabricated in PEGDA having low protein-binding surface properties to prevent unwanted cell attachment. The material properties of cross-linked PEGDA vary greatly with the concentration of the printing solution components and with the exposure time. Solution composition and exposure times are chosen to provide robust and reproducible manufacturing of the chosen cantilever designs.

Mechanical Characterization of 3D Printed PEGDA Hydrogels. The shear modulus of hydrogels printed using 20% PEGDA and 50% PEGDA is determined by a uniaxial compression test. Increasing the PEGDA concentration from 20% to 50% results in nearly an 8-fold increase in shear modulus from 0.47 ± 0.046 MPa to 3.6 ± 0.46 MPa. The denser network formed at the higher PEGDA concentration results in a more brittle platform, which makes it more susceptible to notching and subsequent failure during handling. The lower PEGDA concentration is consequently preferred to create a more flexible and stable MAP³⁸ in the handling process during cell seeding and analysis.

Dimensional Stability of 3D printed PEGDA Hydrogels. MAP design features are carefully selected to give a robust platform with visible markers and robust structures. Reliable dimensions are therefore essential to MAP characteristics. PEGDA has a higher affinity for water than for itself and will swell after printing, when transferred from the printing solution to pure water.³⁹ The equilibrium volumetric swelling ratio, Q , is reached after 3 h for 3D printed objects in 20% PEGDA and in 50% PEGDA immersed in MQ water at room temperature (Figure 2). The relative volumetric increase from pristine print to equilibrium swelling is 15.3% for 50% PEGDA and 9.2% for 20% PEGDA. The swelling ratio is higher at lower PEGDA concentration due to a higher initial water content in the samples. However, the relative volumetric swelling from pristine print to equilibrium swollen state will increase with increasing concentrations of PEGDA, as seen in

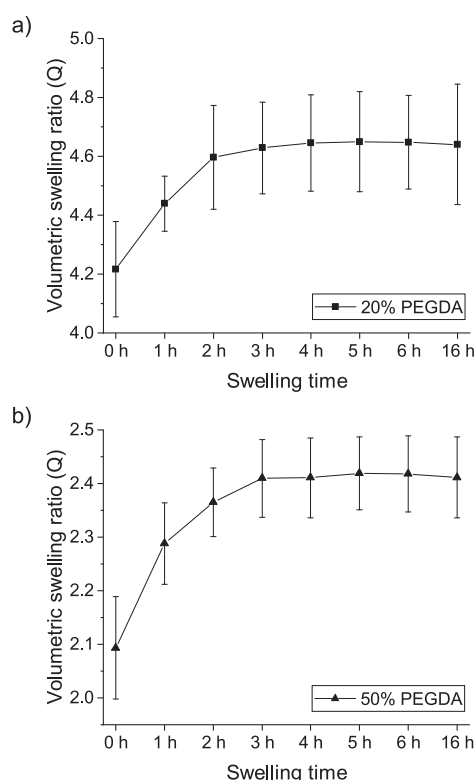


Figure 2. Mean volumetric swelling ratio of (a) 20% PEGDA and (b) 50% PEGDA measured on 5 mm high and 6 mm diameter cylinders immersed in MQ water after printing. Cylinders incubated for 16 h are dried for 8 h at 60 °C before measuring the dry polymer mass. Error bars show the standard deviation ($n = 5$).

Figure 2. Thus, the change in size over the designed dimensions will be larger at higher PEGDA concentrations.

Extruded features will increase in size post swelling as described above. The cantilevers of the printed MAP will therefore be larger than their CAD design dimensions. The microscopic dimensional change of the printed samples is determined by making CAD designs with rectangular indentations and protrusions (Supporting Information, Figure S2). The feature widths are measured immediately after printing, as well as after swelling to equilibrium. Measured dimensions are compared to the original CAD dimensions. Figure 3 compares the CAD design to the initially printed dimensions and the final postswelling dimensions. For both PEGDA concentrations, protrusions exhibit less deviation from nominally designed dimensions to postswelling than indentations. MAP designs are therefore largely constructed as protrusions with regards to cantilevers and well boundaries to ensure stability. Protrusion-based designs such as the MINIMAP and LOWSTRESSMAP further benefit from using less material, thus easing the postmanufacture washing procedure.

Indentations in selected structures of the LOWSTRESSMAP function are chosen as optical markers since indentations are easier to visualize by microscopy than extrusions. In general, the relative precision is higher for larger structures than for smaller structures at both PEGDA concentrations (Figure 3). Feature sizes are, therefore, carefully considered when designing features such as optical markers and mechanical cues to ensure manufacturability.

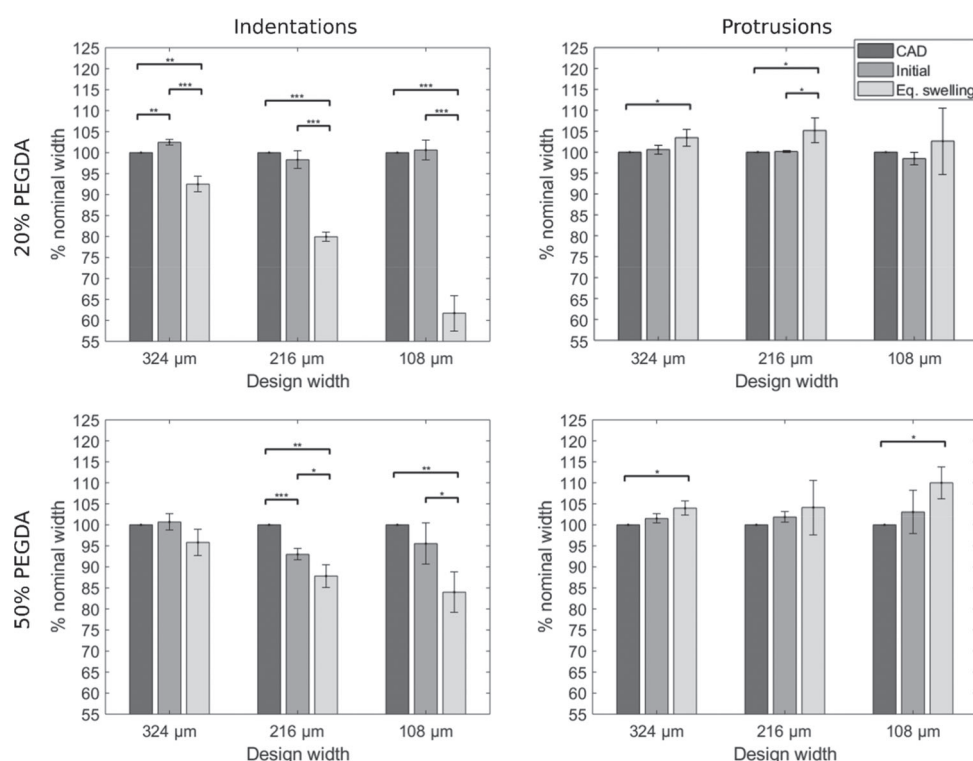


Figure 3. Measured dimensional change of the initial printed width and the equilibrium swelling width of rectangular indentations and protrusions, relative to the nominal width of the CAD design. Nominal widths range from 108 to 324 μm , and the designs are printed in 20% PEGDA and 50% PEGDA. Error bars show the standard deviation ($n = 3$); * $p < 0.05$, ** $p < 0.01$, *** $p < 0.001$.

Controlling Cantilever Stiffness by Design and Print Composition.

Quantitative readout of the MTS contraction force depends on knowledge of the mechanical properties of the cantilevers on which the MTS is anchored. The cantilever stiffness depends strongly on its dimensions and can therefore easily be modified by design. The moment of inertia and thereby the stiffness of cantilevers with a circular cross-sectional area is predicted to depend on the fourth power of cantilever diameter, as described by eq 5. The stiffness of 850 μm long circular 3D printed cantilevers with diameters of 100, 200, and 300 μm is determined directly by measuring the force needed to deflect the cantilevers by a fixed distance (220 μm). The stiffness of cantilevers in 20% PEGDA is 0.07 ± 0.006 N/m (mean \pm SD) for a nominal diameter of 100 μm , 0.3 ± 0.08 N/m at 200 μm diameter, and 2.4 ± 0.3 N/m at 300 μm diameter. A similar correlation is observed for cantilevers in 50% PEGDA with a measured stiffness of 0.16 ± 0.04 N/m for a nominal diameter of 100 μm , 3.05 ± 0.35 N/m at 200 μm nominal diameter, and 19.2 ± 0.66 N/m at 300 μm nominal diameter. Figure 4 illustrates that cantilever stiffnesses covering almost 3 orders of magnitude are accessible by varying the print design and the PEGDA composition. As a lower bound on the available dimensions, we found that the aspect ratio of 100 μm diameter cantilevers is too high to be stably produced in 20% PEGDA, whereas the 100 μm cantilevers in 50% PEGDA are robustly printed due to the higher cross-linking density. Even lower stiffnesses can be achieved by using longer cantilever designs, since their stiffness scales with the negative third power of their length (see eq 4). Contractile cells adapt their cytoskeleton to form an elongated structure depending on the mechanical influence provided by the cantilevers. The

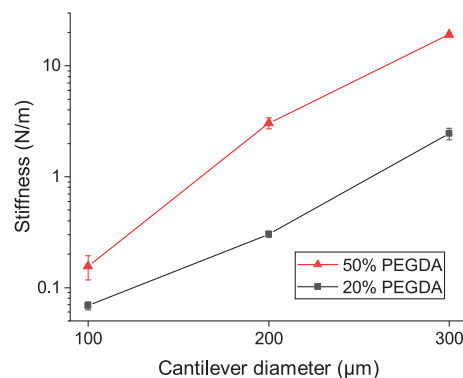


Figure 4. Cantilever stiffness dependence on the design diameter for 850 μm long circular cantilevers printed in 20% PEGDA or 50% PEGDA. Error bars show the standard deviations ($n = 5$).

optimal stiffness for robust formation of contractile tissue will depend on the specific cell line. It is important to match the cantilever stiffness to the contractile strength of the cells to avoid tissue necking and subsequent breaking.^{31,32}

Varying the PEGDA concentration or the cantilever diameter changes the cantilever stiffness and thus the force needed to deflect it. Using the mouse myoblasts C2C12 cell line, we show a strong correlation between cantilever stiffness and the ability of the tissues to deflect the cantilevers. Figure 5 shows that stiffnesses up to 0.3 N/m (compare with Figure 4) allow the formed tissues to deflect the cantilevers with larger deflection observed at lower stiffness. The tissues exert a force of 38 ± 7 μN (mean \pm SD, $n = 5$) calculated from the

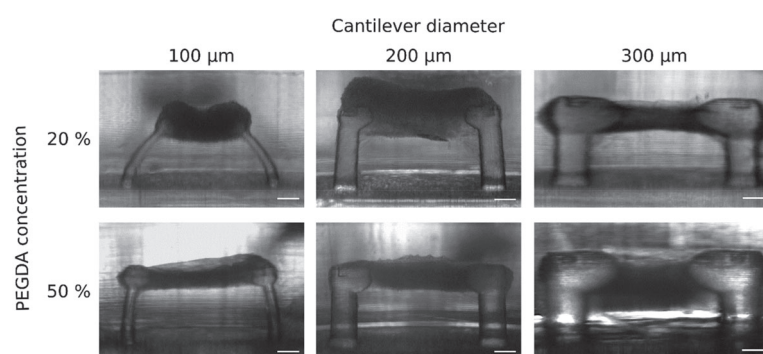


Figure 5. Deflection of cantilevers with varying diameter and PEGDA concentration. All cantilevers are of equal height and the formed tissues consist of an equal number of cells. A strong correlation between cantilever stiffness and the ability of the mouse myoblast tissue to deflect the cantilevers is observed. Cantilever deflection is seen at both concentrations for cantilevers of 100 μm diameter and for 20% PEGDA 200 μm diameter. No deflection is observed for the remaining cantilevers. Scale bars: 200 μm .

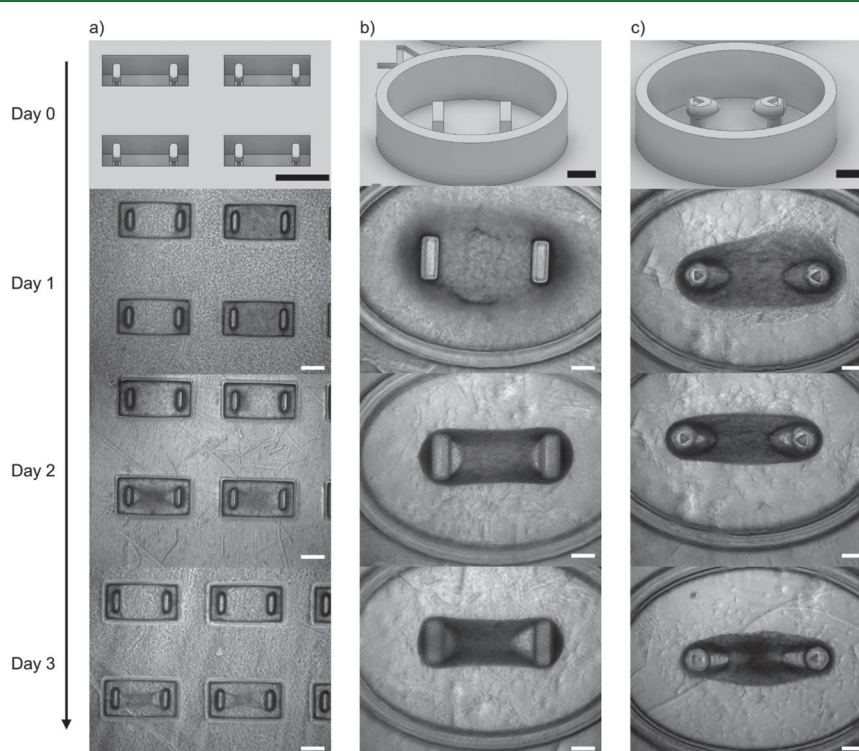


Figure 6. Tissue formation is observed over 4 days from cell loading into (a) MICROMAPS, (b) MINIMAPS, and (c) LOWSTRESSMAPs, until compacted tissues are observed at day 3. White scale bars: 250 μm . Black scale bars: 500 μm .

deflection of the cantilevers seen in side view (Figure 5) and the measured cantilever stiffness (Figure 4).

Formation of Muscle Tissue Strips. C2C12 mouse myoblasts are cast at 10×10^6 cells/mL in a fibrin/Matrigel matrix in the three different MAPs. C2C12 cells will start to differentiate when they are in close proximity to each other.⁴⁰ Upon differentiation, the myoblasts fuse and form myotubes. Elongation of the cells is a sign of differentiation and shows alignment of the sarcomeres responsible for cell contraction.⁴¹ When the sarcomeres align, the cells can exert more force in the direction of the elongation. As the cell laden fibrin matrix is embedded around the cantilevers, the cells' contraction of the matrix is restricted by the cantilevers causing them to form an elongated structure and eventually an MTS. The stiffness of the cantilevers will continue to provide an opposing force

when the cells are contracting, which is believed to aid the differentiation of the myoblasts into muscle cells.^{9,42} After 24 h of culture, the cells have started to contract the fibrin matrix and form a tissue surrounding the two cantilevers (Figure 6). Two days after seeding, well-defined tissues are seen in all designs.

In the MICROMAP, the formed tissue is surrounded by excess cells captured in the matrix without contributing to the tissue formation (Figure 7a,b). The MICROMAP format requires fewer cells per well due to the small well size, but requires a highly inefficient cell seeding method with a lot of lost cells. In both the MICROMAP and MINIMAP, tissues are at risk of thinning and ultimately breaking due to necking, as seen in Figure 7b,d, marked with yellow dashed lines. Necking is known to cause engineered tissues to fracture, regardless of

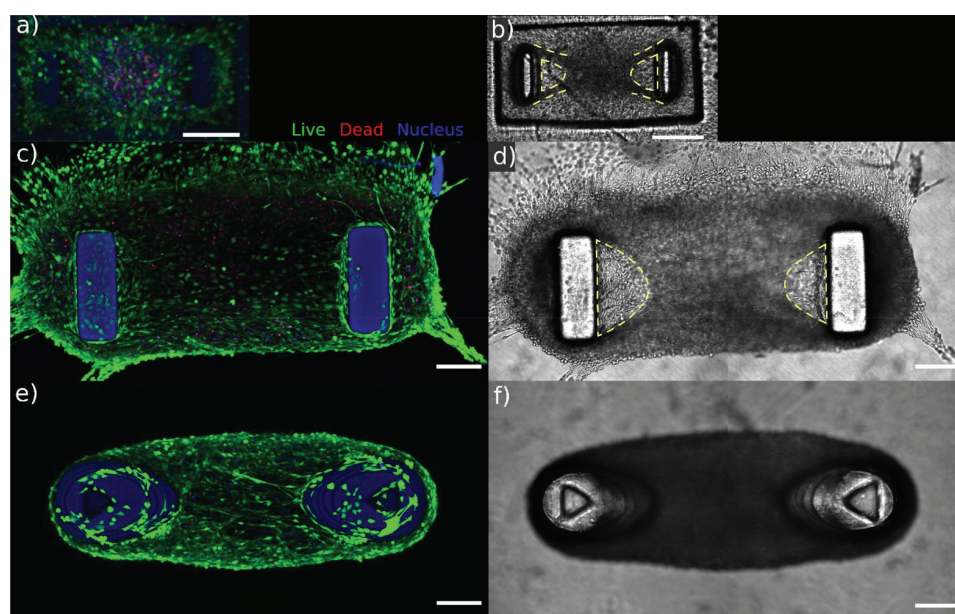


Figure 7. Optical micrographs of C2C12 microtissues cultured for 3 days in MICROMAP (a, b), MINIMAP (c, d), and LOWSTRESSMAP (e, f) designs. All seedings use C12C12 at 10×10^6 cells/mL in a 10 mg/mL fibrin gel with 20% v/v Matrigel. (a, c, e) Maximum intensity projections of confocal fluorescence stacks of cells stained for live cells (green, calcein AM), dead cells (red, propidium iodide), and nuclei (blue, Hoechst 33450). The printed cantilevers are also seen in the blue channel due to autofluorescence of PEGDA. (b, d, f) Maximum intensity projections of confocal bright field stacks. Yellow dashed lines indicate the areas where the tissues are thinning from the stress induced by the edge of the cantilevers. Scale bars: 200 μm .

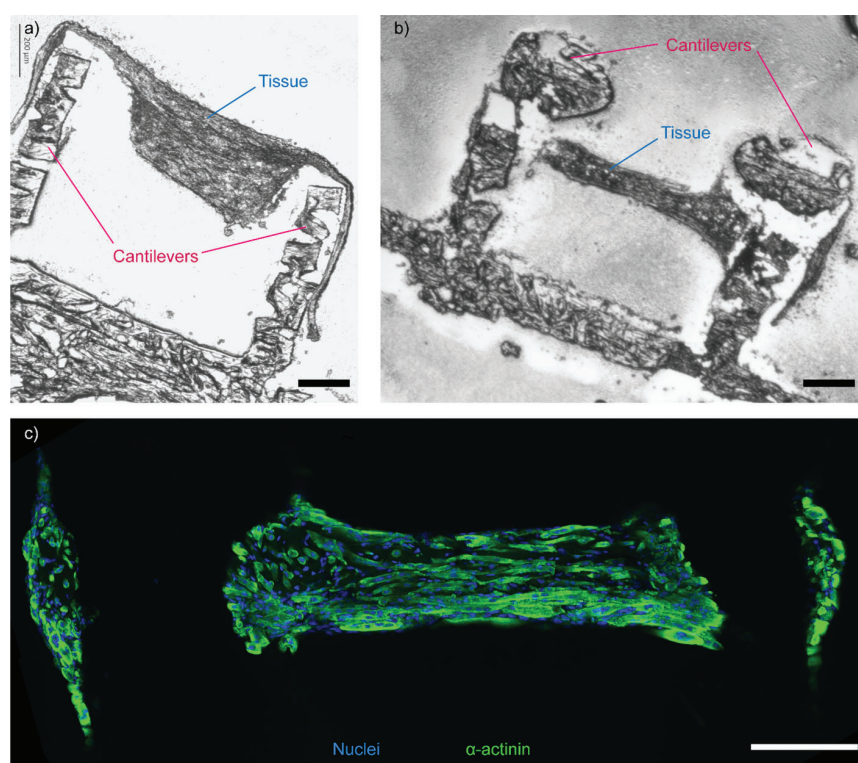


Figure 8. Brightfield micrographs of (a) MINIMAP and (b) LOWSTRESSMAP designs with C2C12 muscle tissue strips after fixation and cryosectioning (20 μm thick slice). (c) Spinning disc confocal image of the LOWSTRESSMAP muscle tissue strip seen in (b) stained for α -actinin (green) and nuclei (blue). Scale bars: 200 μm .

cell type, and poses a serious challenge in tissue engineering.^{25,31,32} Circular cantilevers provide an advantage over

rectangular cantilevers by not introducing the same degree of stress concentrations around the corners. This reduces the risk

of the thinning and ultimately breaking of the tissue that is seen in the MICROMAP and MINIMAP tissues (Figure 6). Tissues created in our LOWSTRESSMAP design using circular cantilevers with soft-edged biomechanical cues show no thinning around the cantilevers at day 3 of culture. This MTS also exhibit a more defined tissue formation as seen in Figure 6c and Figure 7e,f. All engineered tissues show a high cell viability and a tight cellular structure with aligned cells (Figure 7a,c,e).

Cryosectioned slices of the MINIMAP and LOWSTRESSMAP tissues show that the tissue wraps around the cantilevers at the top so that these are fully surrounded by the tissues formed, as required for optimal force transmission (Figure 8a,b). The tissue in the MINIMAP design fully enclose the cantilever ends and substantial parts of the cantilever length, which does not allow for a well-defined attachment point as required in the Euler–Bernoulli theory for calculating the contraction force (Figure 8a). In contrast, the mechanical cue added at the top of the circular cantilevers in the LOWSTRESSMAP design causes less necking and better confinement of the tissue near the free cantilever end (Figure 8b). Figure 8c shows that the cells in the LOWSTRESSMAP design are aligned in the direction of the opposing force acting on the tissue from the cantilever. Cells are multinucleated suggesting that the myoblasts have fused to form myotubes. Introducing a biomechanical cue at the top of the cantilever makes the tissue form uniformly around the cantilever (Figure 8b). The alignment and uniformness of the MTS indicate that all cells experience the same opposing force and develop uniformly within the tissue.

As discussed, the new LOWSTRESSMAP design includes a visually distinct marker on top of each cantilever. The marker is seen as a triangle in Figure 6c and Figure 7f. When tissues form around the cantilever at the cue on top of the cantilevers, the height of tissue attachment is well-defined. This enables reliable calculation of the contractile force based on cantilever stiffness and deflection. The time-dependent cantilever deflection can be determined by optical tracking of the incorporated optical markers (Supporting Information, Videos V1 and V2), thus, enabling calculation of the force exerted by the cells in the engineered muscle tissue strip.

CONCLUSIONS

Our results show that high-resolution stereolithographic 3D printing of PEGDA hydrogels can mass-produce micro-mechanical objects, such as cantilevers, with high precision and with high accuracy. High accuracy is achieved by characterizing and accounting for postprinting swelling properties of hydrogels in the print design and in the choice of printing solution composition. Precise and accurate micro-manufacturing enables fast and robust fabrication of cell seeding platforms for use in microtissue engineering, in a format that can be upscaled for commercial production. The cantilever stiffness is easily controlled by changing its design, which makes the platform suitable for various cell types with different contractile properties. The use of circular cylindrical cantilevers with an integrated stress-reducing biomechanical cue at their ends results in well-defined muscle tissue strips without observable necking. Tissues are consistently formed at the bottom of the biomechanical cue, thus, fixing the height of attachment on the cantilever. This is in contrast to the extended and variable length of attachment observed on rectangular cantilevers. A consistent and short length of

tissue–cantilever attachment is key to subsequent reliable force readout, as the underlying Euler–Bernoulli theory requires a single well-defined point of actuation to translate observed cantilever deflection to exerted tissue force.

ASSOCIATED CONTENT

Supporting Information

The Supporting Information is available free of charge at <https://pubs.acs.org/doi/10.1021/acs.biomac.9b01274>.

Optical micrographs of the experimental stiffness measurement of 3D printed cantilever structures. Drawing of the test structures used for assessing dimensional changes (PDF)

Video V1 (MP4)

Video V2 (MP4)

AUTHOR INFORMATION

Corresponding Author

*E-mail: nibl@dtu.dk. Fax: +45 4588 7762. Tel.: +45 4525 8161.

ORCID

Christoffer von Halling Laier: 0000-0001-9398-5344

Niels Bent Larsen: 0000-0001-6506-3991

Present Address

[§]Central Laboratory, Middle East Technical University (METU), Ankara, Turkey.

Author Contributions

The manuscript was written through contributions of all authors. All authors have given approval to the final version of the manuscript.

Notes

The authors declare no competing financial interest.

ACKNOWLEDGMENTS

We acknowledge financial support from Innovation Fund Denmark (industrial Ph.D. Grant 5189-00149B) and EUREKA Eurostars (CARDIOCONTRACT Grant 01032018).

REFERENCES

- (1) Kolesky, D. B.; Truby, R. L.; Gladman, A. S.; Busbee, T. A.; Homan, K. A.; Lewis, J. A. 3D Bioprinting of Vascularized, Heterogeneous Cell-Laden Tissue Constructs. *Adv. Mater.* **2014**, *26* (19), 3124–3130.
- (2) Zhang, R.; Larsen, N. B. Stereolithographic Hydrogel Printing of 3D Culture Chips with Biofunctionalized Complex 3D Perfusion Networks. *Lab Chip* **2017**, *17* (24), 4273–4282.
- (3) Larsen, E. K. U.; Larsen, N. B. One-Step Polymer Surface Modification for Minimizing Drug, Protein, and DNA Adsorption in Microanalytical Systems. *Lab Chip* **2013**, *13* (4), 669–675.
- (4) Larsen, E. K. U.; Mikkelsen, M. B. L.; Larsen, N. B. Facile Photoimmobilization of Proteins onto Low-Binding PEG-Coated Polymer Surfaces. *Biomacromolecules* **2014**, *15* (3), 894–899.
- (5) Ulmer, B. M.; Stoeck, A.; Schulze, M. L.; Patel, S.; Gucek, M.; Mannhardt, I.; Funcke, S.; Murphy, E.; Eschenhagen, T.; Hansen, A. Contractile Work Contributes to Maturation of Energy Metabolism in hiPSC-Derived Cardiomyocytes. *Stem Cell Rep.* **2018**, *10* (3), 834–847.
- (6) Vandenburgh, H.; Shansky, J.; Benesch-Lee, F.; Barbata, V.; Reid, J.; Thorrez, L.; Valentini, R.; Crawford, G. Drug-Screening Platform Based on the Contractility of Tissue-Engineered Muscle. *Muscle Nerve* **2008**, *37* (4), 438–447.
- (7) Lux, M.; Andr  e, B.; Horvath, T.; Nosko, A.; Manikowski, D.; Hilfiker-Kleiner, D.; Haverich, A.; Hilfiker, A. In Vitro Maturation of

- Large-Scale Cardiac Patches Based on a Perfusable Starter Matrix by Cyclic Mechanical Stimulation. *Acta Biomater.* **2016**, *30*, 177–187.
- (8) Gaio, N.; van Meer, B.; Quirós Solano, W.; Bergers, L.; van de Stolpe, A.; Mummery, C.; Sarro, P.; Dekker, R. Cytostretch, an Organ-on-Chip Platform. *Micromachines* **2016**, *7* (7), 120.
- (9) Liao, L.-C.; Liu, J. B.; Bursac, N.; Leong, K. W. Effect of Electromechanical Stimulation on the Maturation of Myotubes on Aligned Electrospun Fibers. *Cell. Mol. Bioeng.* **2008**, *1* (2–3), 133–145.
- (10) Li, N.; Schwartz, M.; Ionescu-Zanetti, C. PDMS Compound Adsorption in Context. *J. Biomol. Screening* **2009**, *14* (2), 194–202.
- (11) Cvetkovic, C.; Raman, R.; Chan, V.; Williams, B. J.; Tolish, M.; Bajaj, P.; Sakar, M. S.; Asada, H. H.; Saif, M. T. A.; Bashir, R. Three-Dimensionally Printed Biological Machines Powered by Skeletal Muscle. *Proc. Natl. Acad. Sci. U. S. A.* **2014**, *111* (28), 10125–10130.
- (12) Kensah, G.; Roa Lara, A.; Dahlmann, J.; Zweigerdt, R.; Schwanke, K.; Hegemann, J.; Skvorc, D.; Gawol, A.; Azizian, A.; Wagner, S.; Maier, L. S.; Krause, A.; Dräger, G.; Ochs, M.; Haverich, A.; Gruh, I.; Martin, U. Murine and Human Pluripotent Stem Cell-Derived Cardiac Bodies Form Contractile Myocardial Tissue in Vitro. *Eur. Heart J.* **2013**, *34* (15), 1134–1146.
- (13) Mills, R. J.; Parker, B. L.; Monnot, P.; Needham, E.; Vivien, C. J.; Ferguson, C.; Parton, R. G.; James, D. E.; Porrello, E. R.; Hudson, J. E. Development of a Human Skeletal Muscle Platform with Pacing Capabilities. *Biomaterials* **2019**, *198*, 217–227.
- (14) Sidorov, V. Y.; Samson, P. C.; Sidorova, T. N.; Davidson, J. M.; Lim, C. C.; Wikswo, J. P. I-Wire Heart-on-a-Chip I: Three-Dimensional Cardiac Tissue Constructs for Physiology and Pharmacology. *Acta Biomater.* **2017**, *48*, 68–78.
- (15) Schroer, A. K.; Shotwell, M. S.; Sidorov, V. Y.; Wikswo, J. P.; Merryman, W. D. I-Wire Heart-on-a-Chip II: Biomechanical Analysis of Contractile, Three-Dimensional Cardiomyocyte Tissue Constructs. *Acta Biomater.* **2017**, *48*, 79–87.
- (16) Lemoine, M. D.; Krause, T.; Koivumäki, J. T.; Prondzynski, M.; Schulze, M. L.; Girdauskas, E.; Willems, S.; Hansen, A.; Eschenhagen, T.; Christ, T. Human Induced Pluripotent Stem Cell-Derived Engineered Heart Tissue as a Sensitive Test System for QT Prolongation and Arrhythmic Triggers. *Circ.: Arrhythmia Electrophysiol.* **2018**, *11* (7), No. e006035.
- (17) Nugraha, B.; Buono, M. F.; von Boehmer, L.; Hoerstrup, S. P.; Emmert, M. Y. Human Cardiac Organoids for Disease Modeling. *Clin. Pharmacol. Ther.* **2019**, *105* (1), 79–85.
- (18) Nawroth, J. C.; Scudder, L. L.; Halvorson, R. T.; Tresback, J.; Ferrier, J. P.; Sheehy, S. P.; Cho, A.; Kannan, S.; Sunyovszki, I.; Goss, J. A.; Campbell, P. H.; Parker, K. K. Automated Fabrication of Photopatterned Gelatin Hydrogels for Organ-on-Chips Applications. *Biofabrication* **2018**, *10* (2), 025004.
- (19) Benam, K. H.; Dauth, S.; Hassell, B.; Herland, A.; Jain, A.; Jang, K.-J.; Karalis, K.; Kim, H. J.; MacQueen, L.; Mahmoodian, R.; Musah, S.; Torisawa, Y.-S.; van der Meer, A. D.; Villenave, R.; Yadid, M.; Parker, K. K.; Ingber, D. E. Engineered In Vitro Disease Models. *Annu. Rev. Pathol.: Mech. Dis.* **2015**, *10* (1), 195–262.
- (20) Marelli, M.; Gadhar, N.; Boero, G.; Chiquet, M.; Brugger, J. Cell Force Measurements in 3D Microfabricated Environments Based on Compliant Cantilevers. *Lab Chip* **2014**, *14* (2), 286–293.
- (21) Chan, V.; Jeong, J. H.; Bajaj, P.; Collens, M.; Saif, T.; Kong, H.; Bashir, R. Multi-Material Bio-Fabrication of Hydrogel Cantilevers and Actuators with Stereolithography. *Lab Chip* **2012**, *12* (1), 88–98.
- (22) McCain, M. L.; Agarwal, A.; Nesmith, H. W.; Nesmith, A. P.; Parker, K. K. Micromolded Gelatin Hydrogels for Extended Culture of Engineered Cardiac Tissues. *Biomaterials* **2014**, *35* (21), S462–S471.
- (23) Mannhardt, I.; Breckwoldt, K.; Letuffe-Brenière, D.; Schaaf, S.; Schulz, H.; Neuber, C.; Benzin, A.; Werner, T.; Eder, A.; Schulze, T.; Klampe, B.; Christ, T.; Hirt, M. N.; Huebner, N.; Moretti, A.; Eschenhagen, T.; Hansen, A. Human Engineered Heart Tissue: Analysis of Contractile Force. *Stem Cell Rep.* **2016**, *7* (1), 29–42.
- (24) Legant, W. R.; Pathak, A.; Yang, M. T.; Deshpande, V. S.; McMeeking, R. M.; Chen, C. S. Microfabricated Tissue Gauges to Measure and Manipulate Forces from 3D Microtissues. *Proc. Natl. Acad. Sci. U. S. A.* **2009**, *106* (25), 10097–10102.
- (25) Mills, R. J.; Titmarsh, D. M.; Koenig, X.; Parker, B. L.; Ryall, J. G.; Quaife-Ryan, G. A.; Voges, H. K.; Hodson, M. P.; Ferguson, C.; Drowley, L.; et al. Functional Screening in Human Cardiac Organoids Reveals a Metabolic Mechanism for Cardiomyocyte Cell Cycle Arrest. *Proc. Natl. Acad. Sci. U. S. A.* **2017**, *114* (40), E8372–E8381.
- (26) Ikeda, K.; Ito, A.; Imada, R.; Sato, M.; Kawabe, Y.; Kamihira, M. In Vitro Drug Testing Based on Contractile Activity of C2C12 Cells in an Epigenetic Drug Model. *Sci. Rep.* **2017**, *7* (1), 44570.
- (27) Wanjare, M.; Huang, N. F. Regulation of the Microenvironment for Cardiac Tissue Engineering. *Regener. Med.* **2017**, *12* (2), 187.
- (28) Yang, C.; DelRio, F. W.; Ma, H.; Killaars, A. R.; Basta, L. P.; Kyburz, K. A.; Anseth, K. S. Spatially Patterned Matrix Elasticity Directs Stem Cell Fate. *Proc. Natl. Acad. Sci. U. S. A.* **2016**, *113* (31), E4439–E4445.
- (29) Zhang, W.; Kong, C. W.; Tong, M. H.; Chooi, W. H.; Huang, N.; Li, R. A.; Chan, B. P. Maturation of Human Embryonic Stem Cell-Derived Cardiomyocytes (HESC-CMs) in 3D Collagen Matrix: Effects of Niche Cell Supplementation and Mechanical Stimulation. *Acta Biomater.* **2017**, *49*, 204–217.
- (30) Wang, Z.; Lee, S. J.; Cheng, H.-J.; Yoo, J. J.; Atala, A. 3D Bioprinted Functional and Contractile Cardiac Tissue Constructs. *Acta Biomater.* **2018**, *70*, 48–56.
- (31) Wang, H.; Svoronos, A. A.; Boudou, T.; Sakar, M. S.; Schell, J. Y.; Morgan, J. R.; Chen, C. S.; Shenoy, V. B. Necking and Failure of Constrained 3D Microtissues Induced by Cellular Tension. *Proc. Natl. Acad. Sci. U. S. A.* **2013**, *110* (52), 20923–20928.
- (32) Boudou, T.; Legant, W. R.; Mu, A.; Borochin, M. A.; Thavandiran, N.; Radisic, M.; Zandstra, P. W.; Epstein, J. A.; Margulies, K. B.; Chen, C. S. A Microfabricated Platform to Measure and Manipulate the Mechanics of Engineered Cardiac Microtissues. *Tissue Eng., Part A* **2012**, *18* (9–10), 910–919.
- (33) Sakar, M. S.; Neal, D.; Boudou, T.; Borochin, M. A.; Li, Y.; Weiss, R.; Kamm, R. D.; Chen, C. S.; Asada, H. H. Formation and Optogenetic Control of Engineered 3D Skeletal Muscle Bioactuators. *Lab Chip* **2012**, *12* (23), 4976–4985.
- (34) Schindelin, J.; Arganda-Carreras, I.; Frise, E.; Kaynig, V.; Longair, M.; Pietzsch, T.; Preibisch, S.; Rueden, C.; Saalfeld, S.; Schmid, B.; Tinevez, J.-Y.; White, D. J.; Hartenstein, V.; Eliceiri, K.; Tomancak, P.; Cardona, A. Fiji: An Open-Source Platform for Biological-Image Analysis. *Nat. Methods* **2012**, *9* (7), 676–682.
- (35) Treloar, L. R. G. *The Physics of Rubber Elasticity*, 3rd ed.; Oxford University Press, 1975.
- (36) Yoshida, N.; Yoshida, S.; Koishi, K.; Masuda, K.; Nabeshima, Y. Cell Heterogeneity upon Myogenic Differentiation: Down-Regulation of MyoD and Myf-5 Generates ‘Reserve Cells’. *J. Cell Sci.* **1998**, *111* (6), 769–779.
- (37) Schaaf, S.; Eder, A.; Vollert, I.; Stöhr, A.; Hansen, A.; Eschenhagen, T. Generation of Strip-Format Fibrin-Based Engineered Heart Tissue (EHT). In *Methods Mol. Biol.*; Radisic, M., Black, L. D., III, Eds.; Humana Press: New York, 2014; Vol. 1181, pp 121–129, DOI: 10.1007/978-1-4939-1047-2_11.
- (38) Yamaguchi, T.; Sato, R.; Sawae, Y. Propagation of Fatigue Cracks in Friction of Brittle Hydrogels. *Gels* **2018**, *4* (2), 53.
- (39) Ehrenhofer, A.; Elstner, M.; Wallmersperger, T. Normalization of Hydrogel Swelling Behavior for Sensoric and Actuatoric Applications. *Sens. Actuators, B* **2018**, *255*, 1343–1353.
- (40) Tanaka, K.; Sato, K.; Yoshida, T.; Fukuda, T.; Hanamura, K.; Kojima, N.; Shirao, T.; Yanagawa, T.; Watanabe, H. Evidence for Cell Density Affecting C2C12 Myogenesis: Possible Regulation of Myogenesis by Cell-Cell Communication. *Muscle Nerve* **2011**, *44* (6), 968–977.
- (41) Ostrovidov, S.; Ahadian, S.; Ramon-Azcon, J.; Hosseini, V.; Fujie, T.; Parthiban, S. P.; Shiku, H.; Matsue, T.; Kaji, H.; Ramalingam, M.; Bae, H.; Khademhosseini, A. Three-Dimensional Co-Culture of C2C12/PC12 Cells Improves Skeletal Muscle Tissue Formation and Function. *J. Tissue Eng. Regener. Med.* **2017**, *11* (2), S82–S95.

(42) Engler, A. J.; Griffin, M. A.; Sen, S.; Bönnemann, C. G.; Sweeney, H. L.; Discher, D. E. Myotubes Differentiate Optimally on Substrates with Tissue-like Stiffness: Pathological Implications for Soft or Stiff Microenvironments. *J. Cell Biol.* **2004**, *166* (6), 877–887.

Electronic supplementary information for 3D printed hydrogel multi assay platforms for robust generation of engineered contractile tissues

Experimental determination of the cantilever stiffness.

The stiffness of 3D printed PEGDA cantilevers was determined by deflecting the end of the cantilever by a defined distance of 220 μm using a metal pin controlled by a piezo actuator. Figure S1 shows an example of a cantilever before and after actuation.

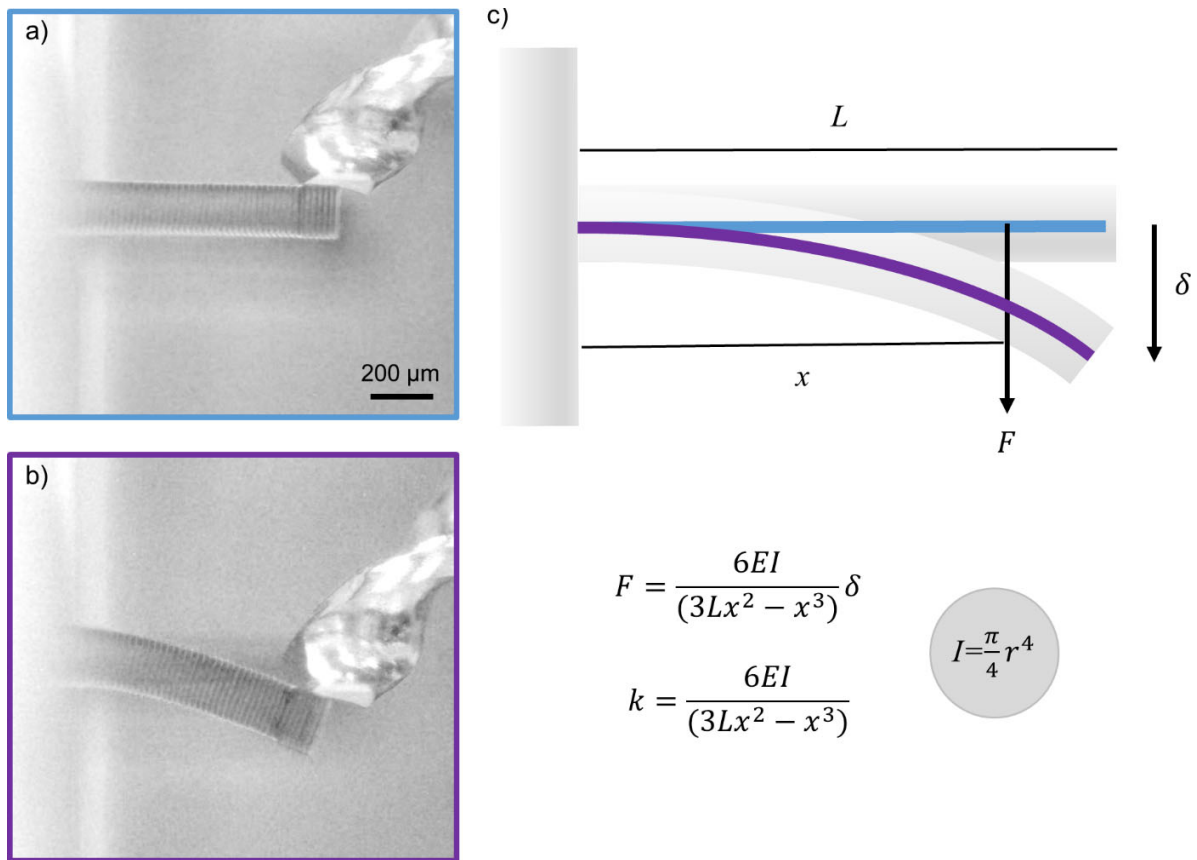


Figure S1. Optical micrographs of a horizontally oriented 200 μm diameter and 850 μm long cantilever (a) before displacement and (b) after vertical displacement of its end by 220 μm . The resulting force, F , is measured and used with the applied displacement, δ , for (c) calculating the elastic modulus, E , using Euler-Bernoulli beam theory. I is the moment of inertia, L is the length of the cantilever, and x is the point of applied force measured by the fixed cantilever end.

Determining the dimensional stability of indentations and protrusions

Blocks of 20% PEGDA and 50% PEGDA were printed with indentations and protrusions at their top surface, as seen in Figure S2. Rectangles are 3:1 in length to width ratio. The width of the rectangles are measured immediately after printing as well as after reaching equilibrium swelling in water.

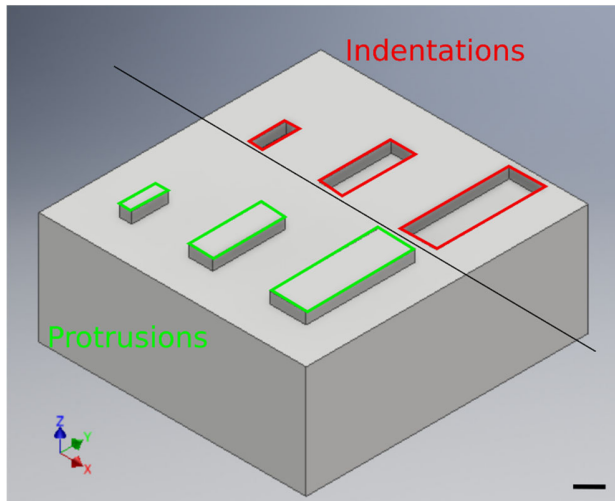


Figure S2. A PEGDA block 10 times the height of the geometries of importance are produced with indentations (marked in red) and protrusions (marked in green). Protrusions are 100 μm tall, and indentations are 100 μm deep. The width of the rectangles are 324 μm , 216 μm , and 108 μm , respectively. Scale bar: 200 μm .